THE UNIVERSITY OF QUEENSLAND

SCHOOL OF CIVIL ENGINEERING

REPORT CH95/14

PRESSURE, TURBULENCE AND TWO-PHASE FLOW MEASUREMENTS IN HYDRAULIC JUMPS

AUTHORS: Hang WANG, Frédéric MURZYN
and Hubert CHANSON

HYDRAULIC MODEL REPORTS

This report is published by the School of Civil Engineering at the University of Queensland. Lists of recently-published titles of this series and of other publications are provided at the end of this report. Requests for copies of any of these documents should be addressed to the Civil Engineering Secretary.

School of Civil Engineering
The University of Queensland
Brisbane QLD 4072
AUSTRALIA

Telephone: (61 7) 3365 4163
Fax: (61 7) 3365 4599

URL: http://www.eng.uq.edu.au/civil/

First published in 2014 by
School of Civil Engineering
The University of Queensland, Brisbane QLD 4072, Australia

ISBN No. 9781742721064

The University of Queensland, St Lucia QLD, Australia

Pressure, Turbulence and Two-Phase Flow Measurements in Hydraulic Jumps

by

Hang WANG

Ph.D. research student, The University of Queensland, School of Civil Engineering, Brisbane QLD 4072, Australia, E-mail: hang.wang@uqconnect.edu.au

Frédéric MURZYN

Lecturer, ESTACA Campus Ouest, Parc Universitaire de Laval Changé, Rue Georges Charpak, BP 76121, 53061 Laval Cedex 9, France, Email: frederic.murzyn@estaca.fr

and

Hubert CHANSON

Professor, The University of Queensland, School of Civil Engineering, Brisbane QLD 4072, Australia, Email: h.chanson@uq.edu.au

REPORT No. CH95/14

ISBN 9781742721064

School of Civil Engineering, The University of Queensland

April 2014

Hydraulic jump roller downstream of a sill along Katashima River at Oigami township (Japan) on 7 October 2012

ABSTRACT

A hydraulic jump takes place when a shallow high-speed free-surface flow impinges into a deeper slower flow region. Besides a sudden increase in depth, the most significant flow features include large turbulence seen both at the free-surface and inside the jump roller, as well as substantial air entrainment into the roller. The flow hydrodynamics is extremely complicated because of the interactions between a large number of turbulent two-phase flow properties with a broad range of relevant length and time scales. This report presents a detailed experimental study of the hydraulic jump. The total pressure field was measured in a series of vertical cross sections conducted in the roller, using a miniature probe. The air-water flow properties were measured simultaneously at the same location with a dual-tip phase-detection probe. The instantaneous free surface positions were scanned non-intrusively with a series of acoustic displacement meters, including immediately above the total pressure and air-water flow measurement location. The investigations were characterised by partially developed inflow conditions with Froude numbers ranging from 3.8 to 8.5 corresponding to Reynolds numbers between 3.5×10^4 and 8.0×10^4. The time-averaged free surface and air-water flow properties showed good agreement with previous findings. The free-surface fluctuation amplitude and frequency were larger in the first half roller close to the toe, than in the second half of roller. The longitudinal jump toe oscillations were associated with an instantaneous deformation of the roller free-surface. The vertical distributions of time-averaged air-water flow properties showed two main air-water flow regions: namely the turbulent shear layer for $y < y_*$ and a recirculation region above. The total pressure measurement was validated in the shear layer through a comparison with theoretical calculations based upon the measured two-phase flow data. The results showed that the pressure distribution was quasi-hydrostatic in the roller taking into account the flow aeration. In the shear layer, the vertical profiles of mean pressure and pressure fluctuations exhibited some marked maxima. The magnitudes of mean and fluctuation maxima increased with increasing Froude numbers and decreased with increasing distance from the jump toe for a given Froude number. Some cross-correlation analyses were performed between any two instantaneous signals of the horizontal jump toe oscillations, vertical free surface fluctuations, instantaneous total pressure and instantaneous void fraction. Some marked maximum correlation coefficients indicated the co-variation relationships. The simultaneous sampling of instantaneous free-surface, total pressure and void fraction fluctuations indicated two different sub-regions in the shear layer: the main shear layer and the lower shear layer next to the invert. The characteristic differences of each sub-region were discussed in terms of the two-phase flow and turbulence properties.

Keywords: Hydraulic jump, Free-surface measurements, Total pressure measurements, Two-phase flow measurement, Interactions between turbulence and air entrainment, co-variance.

TABLE OF CONTENTS

APPENDICES

LIST OF SYMBOLS

The following symbols are used in this report:

A	flow cross-section area (m^2);
A_1	inflow cross-section area (m^2);
A_2	downstream conjugate flow cross-section area (m^2);
B	characteristic channel width (m);
B'	characteristic channel width (m);
B_1	inflow free-surface width (m);
C	time-averaged void fraction defined as the volume of air per unit volume of air and water;
C_{max}	local maximum void fraction in the developing shear layer
C^*	local minimum void fraction at the boundary between the shear layer and recirculation regions;
c	instantaneous void fraction: c = 0 in water and c = 1 in air;
$D^\#$	dimensionless air bubble diffusivity in the air-water shear layer;
D^*	dimensionless air bubble diffusivity at the roller free-surface;
d	water depth (m);
d_1	inflow water depth (m) immediately upstream of the jump;
d_2	downstream conjugate water depth (m) measured immediately downstream of the jump roller;
F	bubble count rate (Hz) defined as the number of bubbles per second;
F_{clu}	cluster rate (Hz) defined as the number of clusters per second;
F_{cutoff}	cutoff frequency (Hz);
F_{ej}	production rate (Hz) of large vortical structures in the shear layer;
F_{fric}	boundary friction force (N);
F_{fs}	characteristic frequency (Hz) of free surface fluctuations;
F_{max}	maximum bubble count rate (Hz) in the developing shear layer;
$F_p^{(H)}$	upper characteristic frequency (Hz) of total pressure fluctuations;
$F_p^{(L)}$	lower characteristic frequency (Hz) of total pressure fluctuations;
F_{toe}	fluctuation frequency (Hz) of longitudinal jump toe location;
F_2	secondary maximum bubble count rate (Hz) next to the free surface;
Fr	Froude number;
Fr_1	inflow Froude number defined as: $Fr_1 = V_1/(g \times A_1/B_1)^{1/2}$; for a rectangular channel: $Fr_1 = \frac{V_1}{\sqrt{g \times d_1}}$
g	gravity acceleration (m/s^2): g = 9.794 m/s^2 in Brisbane;
h	upstream sluice gate opening (m);
Ku	excess kurtosis;
L_r	roller length (m);

L_t turbulent length scale (m);

Mo Morton number;

N number of data points;

N_{clu} cluster size defined as the average number of particles per cluster;

P time-averaged total pressure (Pa) relative to the atmospheric pressure;

P_{clu} cluster proportion defined as the total percentage of bubbles/droplets travelling in clusters;

P_k kinetic pressure (Pa);

P_{max} maximum time-averaged total pressure (Pa);

P_{stat} (static) pressure (Pa);

P_o piezometric pressure (Pa);

p instantaneous total pressure (Pa) relative to the atmospheric pressure;

p_{max} maximum instantaneous total pressure (Pa);

p_{min} minimum instantaneous total pressure (Pa);

p' standard deviation of total pressure (Pa);

p'_{max} maximum standard deviation of total pressure (Pa);

Q water discharge (m^3/s);

q water discharge per unit width (m^2/s);

R normalised correlation coefficient;

R_{max} maximum correlation coefficient;

R_{pc} normalised correlation coefficient between instantaneous void fraction and instantaneous total pressure;

$(R_{pc})_{max}$ maximum correlation coefficient between the instantaneous void fraction & instantaneous total pressure;

R_{xc} normalised correlation coefficient between horizontal jump toe oscillations and instantaneous void fraction;

$(R_{xc})_{max}$ maximum correlation coefficient between the horizontal jump toe oscillations and instantaneous void fraction;

R_{xp} normalised correlation coefficient between the horizontal jump toe oscillations and instantaneous total pressure;

$(R_{xp})_{max}$ maximum correlation coefficient between the horizontal jump toe oscillations and instantaneous total pressure;

R_{xx} normalised auto-correlation coefficient;

R_{xy} normalised correlation coefficient between horizontal jump toe oscillations and vertical free surface fluctuations;

$(R_{xy})_{max}$ maximum correlation coefficient between the horizontal jump toe oscillations and vertical free surface fluctuations;

R_{yc} correlation coefficient between vertical free surface fluctuations and instantaneous void fraction;

$(R_{yc})_{max}$	maximum correlation coefficient between the vertical free surface fluctuations & instantaneous void fraction;
R_{yp}	correlation coefficient between vertical free surface fluctuations and instantaneous total pressure;
$(R_{yp})_{max}$	maximum correlation coefficient between the vertical free surface fluctuations & instantaneous total pressure;
Re	Reynolds number defined as: $Re = \rho \times V_1 \times d_1/\mu$;
Sk	excess skewness;
T	average air-water interfacial travel time (s) between phase-detection probe sensor tips;
Tu	turbulence intensity defined as: Tu = v'/V;
$T_{0.5}$	characteristic time lag (s) for which the auto-correlation function equals 0.5;
t	time (s);
V	time-averaged air-water interfacial velocity (m/s): $V = \Delta x_{tip}/T$;
V_{max}	maximum interfacial velocity (m/s) in the shear layer;
V_{recirc}	recirculation velocity (m/s) in the roller recirculation region;
V_1	inflow velocity (m/s): $V_1 = Q/(W \times d_1)$;
V_2	downstream conjugate flow velocity (m/s): $V_2 = Q/(W \times d_2)$;
Vol	control volume size (m^3);
v'	standard deviation of longitudinal interfacial velocity (m/s);
W	rectangular channel width (m);
We	Weber number;
x	longitudinal distance (m) from the upstream sluice gate positive downstream;
x_1	jump toe position (m)
y	vertical elevation (m) above invert positive upwards;
y_{Cmax}	characteristic elevation (m) of local maximum void fraction in the shear layer;
y_{Fmax}	characteristic elevation (m) of maximum bubble count rate in the shear layer;
y_{Pmax}	characteristic elevation (m) of maximum mean total pressure in the shear layer;
$y_{p'max}$	characteristic elevation (m) of maximum total pressure fluctuations in the shear layer;
y_{Vmax}	characteristic elevation (m) of maximum velocity in the shear layer;
y_{F2}	characteristic elevation (m) of secondary maximum bubble count rate near the free surface;
$y_{0.5}$	characteristic elevation (m) where the time-averaged velocity is half of maximum: $y_{0.5} = y(V=V_{max}/2)$;
y_{50}	characteristic elevation (m) where C = 0.50;
y_{90}	characteristic elevation (m) where C = 0.90;
y_*	characteristic elevation (m) where $C = C_*$; boundary between shear layer and recirculation regions;
y_{**}	characteristic elevation (m) corresponding to the boundary between main shear layer and lower shear layer sub-regions;

z	transverse distance (m) positive towards the right sidewall, with z = 0 on the channel centreline;
ΔH	total head loss (m) in hydraulic jump;
Δx_{tip}	longitudinal distance (m) between probe sensor tips;
Δz_{PP}	transverse distance (m) between phase-detection probe and pressure probe;
Δz_{tip}	transverse distance (m) between phase-detection probe sensor tips;
ε	dimensionless coefficient;
η	water elevation (m) above the invert;
η'	standard deviation of instantaneous water elevation (m);
η'_{max}	maximum standard deviation of instantaneous water elevation (m);
μ_w	dynamic viscosity (Pa.s) of water;
ν	kinematic viscosity (m^2/s);
θ	angle between channel bed slope and horizontal;
ρ_w	water density (kg/m^3);
σ	surface tension (m^2/s) between air and water (N/m);
τ	time lag (s);
$\tau_{0.5}$	characteristic time lag (s) for which the cross-correlation function equals $0.5 \times R_{max}$;
Ø	diameter (m);

Subscript

max	maximum;
x	longitudinal direction positive downstream;
y	vertical direction positive upwards;
w	water;
z	transverse direction;
1	inflow property;
2	downstream conjugate flow property;

Abbreviations

ADM	acoustic displacement meter;
C	Celsius;
CB00	CHANSON and BRATTBERG (2000).
fps	frames per second;
GC07	GUALTIERI and CHANSON (2007).
HDPE	high-density polyethylene;
h	hour;
min	minute;
MEMS	micro-electro-mechanical system;
Nb	number;

PDF	probability distribution function;
PDP	phase-detection probe;
PSD	power spectral density;
Std	standard deviation;
s	second;
TPP	total pressure probe;
WC13	WANG and CHANSON (2013).

1. INTRODUCTION

1.1 PRESENTATION

A hydraulic jump is a rapidly-varied open channel flow characterised by the sudden transition from a supercritical open channel flow regime (Fr > 1) to a subcritical regime (Fr < 1). The transition is associated with a rapid increase of water depth, a highly turbulent flow with macro-scale vortices, significant kinetic energy dissipation, a two-phase flow region and some strong turbulence interactions with the free surface leading to splashes and droplet formation. When the inflow Froude number Fr_1 is large, the hydraulic jump features a breaking roller with "white waters" highlighting the strong mixing of air and water close to the free surface and the foamy appearance of the upper free-surface region. A hydraulic jump may take place in natural rivers at a depth discontinuity, a change in bed slope or a man-made structure (Fig. 1-1). This free surface flow is also commonly encountered in dam spillways and industrial plants in order to dissipate energy and/or to enhance mixing and aeration for ecological purposes and/or chemical treatments (Fig. 1-2). Industrial applications include energy dissipation downstream of high-velocity spillways, in-stream re-aeration structures, and mixing enhancement (AVERY and NOVAK 1978, HAGER 1992, CHANSON 2009). Leisurely applications encompass artificial generation of hydraulic jumps in river streams and man-made course for extreme sports such as kayaking and rafting.

Figure 1-3A shows a sketch of a hydraulic jump in a rectangular, horizontal and smooth channel together with the relevant notations. Figure 1-3B illustrates the typical vertical profiles of void fraction and bubble count rate in the hydraulic jump roller. In Figure 1-3A, x and y define the longitudinal and vertical directions respectively, x_1 denotes the longitudinal position of the jump toe, d_1 is the upstream flow depth, V_1 is the upstream flow velocity, d_2 is the downstream conjugate flow depth and V_2 is the downstream flow velocity. In Figure 1-3B, y_{Cmax} is the vertical position where the void fraction reaches a local maximum C_{max} in the shear layer and y_{Fmax} is the vertical position where the bubble count rate is maximum ($F = F_{max}$).

(A) Hydraulic jump on Mattervispa stream, Zermatt (Switzerland) on 14 December 2013, looking downstream

(B) Three-dimensional hydraulic jump roller downstream of a sill along Katashima River at Oigami township (Japan) on 7 October 2012

(C) Hydraulic jump roller and details of upper spray region along Katashima River at Oigami township (Japan) on 7 October 2012 (shutter speed: 1/8,000 s)

Fig. 1-1 - Hydraulic jumps in rivers

(A) Hydraulic jump downstream of a weir along Katashima River at Oigami township (Japan) on 7 October 2012 0- Top view looking downstream of a concrete ramp

(B) Drop structures along Daiya River below Mount Nantai, Nikko City (Japan) close to the railway station on 8 October 2012

(C) Hydraulic jump at a weir toe on Ogika River, upstream of Ikari dam, Tochigi Prefecture (Japan) on 8 October 2012 - $q \sim 0.1$ m^2/s, $Re \sim 1 \times 10^5$

Fig. 1-2 - Hydraulic jumps at weirs and dams

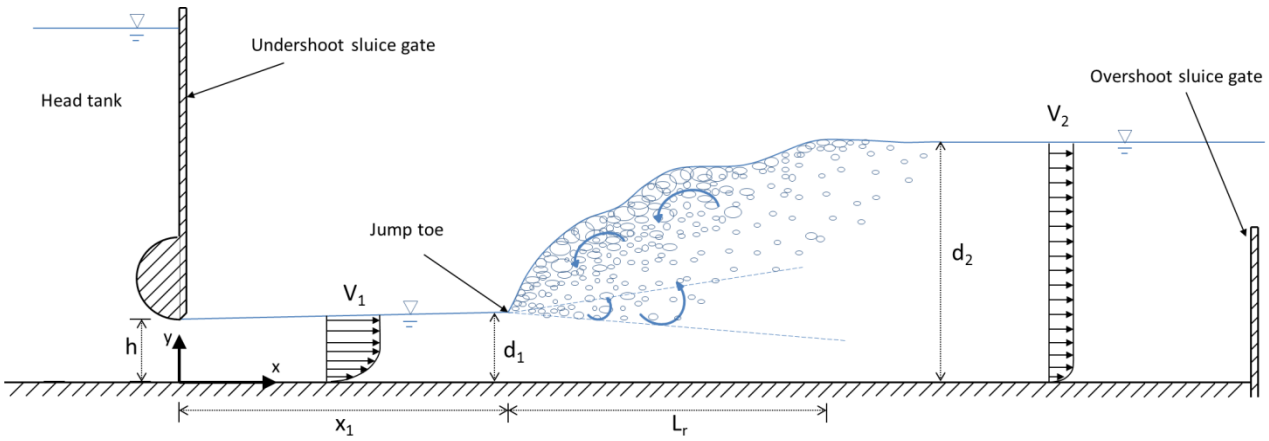

(A) Sketch of hydraulic jump in a laboratory channel

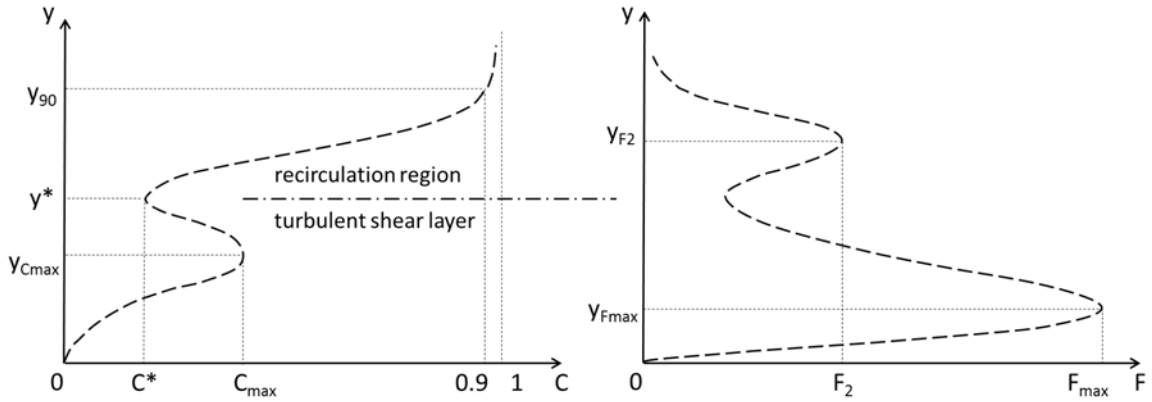

(B) Vertical distributions of air-water flow properties (Left: void fraction; Right: bubble count rate)

Fig 1-3 - Sketch of experimental hydraulic jump and vertical distributions of basic air-water flow properties

1.2 THEORETICAL CONSIDERATIONS

A hydraulic jump is defined by its inflow Froude number Fr_1:

$$Fr_1 = \frac{V_1}{\sqrt{g \times d_1}} \quad (1.1)$$

where g is the gravity acceleration. In a hydraulic jump, Fr_1 is always greater than unity. Depending on the inflow Froude number, a hydraulic jump may be undular (Fr_1 > 1.5 to 4) or exhibit a marked roller at higher Froude numbers (CHANSON 2009).

The first significant experimental and theoretical works on hydraulic jumps were conducted by BIDONE (1819) and BELANGER (1841) (CHANSON 2009b). BIDONE (1819) measured the upstream and downstream flow depths as well as the length of the jump for 2.6 < Fr_1 < 3.2. BELANGER (1841) developed a theoretical solution for the ratio of conjugate depths based upon the momentum principle:

$$\frac{d_2}{d_1} = \frac{1}{2} \times \left(\sqrt{1 + 8 \times Fr_1^{\ 2}} - 1 \right) \tag{1.2}$$

where d is the flow depth and the subscript 1 and 2 refer to the upstream and downstream flow conditions respectively. Equation (1.2) is valid only for a smooth horizontal rectangular channel. An expanded result may be derived in terms of the ratio of conjugate cross-sectional areas for an irregular prismatic channel (CHANSON 2012):

$$\frac{A_2}{A_1} = \frac{1}{2} \times \frac{\sqrt{\left(2 - \frac{B'}{B}\right)^2 + 8 \times \frac{\frac{B'}{B}}{\frac{B_1}{B}} \times Fr_1^{\ 2}} - \left(2 - \frac{B'}{B}\right)}{\frac{B'}{B}} \tag{1.3}$$

where A is the flow cross-section area, B_1 is the upstream free-surface width, and B and B' are characteristic channel widths defined respectively as:

$$B = \frac{A_2 - A_1}{d_2 - d_1} \tag{1.4}$$

$$B' = \frac{\int_{A_1}^{A_2} \int \rho \times g \times (d_2 - y) \times dA}{\frac{1}{2} \times \rho \times g \times (d_2 - d_1)^2} \tag{1.5}$$

with y the vertical elevation above the invert. In Equation (1.3), the Froude number is defined as:

$$Fr_1 = \frac{V_1}{\sqrt{g \times \frac{A_1}{B_1}}} \tag{1.6}$$

For a rectangular channel, Equation (1.3) yields the Bélanger equation (Eq. (1.2)).

The total head loss may be derived from the energy principle. For a rectangular channel, it gives:

$$\frac{\Delta H}{d_1} = \frac{1}{16} \times \frac{\left(\sqrt{1 + 8 \times Fr_1^{\ 2}} - 3\right)^3}{\sqrt{1 + 8 \times Fr_1^{\ 2}} - 1} \tag{1.7}$$

Equation (1.7) implies that the rate of energy dissipation in the hydraulic jump exceeds 70% for $Fr_1 > 9$.

Discussion

In presence of flow resistance, the momentum principle may be derived for a hydraulic jump in a flat irregular channel (CHANSON 2012):

$$(V_1 - V_2)^2 = \frac{1}{2} \times \frac{g \times (A_2 - A_1)^2}{B \times A_1 \times A_2} \times \left(\left(2 - \frac{B'}{B} \right) \times A_1 + \frac{B'}{B} \times A_2 \right) + \frac{A_2}{A_2 - A_1} \times \frac{F_{fric}}{\rho \times g \times \frac{A_1^2}{B}} \quad (1.8)$$

where F_{fric} is the flow resistance force. After re-arrangement, it yields:

$$Fr_1^2 = \frac{1}{2} \times \frac{A_2}{A_1} \times \frac{B_1}{B} \times \left(\left(2 - \frac{B'}{B} \right) + \frac{B'}{B} \times \frac{A_2}{A_1} \right) + \frac{A_2}{A_2 - A_1} \times \frac{F_{fric}}{\rho \times g \times \frac{A_1^2}{B}} \quad (1.9)$$

Equation (1.9) gives a theoretical solution with the upstream Froude number being a function of the ratio of conjugate cross-sectional areas A_2/A_1 and the flow resistance force. For a given upstream Froude number, Equation (1.9) implies a smaller ratio of conjugate depths d_2/d_1 with increasing flow resistance, a result consistent with the physical data of LEUTHEUSSER and SCHILLER (1975), EAD and RAJARATNAM (2002) and PAGLIARA et al. (2008). The effects of flow resistance on the ratio of conjugate depths become negligible for $Fr_1 > 2$ to 3 (CHANSON 2012).

For a hydraulic jump down a smooth sloping rectangular prismatic channel, the momentum principle gives an analytical solution for a flat slope, i.e. $\cos\theta \approx 1$, where θ is the angle between the invert slope and horizontal, and positive downwards (CHANSON 2013). The ratio of conjugate depths equals:

$$\frac{d_2}{d_1} = \frac{1}{2} \times \left(\sqrt{(1-\varepsilon)^2 + 8 \times \frac{Fr_1^2}{1-\varepsilon}} - (1-\varepsilon) \right) \quad (1.10)$$

where ε is a dimensionless coefficient defined as:

$$\varepsilon = \frac{Vol \times \sin\theta}{B_1 \times d_1^2 \times (Fr_1^2 - 1)} \quad (1.11)$$

with Vol the volume of the control volume encompassing the jump roller, such as the weight force component in the flow direction is $\rho \times g \times Vol \times \sin\theta$. The result (Eq. (1.11)) shows that the ratio of conjugate depths decreases with increasing downward bed slope for a fixed inflow Froude number.

1.3 DIMENSIONAL CONSIDERATIONS

All theoretical and numerical analyses of hydraulic jumps at the sub-millimetric scale are based upon a large number of relevant equations to describe the two-phase gas-liquid turbulent flow motion and the interactions between entrained air and turbulence. For a hydraulic jump with a marked roller, the analysis outputs must be tested against a broad range of air-water flow measurements: "*Unequivocally [...] experimental data are the sine qua non of validation; no experimental data means no validation*" (ROACHE 2009). Physical modelling may provide some relevant information into the flow motion, provided the proper selection of a suitable dynamic similarity (LIGGETT 1994, FOSS et al. 2007, CHANSON 2013b). Considering a hydraulic jump in

a smooth horizontal rectangular channel, dimensional considerations give a series of dimensionless relationships in terms of the turbulent flow properties at a position (x,y,z) within the hydraulic jump roller as functions of the inflow properties, fluid properties and channel configurations. Using the upstream flow depth d_1 as the characteristic length scale, a dimensional analysis yields:

$$\frac{P}{0.5\times\rho_w\times V_1^2},\frac{p'}{0.5\times\rho_w\times V_1^2},\frac{V}{V_1},\frac{v'}{V_1},C,\frac{F\times d_1}{V_1},\frac{L_t}{d_1},\ldots = F_1\left(\frac{x-x_1}{d_1},\frac{y}{d_1},\frac{z}{d_1},\frac{V_1}{\sqrt{g\times d_1}},\rho_w\times\frac{V_1\times d_1}{\mu_w},\frac{\rho_w\times V_1^2\times d_1}{\sigma},\frac{v_1'}{V_1},\frac{x_1}{d_1},\frac{W}{d_1},\ldots\right) \quad (1.12)$$

where P is the pressure, p' is a characteristic pressure fluctuation, V is the interfacial velocity, v' is a characteristic turbulent velocity, C is the void fraction, F is the bubble count rate defined as the number of bubbles detected per second in a small control volume, L_t is a turbulent length scale, x is the longitudinal coordinate, y is the vertical elevation above the invert, z is the transverse coordinate measured from the channel centreline, ρ_w and μ_w are the water density and dynamic viscosity respectively, σ the surface tension between air and water, x_1 is the longitudinal coordinate of the jump toe, W is the channel width, v_1' is a characteristic turbulent velocity at the inflow (Fig. 1-3A). In the right hand side of Equation (1.12), the 4th, 5th and 6th terms are respectively the upstream Froude number Fr_1, the Reynolds number Re and the Weber number We.

In a hydraulic jump, the momentum considerations demonstrate the significance of the inflow Froude number (BELANGER 1841, LIGHTHILL 1978) and the selection of the Froude similitude derives implicitly from basic theoretical considerations (LIGGETT 1994, CHANSON 2012). The Froude dynamic similarity is commonly applied in the hydraulic literature (HENDERSON 1966, NOVAK and CABELKA 1981), while the Reynolds number is another relevant Π-term since the hydraulic jump roller is a turbulent shear flow (ROUSE et al. 1959, RAJARATNAM 1965, HOYT and SELLIN 1989). The Π-Buckingham theorem implies that any dimensionless number may be replaced by a combination of itself and other dimensionless numbers. For example, the Froude, Reynolds or Weber number may be replaced by the Morton number Mo since:

$$Mo = \frac{g\times\mu_w^4}{\rho_w\times\sigma^3} = \frac{We^3}{Fr^2\times Re^4} \quad (1.13)$$

When the same fluids (air and water) are used in models and prototype as in the present study, the Morton number Mo becomes an invariant and this adds an additional constraint upon the dimensional analysis. Equation (1.12) gives as simplified expression:

$$\frac{P}{0.5\times\rho_w\times V_1^2},\frac{p'}{0.5\times\rho_w\times V_1^2},\frac{V}{V_1},\frac{v'}{V_1},C,\frac{F\times d_1}{V_1},\frac{L_t}{d_1},\ldots = F_2\left(\frac{x-x_1}{d_1},\frac{y}{d_1},\frac{z}{d_1},Fr_1,Re,\frac{v_1'}{V_1},\frac{x_1}{d_1},\frac{W}{d_1},\ldots\right) \quad (1.14)$$

Usually, as in Equation (1.14), the Reynolds number is selected instead of the Weber number because prototype hydraulic jumps operate with Reynolds numbers from 10^6 to in excess of 10^9 (Fig. 1-1 & 1-2). For such large Reynolds numbers, the surface tension is considered of lesser significance compared to the viscous effects in the turbulent shear regions (WOOD 1991, CHANSON 1997, ERVINE 1998). Note further that the Froude and Morton similarities imply that $We \propto Re^{4/3}$ (Eq. (1.13)).

Physically it is impossible to fulfil simultaneously the Froude and Reynolds similarity requirements, unless working at full scale (Eq. (1.14)). Laboratory modelling is typically conducted based upon a Froude similitude, including the present study. It is acknowledged the air bubble entrainment is adversely affected by significant scale effects in small size models (RAO and KOBUS 1971, CHANSON 1997).

1.4 BIBLIOGRAPHY

For the last five decades, many experimental investigations of hydraulic jumps were undertaken. Some significant contributions included, in alphabetical order, BEN MEFTAH et al. (2007), CHACHEREAU and CHANSON (2011a,2011b), CHANSON (1995,1997,2007,2009,2010,2011a,2011b), CHANSON and MONTES (1995), CHANSON and BRATTBERG (2000), CHANSON and GUALTIERI (2008), CHANSON and CHACHEREAU (2013), HAGER et al. (1990), KUCUKALI and CHANSON (2008), LENNON and HILL (2006), LIU et al. (2004), MOSSA and TOLVE (1998), MOUAZE et al. (2005), MURZYN and CHANSON (2008,2009), MURZYN et al. (2005,2007), RAJARATNAM (1962,1965), RESCH and LEUTHEUSSER (1972,1972b), RESCH et al. (1974), RICHARD and GAVRILYUK (2013), ROUSE et al. (1959), WANG and CHANSON (2014), ZHANG et al. (2013)... These studies focused on the two-phase flow properties, free surface motions and turbulent flow structures.

The main conclusions to date may be summarised as:

(a) The pioneering works of RAJARATNAM (1962,1965) and RESCH and LEUTHEUSSER (1972,1972b) brought some basic fundamental knowledge dealing with the turbulent and bubbly flow structures as well as with the influence of the inflow conditions on the bubbly flow structures;

(b) The longitudinal profile of the roller was investigated theoretically by VALIANI (1997) and RICHARD and GAVRILYUK (2013), while the latters predicted also the jump toe oscillations and free-surface fluctuations. The free surface and motions were investigated using either intrusive wire gauges by MOUAZE et al. (2005) and MURZYN et al. (2007) or non-intrusive acoustic displacement meters by CHACHEREAU and CHANSON (2011b), MURZYN and CHANSON (2009), ZHANG et al. (2013) depicting the mean and turbulent free surface profiles as well as the longitudinal and transversal length scales developing at the free surface, the jump roller and the

aeration lengths;

(c) A few studies developed a similitude between hydraulic jumps and plunging/wall jet flows in terms of velocity profiles (CHANSON 1995, CHANSON and BRATTBERG 2000, HOYT and SELLIN 1989, RAJARATNAM 1965), while CHANSON (1995,2007,2010) and MURZYN et al. (2005) showed that self-similar vertical profiles of interfacial velocity and void fraction, bubble count rate were observed;

(d) At the small scales, a number of two-phase flow studies showed that bubble clustering is a characteristic feature of turbulence-bubble interactions in a hydraulic jump (CHANSON 2007, GUALTIERI and CHANSON 2010);

(e) Scale effects affecting air entrainment in hydraulic jumps were investigated with experiments conducted with the same Froude number but different Reynolds numbers by CHANSON and GUALTIERI (2008), MURZYN and CHANSON (2008) and CHANSON and CHACHEREAU (2013). The results showed drastic scale effects in terms of the two-phase flow properties, implying that a true dynamic similitude could not be achieved with a Froude similitude in laboratory experiments; hence further investigations are required at near full-scale for a better knowledge of the two-phase flow dynamics;

(f) In the last fifteen years, the development and improvement of optical technology led to some experimental investigations using acoustic Doppler velocimetry (ADV), laser Doppler anemometry (LDA), particle image velocimetry (PIV) and video analysis to characterise the internal structure of the flow and the motion of the toe. These techniques are often limited because of limited optical access caused by the presence of air bubbles. LIU et al. (2004) restricted their measurements to low Froude numbers. MOSSA and TOLVE (1998), LIN et al. (2012) and LEANDRO et al. (2012) brought informations about the fluctuating nature of the jump and the two-phase flow properties close to the glass sidewall;

(g) To date few studies presented the pressure measurements inside the jump. Some earlier studies investigated the pressure fluctuations beneath hydraulic jumps (VASILIEV and BUKREYEV 1967, ABDUL KHADER and ELANGO 1974, LOPARDO and HENNING 1985, FIOROTTO and RINALDO 1992). Recently LOPARDO (2013) found a relationship between turbulence intensity and a pressure fluctuation coefficient, albeit from different sets of experiments which were not performed at the same time.

1.5 STRUCTURE OF THE REPORT

The novelty of the present experimental work deals with the simultaneous measurements the free surface, two-phase flow properties and internal total pressure at the same point. This approach enables a detailed characterisation of the air-water flow field, including some correlative results

between the sensor outputs. New experiments were performed and the experimental data were carefully analysed.

After a brief introduction, the experimental setup, data processing techniques and experimental conditions are presented in Chapter 2. Chapter 3 focuses on the experimental results dealing with the free surface and the two-phase flow properties, which were compared to previous relevant studies. Chapter 4 presents the pressure probe measurements and associated results. Some cross-correlations between the probe signals will be presented in Chapter 5 and final conclusions will follow in Chapter 6. A number of appendices are available, summarising the experimental flow conditions, showing some photographs taken during the experiments and giving all the experimental data.

2. EXPERIMENTAL SETUP, DATA ANALYSIS AND EXPERIMENTAL CONDITIONS

2.1 EXPERIMENTAL SETUP

New experiments were performed in a horizontal rectangular flume at the University of Queensland (Fig. 2-1). The facility was a relatively large-size channel of 0.5 m width and 3.2 m length. The sidewalls were 0. 4 m high made of glass while the channel bed was made out of HDPE with a very smooth surface. The inflow was controlled by an upstream rounded undershoot gate seen in Figure 2-1A and the downstream flow conditions were controlled by a vertical overshoot gate. The channel was previously used by WANG and CHANSON (2013,2014), but new flow conditions were tested herein. Some photographs of the experimental facility are shown in Figure 2-1.

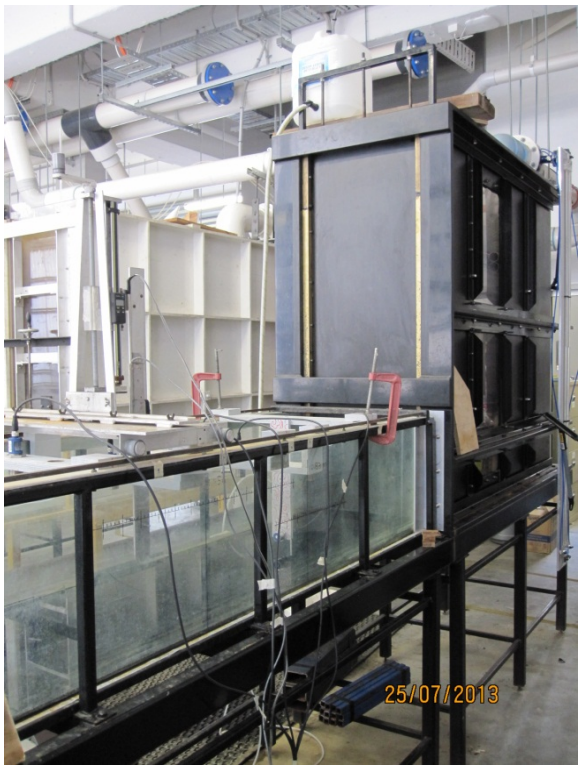

(A) General view of channel with HDPE bed and glass sidewalls - Flow direction from right to left

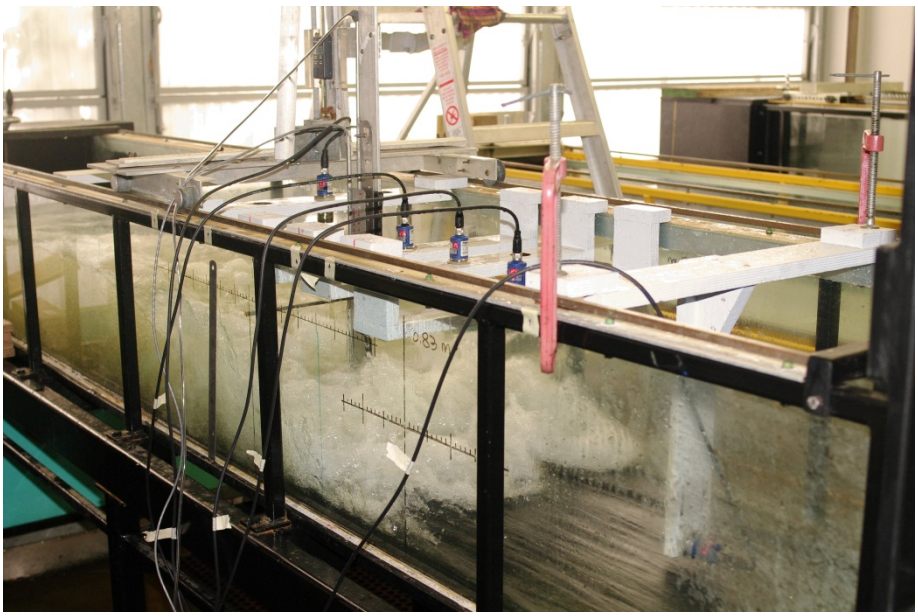

(B) Hydraulic jump: Q = 0.0399 m^3/s, d_1 = 0.02 m, x_1 = 0.083 m, Fr_1 = 8.5, Re = 79,800 - View from upstream with flow direction from right to left

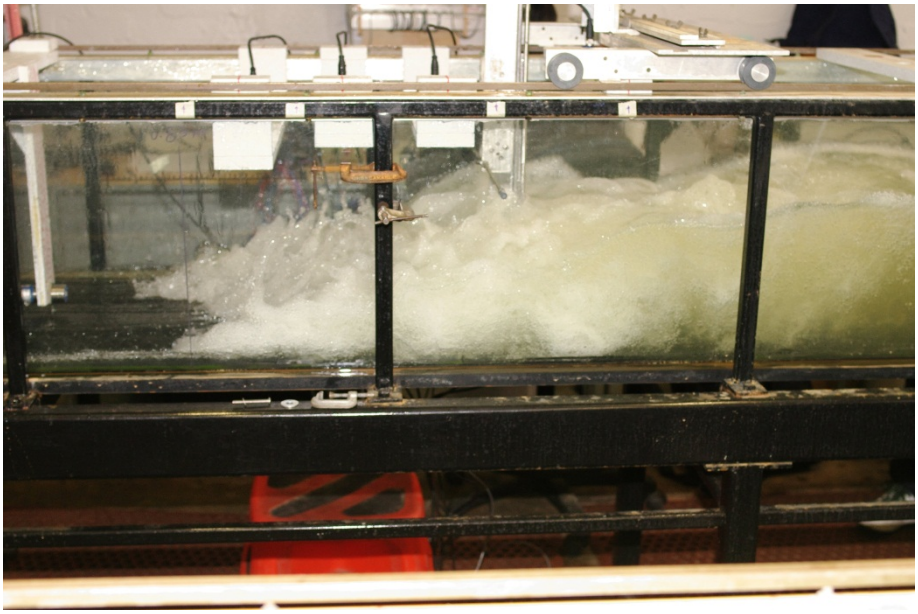

(C) Side view of hydraulic jump roller - Flow direction from right to left (Same flow conditions as Fig. 2-1B)

Fig 2-1 - Experimental channel for hydraulic jump modelling at the University of Queensland

2.2 INSTRUMENTATION AND CALIBRATION

The channel was fed by two parallel water lines supplied with a large constant head reservoir system. The water discharge was measured with Venturi meters located in each supply line. The Venturi meters were calibrated on-site with a thin plate V-notch for discharges under 0.01 m^3/s and with a full-width thin plate weir for discharges from 0.01 to 0.05 m^3/s. The discharge measurement was accurate within $\pm$2%. The maximum discharge was 0.090 m^3/s with both supply lines.

The inflow conditions were controlled by a vertical undershoot sluice gate with semi-circular rounded shape (Ø = 0.3 m). For all the experiments, the gate opening was set at h = 0.020 m. The upstream clear water flow depth d_1 was measured using rail mounted point gauges with a 0.2 mm accuracy. In the present study, d_1 was equal to the gate opening: d_1 = h within the experimental error.

2.2.1 Acoustic displacement meters (ADMs)

The instantaneous free surface elevations were recorded using several Microsonic^{TM} acoustic displacement meters (ADMs). The principle of acoustic displacement meter is based upon the travel time measurement of an acoustic beam emitted by the sensor, propagating (downward or horizontally) toward the free surface and being reflected back to the sensor. MURZYN and CHANSON (2007) discussed the accuracy of this technique to depict the motion of fluctuating free-surface. Importantly the measurement technique was non-intrusive and did not disturb the jump motion.

Herein four Microsonic^{TM} Mic+25/IU/TC sensors were mounted above the jump. The measurement distance ranged from 30 to 250 mm with 0.18 mm accuracy and 50 ms response time. One Mic+35/IU/TC sensor was mounted horizontally upstream the jump, 5 cm above the channel bed. It captured the horizontal motion of the jump roller. The measurement distance was between 60 and 350 mm with 0.18 mm accuracy and 70 ms response time. Special care was taken during the experiments to wipe the sensitive part of ADMs to avoid droplets or water projection interferences. Each probe signal output was scanned at 5 kHz for 180 s. The sensors are seen in Figures 2-1B and 2-1C. Before each experiment, the ADM sensors were calibrated. A linear relationship between the voltage output and the distance from the sensor head to a fixed boundary was obtained for each sensor (App. E). Figure 2-2 shows typical calibration curves.

During the experiments, some erroneous samples could be recorded for a number of different reasons: e.g., free surface not horizontal/vertical, measurement area too bubbly/foamy, out of range measurements, droplets, splashing….This led to erroneous spikes which did not reflect the real position of the free surface. The erroneous data were manually removed using a simple threshold technique. Overall only a small part of points were removed (less than 3%).

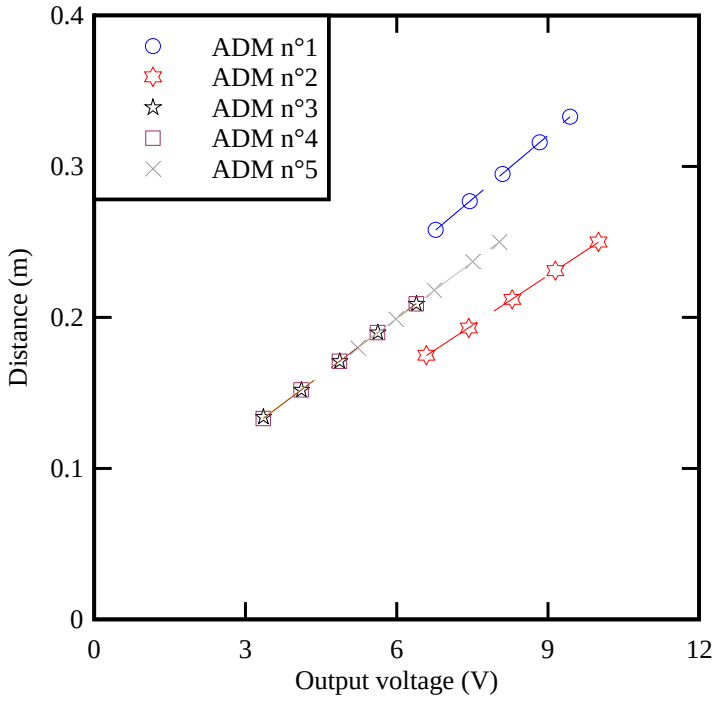

Fig 2-2 - Calibration of five acoustic displacement meters

2.2.2 Phase-detection probe (PDP)

The air-water flow properties were recorded using a dual-tip phase-detection probe (Fig. 2-3). The probe was manufactured based upon a needle design to pierce bubbles and droplets and worked based upon the difference in electrical resistance between air and water. The probe was equipped with two identical sensors with an inner diameter of 0.25 mm. The longitudinal distance between probe tips was Δx_{tip} = 7.25 mm (Distance 1, Fig. 2-3) while the trailing tip was offset in the transverse direction by Δz_{tip} = 2.2 mm (Distance 2, Fig. 2-3).

The dual-tip probe was excited by an electronic system (Ref. UQ82.518) designed with a response time of less than 10 µs. The vertical elevation of the probe was controlled by a Mitutomo™ digimatic scale unit with an accuracy of 0.01 mm. Each probe sensor was sampled at 5 kHz for 180 s: that is, using the sampling rate as MURZYN and CHANSON (2009) and CHACHEREAU and CHANSON (2011b) ([1]) but with a longer sampling duration. During the present study, the probe leading tip was aligned vertically with an acoustic displacement meters Microsonic™ Mic+25.

[1] That is, the sampling frequency when the phase-detection probe and acoustic displacement meters were used simultaneously.

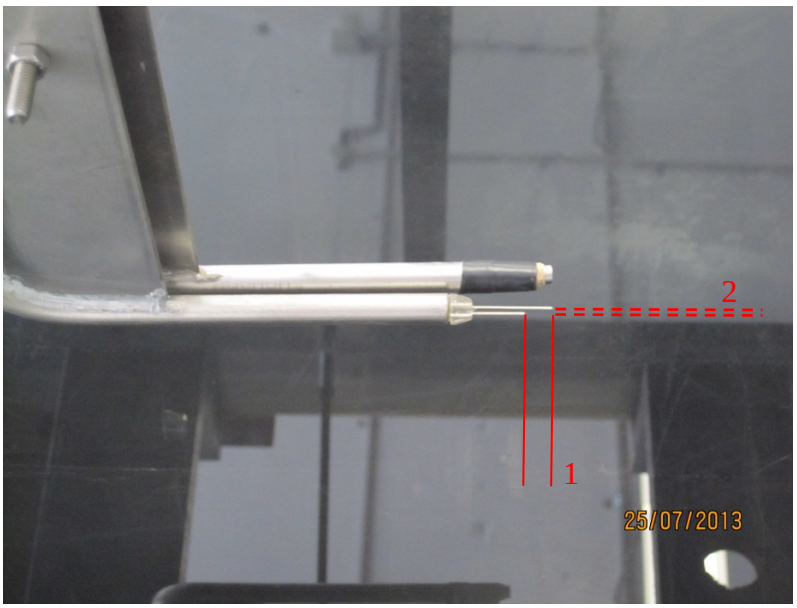

Fig 2-3 - Dual-tip conductivity phase-detection probe and pressure probe mounted together (view in elevation) - Flow from right to left - Longitudinal distance (1) between tips Δx_{tip} = 7.25 mm; transverse distance (2) between tips Δz_{tip} = 2.2 mm.

The analysis of the probe voltage output was based upon a single threshold technique with a threshold set between 45% and 55% of air-water range. The single threshold technique is a robust method that is well-suited to free surface flows (TOOMBES 2002, CHANSON and CAROSI 2007). A number of air-water flow properties were derived from the signal analysis. These included the void fraction C defined as the volume of air per unit volume of air and water, the bubble count rate F defined as the number of bubbles impacting the probe tip per second, and the air chord time distribution where the chord time is defined as the time spent by the bubble on the probe tip. Further air-water flow properties were derived from a cross-correlation analysis, namely the interfacial velocity V and the turbulence intensity Tu. The air-water interfacial velocity was calculates as:

$$V = \frac{\Delta x_{tip}}{T} \quad (2.1)$$

where T is the average interfacial travel time between the two probe sensors. T equals the time lag for which the normalised cross-correlation function is maximum. The turbulence intensity was deduced from the shapes of the auto- and cross-correlation functions:

$$Tu = 0.851 \times \frac{\sqrt{\tau_{0.5}{}^2 - T_{0.5}{}^2}}{T} \quad (2.2)$$

where $\tau_{0.5}$ is the time lag for which the normalised cross-correlation function is half of its maximum value: $R(T+\tau_{0.5}) = R_{max}(T)/2$, R_{max} is the maximum cross-correlation coefficient observed for $\tau = T$, and $T_{0.5}$ is the time lag for which the normalised auto-correlation function equals 0.5 (CHANSON and TOOMBES 2002, CHANSON 2002).

2.2.3 Total pressure probe (TPP)

The total pressure probe consisted of a miniature silicon diaphragm sensor mounted at the tip of a probe holder (Fig. 2-4). The sensor was a MEMS technology-based pressure transducer manufactured by MeasureX ([2]) (pressure transmitter model MRV21). The sensitive part had a 5 mm outer diameter and the pressure measurement range was from 0 to 1.5 bars with a corresponding output voltage between 0 and 62.19 mV (data from the manufacturer). The maximum response frequency of the sensor was 100 kHz. For the present experiments, an amplifier was added to provide a larger output voltage range (up to 1 V). The amplification system filtered the signal to eliminate noises above 2 kHz. During the experiments, a daily calibration (static and/or dynamic) was conducted and regularly checked, because the output voltage appeared to be temperature and ambient pressure sensitive.

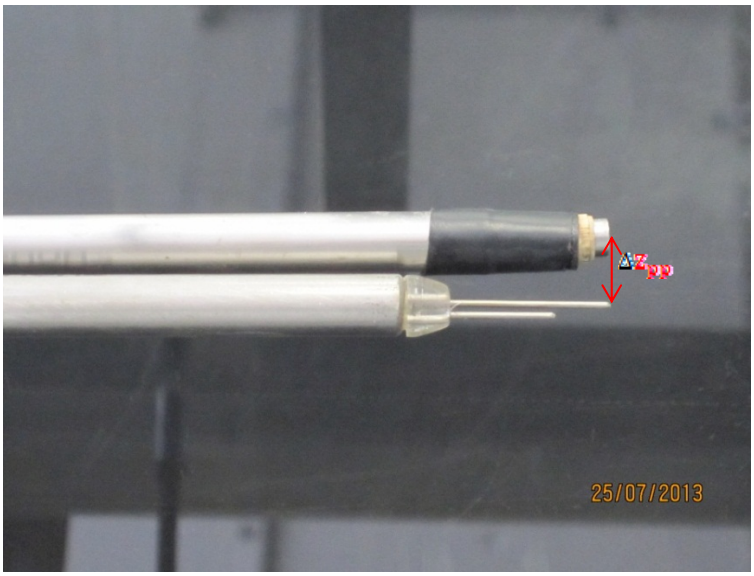

Fig. 2-4 - Pressure probe mounted beside a double-tip conductivity probe (view in elevation)

The pressure sensor was mounted at the tip of a Pitot tube-like holder (Fig. 2-4). The probe sensor was facing upstream, thus recording the total pressure (i.e. stagnation pressure). Note that such a miniature diaphragm pressure sensor was not affected by the presence of bubbles and did not require to be primed or purged. The pressure sensor was scanned at 5 kHz for 180 s simultaneously with the phase-detection probe. During the experiments, the sensor was mounted close to the phase-detection probe: the separation distance between the probes was Δz_{PP} = 9 mm (Fig. 2-4). The probes were carefully aligned with the flow direction as well as the acoustic displacement meter located above. The vertical elevation of the probe was controlled by the same Mitutomo^{TM} digimatic scale unit as the PDP with an accuracy of 0.01 mm.

[2] MeasureX Pty Ltd, 42 Garden Boulevard, Melbourne VIC 3172, Australia.

2.3 DATA PROCESSING

For the acoustic displacement meters, erroneous spikes were manually removed, following the same protocol as WANG and CHANSON (2013).

The signal of dual-tip phase-detection probe was processed following the method of TOOMBES (2002), CHANSON (2002) and CHANSON and CAROSI (2007). This processing technique was previously used in hydraulic jump flows by KUCUKALI and CHANSON (2008), MURZYN and CHANSON (2008,2009), CHACHEREAU and CHANSON (2011a,b) and ZHANG et al. (2013).

The pressure probe signal was amplified and filtered analogically (see above). No further post-processing was applied.

With the ADM, TPP and PDP probes being sampled simultaneously, a dedicated pre-processing technique was developed prior to the cross-correlation analyses. The signals were filtered. A cut-off frequency of 2 kHz was applied to the phase-detection and pressure probe output signals, while a cut-off frequency of 50 Hz was applied to the acoustic displacement meter signals. Such cut-off frequencies were consistent with the instrument responses. The cross-correlation calculations were performed on six non-overlapping signal segments (30 s each), and the cross-correlation function data were averaged.

2.4 EXPERIMENTAL CONDITIONS

A range of experimental flow conditions were tested. The sluice gate opening was h = 20 mm and the impingement point (hydraulic jump toe) was set at a longitudinal position x_1 = 0.83 m for all experiments. The upstream gate contraction was basically unity. Based on previous experimental measurements (ZHANG et al. 2013), the present investigation was performed with partially-developed inflow conditions.

The aim and novelty of the present measurements were to acquire simultaneously, at the same position, the instantaneous free-surface position, instantaneous void fraction and instantaneous total pressure. The experiments were conducted with different Froude numbers, ranging from 3.8 to 8.5. For each Froude number, three to four vertical profiles were measured at different longitudinal positions in the roller (Table 2-1). A summary of experimental flow conditions is given in Table 2-1, where Q is the water discharge, W is the channel width, x_1 is the jump toe position downstream of the upstream gate, d_1 is the upstream flow depth, V_1 is the upstream flow velocity, Fr_1 is the inflow Froude number and Re is the Reynolds number defined as:

$$\mathrm{Re} = \rho_w \times \frac{V_1 \times d_1}{\mu_w} \tag{2.3}$$

where ρ_w and μ_w are the density and dynamic viscosity of water respectively.

Table 2-2 lists the positions of the acoustic displacement meters for each set of experiments. It is

important to note that the free surface elevation was recorded far downstream of the toe for each series of flow conditions, to estimate accurately the roller surface properties.

Table 2-1 - Experimental conditions for simultaneous acquisitions of free surface, two-phase flow properties and pressure outputs at the same location

Q (m^3/s)	W (m)	d_1 (m)	x_1 (m)	Fr_1	Re	$(x-x_1)/d_1$	Number of sample points per profile
0.0179	0.5	0.02	0.83	3.8	3.5×10^4	4.15	19
						8.35	21
						12.5	13
0.0239	0.5	0.02	0.83	5.1	4.8×10^4	4.15	25
						8.35	24
						12.5	26
						18.75	23
0.0347	0.5	0.02	0.83	7.5	6.8×10^4	4.15	19
						8.35	22
						12.5	23
						18.75	26
0.0397	0.5	0.02	0.83	8.5	8.0×10^4	4.15	18
						8.35	22
						12.5	24
						18.75	26

Table 2-2 - Experimental free-surface measurements using the acoustic displacement meters

Q (m^3/s)	W (m)	d_1 (m)	x_1 (m)	Fr_1	Re	$(x-x_1)/d_1$					
0.0179	0.5	0.02	0.83	3.8	3.5×10^4	-11.50,	0.85,	4.15,	4.50,	8.35,	12.50,
						14.15,	18.35,	21.65,	22.50,	29.15,	31.60,
						36.00					
0.0239	0.5	0.02	0.83	5.1	4.8×10^4	-11.50,	0.85,	4.15,	4.50,	8.35,	11.75,
						12.50,	14.15,	18.75,	21.65,	21.85,	22.50,
						28.75,	30.65,	31.85,	36.50		
0.0347	0.5	0.02	0.83	7.5	6.8×10^4	-11.50,	0.835,	4.15,	4.50,	8.35,	11.50,
						12.50,	14.15,	18.75,	20.85,	24.15,	25.00,
						31.25,	33.35,	36.65,	37.50		
0.0397	0.5	0.02	0.83	8.5	8.0×10^4	-11.50,	0.835,	4.15,	4.50,	8.35,	11.50,
						12.50,	14.15,	18.35,	18.75,	22.50,	24.15,
						31.25,	33.35,	35.50,	39.15		

Notes: d_1: inflow depth; Fr_1: inflow Froude number; Q: flow rate; Re: Reynolds number; W: channel width; x_1: longitudinal jump toe position.

3. EXPERIMENTAL RESULTS. (1) BASIC FREE SURFACE AND TWO-PHASE FLOW PROPERTIES

3.1 BASIC FEATURES OF THE FREE SURFACE

3.1.1 Mean free surface profiles

A hydraulic jump has a well-defined mean free surface profile. Using a series of acoustic displacement meters, the time-averaged water elevation η above the channel invert was recorded at various longitudinal locations along the channel centreline. Typical results are presented in Figure 3-1A for several inflow Froude numbers, where d_1 is the upstream water depth, x is he longitudinal coordinate and x_1 is the jump toe position. The time-averaged free surface profiles were in good agreements with visual observations (Fig. 2-1 & App. F). For the lowest Froude numbers ($Fr_1 < 5.1$), the data exhibited a flat horizontal profile far downstream. For the largest Froude number ($Fr_1 = 8.5$), the mean water level increased monotonically beyond $(x-x_1)/d_1 > 40$. The ratio of conjugate depths was documented based upon the time-averaged free-surface profiles, except for the largest Froude number. The data are reported in Figure 3-1B in which they are compared with earlier experimental data and the theoretical solution of the momentum principle:

$$\frac{d_2}{d_1} = \frac{1}{2} \times \left(\sqrt{1 + 8 \times Fr_1^2} - 1 \right) \quad (3.1)$$

where d_2 is the conjugate water depth measured far downstream of the roller. Equation (3.1) is called the Bélanger equation. The present findings were in good agreement with earlier data (MURZYN et al. 2007, KUCUKALI and CHANSON 2008, CHACHEREAU and CHANSON 2011b, WANG and CHANSON 2013) and with Equation (3.1).

Visual observations through side and top views showed that the free surface was basically flat upstream of the jump toe ($(x-x_1)/d_1 < 0$). Immediately downstream of the toe ($(x-x_1)/d_1 > 0$), the water level increased monotonically. For $0 < (x-x_1)/d_1 < 10$, the free-surface slope was nearly identical independently of the Froude number, with $\partial\eta/\partial x \approx 0.55$ on average. Turbulent fluctuations associated with splashes and droplet projections were observed with length and time scales functions of the Froude number. Further downstream, the water surface became flatter until it reached a constant conjugate water depth far downstream. This was associated with lesser free-surface fluctuations. Herein, the distance over which the free surface level increased monotonically was defined as the roller length L_r and it was estimated based on the time-averaged free-surface profiles. The results are plotted in Figure 3-2 showing an increasing roller length with increasing Froude number. The present data were compared with previous experiments (KUCUKALI and CHANSON 2007, MURZYN et al. 2007, WANG and CHANSON 2013), computational data (RICHARD and GAVRILYUK 2013) and an empirical correlation (HAGER et al. 1990), showing

altogether a reasonable agreement between all data sets (Fig. 3-2).

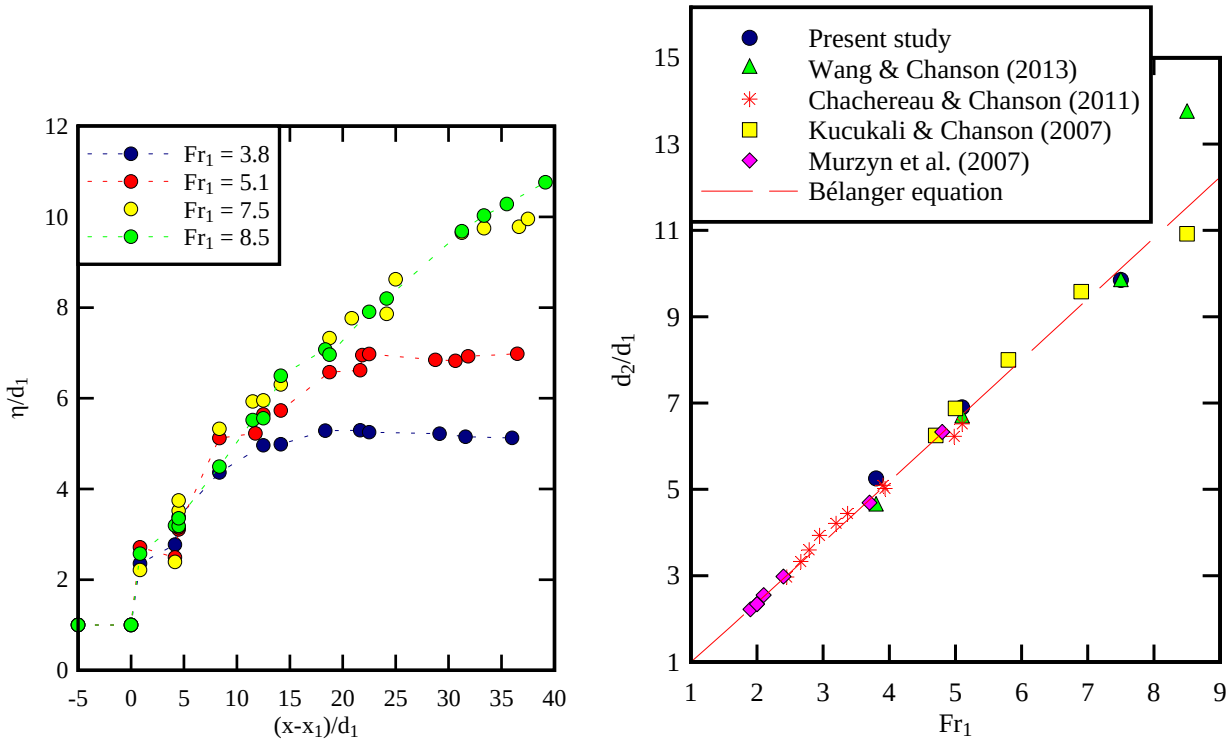

(A) Time-averaged free surface profiles (Present study)

(B) Ratio of conjugate depths d_2/d_1 Comparison with data and Bélanger equation

Fig 3-1 - Dimensionless free surface profiles and ratio of conjugate depths for $3.8 < Fr_1 < 8.5$.

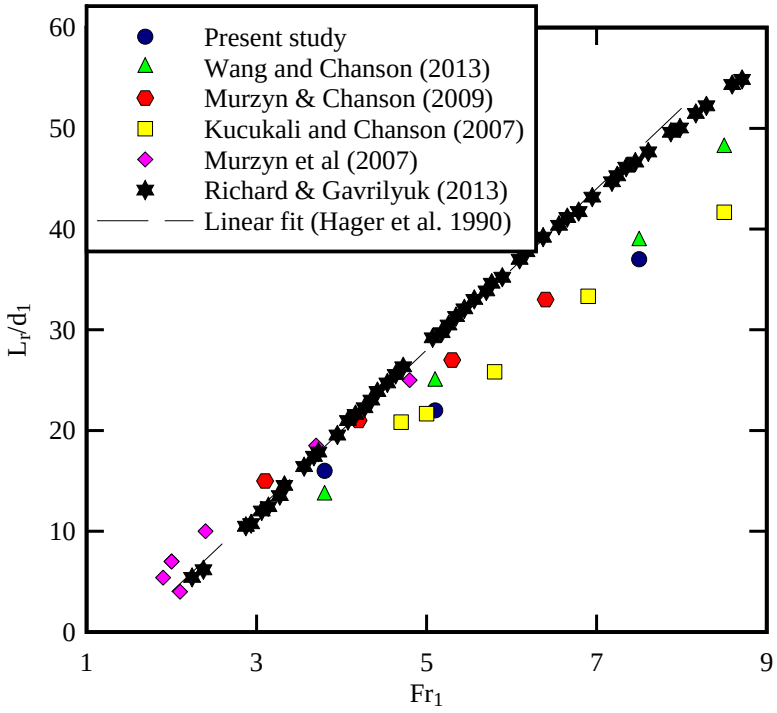

Fig 3-2 - Dimensionless roller length as a function of the Froude number - Comparison with experimental data (KUCUKALI and CHANSON 2007, MURZYN et al. 2007, MURZYN and

CHANSON 2009, WANG and CHANSON 2013), computational data (RICHARD and GAVRILYUK 2013) and the correlation of HAGER et al. (1990)

3.1.2 Turbulent free surface fluctuations

The free-surface elevation observations indicated large and rapid fluctuations at all positions along the roller. Herein the free-surface fluctuations were quantified in terms of the standard deviation η' of water elevation measured by the acoustic displacement meters. The results are presented in Figure 3-3 in form of longitudinal distributions of dimensionless turbulent fluctuations. The data showed a rapid increase in turbulent intensities in the first third of the roller up to a maximum value η'_{max} (Fig. 3-3) This was followed by a slight and progressive decrease in fluctuation levels with increasing distance from the jump toe, suggesting that a dissipative motion took place. The findings were consistent with visual observations and previous experiments (MOUAZE et al. 2005, MURZYN and CHANSON 2009, CHACHEREAU and CHANSON 2011b). Visually, most droplet and air-water ejections were seen close to the jump toe where the flow motion was the most turbulent (Appendix F).

The maximum free-surface fluctuation η'_{max} increased with increasing Froude numbers (Fig. 3-4). Figure 3-4 shows the maximum free-surface fluctuation η'_{max} as a function of the Froude number. The present data were compared with previous experimental results as well as recent computations (RICHARD and GAVRILYUK 2013). The results compared well with an empirical correlation proposed by MURZYN and CHANSON (2009):

$$\frac{\eta'_{max}}{d_1} = 0.116 \times (Fr_1 - 1)^{1.235} \quad (3.2)$$

Equation (3.2) is plotted in Figure 3-4 showing a good agreement with all data for $Fr_1 < 7$ and a larger data scatter above. At the largest Froude numbers, the jump flow was highly turbulent with severe spray and splashing. The detection of free surface elevations was adversely affected by droplets stuck on the sensor heads in present and past studies using the same metrology. WANG and CHANSON (2013) showed that the signal processing might affect the free-surface fluctuation estimates.

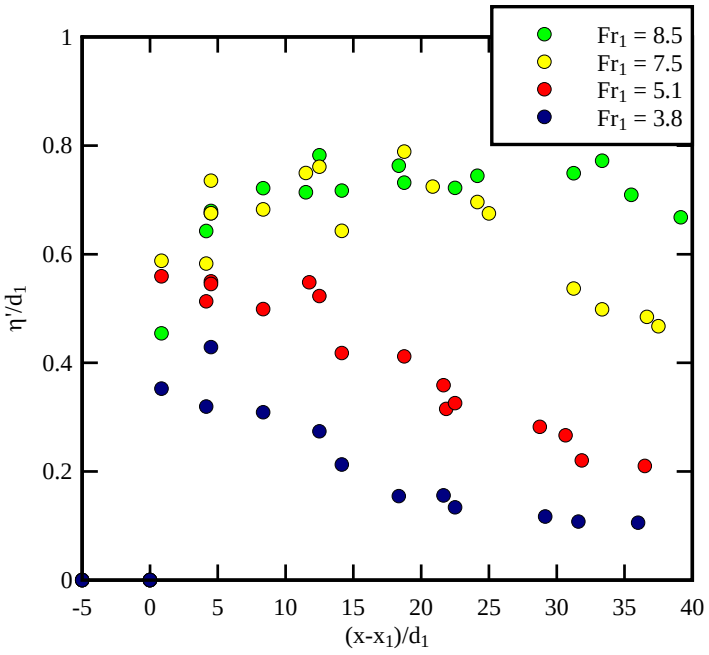

Fig 3-3 - Dimensionless turbulent fluctuations η'/d_1 of the free surface as a function of the dimensionless distance to the jump toe $(x-x_1)/d_1$

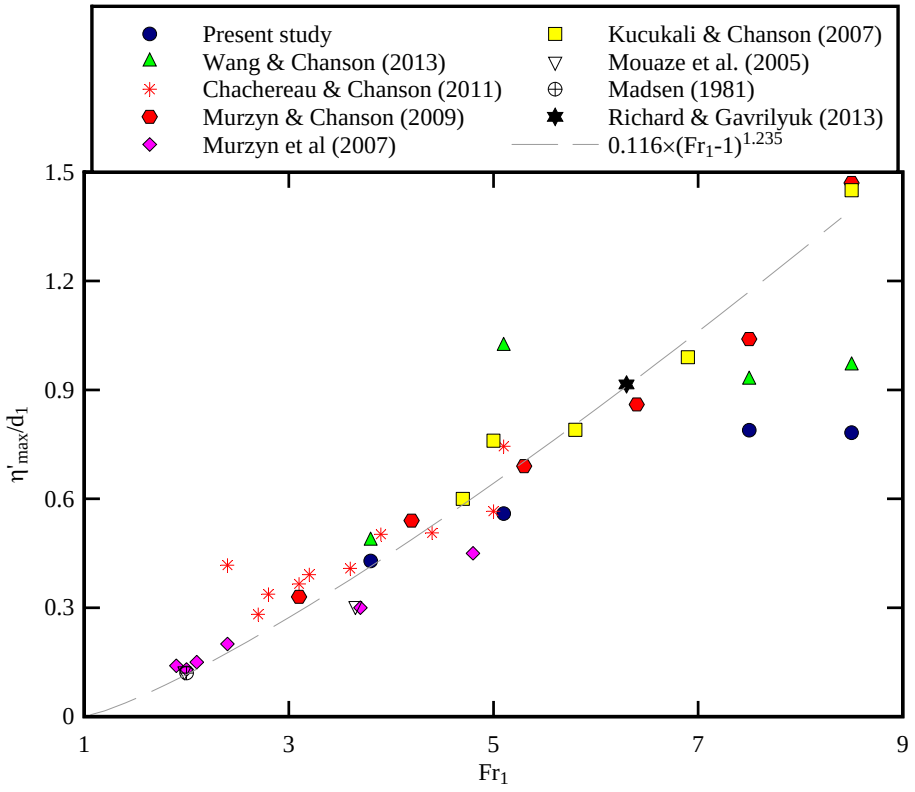

Fig 3-4 - Maximum turbulent fluctuations of the free surface elevation as a function of the Froude number - Comparison with experimental data (MADSEN 1981, MOUAZE et al. 2005, KUCUKALI and CHANSON 2007, MURZYN et al. 2007, MURZYN and CHANSON 2009, CHACHEREAU and CHANSON 2011b, WANG and CHANSON 2013), computational data (RICHARD and GAVRILYUK 2013) and Equation (3.2)

The hydraulic jumps were characterised by large fluctuations of the free-surface, longitudinal oscillations of the jump position as well as formation and downstream advection of large size vortices within the roller. The longitudinal oscillations of jump toe position and vortices formations were documented by CHANSON (2007,2010), MURZYN and CHANSON (2009), CHACHEREAU and CHANSON (2011b) and ZHANG et al. (2013). The free surface fluctuations were more specifically investigated by MURZYN and CHANSON (2009), CHACHEREAU and CHANSON (2011b) and WANG and CHANSON (2014). Based upon some power spectral analysis, the free surface fluctuation frequencies were within 1.2 to 3.7 Hz, while the jump toe oscillations were typically 0.5 – 1.3 Hz (WANG and CHANSON 2014).

In the present study, the characteristic frequencies of free surface fluctuations were analysed at several longitudinal positions. Based upon fast Fourier transform (FFT) analyses of the ADM signals, the power spectral density (PSD) function data exhibited a characteristic peak for a dominant frequency. Some secondary characteristic frequencies were also noted and believed to be the effect of longitudinal oscillations of jump position (WANG and CHANSON 2014). A typical PSD function is shown in Figure 3-5. Both original and smoothed functions are presented, highlighting a dominant frequency about 2.5 Hz. No secondary frequency was recorded when the local peaks were too ambiguous.

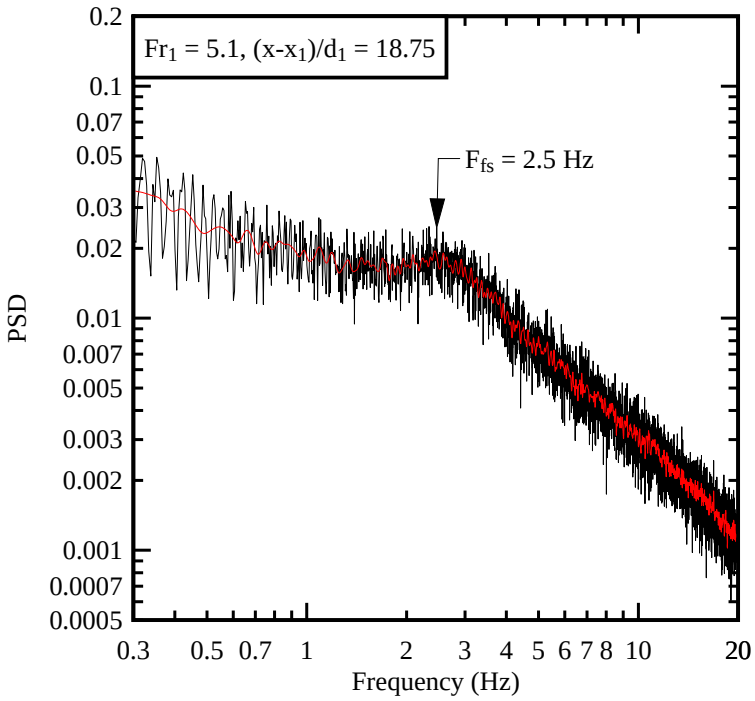

Fig 3-5 - Power spectral density function of the acoustic displacement meter signal - Flow conditions: d_1 = 0.020 m, x_1 = 0.83 m, Fr_1 = 5.1, $(x-x_1)/d_1$ = 18.75

The longitudinal distributions of dominant free-surface fluctuation frequencies F_{fs} are shown in Figure 3-6A. The data indicated a slight decrease in frequency with increasing distance from the jump toe. The result implied that the turbulent free-surface fluctuations close to the toe had not only larger amplitude (Fig. 3-3) but also higher in frequency. The decay was slight and it was not reported in the previous studies (CHACHEREAU and CHANSON 2011b, WANG and CHANSON 2014). Overall the mean characteristic frequency of free-surface fluctuations tended to decrease with increasing Froude number (Fig. 3-6B). For example, the average frequency was F_{fs} = 3.5 Hz for Fr_1 = 3.8 compared to F_{fs} = 2.2 Hz for Fr_1 = 8.5. The data tended to suggest an exponential decay best fitted by:

$$\frac{F_{fs} \times d_1}{V_1} = 0.115 \times \exp(-0.293 \times Fr_1) \quad (3.3)$$

Equation (3.3) is compared with the experimental data in Figure 3-6B, as well as with the data of WANG and CHANSON (2014) for similar Froude numbers, but over a wider range of Reynolds numbers up to 1.6×10^5.

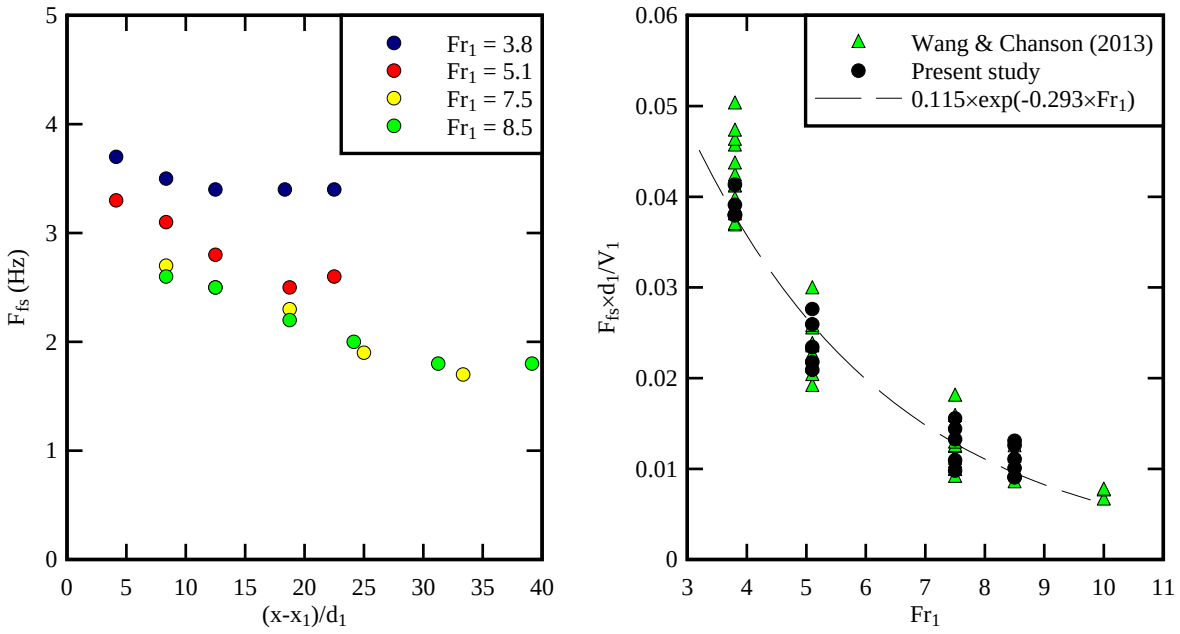

(A, Left) Longitudinal distributions of free surface fluctuation frequencies

(B, Right) Dimensionless characteristic frequency $F_{fs} \times d_1/V_1$ as function of the Froude number - Comparison with Equation (3.3)

Fig 3-6 - Free surface fluctuation frequencies in hydraulic jumps

3.1.3 Jump toe oscillations and roller surface deformation

The hydraulic jump toe is defined at the impingement point of the supercritical flow into the roller.

The toe is characterised by a sudden, somehow discontinuous increase of water depth. Although its mean position is $x = x_1$, the jump toe oscillates back and forth around it. The longitudinal oscillating motion was recorded with an acoustic displacement meter placed horizontally, upstream of the jump, about 30 mm above the inflow water surface and detecting the longitudinal position of the roller surface. The signal analysis provided some information on the oscillation frequency. The results are plotted in Figure 3-7, where F_{toe} denotes the characteristic frequency of the jump toe oscillation. The present data were compared with the observations of WANG and CHANSON (2013) obtained using a similar method and other data obtained visually by means of video recordings. The present data indicated a slight decrease in dimensionless frequency with increasing Froude number, close to the computational results of RICHARD (2013) (Fig. 3-7). RICHARD (2013) tested the effects of the channel length and his results were independent of the test section length. Note that the experimental data presented some scatter for Froude numbers smaller than 5 (CHACHEREAU and CHANSON 2011d, ZHANG et al. 2013). It is acknowledged that, for the smallest Froude number, the displacement meter might not capture the roller motion close to the toe. Figure 3-7 also presents the production rates F_{ej} of large vortices in the roller observed by CHANSON (2010) and ZHANG et al. (2013). The dimensionless production rates were comparable to the jump toe oscillation frequencies, especially for the large Froude numbers ([3]). Indeed the hydraulic jump toe oscillations are believed to be caused by the production and advection of large-scale vortices in the developing shear layer (LONG et al. 1991).

Both jump toe oscillations and free surface fluctuations characterised the surface deformation of the roller. Herein the instantaneous horizontal jump front position was correlated with the instantaneous vertical surface elevations. The sign of cross-correlation function maximum/minimum, around zero time lag between the two signals, reflected the interactions between the two motions, hence a pattern of roller surface deformation. Though the acoustic displacement meters (ADMs) were sampled at 5 kHz together with the phase-detection and total pressure probes, the ADM signals were filtered at 50 Hz, a cut-off frequency corresponding to the sensor response frequency. Erroneous signals caused by droplets projection were removed, and the filtered signals were smoothed to minimise any random scattering. The 180 s data set was sub-divided into six non-overlapping 30 s intervals. Cross-correlation functions were obtained for each 30 s segment, and the average correlation function was used to determine the maximum/minimum correlation coefficient. For each set of flow conditions, the correlation analysis was performed between the signals of the horizontal displacement meter and each vertical displacement meter along the channel centreline.

[3] For the smaller Froude numbers, the advection of vortices could not be observed distinctively through the glass sidewalls of the channel.

The results in terms of maximum/minimum correlation coefficients $(R_{xy})_{max}$ are plotted in Figure 3-8 as functions of the relative position $(x-x_1)/L_r$ within the roller ([4]).

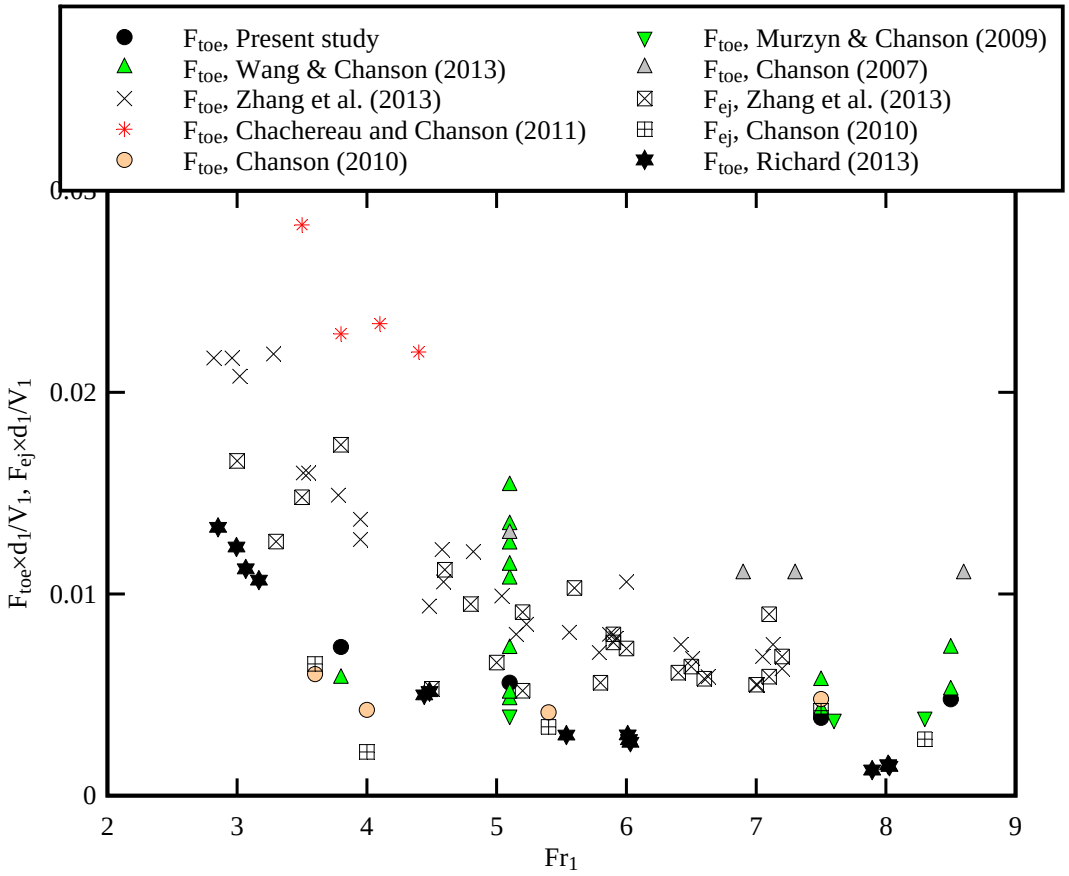

Fig 3-7 - Dimensionless frequencies of longitudinal jump toe oscillations $F_{toe}\times d_1/V_1$ as a function of the Froude number - Comparison with experimental data (CHANSON 2007, MURZYN and CHANSON 2009, CHANSON 2010, CHACHEREAU and CHANSON 2011b, ZHANG et al. 2013, WANG and CHANSON 2013) and computational data (RICHARD 2013), and physical observations of formation rates of large-size vortices in the roller shear layer $F_{ej}\times d_1/V_1$ (CHANSON 2010, ZHANG et al. 2013)

With x positive in the downstream direction and y positive in the upward direction, a positive maximum correlation coefficient indicated that the jump front moved downstream when the free surface move upwards, and vice versa. Conversely a negative coefficient implied that the jump toe travelled downstream when the water surface elevation increased. The present data (Fig. 3-8) showed negative maximum correlation in the first half of the roller ($(x-x_1)/L_r < 0.5$), and positive coefficients in the second half of the roller ($(x-x_1)/L_r > 0.5$). The findings were similar to the data of

[4] Although the roller length was not recorded for $Fr_1 = 8.5$, it was assumed to be $L_r = 45\times d_1$ based upon a linear extrapolation of the data trend seen in Figure 3-2.

WANG and CHANSON (2013), shown in Figure 3-8. The result suggested a free-surface deformation pattern as sketched in Figure 3-9. That is, the jump toe oscillations were not linked with a simple translation of the roller, rather with a deformation of the roller surface (Fig. 3-9). The cross-correlation analyses demonstrated a coupling between the horizontal and vertical surface motions over the length of roller. Further instantaneous surface deformation patterns, other than those shown in Figure 3-9, might be visually observed (e.g. App. F), but their occurrences were not common.

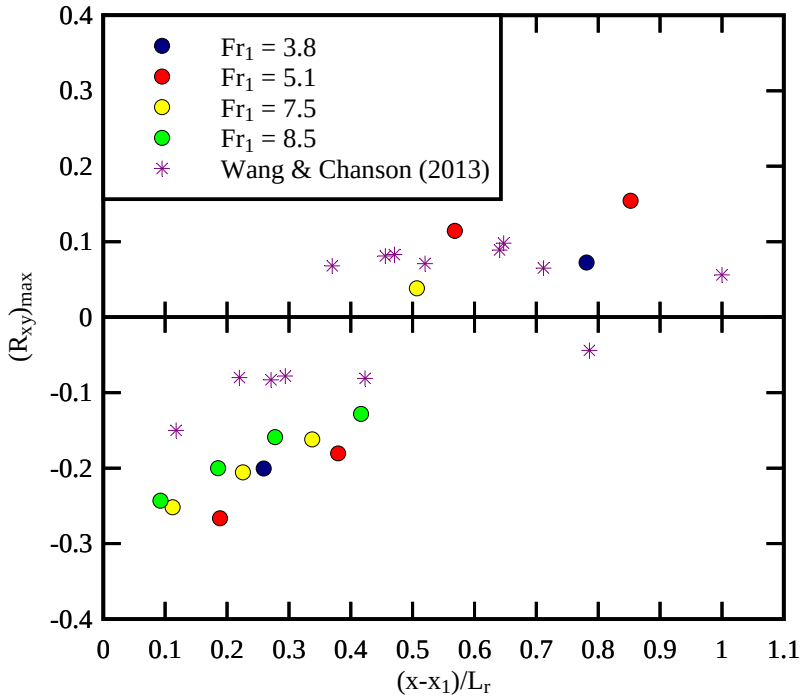

Fig 3-8 - Longitudinal distributions of maximum correlation coefficient $(R_{xy})_{max}$ between horizontal and vertical roller free-surface motions

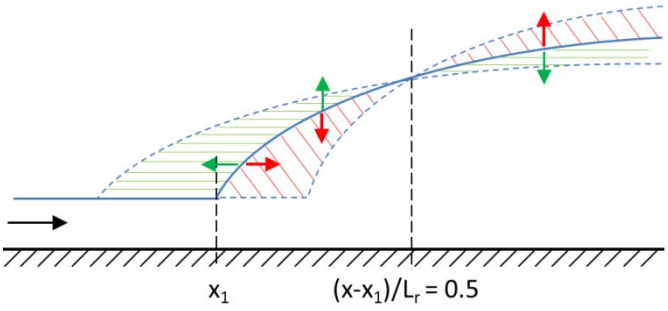

Fig 3.9 - Sketch of hydraulic jump roller surface deformations

3.2 TIME-AVERAGED TWO-PHASE FLOW PROPERTIES

Hydraulic jumps are characterised by substantial air entrapment at the jump toe, air bubble

entrainment in the roller, and spray and splashing above the roller. A number of experimental investigations were undertaken to assess the two-phase flow properties with special focus on the time-averaged void fraction, bubble count rate, interfacial velocity, turbulence intensity, turbulent time/length scales... Different experimental techniques were used, including imaging, conductivity probe and optical fibre probe measurements (RAJARATNAM 1962, MOSSA and TOLVE 1998, MURZYN et al. 2005, KUCUKALI and CHANSON 2008, MURZYN and CHANSON 2008, LEANDRO et al. 2012, WANG and CHANSON 2014). In this section, the present results are presented in terms of time-averaged void fraction C, bubble count rate F, interfacial velocity V, turbulence intensity Tu, bubble chord time and longitudinal bubble clustering characteristics such as cluster size N_{clu}, cluster count rate F_{clu} and cluster proportion P_{clu}. The data were sampled continuously at 5 kHz for 180 s. It is acknowledged that the sampling rate was lower than those used in earlier studies, but it was large enough to estimate accurately the void fraction and bubble count rate as shown by the sensitivity analysis results of CHANSON (2007b).

3.2.1 Distributions of void fraction and bubble count rate

The vertical profiles of time-averaged void fraction C are plotted in Figure 3-10. In Figure 3-10D, the present data are compared with experimental data of WANG and CHANSON (2013) for the same flow conditions. The close agreement between the two data sets showed the repeatability of the measurements.

For all flow conditions, the present measurements showed a similar trend. In the turbulent shear region, the void fraction profiles presented a Gaussian shape with a local maximum in void fraction C_{max} at an elevation y_{Cmax}. The maximum void fraction decreased with increasing distance from the jump toe. At an elevation $y_* > y_{Cmax}$, the void fraction distribution presented a local minimum C_*, above which the void fraction increased monotonically to unity. The upper free-surface region ($y > y_*$) corresponded to a recirculation region, while the turbulent shear region corresponded to $0 < y < y_*$.

In the shear region, the void fraction data compared favourably with an analytical solution of the advective convection equation for air bubbles (CHANSON 1995,2010):

$$C = C_{max} \times \exp\left(-\frac{1}{4 \times D^{\#}} \times \frac{\left(\frac{y - Y_{Cmax}}{d_1} \right)^2}{\frac{x - x_1}{d_1}} \right) \qquad 0 < y < y_* \quad (3.3)$$

where $D^{\#}$ is a dimensionless diffusion coefficient. In the recirculation region, the void fraction followed a Gaussian error function (CHANSON 1989, BRATTBERG et al. 1988, MURZYN et al.

2007):

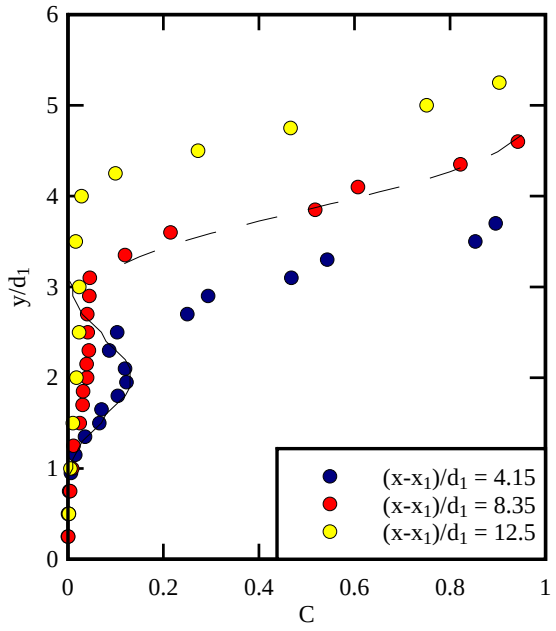

(A) $Fr_1 = 3.8$

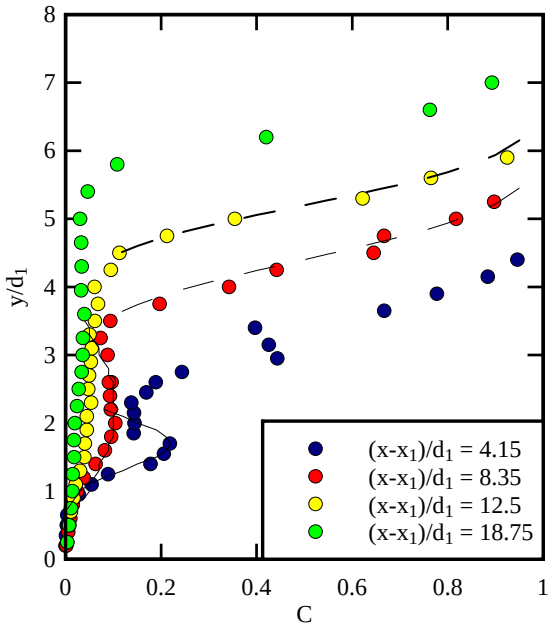

(B) $Fr_1 = 5.1$

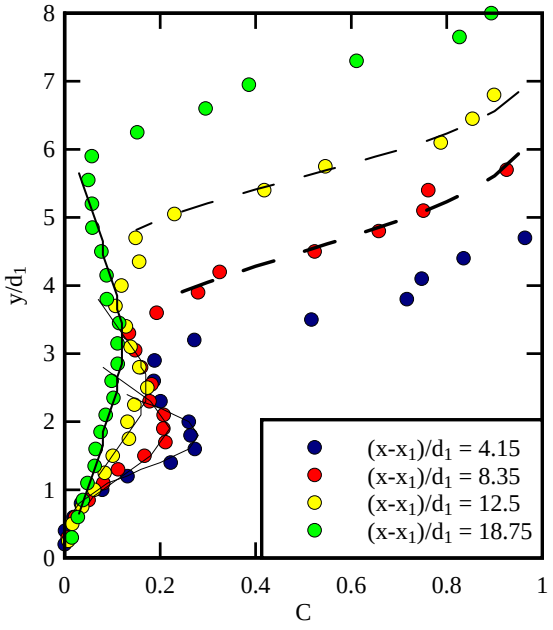

(C) $Fr_1 = 7.5$

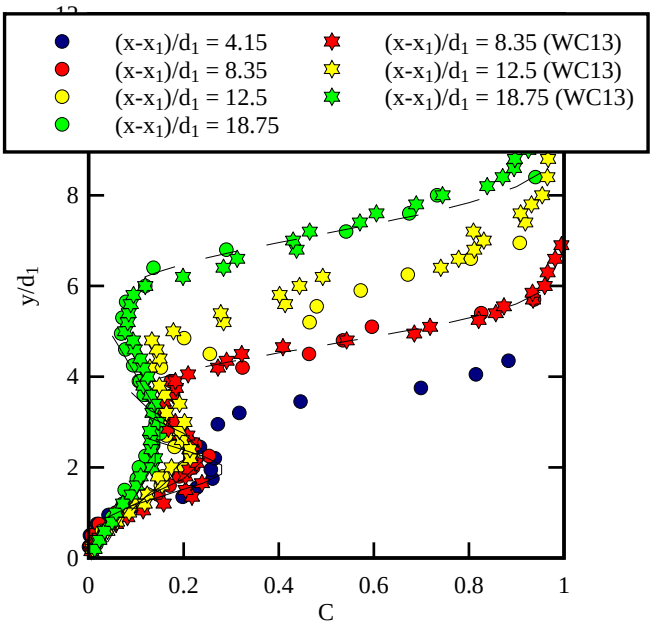

(D) $Fr_1 = 8.5$ - Comparison with data by WANG and CHANSON (2013) (WC13)

Fig 3-10 - Vertical profiles of time-averaged void fraction C in hydraulic jumps - Comparison with Equation (3.3) (solid line) in the shear region and Equation (3.4) (dashed line) in the upper free-surface region

$$C = \frac{1}{2} \times \left(1 + \text{erf}\left(\frac{y - y_{50}}{2 \times \sqrt{\frac{D^* \times (x - x_1)}{V_1}}}\right)\right) \qquad y > y_* \quad (3.4)$$

where erf is the Gaussian error function, y_{50} is the elevation where C = 0.5, and D^* is a dimensionless diffusion coefficient. Both Equations (3.3) and (3.4) are compared with experimental data in Figure 3.10.

The local maximum void fraction C_{max} was a function of the longitudinal position and Froude number as illustrated in Figure 3-11. At a given position $(x-x_1)/d_1$, C_{max} increased with increasing Froude number, while, for a given Froude number, it decreased with increasing distance from the jump toe. This behaviour was predicted theoretically (CHANSON 2010), observed experimentally (CHANSON and BRATTBERG 2000, MURZYN et al. 2005, GUALTIERI and CHANSON 2007) and this was in agreement with visual observations. The dimensionless elevation y_{Cmax}/d_1 where the maximum void fraction was observed was found to increase with increasing distance from the impingement point (Fig. 3-12). All data approximately fitted a linear trend, in agreement with the previous findings. The boundary between turbulent shear layer and recirculation region was estimated as $y = y_*$ where a local void fraction minimum was observed. The data are plotted in Figure 3-13, showing the dimensionless data presented a linear trend independently of the Froude number.

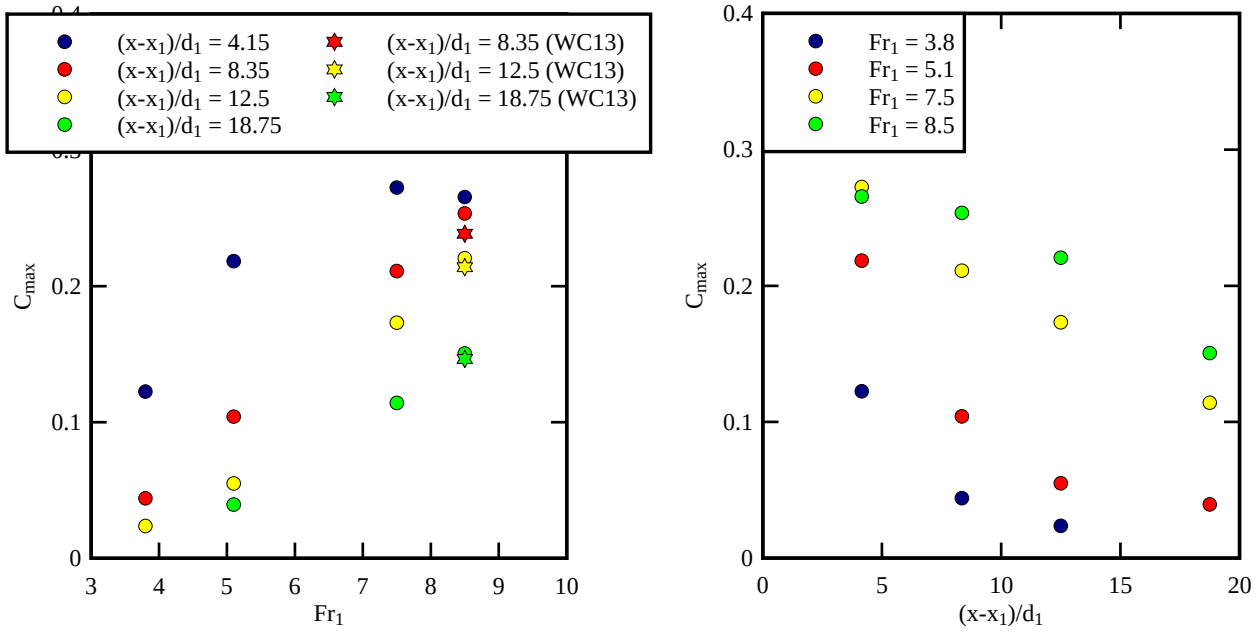

(A) C_{max} as a function of Fr_1 (B) C_{max} as a function of $(x-x_1)/d_1$

Fig 3-11 - Maximum void fraction in the shear layer of hydraulic jumps - Comparison with

experimental by WANG and CHANSON (2013) (WC13)

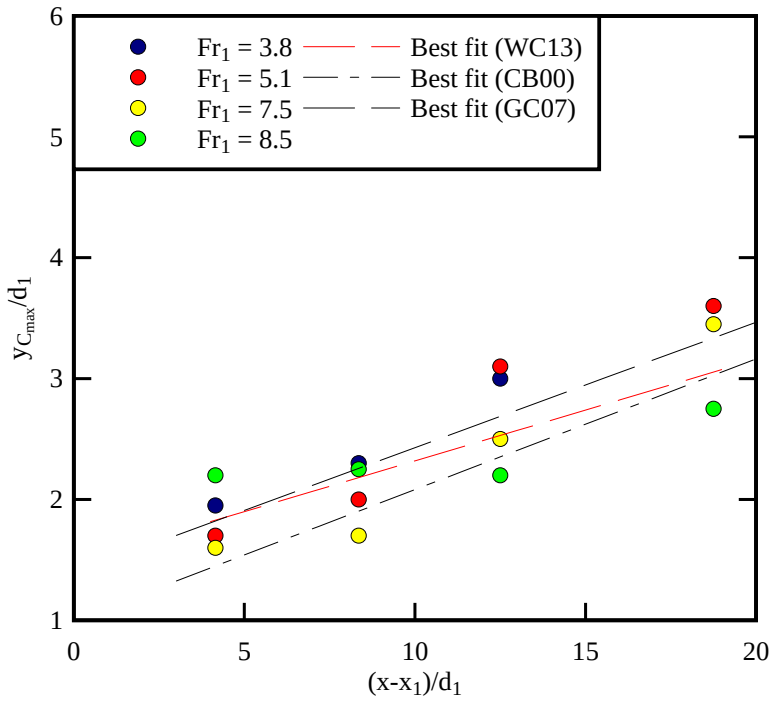

Fig 3-12 - Longitudinal distribution of characteristic elevation y_{Cmax}/d_1 of maximum void fraction in the shear layer - Comparison with the best fits proposed by BRATTBERG and CHANSON (2000), GUALTIERI and CHANSON (2007) and WANG and CHANSON (2013)

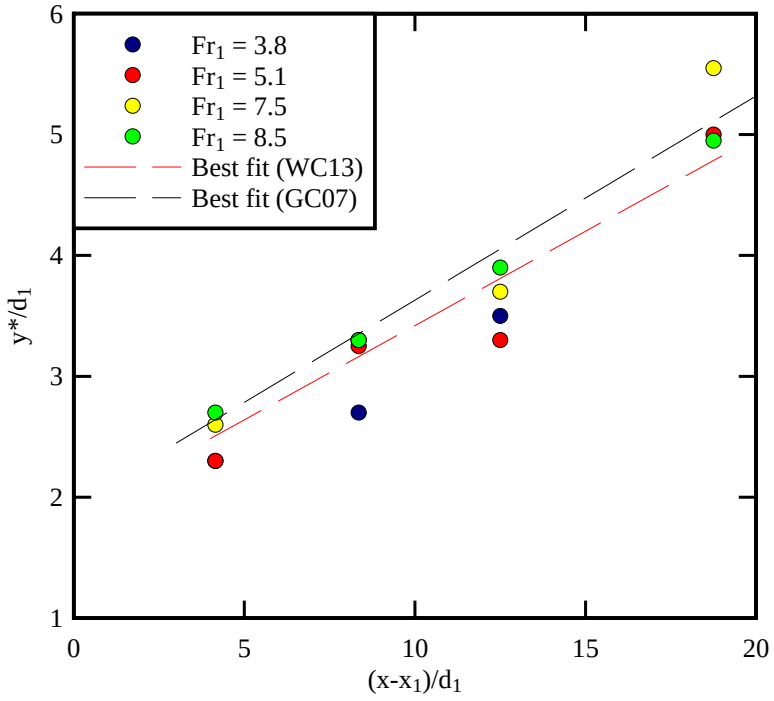

Fig 3-13 - Longitudinal distribution of characteristic elevation y_*/d_1 of boundary between turbulent shear layer and recirculation region - Compared with best fits proposed by GUALTIERI and CHANSON (2007) and WANG and CHANSON (2013)

The dimensionless bubble count rate $F \times d_1/V_1$ data are presented in Figure 3-14. The vertical distributions exhibited a marked peak F_{max} at an elevation y_{Fmax} and a secondary peak F_2 at $y = y_{F2}$, as previously observed (CHANSON and BRATTBERG 2000, MURZYN et al. 2007, MURZYN and CHANSON 2008, KUCUKALI and CHANSON 2008). The maximum bubble count rate was observed in the shear layer. The secondary peak was found to be close to the mean free-surface elevation η measured by the ADMs and where the void fraction ranged between 0.4 and 0.6. A local minimum in bubble count rate was seen between the two peaks at about $y = y_*$.

The maximum bubble count rate was a function of the Froude number and longitudinal distance from the jump toe (Fig. 3-15). Figure 3-15 shows the dimensionless maximum bubble count rate $F_{max} \times d_1/V_1$ as a function of the Froude number (Fig. 3-15A) and dimensionless distance to the toe (Fig. 3-15B). At a given cross-section, the maximum bubble count rate increased with increasing Froude number. For a given Froude number, the maximum bubble count rate decreased with increasing distance from the impingement point as previously observed (CHANSON and BRATTBERG 2000, MURZYN et al. 2005). In the jump roller, the number of bubbles was not only linked to the amount of entrapped air, but also to the turbulent shear. Very close to the jump toe, the large bubble count rate was directly linked to the high shear stress levels close to the source of vorticity. Further downstream, in regions of lesser shear stresses, bubbles merged and coalesced, while the larger bubbles were driven upwards towards the free surface by buoyancy. It is worthwhile to note that the Reynolds number is proportional to the Froude number in this series of experiments since the inflow depth d_1 was kept constant. Hence the results were expected to depend on the Reynolds number. Drastic scale effects were documented in terms of bubble count rate, especially in the turbulence shear layer, at small Reynolds numbers (CHANSON and GUALTIERI 2008, MURZYN and CHANSON 2008, CHANSON and CHACHEREAU 2013, WANG and CHANSON 2013).

Figure 3-16 presents the characteristic elevation y_{Fmax} where the maximum bubble count rate was observed. The data showed an increasing elevation y_{Fmax} with increasing distance from the jump toe. In the present study, the elevation of maximum bubble count rate was consistently lower than that of maximum void fraction, i.e. $y_{Fmax} < y_{Cmax}$. The same finding was first reported by CHANSON and BRATTBERG (2000).

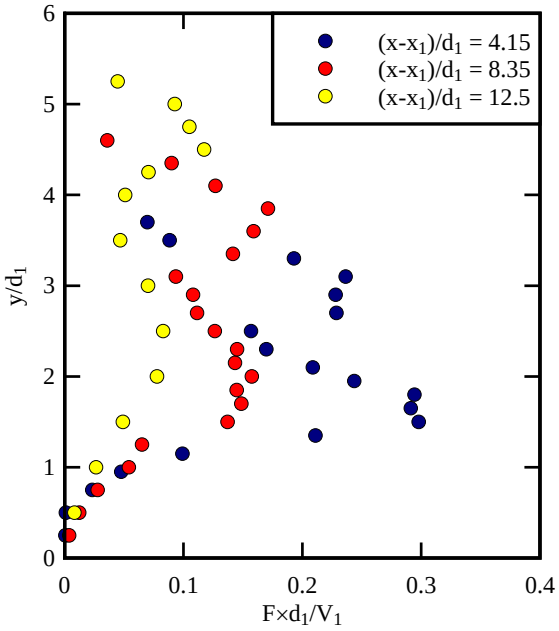

(A) $Fr_1 = 3.8$

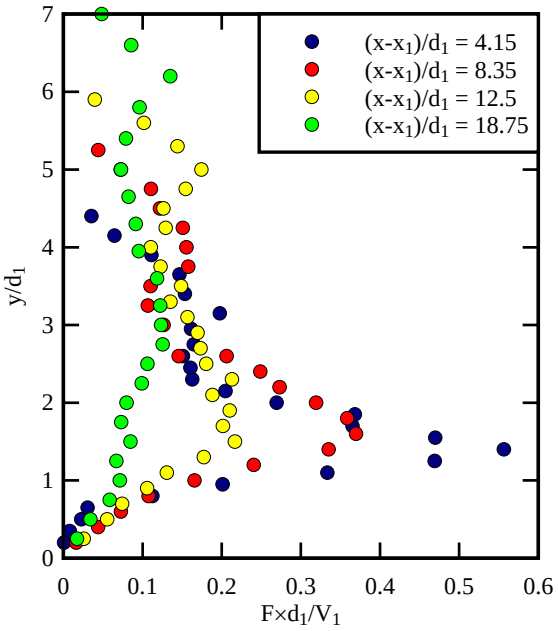

(B) $Fr_1 = 5.1$

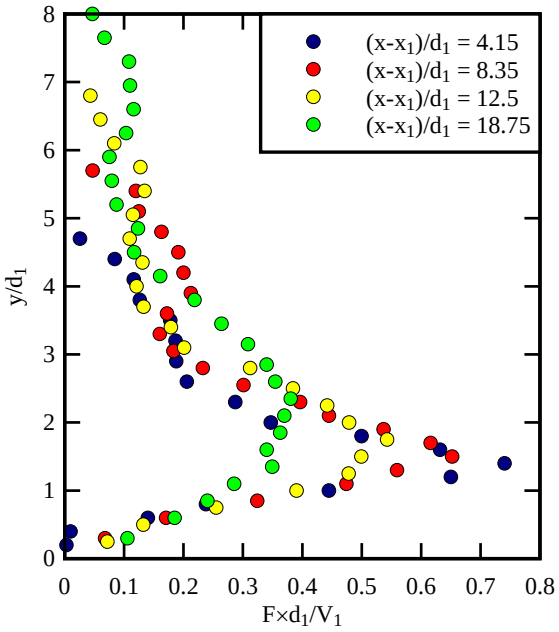

(C) $Fr_1 = 7.5$

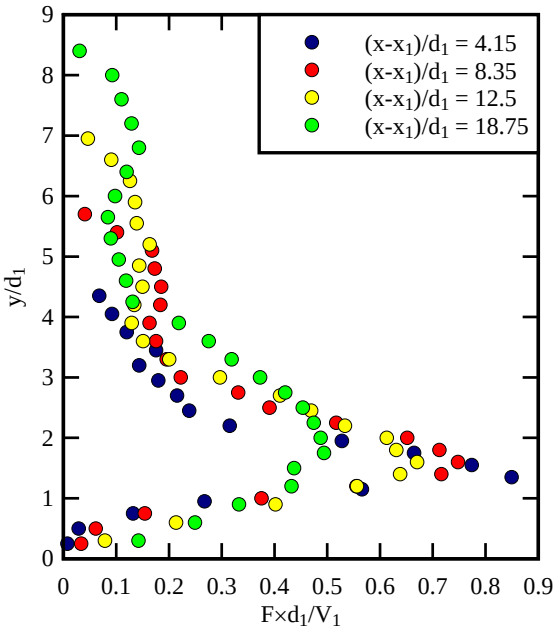

(D) $Fr_1 = 8.5$

Fig 3-14 - Vertical profiles of dimensionless bubble count rate $F \times d_1/V_1$ in hydraulic jumps

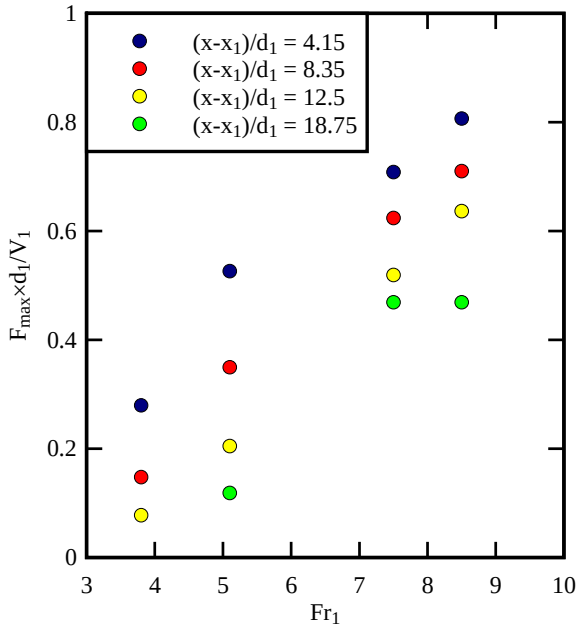

(A) $F_{max} \times d_1/V_1$ as function of Fr1

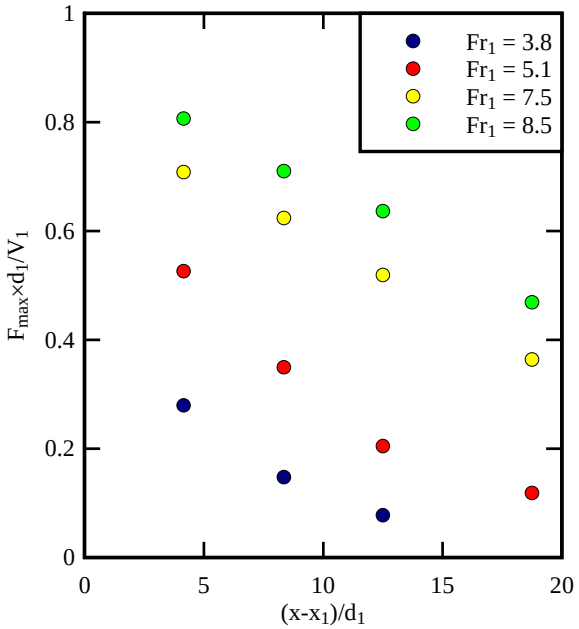

(B) Longitudinal distributions of $F_{max} \times d_1/V_1$

Fig 3-15 - Dimensionless maximum bubble count rate $F_{max} \times d_1/V_1$ in hydraulic jumps

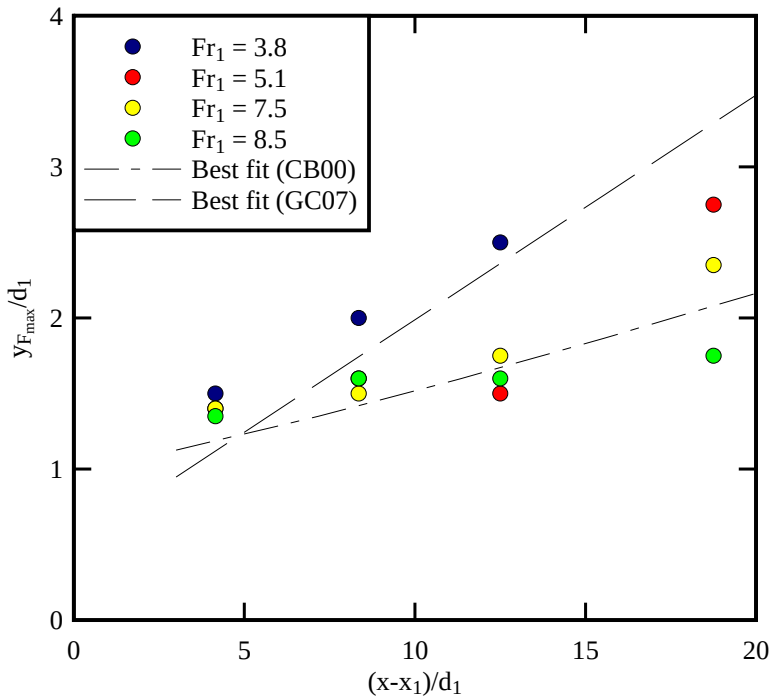

Fig 3-16 - Longitudinal distributions of characteristic elevation y_{Fmax}/d_1 in hydraulic jumps - Comparison with the best fits proposed by BRATTBERG and CHANSON (2000) and GUALTIERI and CHANSON (2007)

3.2.2 Distributions of interfacial velocity and turbulence intensity

The air-water interfacial velocity measurements were conducted using the dual-tip phase-detection probe. The measurement principle is based upon the mean travel time of air-water interfaces between the probe tips aligned with the flow direction, separated herein by Δx_{tip} = 7.25 mm. The results are theoretically restricted to the air-water flow regions where the velocity is positive. In the recirculation region, the measurements were adversely affected by reversal flow conditions (flow going upstream, negative velocities). WANG and CHANSON (2013) showed however that the velocity measurements could be representative. They compared the results given by probe sensors facing the incoming flow with those by probe sensors facing downstream. No significant difference was shown besides some data scatter. The finding suggested that the influence of the probe orientation on the velocity measurement was small, although not negligible because the technique was intrusive. Herein only positive velocity measurements were conducted in the turbulent shear layer ($0 < y < y_*$). Flow recirculation data were not included. Figure 3-17 shows the vertical profiles of dimensionless velocity V/V_{max}, where V_{max} is the maximum velocity in the shear layer observed at an elevation y_{Vmax}. A further assumption was the no slip boundary condition: i.e., V(y=0) = 0.

The results indicated that, at a given cross-section $(x-x_1)/d_1$, a boundary layer developed next to the bed. The boundary layer was characterised by a rapid increase in dimensionless velocity V/V_{max} from 0 to 1. Above, the velocity profile followed a progressive and slight decrease with increasing elevation. Note that the measurement technique was invalid about the boundary between the shear layer and recirculation region because of the frequently changes in turbulent flow directions and the very small velocity amplitudes, implying large positive and negative mean travel times between two probe tips. Despite some data scatter, the velocity distribution exhibited the same shape as a wall jet flow (RAJARATNAM 1965, CHANSON 2010):

$$\frac{V}{V_{max}} = \left(\frac{y}{y_{V\,max}}\right)^{1/N} \qquad 0 < y < y_{Vmax} \quad (3.5a)$$

$$\frac{V - V_{recirc}}{V_{max} - V_{recirc}} = \exp\left(-0.88 \times \left(\frac{y - y_{V\,max}}{y_{0.5}}\right)^2\right) \qquad y_{Vmax} < y \quad (3.5b)$$

where $y_{0.5}$ is the vertical elevation where $V = V_{max}/2$, V_{recirc} is the recirculation velocity and N is a constant ($N \approx 6$ to 10).

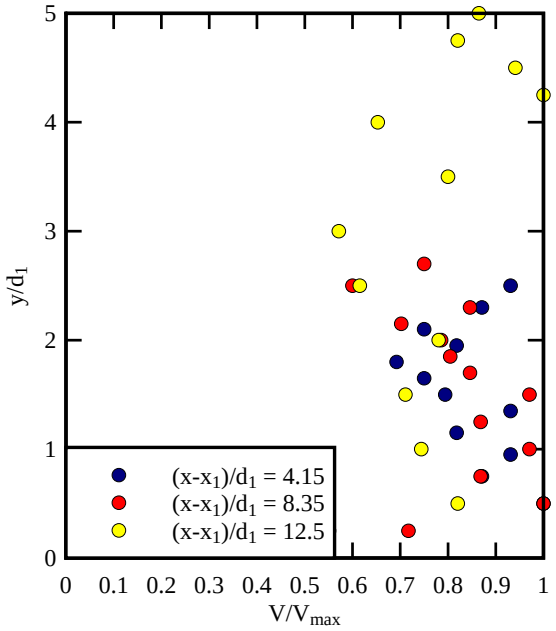

(A) Fr_1 = 3.8

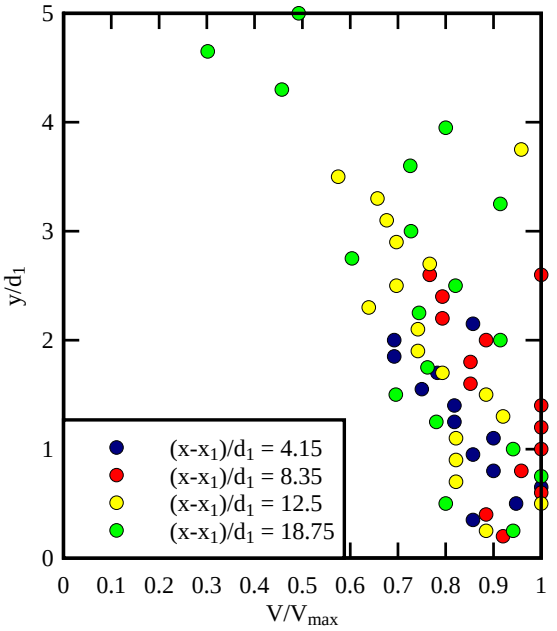

(B) Fr_1 = 5.1

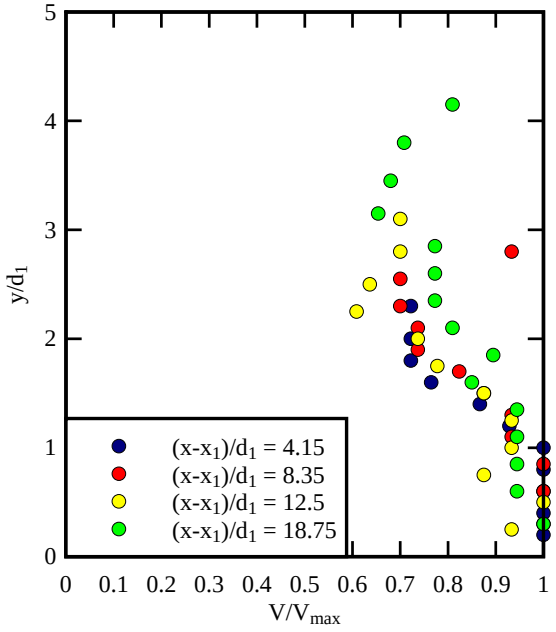

(C) Fr_1 = 7.5

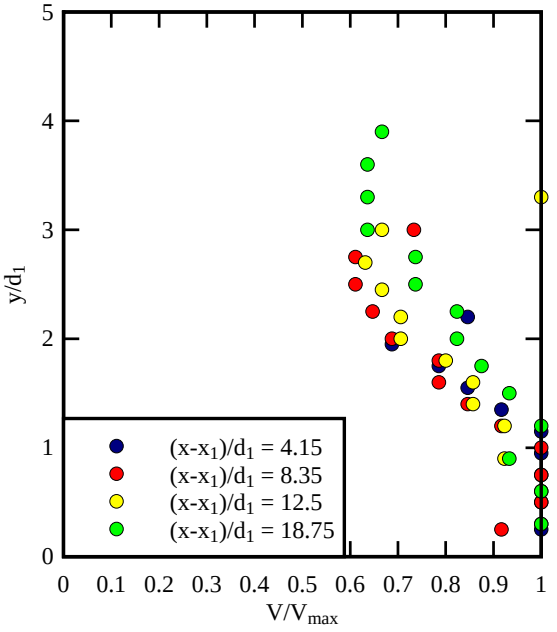

(D) Fr_1 = 8.5

Fig 3-17 - Vertical distributions of dimensionless interfacial velocity V/V_{max} in hydraulic jumps

The turbulence intensity Tu was derived from a cross-correlation analysis between the signals of the two probe sensors. The theoretical considerations were developed by CHANSON and TOOMBES (2002) (also FELDER and CHANSON (2014)). Figure 3-18 presents the turbulence intensity data, including those in the recirculation region. They were found to increase monotonically from the channel bed to the upper boundary of shear layer. High consistency was shown between different longitudinal positions, suggesting that the dissipation of relative turbulence level was limited within

the lower roller, although the absolute turbulent energy dissipation rate was still high. The turbulence intensity data were quantitatively large, but FELDER and CHANSON (2013) pointed out that the fluctuating nature of the flow, of much larger time scales, might also generate some very large turbulence levels, combining the contributions of both slow fluctuations and fast turbulent fluctuations.

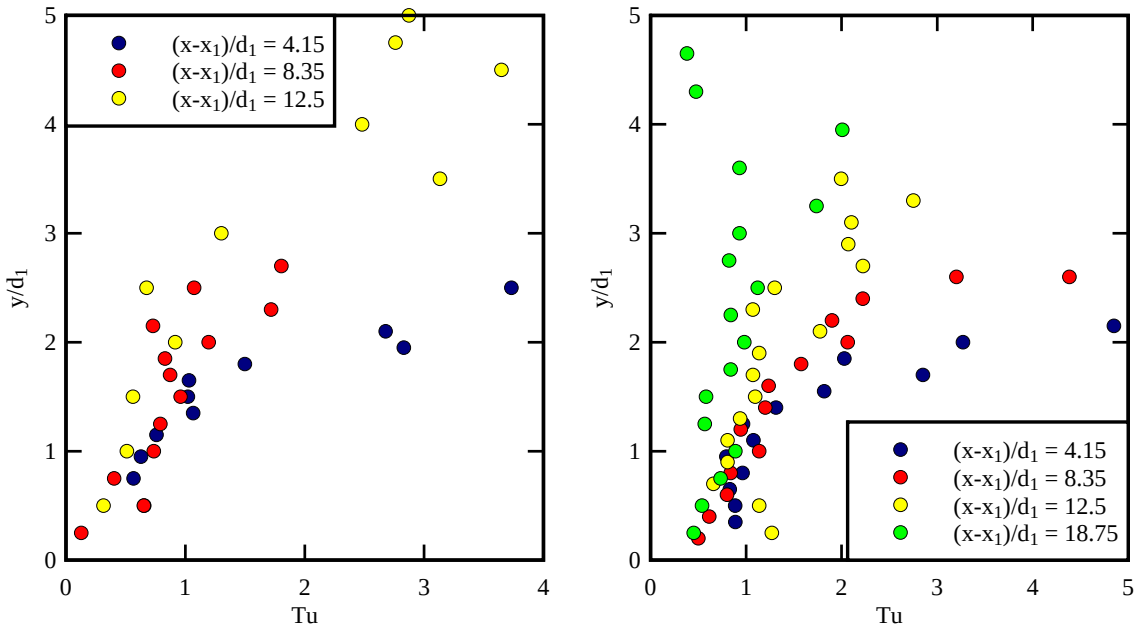

(A) Fr_1 = 3.8 (B) Fr_1 = 5.1

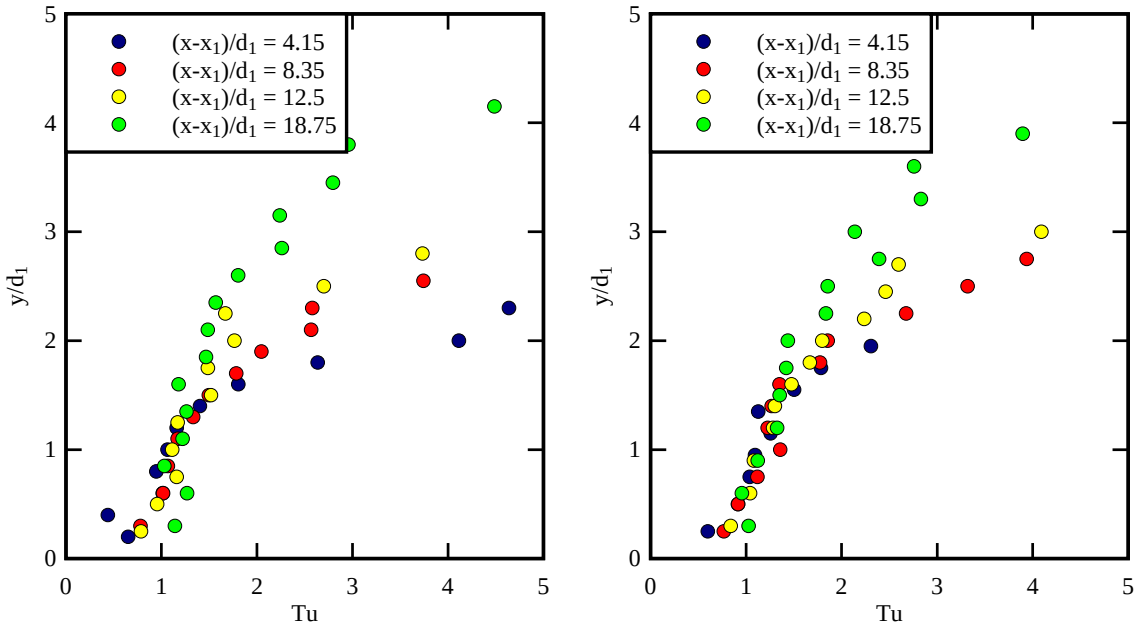

(C) Fr_1 = 7.5 (D) Fr_1 = 8.5

Fig. 3-18 - Vertical distributions of turbulence intensity Tu in hydraulic jumps

3.2.3 Bubble chord time distributions

The bubble chord time represented the time spent by an air bubble on the phase-detection probe tip. It corresponded to the width of the voltage drop in the raw air-water signal. The bubble chord time was proportional to the bubble chord length which statistically reflected the size of the entrapped air bubbles, and inversely proportional to the bubble velocity. Since flow recirculation existed in hydraulic jump, and the phase-detection probe did not discriminate the velocity direction, no information on the bubble chord length was accurately obtained. The bubble chord time was analysed and the probability distribution functions (PDFs) are presented in the form of bar charts with a bin size of 0.25 ms from 0 to 10 ms. Each group was labelled with the lower limit when presented. For example, all the chord times from 1 to 1.25 ms were counted as a group labelled 1 ms. Bubble chord time larger than 10 ms were regrouped and shown in an individual column.

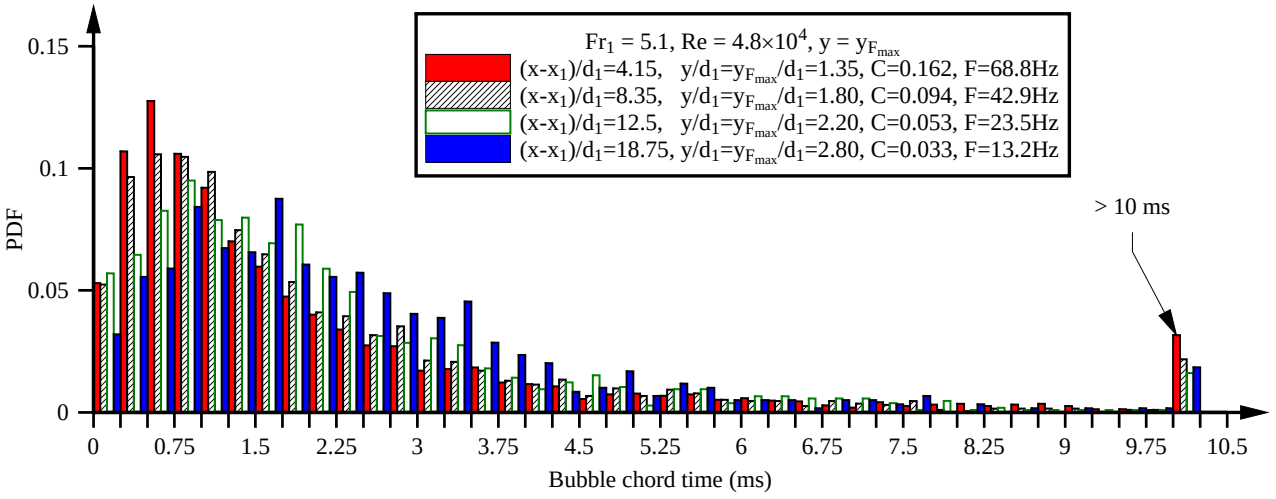

(A) Fr_1 = 5.1

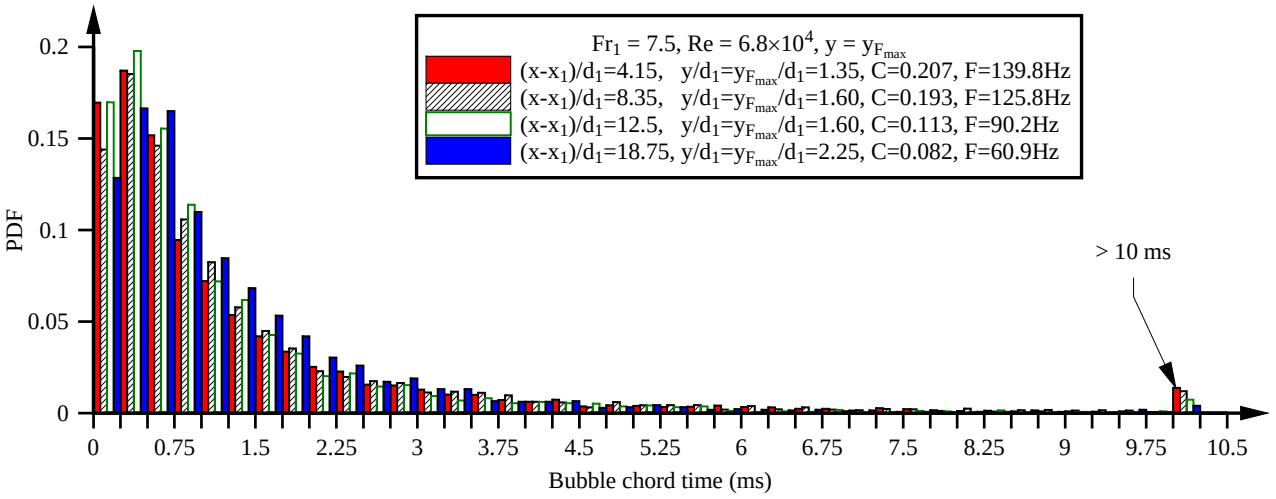

(B) Fr_1 = 7.5

Figure 3-19 - Probability density functions of bubble chord time as functions of longitudinal positions in hydraulic jumps - Data recorded at the characteristic elevation y_{Fmax} of maximum

bubble count rate

Figure 3-19 shows the probability density functions of the bubble chord time measured at the elevation of maximum bubble count rate ($y = y_{Fmax}$). Figures 3-19A and 3-19B present the results at different longitudinal positions for Fr_1 = 5.1 and 7.5 respectively. In each flow, the probability distribution tended to be flatter with increasing distance from the jump toe. This could be the result of either the flow deceleration at downstream, a drop in the proportion of the finest bubbles, a change in shear stress levels or the combination of these. The smaller number of largest bubbles with chord time > 10 ms with increasing downstream distance corresponded to the breaking-up of big air entities and their upward advection by buoyancy. Overall the range of bubble chord times covered orders of magnitude. Figure 3-20 compares the probability distribution of chord time for different flows at the same longitudinal position and elevation $y = y_{Fmax}$. Larger average chord times were seen for the flows with relatively small Froude and Reynolds numbers.

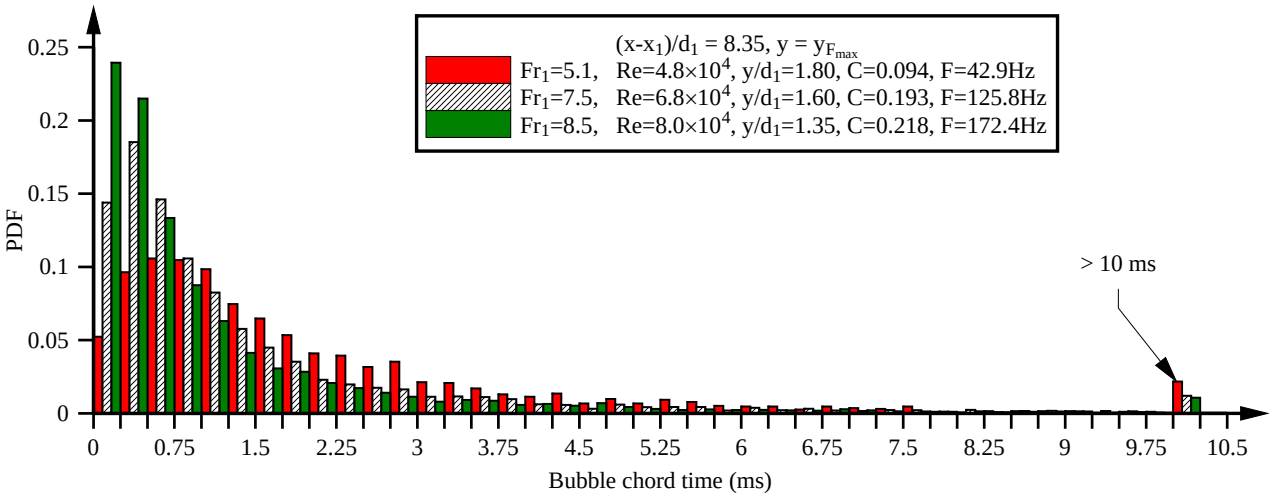

(A) $(x-x_1)/d_1$ = 8.35

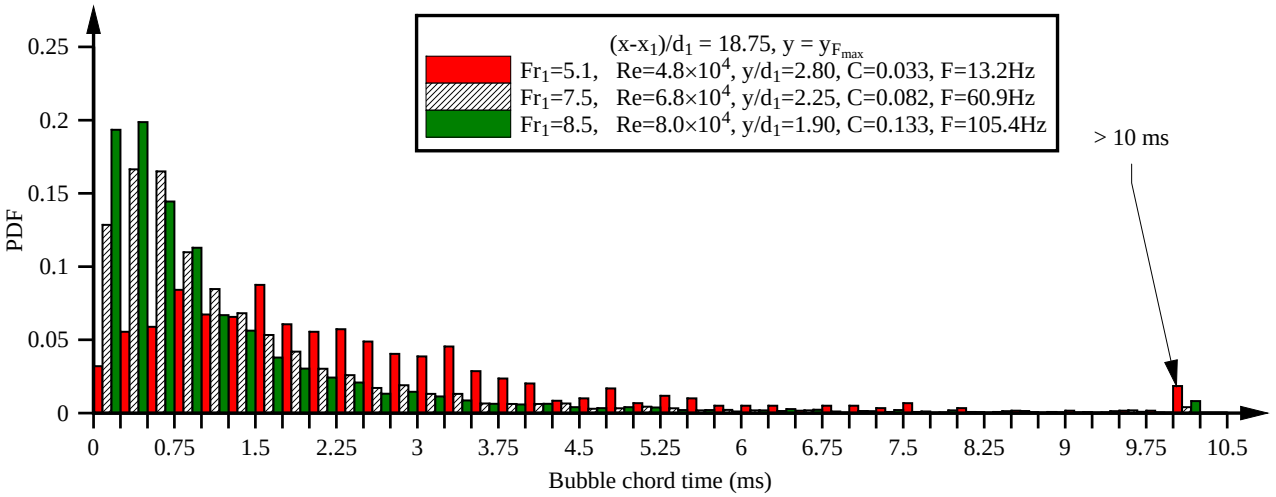

(B) $(x-x_1)/d_1$ = 18.75

Figure 3-20 - Probability density functions of bubble chord time as functions of Froude number in hydraulic jumps - Data recorded at the characteristic elevation y_{Fmax} of maximum bubble count rate

Figure 3-21 illustrates some probability distributions of bubble chord time at several characteristic elevations in the same vertical cross section of roller for Fr_1 = 7.5. The data are presented at the elevations of maximum bubble count rate (y_{Fmax}/d_1), maximum void fraction (y_{Cmax}/d_1) in the shear layer, secondary peak of bubble count rate (y_{F2}/d_1) in the recirculation region and boundary between these two regions (y_*/d_1). Different PDFs were shown at the presented elevations. With increasing distance from the channel bed, the proportion of small bubbles decreased while that of large bubbles increased. A large amount of bubble chord time larger than 10 ms was recorded in the recirculation region, which was consistent with the foamy bubbly flow structure observed next to the free-surface. The change of longitudinal position did not induce much variation in the shape of the probability density functions.

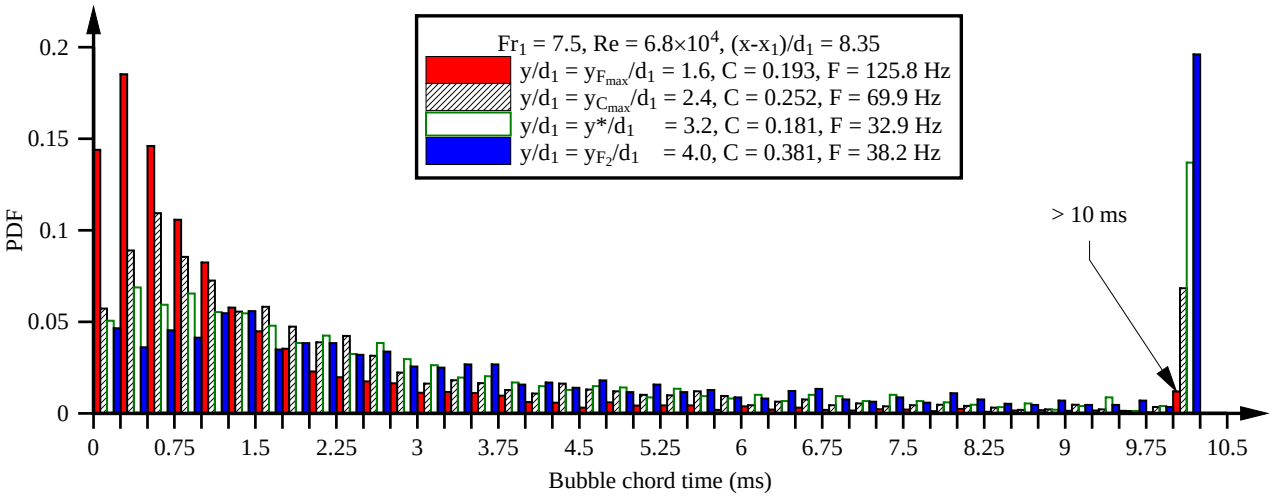

Figure 3-21 - Probability density functions of bubble chord time as function of characteristic elevations in hydraulic jumps - Flow conditions: Q = 0.0347 m^3/s, d_1 = 0.020 m, x_1 = 0.83 m, Fr_1 = 7.5, $x-x_1$ = 0.167 m

Assuming a positive flow direction parallel to the channel bed, the bubble chord length could be obtained based upon the bubble chord time and corresponding local velocity. Figure 3-22 shows the probability distributions of bubble chord length in the shear layer, for the same data set presented in Figure 3-20. The chord lengths were grouped in 0.5 mm bins from 0 to 20 mm, and those larger than 20 mm were regrouped in the last column.

In comparison to Figure 3-20, significant similarities were shown in terms of bubble chord length between different flow conditions. For a given longitudinal position, an increase in Reynolds

number contributed to a slightly higher proportion of small bubbles, reflecting the larger shear stress in the mixing layer. A comparison between longitudinal positions indicated an increasing percentage of small bubbles in the downstream direction. It suggested a dominant process of bubbles being broken up into finer ones in the regions of high shear stresses.

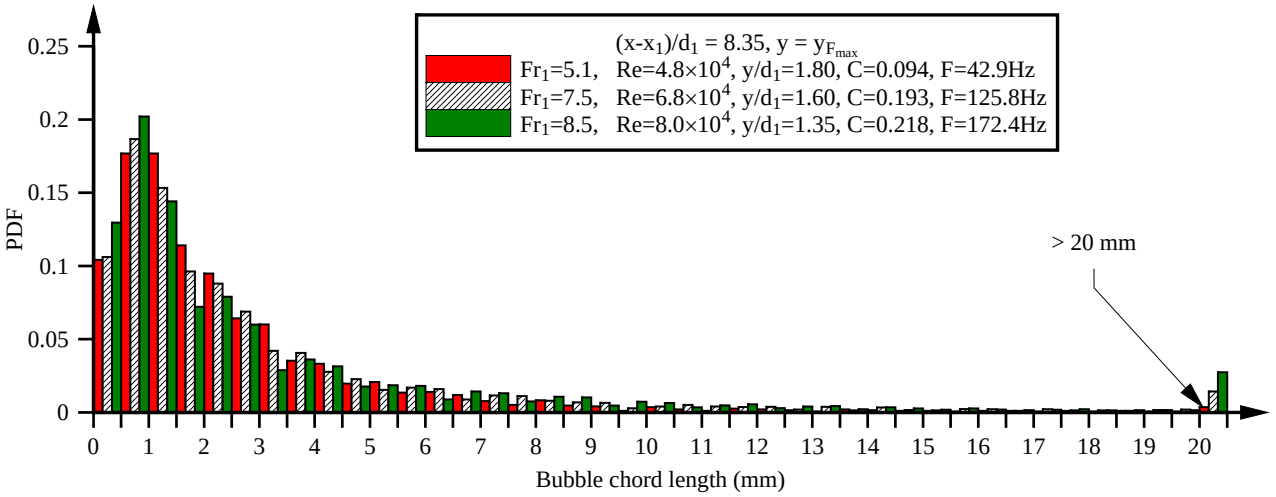

(A) $(x-x_1)/d_1 = 8.35$

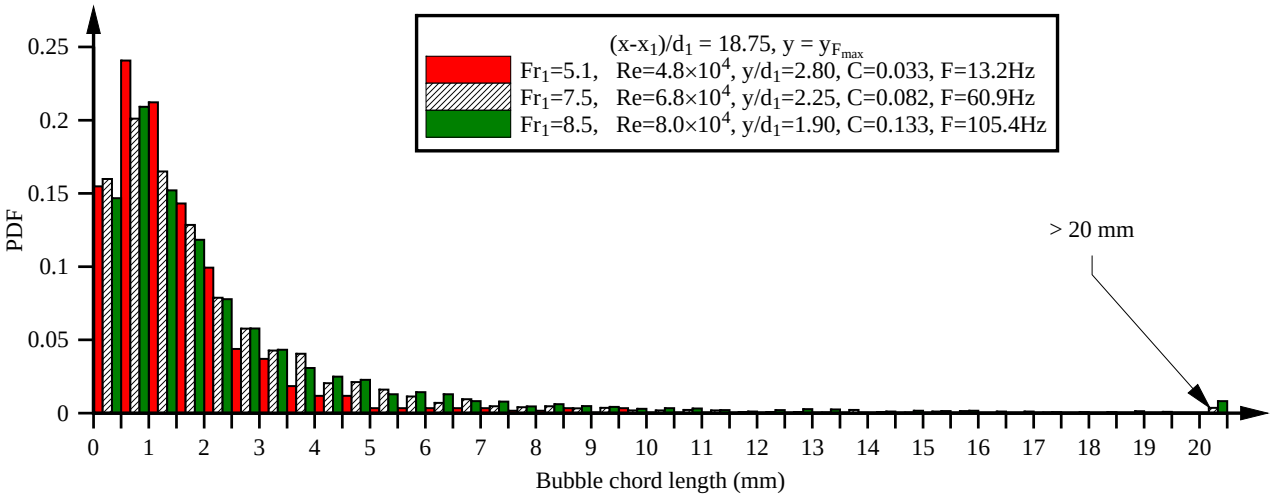

(B) $(x-x_1)/d_1 = 18.75$

Figure 3-22 - Probability density functions of bubble chord length as functions of Froude number in hydraulic jumps - Data recorded at the characteristic elevation y_{Fmax} of maximum bubble count rate

3.2.4 Bubble clustering

Analysis on the interval time between bubbles indicated the existence of clustering in the hydraulic jump rather than a random bubble distribution (CHANSON et al. 2006, CHANSON 2007,2010). A bubble cluster refers to a group of successive bubbles with particle arrival interval time/length smaller than a particular scale. The identification of clustering differs according to the definition of

the characteristic time/length scale. Three criteria were used in air-water flows, namely (a) the constant criterion, (b) the water chord criterion and (c) the near-wake criterion. The near-wake criterion considered bubbles as part of a cluster when the water chord time between two successive bubbles was less than the bubble chord time of the leading particle (CHANSON et al. 2006, CHANSON 2010, CHACHEREAU and CHANSON 2011a). That is, the trailing bubble was in the near-wake of and could be affected by the leading bubble (CHANSON et al. 2006, CHANSON 2010). In the present study, the near-wake criterion was applied because it relies on a comparison between the local characteristic flow times and is believed to be most effective (GUALTIERI and CHANSON 2010). The signal of leading phase-detection probe sensor was analysed at the elevation of maximum bubble count rate in the shear layer, i.e. $y = y_{Fmax}$. A series of clustering properties were derived, including the cluster rate F_{clu} defined as the number of clusters per second, the cluster size N_{clu} defined as the average number of particles per cluster and the cluster proportion P_{clu} defined as the total percentage of bubbles travelling in clusters.

Figure 3-23 shows the longitudinal distribution of dimensionless cluster rate $F_{clu} \times d_1/V_1$, namely the formation frequency of bubble clusters. A large amount of clusters per unit time was recorded immediately downstream the jump toe, and decreased in the streamwise direction. The dimensionless cluster rate varied with different flow conditions. It increased with increasing Froude and Reynolds numbers. The findings were consistent with those of CHANSON (2010) and CHACHEREAU and CHANSON (2011a).

A decrease of dimensionless cluster rate with increasing distance from the jump toe was found to follow an exponential decay:

$$\frac{F_{clu} \times d_1}{V_1} = A \times \exp\left(-B \times \frac{x-x_1}{d_1}\right) \quad (3.6)$$

where A and B are the dimensionless coefficients determined by the flow conditions. Both present experimental results and the data of CHANSON (2010) were correlated by:

$$A = -0.0416 + 0.0465 \times \frac{Re}{10^4} \quad (3.7a)$$

$$B = 0.494 \times \exp\left(-0.233 \times Fr_1\right) \quad (3.7b)$$

giving the expression of cluster rate

$$\frac{F_{clu} \times d_1}{V_1} = \left(-0.0416 + 0.0465 \times \frac{Re}{10^4}\right) \times \exp\left(-\left(0.494 \times \exp\left(-0.233 \times Fr_1\right)\right) \times \frac{x-x_1}{d_1}\right) \quad (3.8)$$

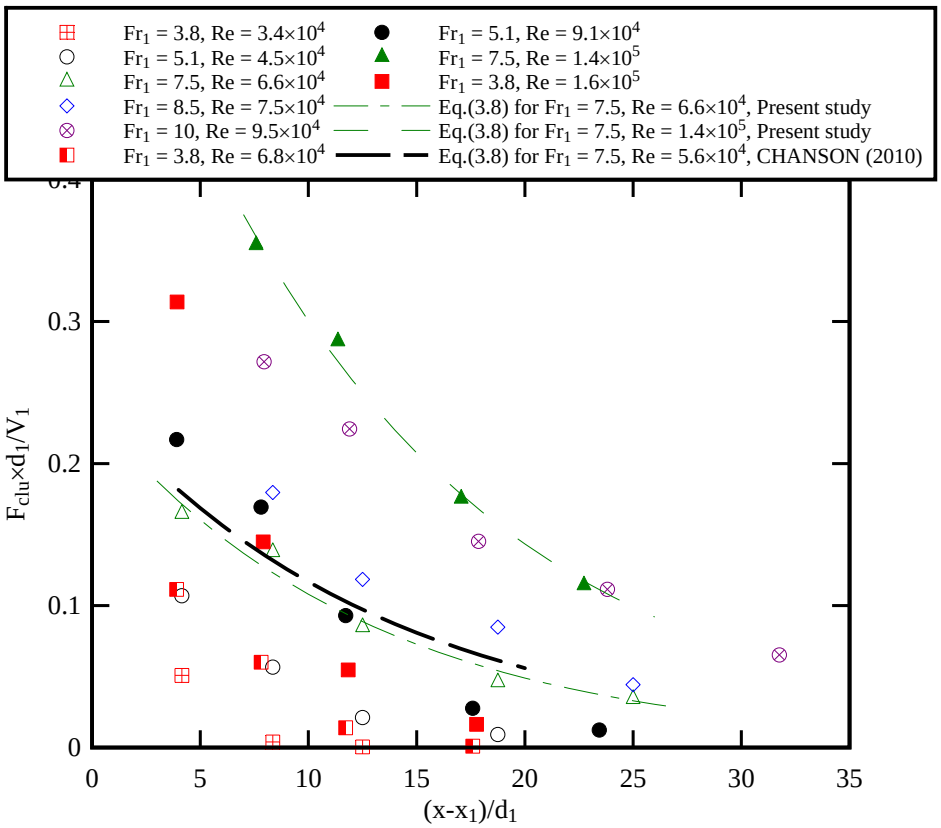

Figure 3-23 - Longitudinal distribution of dimensionless bubble cluster rate in hydraulic jumps - Comparison with best fit correlation and data by CHANSON (2010)

Equation (3.8) implied that the magnitude of dimensionless bubble rate was related to the Reynolds number, while the streamwise decay rate was mostly linked with the Froude number. Note that a similar type of relationships was found in terms of dimensionless maximum bubble count rate $F_{max} \times d_1/V_1$ (WANG and CHANSON 2013). Equation (3.8) is shown in Figure 3-23 for two data sets.

The numbers of bubbles per cluster were documented and the results showed a majority of clusters with only two bubbles. Figure 3-24 presents the probability distributions of the cluster size for Fr_1 = 5.1 and 7.5. The results demonstrated that the large clusters (three or more bubbles) mainly existed at a short distance downstream of the jump toe. The longitudinal decrease in number of large clusters might be linked to the process of bubble diffusion in the shear layer, thus reducing the bubble density and number of large clusters. A comparison between different flow conditions showed that the proportion of large clusters tended to increase with increasing Froude numbers. Figure 3-25 presents the longitudinal distributions of average cluster size for several experiments. The average cluster size increased with increasing Froude or Reynolds number, and decreased with increasing distance from the jump toe. The data ranged from 2.3 to 2.7 immediately downstream the jump toe down to 2 to 2.4 at the end of the roller.

A large proportion of bubbles were associated with clusters, in particular at the beginning of the shear layer. The cluster proportion, that is the percentage of bubbles in clusters, was seen to decrease with increasing longitudinal distance (Fig. 3-26). The magnitude and trend were functions of both Froude and Reynolds numbers. For the wide range of flow conditions investigated in present study, the cluster proportion varied between 30% and 60% immediately downstream the jump toe. The findings agreed with the results of CHANSON (2010) and CHACHEREAU and CHANSON (2011a), showing percentages of bubbles in clusters from 30 to 45% for $7.5 < Fr_1 < 11.2$ and 45-60% for $3.1 < Fr_1 < 5.1$ respectively.

The percentages of bubbles in clusters were best correlated with an exponential relationship:

$$P_{clu} = \left(0.365+0.0269\times\frac{Re}{10^4}\right)\times\exp\left(-\left(0.237\times\exp\left(-0.214\times Fr_1\right)\right)\times\frac{x-x_1}{d_1}\right) \qquad (3.9)$$

Equation (3.9) is plotted in Figure 3-26 for some experimental results.

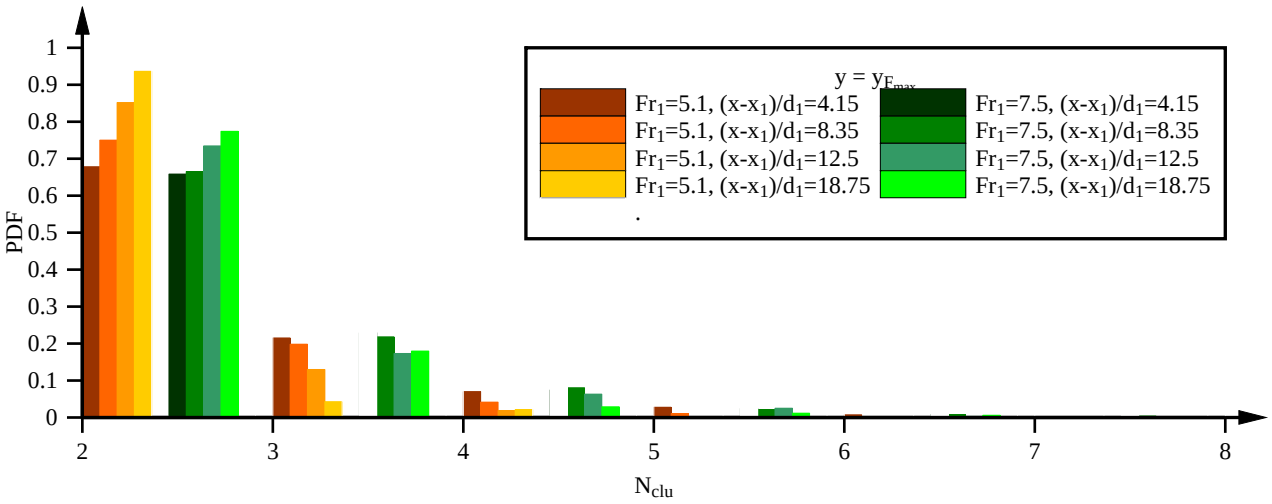

Figure 3-24 – Probability distribution of average number of bubbles per cluster (cluster size) at the characteristic elevation y_{Fmax} of maximum bubble count rate in hydraulic jumps

3.2.5 Comparison with previous studies

In order to assess the repeatability and accuracy of the two-phase flow data, a number of systematic comparisons were performed between the present data and previous experiments performed in the last ten years with phase-detection optical fibre and conductivity probes. The best fits based upon the large number of data sets are presented in Table 3-1 and Figure 3-27 for different characteristic properties.

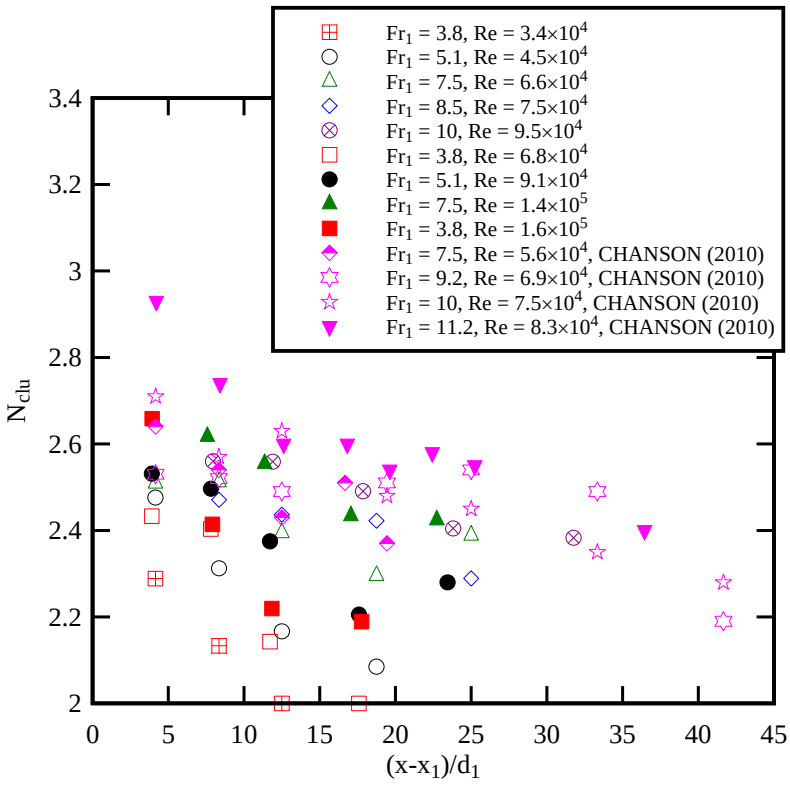

Figure 3-25 - Longitudinal distribution of average cluster size - Comparison with data of CHANSON (2010)

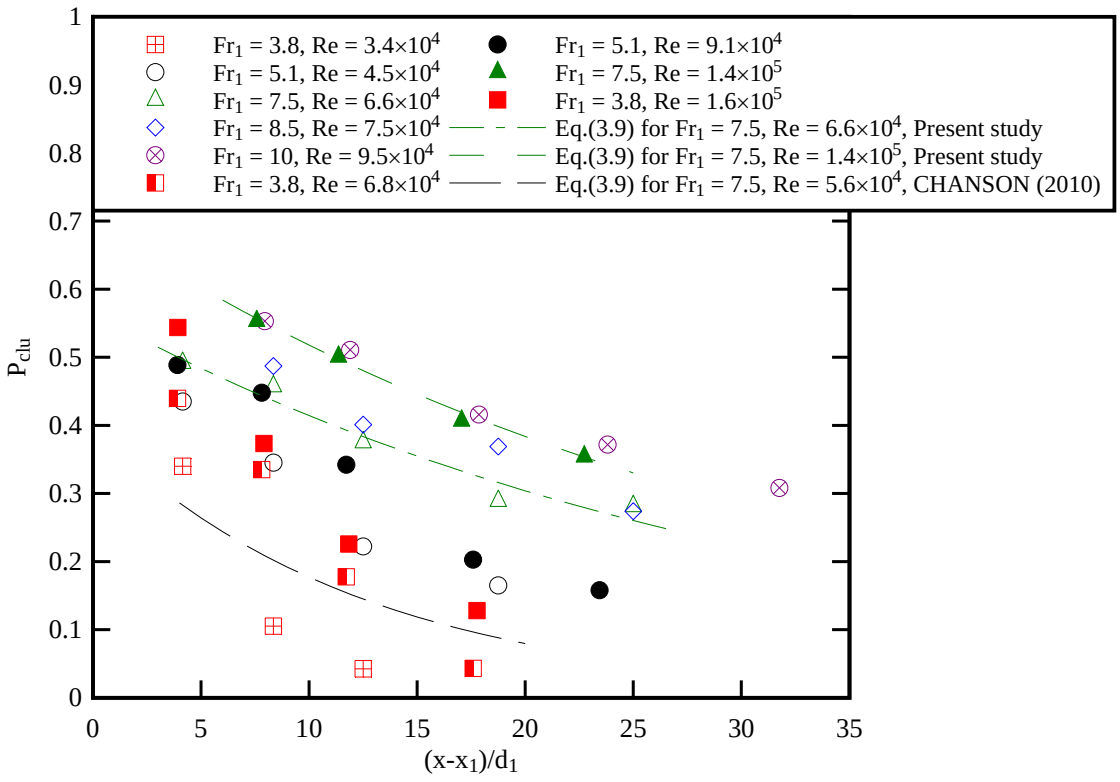

Figure 3-26 - Longitudinal distributions of cluster proportion - Comparison with best fit correlations and data of CHANSON (2010)

Figure 3-27 summarises the experimental results of several studies in terms the dimensionless elevations of maximum void fraction y_{Cmax}/d_1, of boundary between shear and recirculation regions y_*/d_1, of maximum bubble count rate y_{Fmax}/d_1 and of maximum velocity y_{Vmax}/d_1 in hydraulic jumps with a marked roller. Overall the data scatter was relatively low. The data fitted well some linear correlations in terms of the longitudinal distance from the jump toe (Table 3-1). The results suggested that the characteristic elevations were basically independent of Froude or Reynolds numbers. Further the data trend in terms of y_{Cmax} and y_{Fmax} hinted that the characteristic elevations were mostly determined by air bubble diffusion process, buoyancy effect, dissipation of turbulent structure... The data in terms of y_{Vmax} presented a larger data scatter than for other data. This might reflect the turbulent nature of the two-phase flow and the difficulty to conduct the velocity measurement with phase-detection probes in regions of small or zero velocity.

Altogether, the experimental data showed consistently that the maximum velocity was found at a lower elevation than the maximum bubble count rate and maximum void fraction. That is:

$$\frac{y_{Vmax}}{d_1} < \frac{y_{Fmax}}{d_1} < \frac{y_{Cmax}}{d_1} < \frac{y_*}{d_1} \qquad \text{for } 3.8 < Fr_1 < 8.5 \quad (3.10)$$

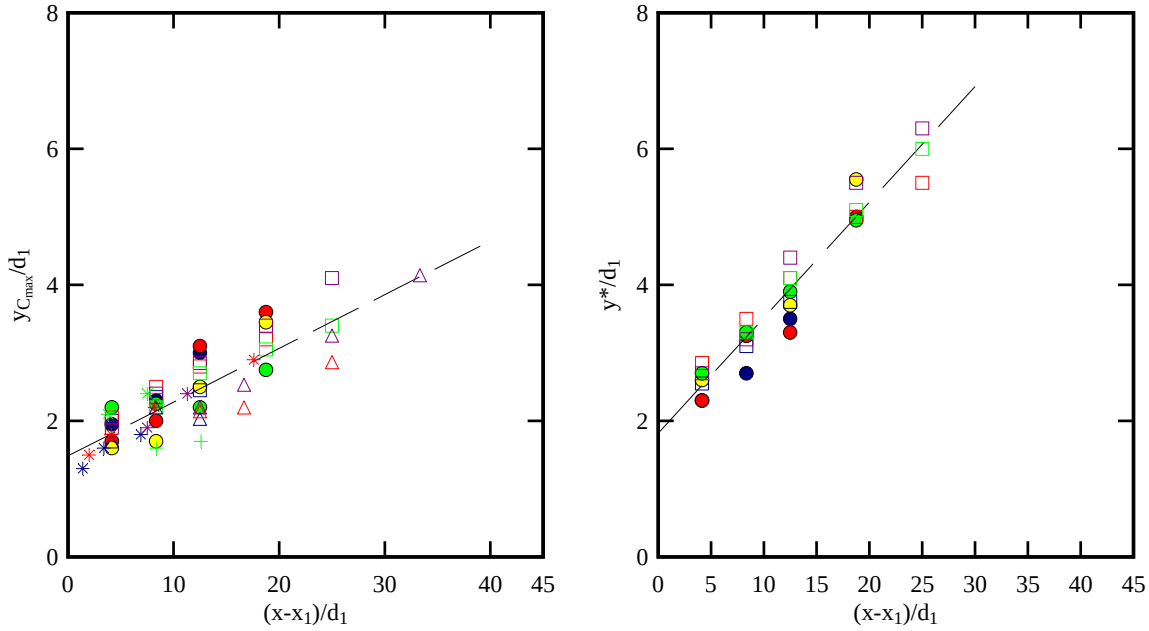

(A) Elevation of local maximum void fraction (B) Elevation of the shear layer upper boundary

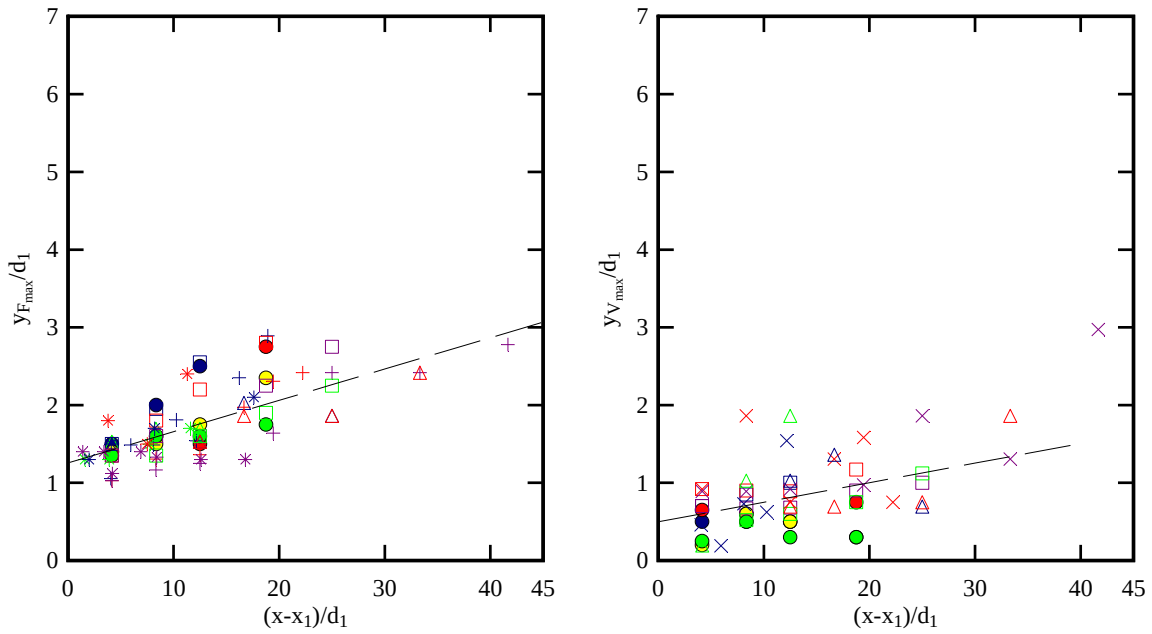

(C) Elevation of maximum bubble count rate (D) Elevation of maximum interfacial velocity

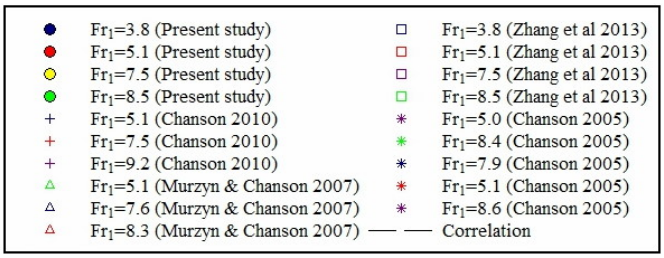

Fig. 3-27 - Longitudinal distributions of characteristic elevations y_{Cmax}/d_1, y_*/d_1, y_{Fmax}/d_1 and y_{Vmax}/d_1 in hydraulic jumps with a marked roller - Comparison between present data and earlier studies (CHANSON 2006,2007, MURZYN and CHANSON 2007,2008, CHANSON 2010, ZHANG et al. 2013)

Table 3-1 - Characteristic elevations y_{Cmax}/d_1, y_*/d_1, y_{Fmax}/d_1 and y_{Vmax}/d_1 in hydraulic jumps with a marked roller: best fit relationship

Parameter	Correlation	Range
$\frac{y_{Cmax}}{d_1}$	$1.486 + 0.079 \times \frac{x - x_1}{d_1}$	$(x-x_1)/d_1 < 33$ $3.8 < Fr_1 < 8.6$
$\frac{y_*}{d_1}$	$1.818 + 0.170 \times \frac{x - x_1}{d_1}$	$(x-x_1)/d_1 < 25$ $3.8 < Fr_1 < 8.5$
$\frac{y_{Fmax}}{d_1}$	$1.255 + 0.0403 \times \frac{x - x_1}{d_1}$	$(x-x_1)/d_1 < 42$ $3.8 < Fr_1 < 9.2$
$\frac{y_{Vmax}}{d_1}$	$0.4968 + 0.0252 \times \frac{x - x_1}{d_1}$	$(x-x_1)/d_1 < 33$ $3.8 < Fr_1 < 9.2$

Note: Experimental data sets: CHANSON (2006,2007), MURZYN and CHANSON (2007,2008), CHANSON (2010), ZHANG et al. (2013), Present study

4. EXPERIMENTAL RESULTS. (2) TOTAL PRESSURE MEASUREMENTS

4.1. MEAN TOTAL PRESSURE AND COMPARISON WITH THEORETICAL PREDICTIONS

To date the investigations of pressure measurements beneath and within the jump roller were limited, especially for highly turbulent aerated jumps with large Froude and Reynolds numbers (ABDUL KHADER and ELANGO 1974, FIOROTTO and RINALDO 1992, YAN and ZHOU 2006, LOPARDO and ROMAGNOLI 2009). Herein a miniature total pressure probe was placed in the jump roller facing the upstream flow.

Figure 4-1 presents the vertical profiles of the time-averaged total pressure measurements at different longitudinal positions in the roller. Figures 4-1A to 4-1D show the results for Fr_1 = 3.8, 5.1, 7.5 and 8.5 respectively. The data presented a similar profile, varying gradually as the distance from the jump toe increased. In the shear region, the mean total pressure exhibited a maximum P_{max} at an elevation $0.5 < y_{Pmax}/d_1 < 0.9$. The maximum total pressure P_{max} decreased with increasing distance from the jump toe, reflecting the dissipation of kinetic energy and turbulence of the flow. The longitudinal decay of dimensionless maximum mean pressure $P_{max}/(0.5\times\rho_w\times V_1^2)$ was nearly identical for all flow conditions.

The instantaneous total pressure was recorded at several elevations above the channel bed up to the free surface. The pressure measurements were the local total pressure relative to the atmospheric pressure. In the horizontal channel, the total pressure P was the sum of the piezometric pressure P_o and the kinetic pressure P_k:

$$P = P_o + P_k \qquad (4.1)$$

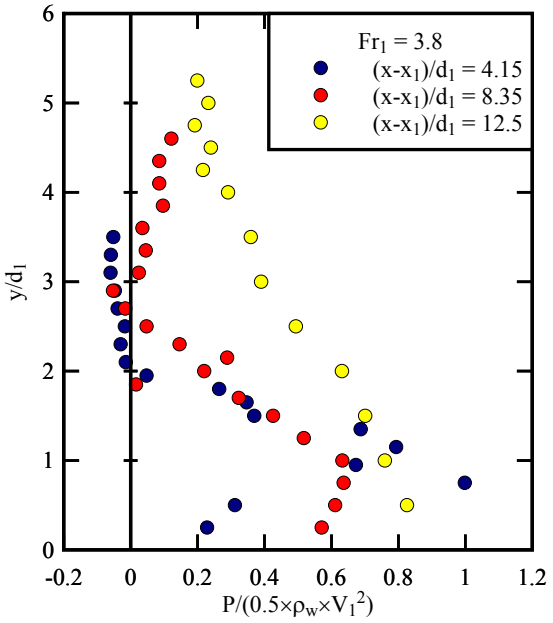

(A) Fr_1 = 3.8

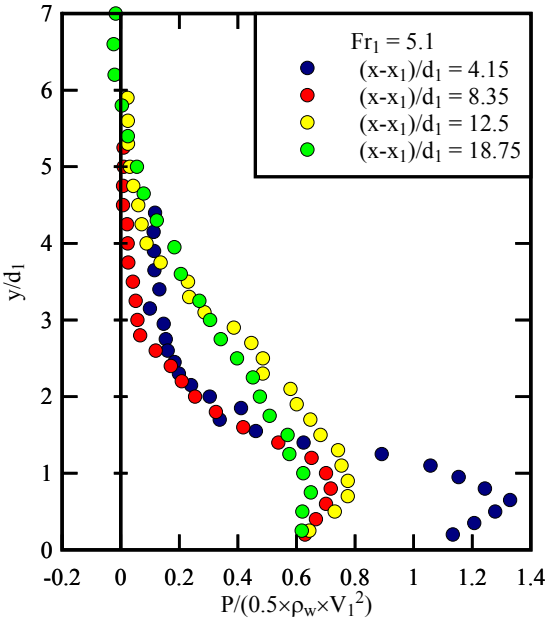

(B) Fr_1 = 5.1

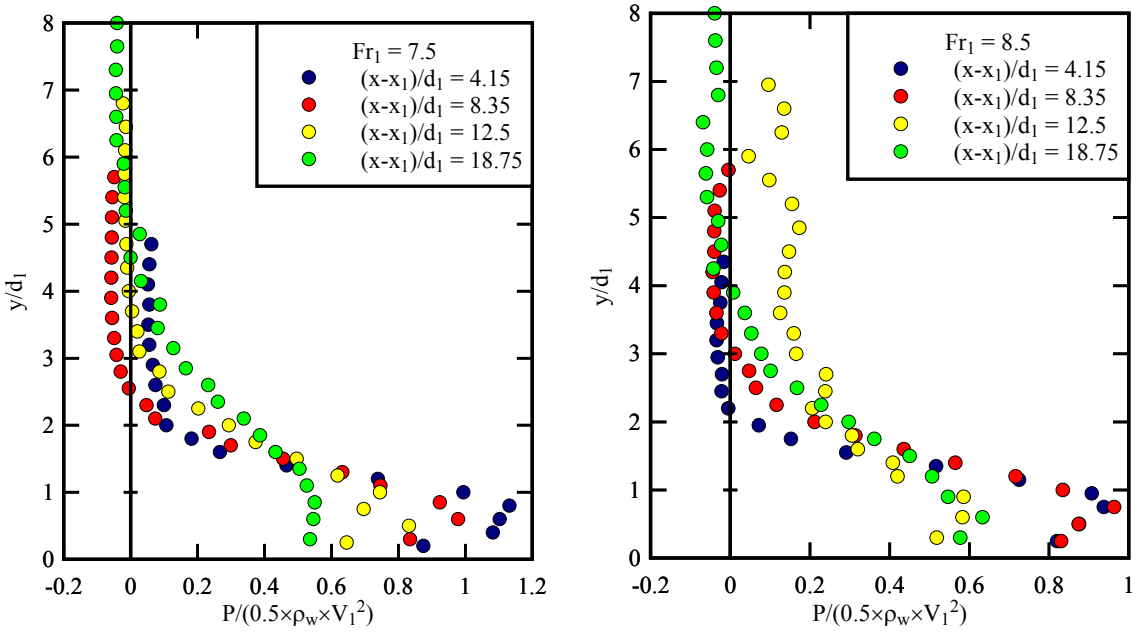

(C) $Fr_1 = 7.5$ (D) $Fr_1 = 8.5$

Fig 4-1 - Vertical profiles of time-averaged total pressure in hydraulic jumps

The piezometric pressure was a function of the flow depth and relative probe elevation, while the kinetic pressure was a function of the local velocity

$$P_o = \int_{y}^{y_{90}} (1-C) \times \rho_w \times g \times dy \quad (4.2)$$

$$P_k = \frac{1}{2} \times (1-C) \times \rho_w \times V^2 \quad (4.3)$$

where C and V are the void fraction and velocity respectively, y is the probe sensor elevation above the invert, ρ_w is the density of water and y_{90} is the vertical position where C = 0.9. Note that Equation (4.2) assumes implicitly a hydrostatic pressure distribution in the roller, and consistent with limited time-averaged pressure data sets (RAJARATNAM 1965, ABDUL KHADER and ELANGO 1974, FIOROTTO and RINALDO 1992). The void fraction and time-averaged interfacial velocity were measured using the dual-tip phase-detection probe. In the present experiments, the dual-tip phase-detection probe was mounted side by side with the pressure probe and sampled simultaneously, thus allowing a direct comparison between the measured total head and the expected value (Eq. (4.1)). In the upper roller, where flow recirculation occurred, the probes were not aligned against the flow direction and the pressure data were not meaningful: the kinetic pressure component might be missed and negative pressure (relative to atmospheric) were sometimes detected when the head of pressure probe was in the wake of the probe itself.

All results were compared with the theoretical values calculated using Equations (4.1) to (4.3). Some typical results are presented in Figure 4-2. The piezometric pressure deduced from Equation

(4.2) is also shown in Figure 4-2. In Figure 4-2A, the data were measured close to the end of roller where the velocity profile was quasi uniform as shown by WU and RAJARATNAM (1996). Therefore the distributions of piezometric and total pressures were expected to be parallel, with a decreasing trend with increasing elevation from the channel bed to the free surface. This is shown in Figure 4-2A, indicating that the pressure measurements were reliable in the less turbulent and low-aerated flow. The data presented in Figures 4-2B to 4-2D were recorded in the turbulent region of the roller. The piezometric pressure profiles were straight lines, indicating that the pressure distribution was hydrostatic ([1]). In the turbulent shear layer, the experimental measurements of total head and the theoretical calculations based on the two-phase flow measurements (Eq. (4.1) to (4.3)) were in good agreement. The total pressure increased rapidly from $P_o(y=0)$ at the channel bed to a maximum P_{max} at an elevation y_{Pmax} very close to the characteristic elevation y_{Vmax}. For $y > y_{Pmax}$, the total pressure decreased gradually till the upper boundary of shear layer y_* (Fig. 4-1 & 4-2). Overall the trend was consistent with a superposition of the piezometric pressure and the kinetic pressure. In the recirculation region (i.e. $y > y_*$), the kinetic pressure component could not be captured accurately by the pressure probe. Overall, the comparison between the experimental and theoretical data confirmed the validity of the total pressure measurement in the turbulent shear layer ($y < y_*$).

Though the mean piezometric pressure increased with increasing free-surface elevation, the total pressure decreased with increasing distance from the jump toe (Fig. 4-1). The data showed a longitudinal decrease in total pressure, consistent with the longitudinal flow deceleration. Figure 4-3 shows the maximum total pressure P_{max} at different longitudinal positions in hydraulic jumps and the corresponding elevation y_{Pmax}. The maximum total pressure decreased with increasing distance from the impingement point, although, at a given distance $(x-x_1)/d_1$ from the jump toe, the maximum total pressure increased with increasing Froude number. The vertical position of the maximum pressure showed limited variation at different longitudinal positions, giving an average of $y_{Pmax}/d_1 = 0.7$. The maximum total pressure took place at close elevations with the maximum velocity (Fig. 4-3B). The elevations of maximum bubble count rate as well as maximum pressure fluctuations which are discussed in the next section are also presented.

[1] taking into account the flow aeration, that is $\partial P_{stat}/\partial y = -\rho_w \times (1-C) \times g$, where P_{stat} is the local pressure.

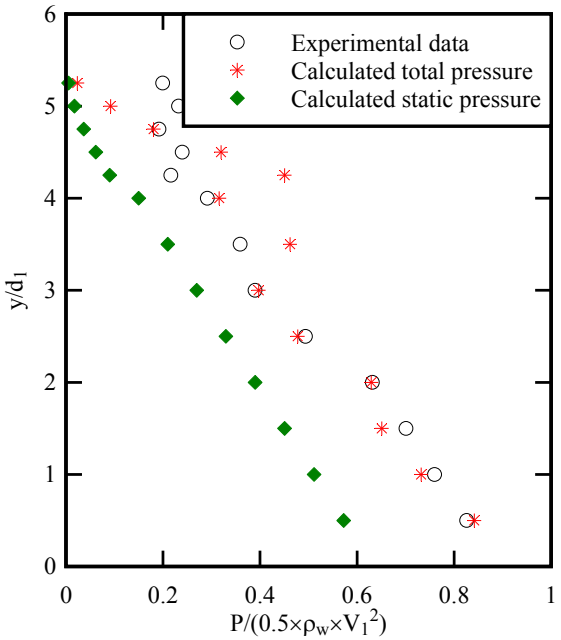

(A) $Fr_1 = 3.8$

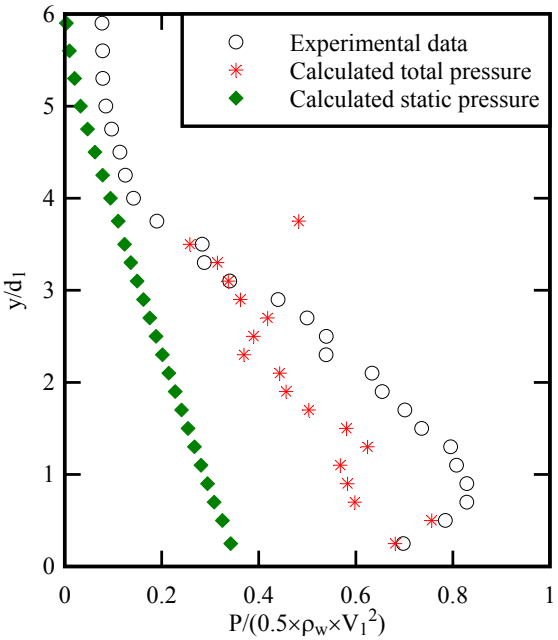

(B) $Fr_1 = 5.1$

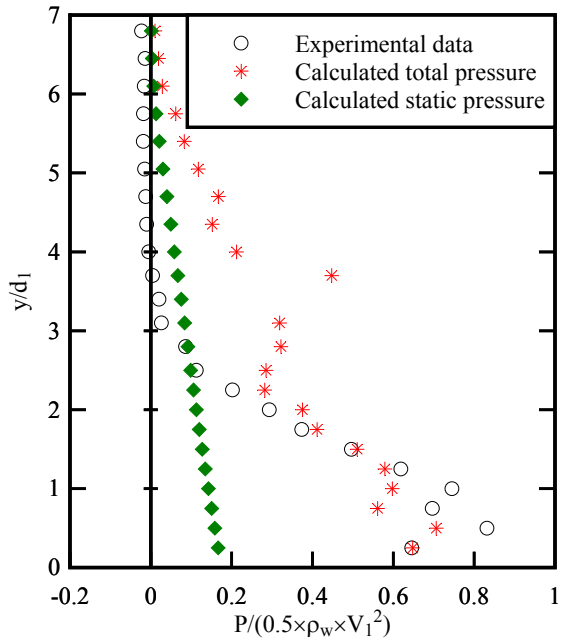

(C) $Fr_1 = 7.5$

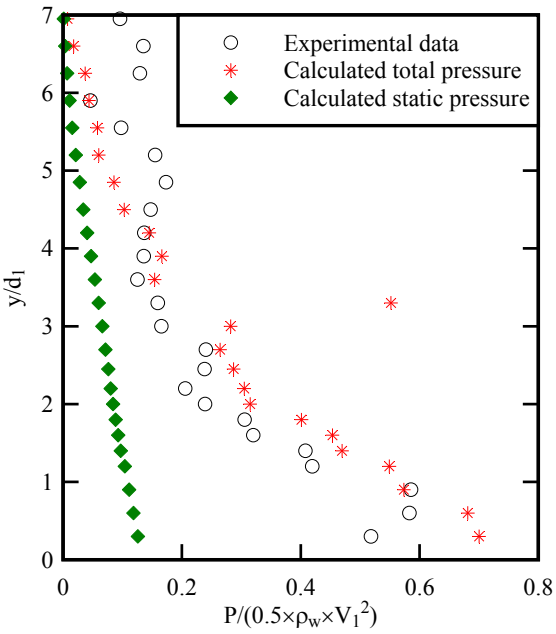

(D) $Fr_1 = 8.5$

Fig. 4-2 - Vertical distributions of measured total pressure profiles and theoretical predictions (Eq. (4.1) & (4.2)) based upon two-phase flow measurements at $(x-x_1)/d_1 = 12.5$ in hydraulic jumps

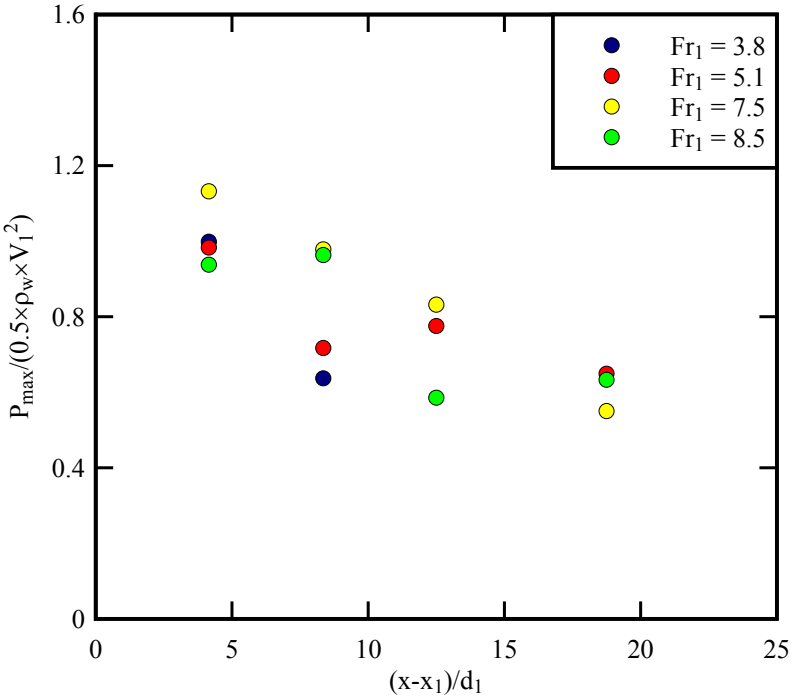

(A) Longitudinal variations of dimensionless maximum total pressure $P_{max}/(0.5\times\rho_w\times V_1^2)$

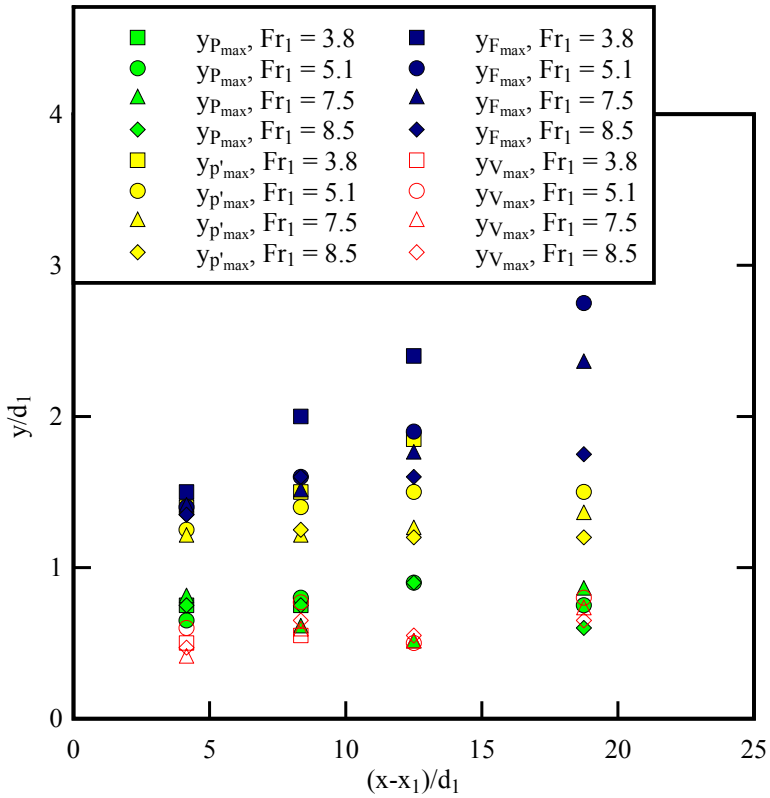

(B) Longitudinal variations of elevations y_{Pmax}/d_1 of maximum total pressure and maximum pressure fluctuation $y_{p'max}/d_1$ - Comparison with elevation of maximum velocity y_{Vmax}/d_1 and elevation of maximum bubble count rate y_{Fmax}/d_1

Fig 4-3 - Maximum total pressure in the shear layer of hydraulic jumps

4.2. TURBULENT PRESSURE FLUCTUATIONS

4.2.1 Total pressure fluctuations and comparison with turbulence intensity

The instantaneous pressure fluctuations were recorded in 5 kHz sampling rate for 180 s, although the signal components above 2 kHz were filtered analogically by the amplification system. Some typical probability distribution functions (PDFs) of total pressure are presented in Figure 4-4. The data were recorded in the shear layer at the elevation y_{Pmax} where the time-averaged total pressure was maximum. Further total pressure PDF data are presented in Appendix A, together with the first four statistical moments of the total pressure data sets.

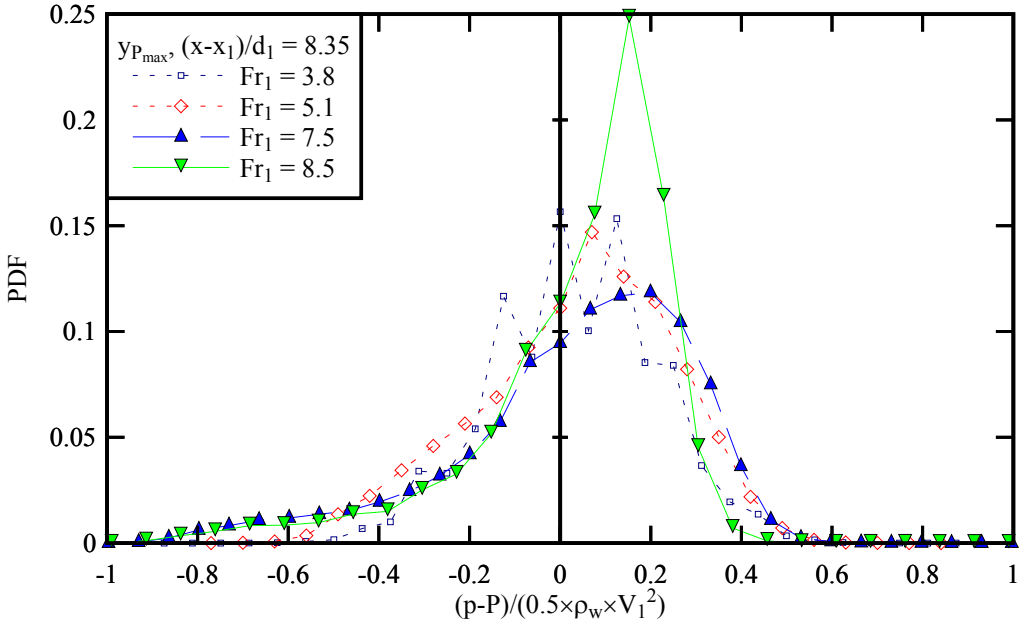

Fig. 4-4 - Probability distribution functions of instantaneous total pressure deviation from the mean in the shear layer of hydraulic jumps - Locations: $y = y_{Pmax}$, $(x-x_1)/d_1 = 8.35$

The total pressure fluctuations are discussed herein in terms of the standard deviation p' of pressure signal. Some typical vertical distributions of total pressure fluctuations p' are plotted in Figure 4-5. Herein the focus was on the turbulent shear layer ($0 < y < y_*$) where the velocity was positive. The vertical distributions of total pressure fluctuations presented a marked peak in the shear layer, corresponding to the occurrence of maximum pressure fluctuations. The magnitude of total pressure fluctuations decreased with increasing distance from the jump toe (Fig. 4-5). The data showed relatively larger pressure fluctuations at higher Froude numbers. It is noteworthy that the vertical position of the maximum pressure fluctuation was not identical to that of the maximum mean total pressure, with $y_{p'max} > y_{Pmax}$ typically.

Figure 4-6 summarises the dimensionless maximum standard deviations of pressure

$p'_{max}/(0.5\times\rho_w\times V_1^2)$ as function of the distance from the jump toe. The data showed a longitudinal decay implying a gradual turbulence dissipation. Differences between different Froude numbers were observed, with larger dimensionless pressure fluctuations with larger Froude numbers. Different amplitudes of fluctuations were clearly shown between Froude numbers.

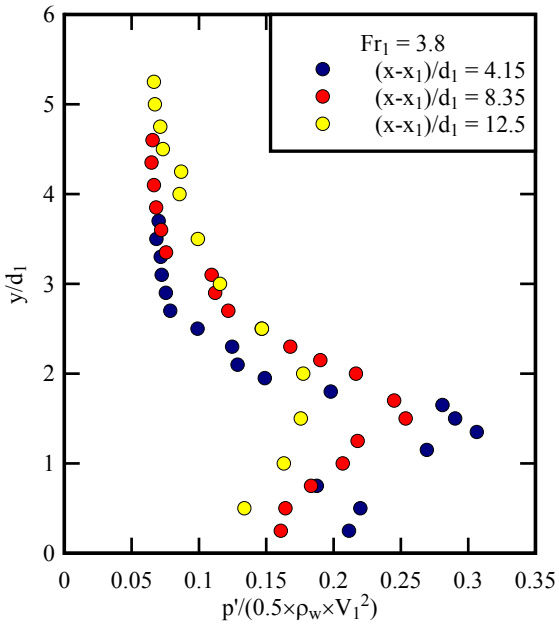

(A) $Fr_1 = 3.8$

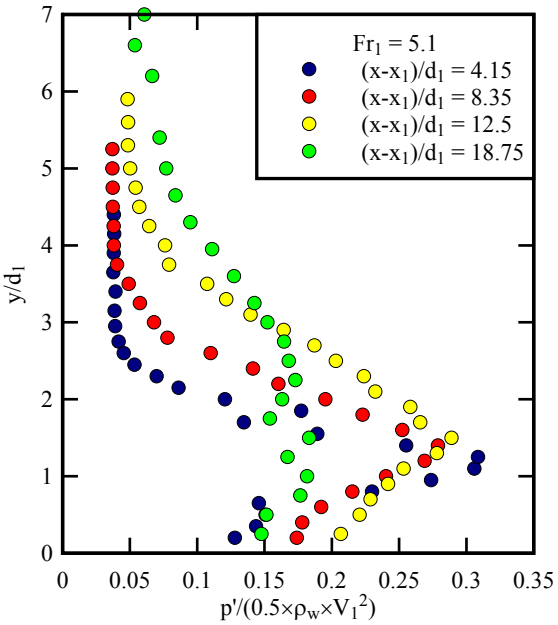

(B) $Fr_1 = 5.1$

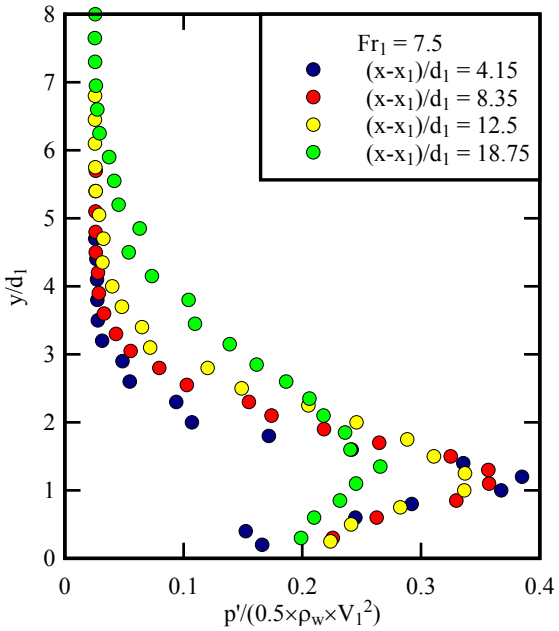

(C) $Fr_1 = 7.5$

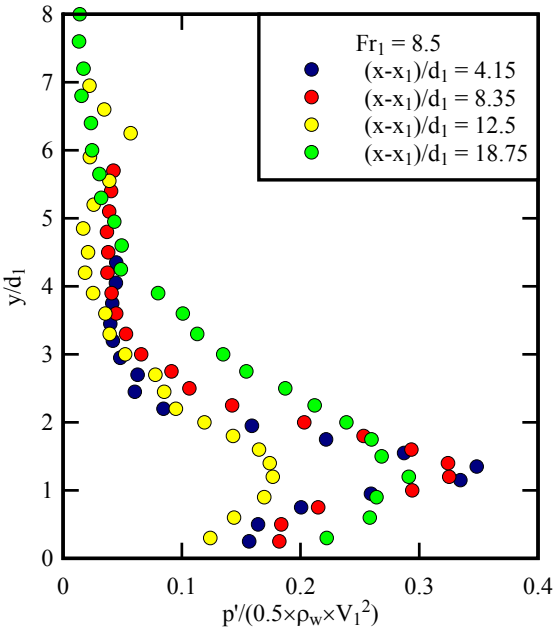

(D) $Fr_1 = 8.5$

Fig 4-5 - Vertical profiles of standard deviation of total pressure in hydraulic jumps

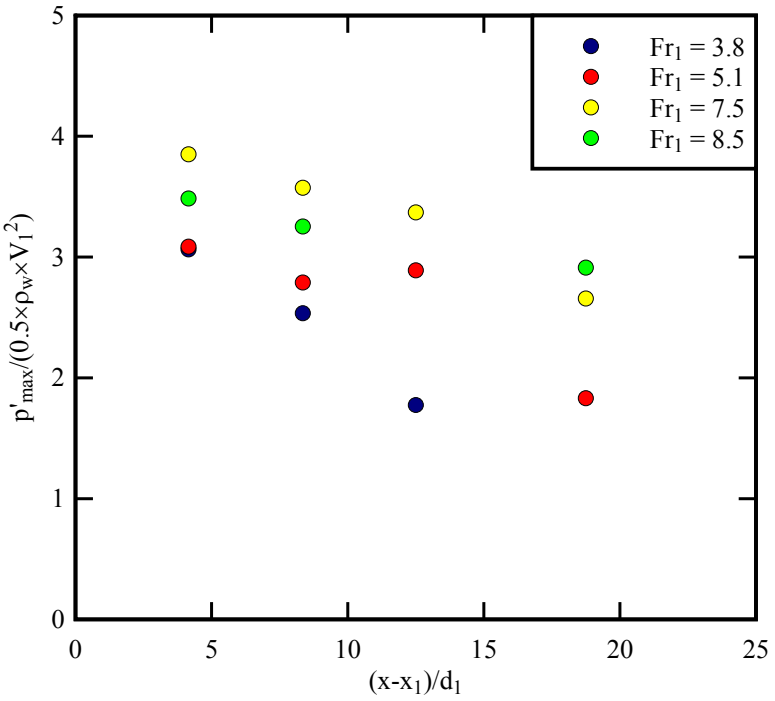

Fig 4-6 - Longitudinal decay of maximum total pressure fluctuation in the shear layer of hydraulic jumps

The corresponding elevation of maximum pressure fluctuation $y_{p'max}/d_1$ is shown in Figure 4-3B. A slight increase in elevation with increasing distance to the jump toe was noted, despite some scattering within $1.2 < y_{p'max}/d_1 < 1.5$. The data are consistently shown at a lower position than the maximum bubble count rate and higher than the maximum mean pressure and velocity, i.e. $y_{Vmax} \approx y_{Pmax} < y_{p'max} < y_{Fmax}$.

Both the total pressure fluctuations and bubble count rate were turbulence-related processes. Several studies showed that the longitudinal decay in maximum bubble count rate F_{max} was a function of the Reynolds number (MURZYN and CHANSON 2008, CHANSON and CHACHEREAU 2013, WANG and CHANSON 2013). The size, hence number of bubbles are linked to the turbulent shear force, hence the local turbulence intensity. The total pressure consists of the piezometric pressure related to the local depth and the kinetic pressure related to the local velocity. The total pressure fluctuations are hence linked to the turbulent velocity fluctuations, i.e. the turbulence intensity. The data showed that the two characteristic elevations y_{Fmax} and $y_{p'max}$ were not identical with $y_{Fmax} > y_{p'max}$ (Fig. 4-3B). It might suggest that the two processes were not directly associated, because the bubble count rate also relied on the void fraction, which increased from bottom till an elevation $y_{Cmax} > y_{Fmax} > y_{p'max}$. Buoyancy effects might be a further factor affecting the location of maximum bubble count rate.

Figure 4-7 presents a comparison between the relative total pressure fluctuations p'/P and the

turbulence intensity Tu = v'/V, where P is the local mean total pressure and V is the local mean velocity. All the data were recorded at the same cross section $(x-x_1)/d_1 = 8.35$ for $3.8 < Fr_1 < 8.5$. The turbulence intensity Tu was measured with a dual-tip phase-detection probe (CHANSON and TOOMBES 2002). The upper boundary of turbulent shear layer y_* is clearly show in Figure 4-7; data for $y > y_*$ are shown for completeness. The data showed that the relative total pressure fluctuation p'/P increased with increasing distance from the invert in the shear layer for all flow conditions. The relative fluctuation of velocity v'/V was consistently higher than that of total pressure: v'/V > p'/P. The results highlighted a similar monotonic increasing trend for p'/P and Tu in the shear layer, suggesting that the total pressure fluctuation intensity p'/P might be strongly associated with the turbulence level Tu in this region. The relative pressure fluctuations reached large values next to the boundary between the shear layer and recirculation region ([2]). Above the relative pressure fluctuation decreased to small values, while the turbulence intensity data were scattered; neither data were reliable in the recirculation region.

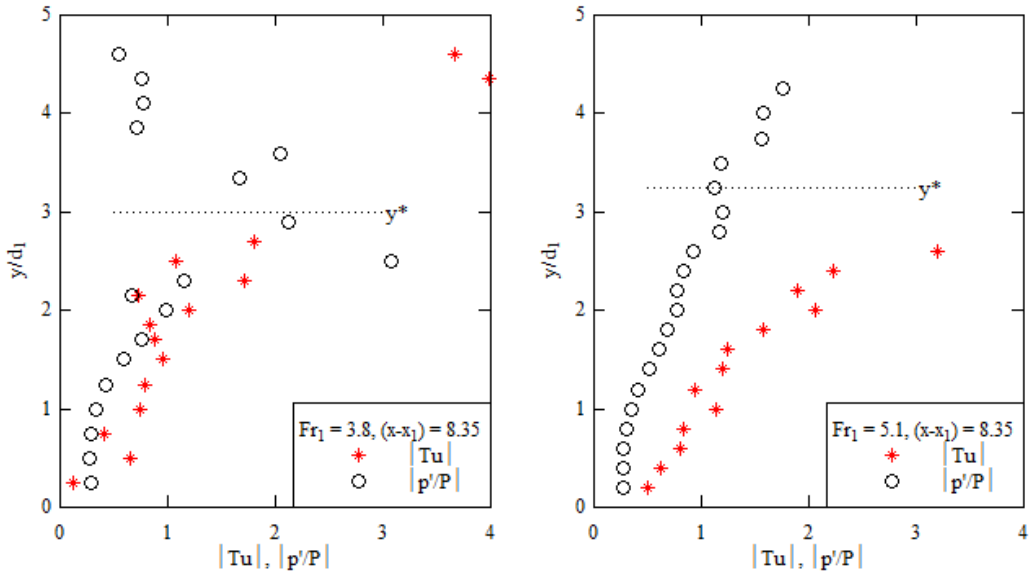

(A) $Fr_1 = 3.8$ (B) $Fr_1 = 5.1$

[2] At that location, the time-averaged velocity was positive (i.e mean downstream motion) but reversed flow motion (i.e. instantaneous negative velocity) were regularly detected.

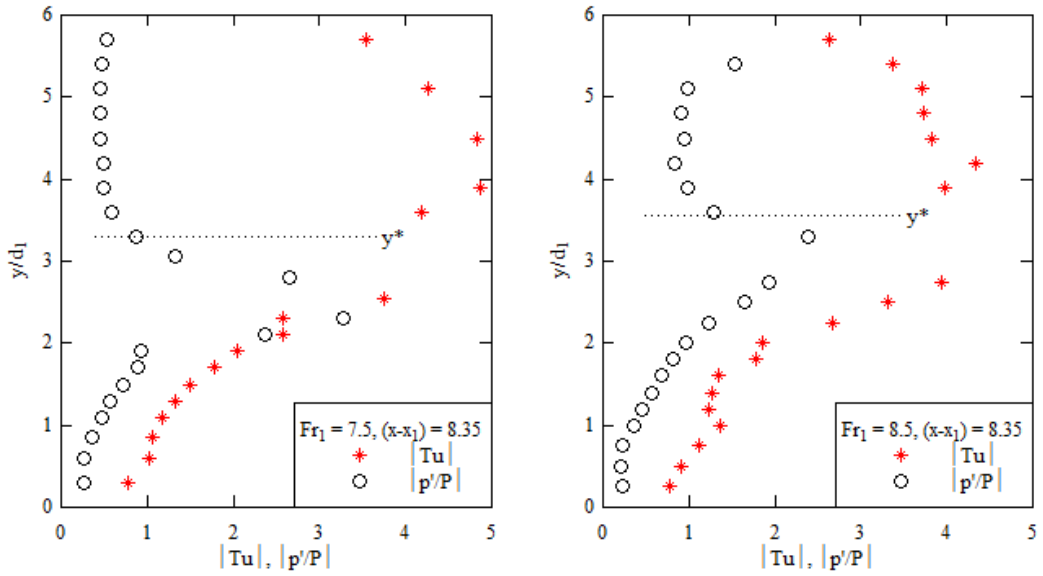

(C) $Fr_1 = 7.5$ (D) $Fr_1 = 8.5$

Fig 4-7 - Vertical distributions of relative total pressure fluctuations and turbulence intensities in hydraulic jumps

4.2.2. Characteristic frequencies of total pressure fluctuations

The instantaneous total pressure signals exhibited some pseudo-periodic patterns. For example, Figure 4-8 presents a typical total pressure signal in the turbulent shear layer, sampled at 5 kHz. The low-pass filtered signal with a cut-off frequency of 25 Hz is shown in black, while the low-pass filtered signal with a cut-off frequency of 5 Hz is shown in green. The signal presented some low-frequency pattern, highlighted by the low-pass filtered data. More the pseudo-periodic pressure pulsations could be easily felt by placing a hand in the roller. The pulse of impinging force seemed to correspond to the large vortical structure ejection. Herein the raw pressure signals were low-pass filtered with two band passes: 0-25 Hz and 0-5 Hz. The upper cut-off frequencies were selected to best outline the fluctuating patterns in a range of scales. In each case, the characteristic frequencies were obtained by counting manually the number of 'waves' over a certain duration. The manual data processing guaranteed maximum reliability of the results. For the relatively high-frequency filtered signals (0-25 Hz), the analysed signal length was 60 s, and it was 180 s for the relatively low-frequency filtered signals (0-5 Hz).

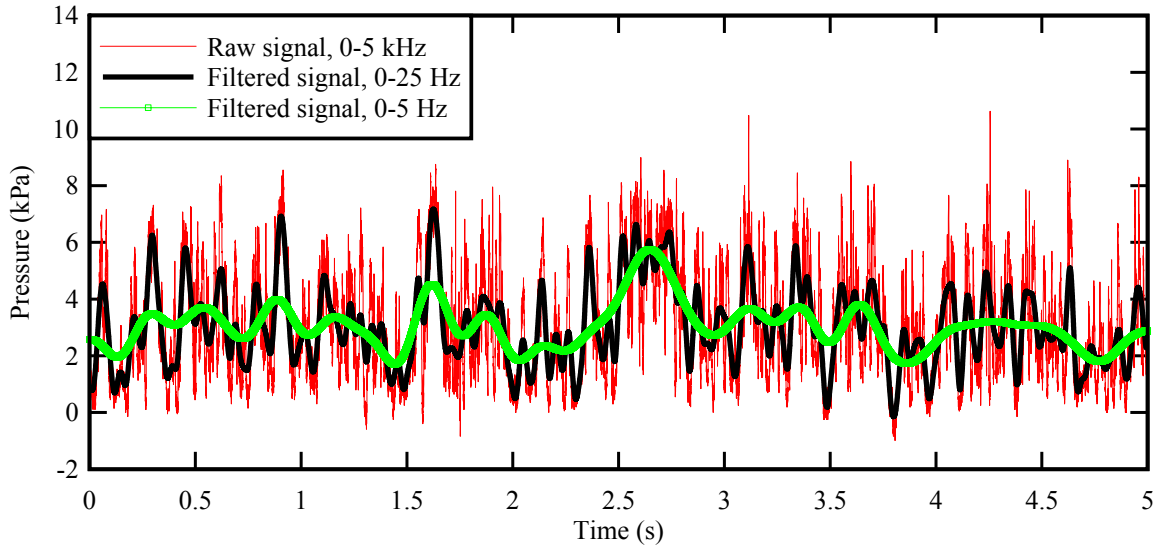

Fig. 4-8 - Total pressure record in the shear layer of a hydraulic jump - Flow conditions: Q = 0.0347 m^3/s, d_1 = 0.02 m, x_1 = 0.83 m, Fr_1 = 7.5, x-x_1 = 0.167 m, y = 0.03 m - Low-pass filtered signals included for comparison

Table 4-1 - Characteristic total pressure fluctuation frequencies based on the manual processing of two low-pass filtered signals: 0-5 Hz and 0-25 Hz - Data recorded in the shear layer at y = y_{Fmax}

Q (m^3/s)	d_1 (m)	x_1 (m)	Fr_1	Re	x-x_1 (m)	$F_p^{(H)}$ [0-25 Hz] (Hz)	$F_p^{(L)}$ [0-5 Hz] (Hz)
0.0179	0.02	0.83	3.8	3.5×10^4	0.083	11.07	2.59
					0.167	9.05	2.64
					0.250	8.35	2.61
0.0239	0.02	0.83	5.1	4.8×10^4	0.083	12.02	2.59
					0.167	10.32	2.65
					0.250	8.78	2.58
					0.375	7.78	2.51
0.0347	0.02	0.83	7.5	6.8×10^4	0.083	11.93	2.59
					0.167	11.18	2.64
					0.250	9.85	2.50
					0.375	8.75	2.67
0.0397	0.02	0.83	8.5	8.0×10^4	0.083	13.02	2.52
					0.167	11.83	2.63
					0.250	10.18	2.38
					0.375	9.30	2.50

Notes: Q: flow rate; d_1: inflow depth; x_1: longitudinal jump toe position; Fr_1: inflow Froude number; Re: Reynolds number; $F_p^{(H)}$: total pressure fluctuation frequency (0-25 Hz); $F_p^{(L)}$: total pressure fluctuation frequency (0-5 Hz).

The characteristic frequencies were investigated in the shear layer at the characteristic elevation of maximum bubble count rate (y_{Fmax}) for a range of flow conditions (Table 4-1). The results are summarised in Table 4-1. The high-frequency filtered signals exhibited a range of typical fluctuation frequencies $F_p^{(H)}$ between 8 and 12 Hz, whereas the low-frequency filtered signals gave a frequency $F_p^{(L)}$ about 2.6 Hz ([3]). The upper characteristic frequencies of the total pressure fluctuations $F_p^{(H)}$ are plotted in Figure 4-9 as functions of the dimensionless longitudinal positions $(x-x_1)/d_1$. The characteristic frequency $F_p^{(H)}$ decreased with the longitudinal direction from the jump toe. Some difference was observed between different flow conditions: flows with larger Froude number had higher pressure fluctuation frequency. In Figure 4-9, the longitudinal distributions of bubble count rate and bubble cluster count rate are plotted for comparison. Similar decreasing trends were seen along the roller, and higher bubble rate and bubble cluster rate were recorded for larger Froude (also Reynolds) number. The decreasing trends were found to fit an exponential decay:

$$\frac{F \times d_1}{V_1} = A \times \exp\left(-B \times \frac{x-x_1}{d_1}\right) \qquad A = f(Re),\ B = f(Fr_1) \quad (4.4)$$

In Equation (4.4), F denotes the bubble or bubble cluster count rate, and the dimensionless coefficients A and B are determined by flow conditions. The magnitude of bubble/bubble cluster rate was a function of the Reynolds number and the rate of longitudinal decline was linked to the Froude number (WANG and CHANSON 2013). The comparable data distributions in Figure 4-9 might suggest that the detected pressure fluctuations were also associated with the turbulent air-water flow features. The longitudinal decay might be related to the diffusion and dispersion of bubbly flow structures as well as the turbulence dissipation. In this case, this high-frequency total pressure fluctuation was mainly linked to the fast periodic variation of kinetic pressure. Furthermore, because the micro-scale turbulent behaviours of hydraulic jump were normally considered with much smaller time scales, this type of fluctuations could be the result of the relatively large-scale of, or accumulative effect of these turbulent behaviours. For example, it is possible that only the bubble clusters larger than a certain size were responsible to the kinetic pressure fluctuations. Herein the change of pressure might be caused directly by the bubbles encountered by the pressure probe, or maybe by the encountered turbulent structures in which the bubble clusters were carried as markers.

[3] Note that the power spectral density functions of total pressure signals did not exhibit convincing energy peaks; hence it was unclear which frequency was predominant.

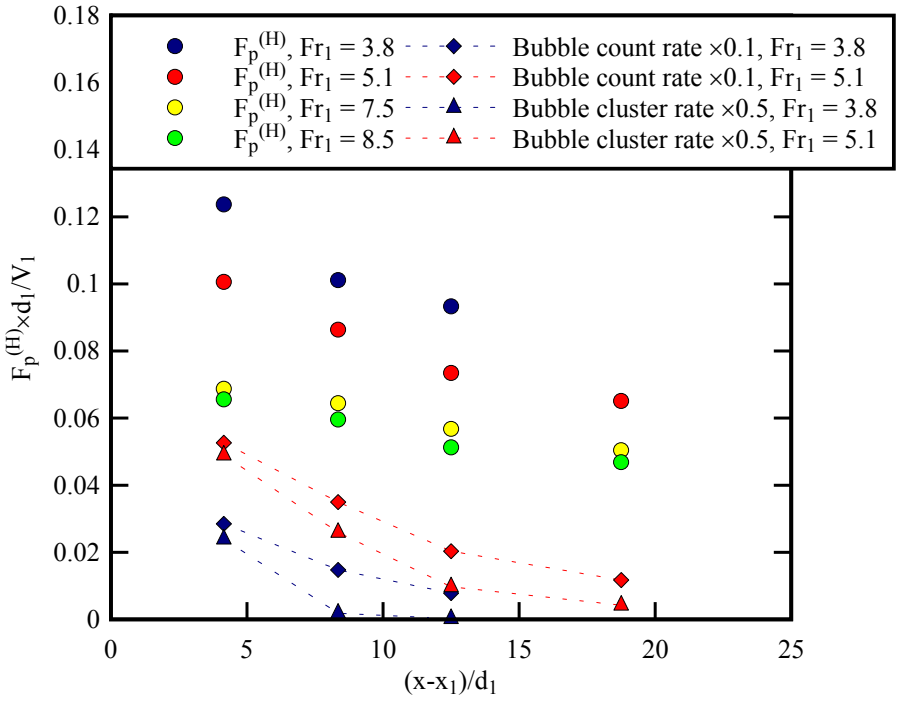

Fig 4-9 - Longitudinal variations of dimensionless upper characteristic frequencies of total pressure in the shear layer of hydraulic jumps - Data at y = y_{Fmax} - Comparison with maximum bubble count rate and bubble cluster count rate

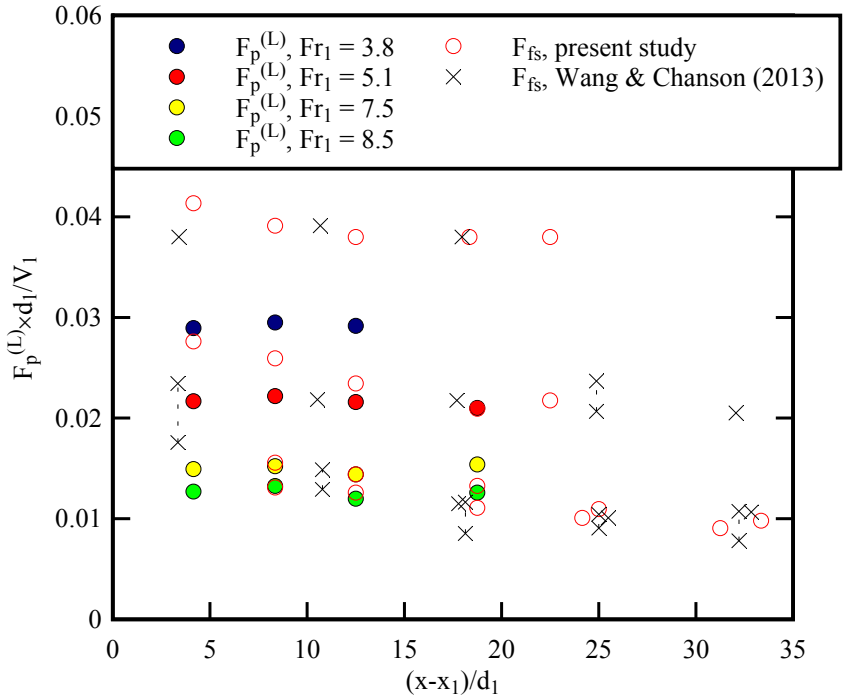

Fig 4-10 - Longitudinal variations of dimensionless low characteristic frequencies of total pressure fluctuations in the shear layer of hydraulic jumps - Data at y = y_{Fmax} - Comparison with the characteristic frequencies of free surface fluctuations (Present study, WANG and CHANSON 2013)

On the other hand, the lower characteristic frequencies $F_p^{(L)}$ data were about constant independently of longitudinal positions and flow conditions (Fr_1 = 3.8 to 8.5) (Fig. 4-10). On average the data yielded an average value $F_p^{(L)}$ = 2.57 Hz. This relatively low characteristic fluctuation was of the same order of magnitude as some low-frequency fluctuation of the jump, which had typical characteristic frequencies lower than 5 Hz. Such low-frequency fluctuations included the free surface fluctuations, longitudinal jump toe oscillations, formation and downstream advection of large size vortices in the shear layer. Figure 4-10 compares the lower characteristic frequencies $F_p^{(L)}$ of total pressure fluctuations with the characteristic frequencies of free surface fluctuations measured with acoustic displacement meters. In Figure 4-10, the symbols connected by dash line represent a range of observed frequencies. Although the free surface fluctuations encompassed a wider frequency range, the total pressure fluctuation frequency $F_p^{(L)}$ data were close, suggesting that the lower range of total pressure fluctuations were predominantly affected by the fluctuations in free surface elevation. Any change of water surface elevation influenced the piezometric pressure term, thus the total pressure.

FELDER and CHANSON (2013) selected a cut-off frequency of 10 Hz to distinguish between high- and low-frequency air-water motions in a hydraulic jump flow. The influence of the low-frequency motions was estimated on the air-water turbulent properties. Surprisingly such a cut-off frequency selection would seem inconsistent with a characteristic pressure fluctuation frequency about 8 to 12 Hz.

In summary the total pressure fluctuation data showed two characteristic frequencies in the shear layer. The upper frequency $F_p^{(H)}$ was thought to be linked to the micro-scale air-water flow properties, while the lower frequency $F_p^{(L)}$ tended to be associated with free surface fluctuations.

4.3. COMMENTS ABOUT TOTAL PRESSURE MEASUREMENTS: CALIBRATION AND DATA UNCERTAINTIES

The pressure probe was the MRV21 miniature pressure transducer. The inner sensor diameter was 4 mm with outer diameter of 5 mm. The calibration of the total pressure probe was performed regularly during the experiments. Static response was tested in still water from atmospheric to 103 kPa, and dynamic response was tested in a high-speed open channel flow up to 115 kPa. A linear correlation was obtained between the total head of experimental flow and the voltage output for each calibration. Some typical calibration data are presented in Figure 4-11, showing linear correlation functions obtained with identical experimental setup but on different days. The offset between calibration curves varied and the reason was not clear. It was thought to relate to the change in environmental temperature or the ambient pressure.

As an intrusive instrument, the pressure probe introduced some disturbance to the measured flow

field. The size of the probe (Ø = 5 mm) was several orders of magnitude larger than the size of small bubbles and of a similar order of magnitude to the integral turbulent length scale (CHANSON 2007, ZHANG et al. 2013). Therefore, the pressure fluctuations related to the smallest micro-scale turbulent behaviours of the air-water flow cannot be recorded.

It is worth to note that stagnation pressure was measured only when the probe is aligned with the flow direction. This was true within the shear layer ($0 < y < y_*$) considering the time-averaged velocity field. However, the instantaneous flow in jump roller was three-dimensional, and instantaneous reversed flow was frequently seen from the phase-detection probe signals in the upper shear layer, though the average flow direction was longitudinally downstream. In such a case, the kinetic pressure could be underestimated when an angle existed between the probe orientation and flow direction.

Lastly, the pressure variation range for the present experiments was roughly between 1 and 1.15 bar, whereas the measurement range of the total pressure probe was from 0 to 1.5 bar. The accuracy of measurements could be improved by the application of a total pressure probe with narrower measurement range.

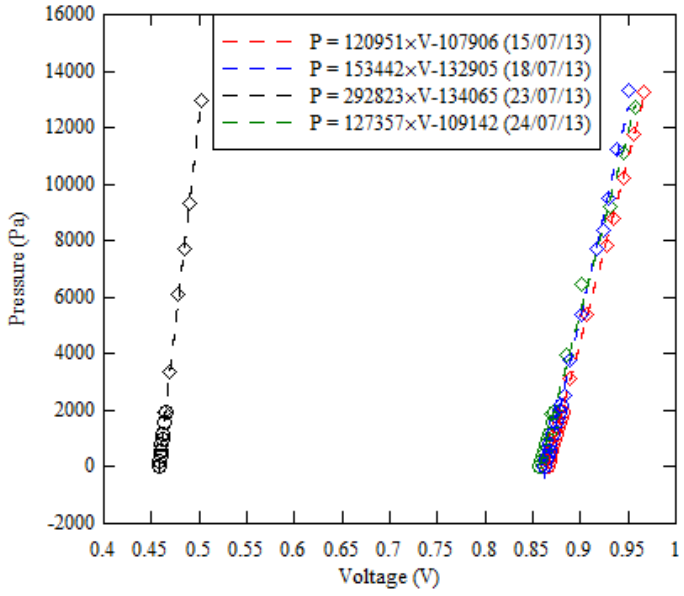

Fig. 4-11 - Calibration curves of the total pressure probe

5. COUPLING BETWEEN ROLLER SURFACE DEFORMATION, PRESSURE FLUCTUATION AND AIR ENTRAINMENT

5.1. PRESENTATION

A hydraulic jump is characterised by a number of non-stationary fluctuating processes with different length and time scales. For example, high-frequency motions include turbulent fluctuations in velocity field, formation and dispersion of bubbles and bubble clusters, while low-frequency motions include fluctuations in free surface, entrapment of large bulk of air and generation of high-aerated vortical flow structures. These fluctuating features further interact. While each single phenomenon is a complex physical process, the interactions between all phenomena can be very complicated. An insight into these interactions may provide may provide a better understanding of the flow physics.

At a measurement point (x-x_1, y), the local total pressure and void fraction were measured simultaneously as well as the free surface fluctuations in both horizontal and vertical directions. The vertical free surface fluctuation was measured at the longitudinal position x-x_1 right above the probe tips, while the horizontal motion, also called longitudinal jump toe oscillation, was recorded at a fixed location about 30 mm above the inflow free-surface (Fig. 5-1). The phase-detection probe and pressure probe were placed side by side with a transverse separation $\Delta z_{pp} = 9$ mm. Figure 5-1 shows a sketch of the instrumental setup, where ADM stands for acoustic displacement meter, PDP stands for phase-detection probe and TPP for total pressure probe. The instantaneous coupling between the corresponding parameters was investigated based upon a cross-correlation analysis. The correlation function is a statistical indicator of the coupling over the sampling duration. Herein the correlation coefficients are denoted R_{xy}, R_{xc}, R_{yc}, R_{xp}, R_{yp} and R_{pc}, where the subscripts x refers to the horizontal jump toe oscillations, y to the vertical free surface fluctuations, c to the instantaneous void fraction and p to the instantaneous total pressure. The order of subscripts corresponds to the order of the cross-correlation calculations. When an instantaneous coupling exists, the correlation function $R_{ij} = f(\tau)$ (i,j = x,y,c,p) exhibits a marked maximum (or minimum) at around $\tau = 0$, where τ is the time lag. Large absolute values indicate a strong correlation, while the sign highlights the trend of the simultaneous variation. In the present study, the 180 s signals were divided into six non-overlapping segments. The correlation functions were calculated for each segment and averaged.

The probe output signals were pre-processed prior to the correlation analyses. The instantaneous phase-detection probe signals were converted into instantaneous void fraction c, either 0 for water or 1 for air. The correlation calculations involving the free surface data were performed on low-pass filtered signals below 50 Hz because of the relatively slow response of the acoustic displacement

meters. For the total pressure and phase-detection probe signals, the correlation calculations were conducted on low-pass filtered signals below 2 kHz. The filtered signals were smoothed over every N points, where N equalled the ratio of 5 kHz to the cut-off frequency. Lastly, the signals were linearly interpolated with equal intervals of N/5000 s. The processed voltage signals were converted to corresponding surface position and pressure data according to the calibrations. The method of signal pre-processing was similar to that used by MURZYN and CHANSON (2009).

The results in terms of coupling between horizontal and vertical free-surface fluctuations R_{xy} were presented in Chapter 3 (Fig. 3-8). A summary of maximum/minimum correlation coefficients $(R_{xy})_{max}$ corresponded typically to a roller surface deformation sketched in Figure 3-9. The free surface motions were independent of the elevation of total pressure and phase-detection probes. For the pressure and void fraction signals, the results are presented below as functions of the vertical probe position y.

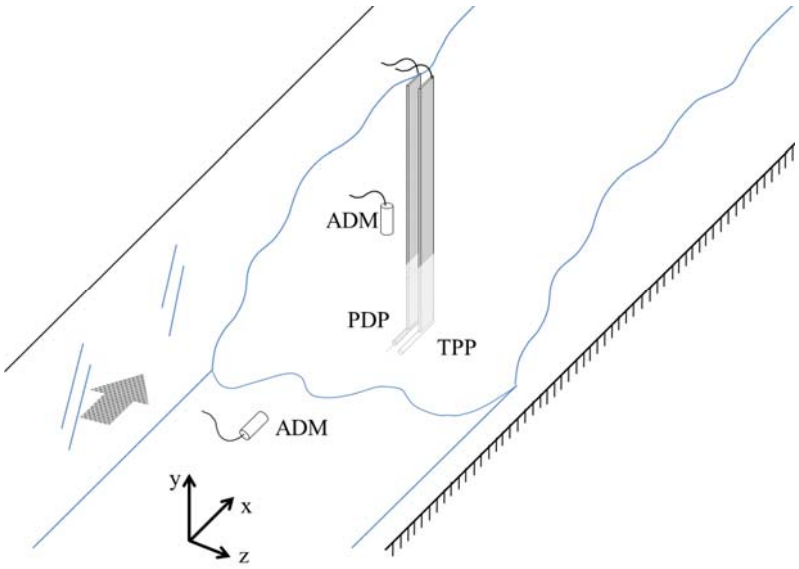

Fig 5-1 - Sketch of instrumentation setup for simultaneous measurements of roller surface deformation, total pressure fluctuation and instantaneous void fraction - ADM: acoustic displacement meter; PDP: phase-detection probe; TPP: total pressure probe

5.2. RESULTS: VERTICAL DISTRIBUTION OF MAXIMUM CORRELATION COEFFICIENTS

5.2.1. Coupling between horizontal/vertical free-surface fluctuations and instantaneous void fraction

The cross-correlation functions between the horizontal jump toe oscillation and instantaneous void fraction R_{xc}, and between the vertical free surface fluctuation and instantaneous void fraction R_{yc}, were calculated at four longitudinal positions $(x-x_1)/d_1$ = 4.15, 8.35, 12.5 and 18.75 for Froude numbers Fr_1 = 3.8, 5.1, 7.5 and 8.5. Their shapes varied gradually with increasing distance from the

invert, suggesting different characteristic shapes between the shear layer and recirculation region. Figure 5-2 presents some typical correlation functions for both flow regions.

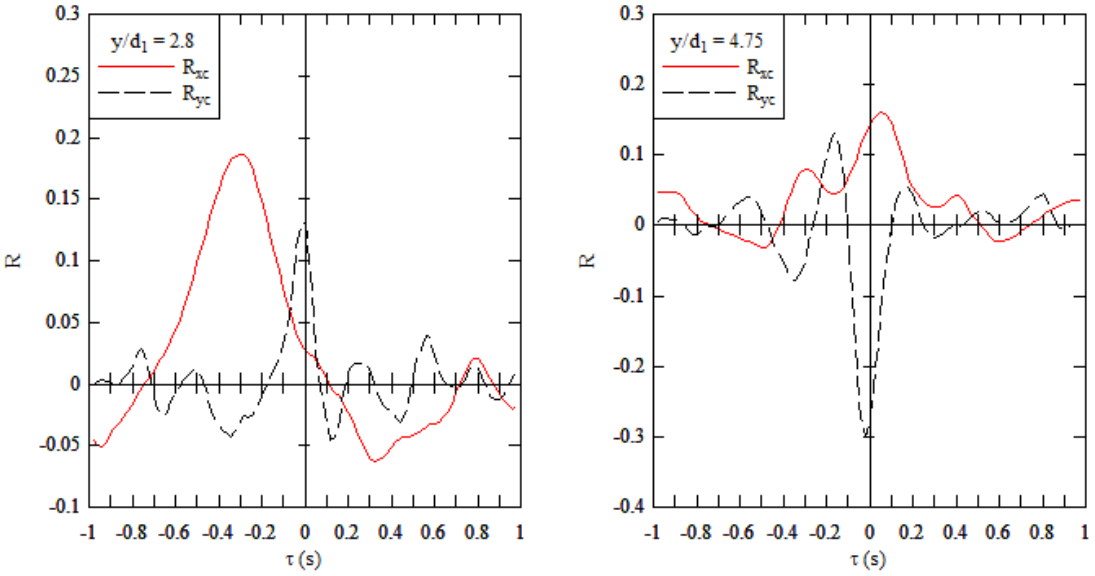

(A) $y/d_1 = 2.8$, Turbulent shear layer (B) $y/d_1 = 4.75$, Recirculation region

Fig 5-2 - Correlation functions between roller surface deformation and instantaneous void fraction (R_{xc} & R_{yc}) in the turbulent shear layer (A, left) and recirculation region (B, right) - Flow conditions: Q = 0.0239 m^3/s, d_1 = 0.02 m, x_1 = 0.83 m, Fr_1 = 5.1, $x-x_1$ = 0.167 m

In the shear region, both correlation functions exhibited a positive maximum as illustrated in Figure 5-2A. Based upon the definition of +x and +y axes, $(R_{xc})_{max} > 0$ meant that the jump toe moved downstream when the instantaneous void fraction increased ([4]). Similarly $(R_{yc})_{max} > 0$ implied that the water level rose when the instantaneous void fraction increased. An example is shown in Figure 5-2A: as the amount of entrapped air increased in the shear layer, the jump toe moved downstream and the free surface elevation above the phase-detection probe sensor shifted upwards. Such a behaviour could correspond to the formation and detachment of large highly-aerated vortices from the jump toe and associated flow bulking. In Figure 5-2A, it is noteworthy that $(R_{xc})_{max}$ was not shown at $\tau = 0$, implying that the correlated behaviours were not exactly simultaneous. This was shown at most elevations in the shear layer for all flow conditions.

In the recirculation region, a positive maximum correlation was seen in terms of R_{xc}, but the correlation function R_{yc} exhibited a negative peak. This is shown in Figure 5-2B. Both peak values

[4] Please note that the void fraction signal was filtered at 50 Hz. An increase of instantaneous void fraction thus hardly reflected the arrival of individual bubbles but more likely of some large amount of entrapped air, e.g. some bubble clusters, air packets.

were observed at about $\tau = 0$. In this recirculation region, the void fraction was high since it was measured close to the free surface. The maximum correlation coefficients indicated that the jump toe moved downstream and the free surface level dropped when the void fraction increased locally. This derived from the roller surface deformation instantaneously placing the phase-detection probe sensor closer to the free surface in a region of higher void fraction. The simultaneous surface motions in the horizontal and vertical directions were consistent with the results in terms of the cross-correlation R_{xy} observed in the first half roller (Fig. 3-9, $(x-x_1)/L_r < 0.5$).

Typical vertical distributions of maximum correlation coefficients $(R_{xc})_{max}$ and $(R_{yc})_{max}$ are plotted in Figures 5-3. The data were recorded in the first half roller. Figure 5-3A and 5-3B present the data at $(x-x_1)/d_1 = 4.15$ and 8.35 for $Fr_1 = 5.1$, and Figures 5-3C and 5-3D present those for $Fr_1 = 7.5$ and 8.5 at $(x-x_1)/d_1 = 8.35$. The full data sets for all flow conditions are available in Appendix D (section D.1). The time-averaged void fraction C is also shown in Figure 5-3 for comparison. In Figures 5-3A and 5-3B, the data of WANG and CHANSON (2013) are included for the same flow conditions: the comparison showed a consistency, proving that the measurements and analysis were repeatable.

In the first half roller close to the toe, the results in terms of $(R_{xc})_{max}$ and $(R_{yc})_{max}$ showed different shapes with three flow regions from bottom to free surface. First, in the lower turbulent shear layer where the time-averaged void fraction was small, the correlation $(R_{yc})_{max}$ between the vertical free surface fluctuation and instantaneous void fraction was unimportant, while the maximum correlation coefficient between the horizontal jump toe oscillation and void fraction was negative $(R_{xc})_{max} < 0$. Second, in the shear layer about the elevation of maximum time-averaged void fraction, both correlation functions showed positive maxima ($(R_{xc})_{max} > 0$ and $(R_{yc})_{max} > 0$ (Fig. 5-2A). Third, in the recirculation region, $(R_{xc})_{max}$ was positive and $(R_{yc})_{max}$ became negative: i.e., $(R_{xc})_{max} > 0$ and $(R_{yc})_{max} < 0$, as illustrated with Figure 5-2B. Similar results were obtained for different Froude numbers. Further the vertical distributions of $(R_{yc})_{max}$ were comparable to the findings of CHACHEREAU and CHANSON (2011b).

Overall the correlation analyses illustrated the complex interactions between the two-dimensional roller surface deformation and air entrainment process through a cross section in the first half of the jump roller. Namely, as the jump toe shifted towards the downstream direction, a large amount of air was entrapped at the toe, corresponding to an increasing void fraction in the shear layer region where the entrapped air was advected by high-aerated vortices, and the flow bulking led to a rise of water elevation. However the downstream movement of jump toe reduced the air content in the lower shear layer region because the relative distance to the toe decreased (as the phase-detection probe was fixed) and the probe sensor location was then beneath the convective shear layer. In the recirculation region, the downstream toe motion led to a decrease in the local free-surface elevation,

thus increasing locally the void fraction measured by the fixed phase-detection probe sensor. Note that the increase in water level caused by flow bulking was not inconsistent with the simultaneous decrease of water level when the jump toe moved downstream. Because both trends were shown as statistical results and they did not necessarily occur at the same moment. The roller surface deformation pattern revealed by the direct correlation between the horizontal and vertical displacement meter signals suggested that the free-surface descent with downstream toe motion was observed more frequently (see Fig. 3.9).

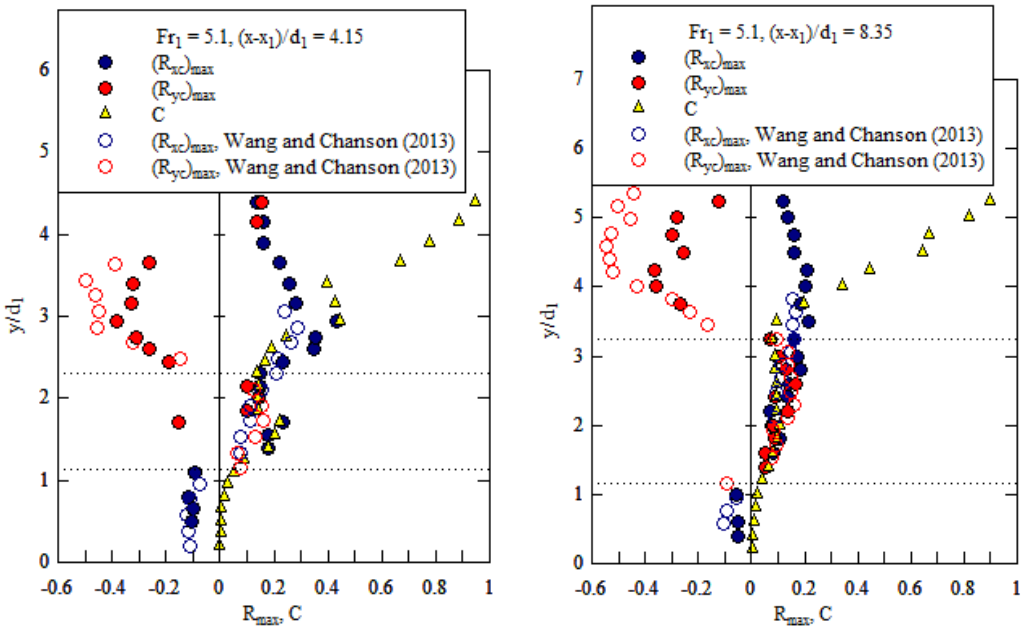

(A) $Fr_1 = 5.1$, $(x-x_1)/d_1 = 4.15$ (B) $Fr_1 = 5.1$, $(x-x_1)/d_1 = 8.35$

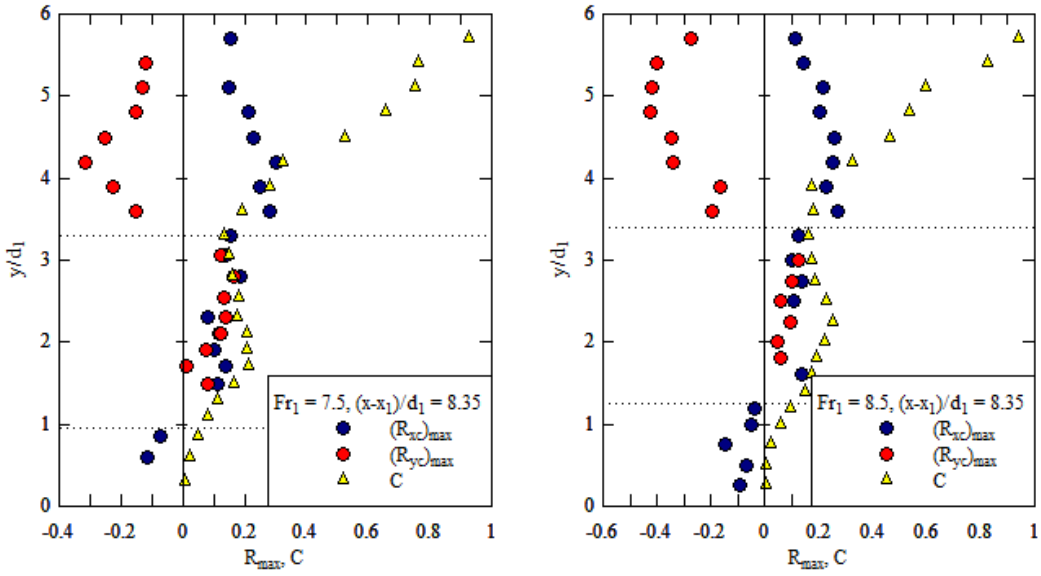

(C) $Fr_1 = 7.5$, $(x-x_1)/d_1 = 8.35$ (D) $Fr_1 = 8.5$, $(x-x_1)/d_1 = 8.35$

Fig 5-3 - Vertical distributions of maximum correlation coefficients between roller surface deformation and instantaneous void fraction - Comparison with vertical distribution of void fraction

Further downstream, the correlation between horizontal surface motion and instantaneous void fraction became weak, while the correlation function between the vertical motion and void fraction remained consistent with the earlier observations: i.e., $(R_{yc})_{max} > 0$ for $y < y_*$ and $(R_{yc})_{max} > 0$ for $y > y_*$. The pattern was consistently observed in the air-water region of the roller, thus reflecting the flow bulking in the shear layer with the advection of large highly aerated vortical structures and the associated change in free-surface elevations in the recirculation region.

5.2.2. Coupling between horizontal/vertical surface fluctuations and instantaneous total pressure

The simultaneous relationships between the roller surface motions and instantaneous total pressure were investigated in the shear layer region ($0 < y < y_*$). Figure 5-4 shows some typical correlation functions for $Fr_1 = 5.1$. Figure 5-4A presents some data in the first half roller close to the jump toe at $(x-x_1)/d_1 = 4.15$, and Figure 5-4B shows data further downstream in the second half roller at $(x-x_1)/d_1 = 18.75$. Herein R_{xp} is the correlation coefficient between the horizontal motion (jump toe oscillations) and total pressure, and R_{yp} is the correlation coefficient between the vertical motion (free surface fluctuations) and total pressure. Similar patterns were observed for all Froude numbers.

The correlation functions exhibited some peak values about $\tau = 0$, as illustrated in Figure 5-4. In the first half of the roller, R_{xp} presented a negative minimum indicating an increasing total pressure in the shear layer with an upstream jump toe motion (Fig. 5-4A). R_{yp} showed a positive maximum corresponding to an increasing total pressure with increasing water surface elevation. In the second half of the roller, R_{yp} presented a positive maximum, but R_{xp} gave a positive maximum, corresponding to a downstream jump toe shift accompanied by an increasing total pressure.

Some typical distributions of maximum correlation coefficients $(R_{xp})_{max}$ and $(R_{yp})_{max}$ through the shear layer are summarised at different longitudinal positions in Figure 5-5. Figures 5-5A and 5-5B present the vertical profiles for $Fr_1 = 5.1$ at $(x-x_1)/d_1 = 4.15$ and 18.75 respectively; Figures 5-5C and 5-5D show the profiles at these two positions for $Fr_1 = 8.5$. The time-averaged void fraction is also plotted for comparison. The results for other flow conditions are enclosed in Appendix D (section D.2).

In the first half roller, the vertical distributions of maximum correlation coefficients showed some characteristic patterns through the shear layer, as shown in Figures 5-5A and 5-5C. In the shear layer region where the time-averaged void fraction was close to the local maximum, the correlation between the horizontal surface motion and total pressure was negative, while the correlation between the vertical surface motion and pressure was positive: i.e., $(R_{xp})_{max} < 0$ and $(R_{yp})_{max} > 0$

(Fig. 5-4A). The correlation data implied that the local total pressure decreased when the jump toe moved downstream and the free surface elevation decreased. The interactions between free surface motions in horizontal and vertical directions were consistent with the roller surface deformation pattern seen in Figure 3-9 for $(x-x_1)/L_r < 0.5$. The change in total pressure was likely linked with the change of water depth and associated piezometric pressure fluctuations. Although the total pressure was the sum of piezometric and kinetic pressures, the effect of kinetic pressure fluctuations was not clearly seen. On the other hand, in the lower part of shear layer close to the invert where the time-averaged void fraction was small, $(R_{xp})_{max}$ and $(R_{yp})_{max}$ exhibited opposite signs: i.e., $(R_{xp})_{max} > 0$ and $(R_{yp})_{max} < 0$. The pattern indicated that the local total pressure increased as the jump toe moved downstream and water level dropped. When the jump toe shifted downstream, the distance from the measurement point to the toe decreased and the local velocity increased, thus leading to larger kinetic pressure and total pressure. In summary, close to the jump toe, the results suggested that when the toe moved downstream and water level decreased, the total pressure decreased in the main shear layer and increased in the lower shear layer below. The total pressure fluctuations were predominantly affected by the piezometric pressure in the shear layer and kinetic pressure close to the invert. The same results were obtained for different Froude numbers.

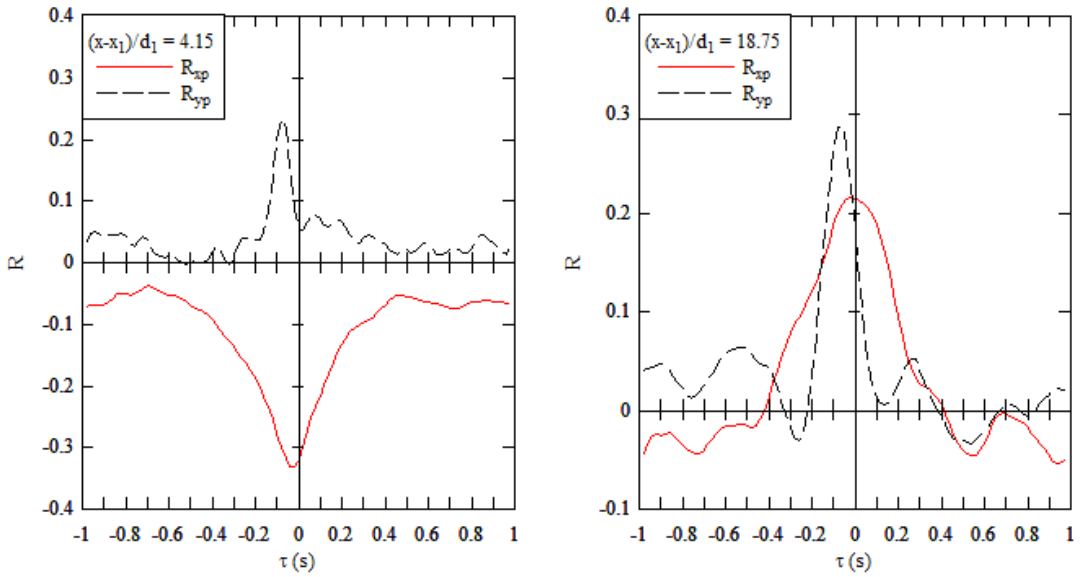

(A) $(x-x_1)/d_1 = 4.15$, $y/d_1 = 1.7$ (B) $(x-x_1)/d_1 = 18.75$, $y/d_1 = 3$

Fig 5-4 - Correlation functions between roller surface deformation and instantaneous total pressure (R_{xp} & R_{yp}) in the first half roller (A, left) and second half roller (B, right) - Flow conditions: Q = 0.0239 m^3/s, $d_1 = 0.02$ m, $x_1 = 0.83$ m, $Fr_1 = 5.1$, $x-x_1 = 0.167$ m

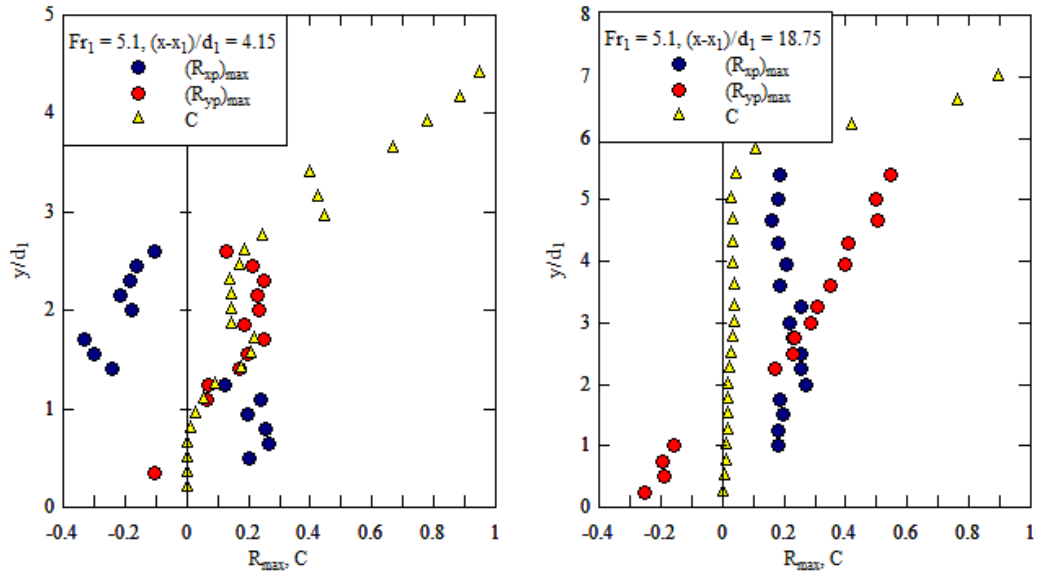

(A) $Fr_1 = 5.1$, $(x-x_1)/d_1 = 4.15$ (B) $Fr_1 = 5.1$, $(x-x_1)/d_1 = 18.75$

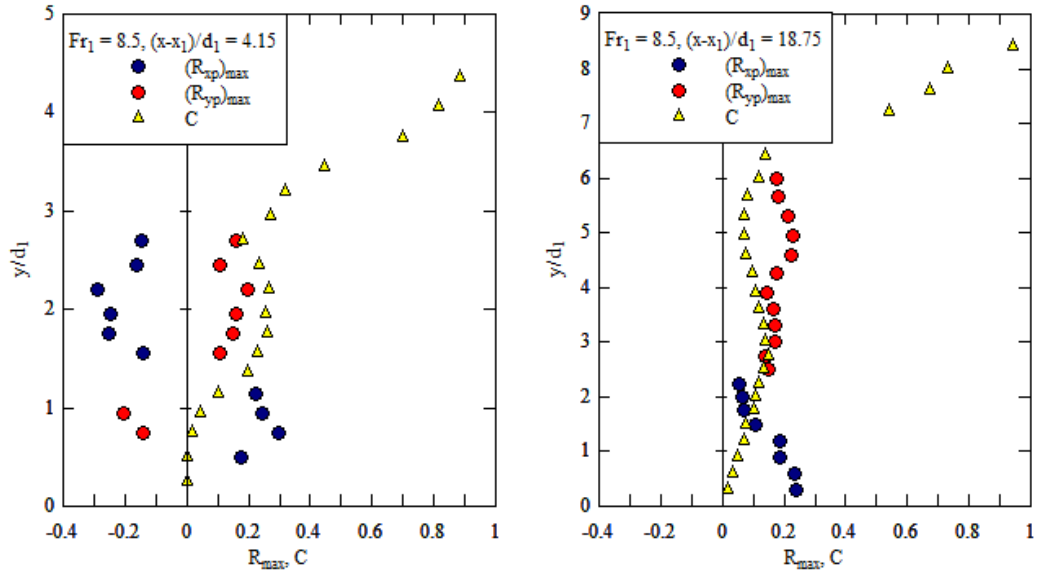

(C) $Fr_1 = 8.5$, $(x-x_1)/d_1 = 4.15$ (D) $Fr_1 = 8.5$, $(x-x_1)/d_1 = 18.75$

Fig 5-5 - Vertical distributions of maximum correlation coefficients between roller surface deformation and instantaneous total pressure - Comparison with vertical distribution of void fraction

In the second half roller, $(R_{yp})_{max}$ presented a similar distribution as in the first half roller, whereas $(R_{xp})_{max}$ was consistently positive through the shear layer (Fig. 5-5B). The data implied an increasing total pressure when the jump toe moved downstream and the water depth increased in the main shear layer region. In the lower shear layer below, the total pressure increased when the toe shifted downstream and the water depth decreased. The results indicated that, in the lower shear layer, the total pressure fluctuations were mainly affected by the turbulent velocity fluctuations. In

the main shear layer above, the results showed the same relative horizontal and vertical surface motions as the surface deformation described in Figure 3-9 for $(x-x_1)/L_r > 0.5$. Though the deformation pattern varied from that in the first half roller, the change in total pressures followed changes of water depth, hence of piezometric pressure. Typical results are shown in Figures 5-5B and Figure 5-5D. In Figure 5-5D, the data supported the basic finding that the total pressure was mainly linked with piezometric (water depth) and kinetic (velocity) pressures in the upper and lower shear layers respectively.

Overall the interactions between the roller surface motions and total pressure fluctuations differed between the two subregions of the shear layer. The relationships were linked to the dominant term affecting the total pressure fluctuations: the piezometric pressure in the main shear layer, and the kinetic pressure in the lower shear layer region below next to the invert. The trends were observed all along the roller.

5.2.3. Coupling between instantaneous total pressure and void fraction

The pressure probe and phase-detection probe were mounted side by side with a transversal separation $\Delta z_{pp} = 9$ mm. Thus the pressure and void fraction were not strictly measured at one point, and the probes might have minor disturbance on the nearby flow fields. Nonetheless the interactions between instantaneous total pressure and void fraction were studied based upon filtered signals with an upper cut-off frequency of 2 kHz. Such a cut-off level was deemed high enough to cover most known turbulent features of the air-water flow. The data were analysed in the shear layer where the pressure measurements were proved valid.

A typical cross-correlation function R_{pc} is presented in Figure 5-6. The data were obtained at $y/d_1 = 1.2$ in the shear layer. The results showed a sharp negative peak at $\tau = 0$ highlighting a marked correlation between the signals. The negative correlation coefficient meant that the instantaneous void fraction increased with a decreasing total pressure. That is, a drop in local total pressure might correspond to the arrival of one or more air bubbles.

Some typical vertical distributions of maximum correlation coefficients $(R_{pc})_{max}$ in the shear layer are plotted in Figure 5-7 for $3.8 < Fr_1 < 8.5$. All cross sections were located at the longitudinal position $(x-x_1)/d_1 = 8.35$. (See Appendix D, section D.3 for the other data.) All the data showed a negative correlation minimum $(R_{pc})_{max} < 0$. The vertical profile indicated a local maximum amplitude, between the main and lower shear layer regions (Fig. 5-7). In Figure 5-7, the correlation data are compared with the distributions of time-averaged void fraction and dimensionless pressure fluctuations p'/P_{max}, where p' is the standard deviation of total pressure and P_{max} is the maximum total pressure at the cross section. The location of $(R_{pc})_{max}$ and p'/P_{max} were very close, suggesting

strong relevance between total pressure and void fraction in the shear layer. Similar results were shown a all longitudinal positions for all inflow Froude numbers.

The negative correlations between instantaneous void fraction and total pressure corresponded to an increasing total pressure with decreasing void fraction. The relationship could be either at the micro- or macro-scale considering the high-frequency signals. That is, the increase in void fraction might correspond to the detection of a single air bubble, a bubble cluster or a large size high-aerated structure. Similarly the decrease of total pressure might correspond to either a high-frequency turbulent kinetic pressure drop (micro-scale) or low-frequency piezometric pressure fluctuation (macro-scale).

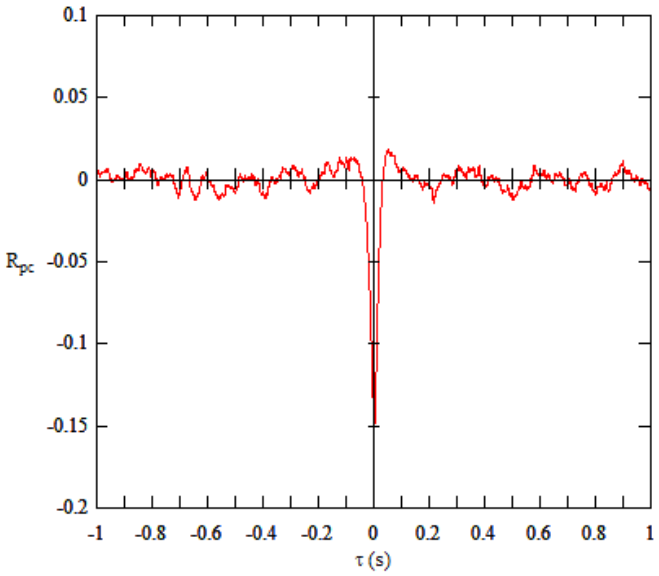

Fig 5-6 - Correlation function R_{pc} between instantaneous total pressure and void fraction in turbulent shear layer – Flow conditions: Q = 0.0239 m^3/s, d_1 = 0.02 m, x_1 = 0.83 m, Fr_1 = 5.1, $x-x_1$ = 0.167 m, y = 0.024 m

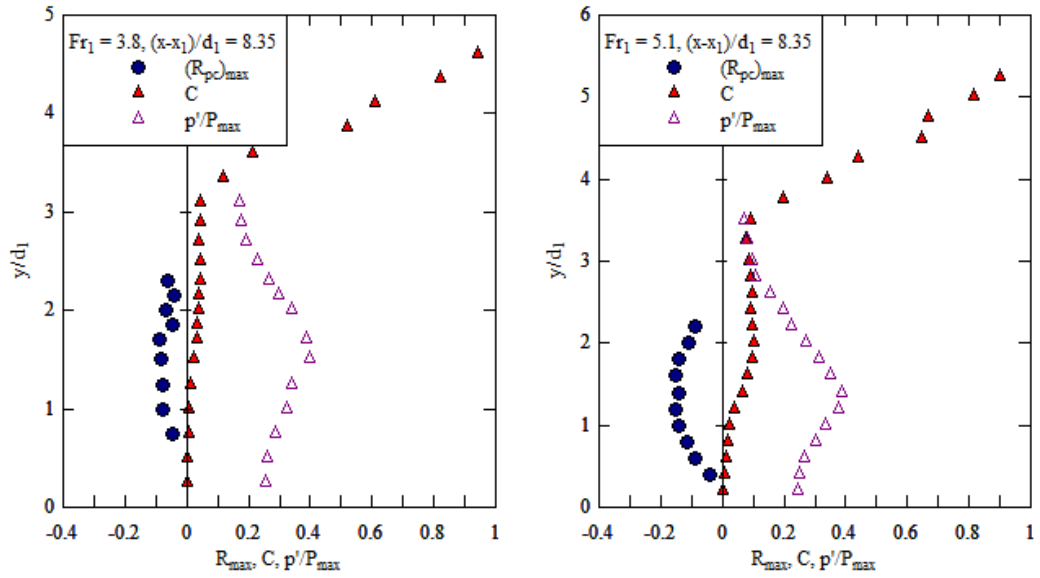

(A) $Fr_1 = 3.8$, $(x-x_1)/d_1 = 8.35$ (B) $Fr_1 = 5.1$, $(x-x_1)/d_1 = 8.35$

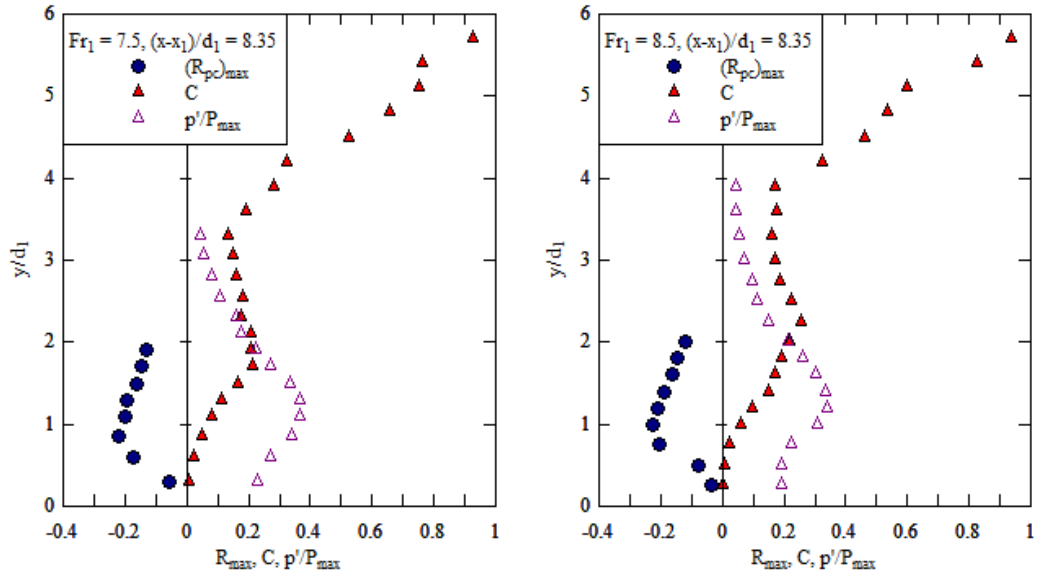

(C) $Fr_1 = 7.5$, $(x-x_1)/d_1 = 8.35$ (D) $Fr_1 = 8.5$, $(x-x_1)/d_1 = 8.35$

Fig 5-7 - Vertical distributions of maximum correlation coefficients between instantaneous total pressure and void fraction - Comparison with vertical distributions of time-averaged void fraction and dimensionless pressure fluctuations p'/P_{max}

5.3. DISCUSSION: SUBREGIONS OF THE TURBULENT SHEAR LAYER

The jump roller is normally divided into two main flow regions, i.e. the turbulent shear layer on the bottom and the recirculation region on the top, according to the distributions of time-averaged air-water flow properties (MURZYN and CHANSON 2009, CHACHEREAU and CHANSON 2011b). In the shear layer, the flow properties are largely controlled by the turbulence field, while the gravity force plays a major role in the recirculation region. Therefore, many flow properties and

regimes differed between the two regions.

The turbulent shear layer is characterised by a convective transport of air bubbles entrapped at the impingement point and advected downstream in large vortical structures (HOYT and SELLIN 1989, CHANSON 2010). The bubbly flow is further affected by de-aeration caused by buoyancy effects. These processes are illustrated by the vertical distributions of the time-averaged void fraction (Fig. 5-8). Figure 5-8 shows a typical series of void fraction profiles along a hydraulic jump roller. The boundary between the recirculation region and shear layer is highlighted with a dotted and dashed red line. In the shear layer, the void fraction profiles showed a broadening of the void fraction bell-shape with increasing distance as the maximum local void fraction C_{max} decreased with increasing distance from the jump toe. This region of relatively high void fraction outlined the preferential path of large high-aerated vortical flow structures. This region is termed the main shear layer region herein and sketched in Figure 5-8. The lower shear layer region ($y < y_{**}$) is sketched in Figure 5-8 beneath the dashed red line. It is a thin layer where the boundary friction is important and the void fraction is small.

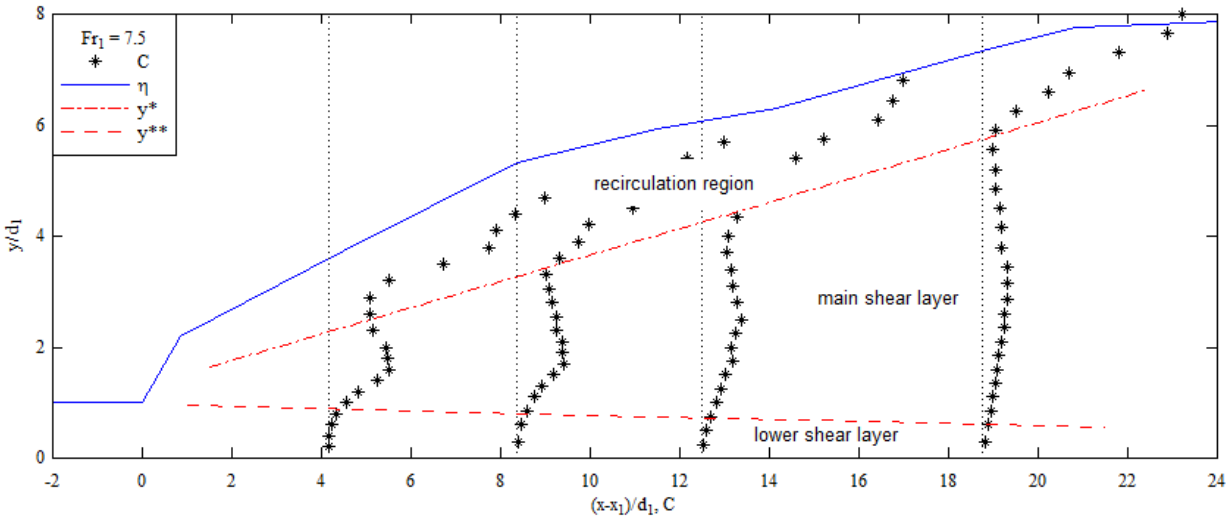

Fig 5-8 - Longitudinal development of void fraction profiles and sketch of the subregions in the turbulent shear layer – Flow conditions: $Q = 0.0347$ m^3/s, $d_1 = 0.02$ m, $x_1 = 0.83$ m, $Fr_1 = 7.5$

The distinction between the two subregions, main shear layer and lower shear layer, was clearly seen in terms of coupling between instantaneous total pressure, void fraction and roller surface location. The correlation analyses revealed some simultaneous variations. The major differences between the main shear layer and lower shear layer regions were two-fold. First the main shear layer was a highly-aerated region, while the air content in the lower shear layer was very small. In the main shear layer, air entrapped at the impingement point was convected in large vortical structures which evolved and enlarged with time through vortex pairing in a manner similar to the

observations of BROWN and ROSHKO (1971,1974). The thickness of the main shear layer increased rapidly along the roller (Fig. 5-8). The vortex path rose with increasing distance because of a combination of buoyancy and interactions between vortical structures and the invert. In the shear layer, the air bubbles diffused across the shear region while convected. The total air content and the maximum void fraction decreased with increasing distance downstream the toe, the decreasing rates being functions of the inflow Froude number. In the lower shear layer, the effects of the invert included boundary friction (no-slip condition) and a symmetry line by analogy with two-dimensional plunging jets (CUMMINGS and CHANSON 1997). Only a small number of air bubbles diffused in the vicinity of the solid boundary. The thickness of the lower shear layer decreased with increasing distance from the jump toe as illustrated in Figure 5-8.

Second the main shear layer was the locus of large velocity shear and velocity fluctuations (i.e. high turbulence intensity), while the lower shear layer tended to experience lower turbulence levels. On one hand, the time-averaged velocity reached a maximum close to the bottom then decreased with increasing elevation till negative in the recirculation region above the shear layer. On the other hand, the turbulence intensity presented a monotonic increasing trend with increasing elevation through the shear layer. The higher turbulent level in the main shear layer was linked to a number of phenomena, including the pseudo-periodic vortical structures, the longitudinal jump toe oscillations and turbulence modulation by entrained air. The lower shear layer was less affected by the large-scale turbulent structures and the velocity field was comparatively more organised than in the main shear layer.

The boundary between the main and lower shear layer was not strictly defined, for example, as a function of local void fraction. Nevertheless, the vertical distributions of maximum correlation coefficients (full dataset in Appendix D) provided the means to estimate of the boundary positions ([5]). Figure 5-9 presents the estimation results as the relative positions in the shear layer, where y_{**} denotes the boundary between the two subregions of shear layer and y_* is the characteristic elevation of the boundary between shear layer and recirculation region. In Figure 5-9, the mean free surface profile η is also shown where η is the time-averaged water elevations measured with the acoustic displacement meters. All data sets presented some self-similar trend best fitted by:

$$\frac{y^{**}-d_1}{d_2-d_1} = 0.0217 \times \frac{x-x_1}{L_r} \quad (5.1)$$

$$\frac{y^{*}-d_1}{d_2-d_1} = 0.623 \times \frac{x-x_1}{L_r} + 0.11 \quad (5.2)$$

[5] It is emphasised that the boundary position y_{**} should not be defined by the correlation analysis results only, and this preliminary estimate could be rough and lack of accuracy.

$$\frac{\eta-d_1}{d_2-d_1} = \left(\frac{x-x_1}{L_r}\right)^{0.56} \quad (5.3)$$

where L_r is the roller length and d_2 is the conjugate flow depth. Equations (5.1) to (5.3) were obtained for $3.8 < Fr_1 < 8.5$ and they are compared with the data in Figure 5-9.

In Figure 5-9, the data illustrated the respective locations of recirculation region, main shear layer and lower shear layer from top to bottom in the roller. Overall the thicknesses of the main and lower shear layers may be estimated as:

$$y^{**} \approx d_1 \quad (5.4a)$$

$$y^{*}-y^{**} \approx (d_2-d_1)\times\left(0.6\times\frac{x-x_1}{L_r}+0.1\right) \quad (5.4b)$$

The data indicated an approximately constant thickness of the lower shear layer. At this elevation $y = y_{**}$, the ratio of local void fraction to maximum void fraction C/C_{max} was between 0.2 and 0.67 depending upon the longitudinal position. The results implied an increasing thickness of the main shear layer with increasing distance from the jump toe (Fig. 5-9). Interestingly the present results compared well qualitatively with classical shear layer observations (BROWN and ROSHKO 1974) and a simplistic mixing layer model for hydraulic jump (HOYT and SELLIN 1989), although the latter investigation was limited to photographic observations in a small size facility

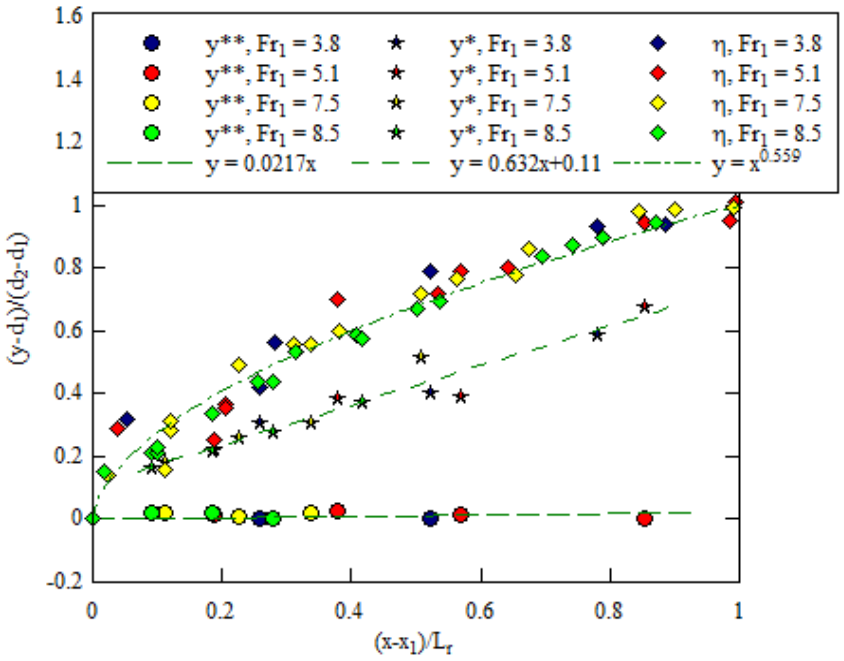

Fig 5-9 - Self-similar flow structures in jump roller: characteristic thickness of main and lower shear layer sub-regions

6. CONCLUSION

Turbulent two-phase flow properties were experimentally investigated in hydraulic jumps with a marked roller. The laboratory study was conducted in a relatively large-size facility with inflow Froude number Fr_1 = 3.8, 5.1, 7.5 and 8.5 and Reynolds numbers from 3.5×10^4 to 8.0×10^4. The instantaneous free surface positions were measured non-intrusively with acoustic displacement meters, while intrusive total pressure and phase-detection probes were used to record the total pressure and air-water flow properties inside the hydraulic jump roller.

The time-averaged free surface and air-water flow properties showed good agreement with previous findings. The free-surface fluctuation characteristics varied with the Froude number. Hydraulic jumps with smaller Froude numbers had smaller fluctuations but higher characteristic frequencies. For a given hydraulic jump, both fluctuation amplitude and frequency were higher in the first half roller close to the toe, than in the second half of roller. The characteristic frequencies of longitudinal jump toe oscillations were also recorded non-intrusively. The results showed that the jump toe oscillations were associated with an instantaneous deformation of the roller free-surface rather than a straight translation. The vertical distributions of time-averaged void fraction and bubble count rate showed two main air-water flow regions: namely the turbulent shear layer for $y < y_*$ and a recirculation region above. The velocity and turbulence intensity results were investigated in the shear layer, showing a similarity with a monophase wall jet flow.

The total pressure distributions were measured with a fixed orientation of pressure probe. The measurement technique was validated in the shear layer through a comparison with theoretical calculations based upon the measured two-phase flow data. The comparative results showed that the pressure distribution was quasi-hydrostatic in the roller: i.e., $\partial P_{stat}/\partial y = -\rho_w\times(1-C)\times g$ taking into account the flow aeration. The piezometric and kinetic pressure terms were comparable for small Froude number jumps, while the kinetic pressure component of the total pressure was the dominant term for stronger jumps. In the turbulent shear layer, the vertical profiles of mean pressure and pressure fluctuations exhibited some marked maxima. The maximum mean pressure was observed close to the invert, beneath the maximum pressure fluctuation location. The magnitudes of mean and fluctuation maxima increased with increasing Froude numbers and decreased with increasing distance to the toe for a given Froude number. The total pressure fluctuations presented two dominant frequencies: (1) an upper frequency between 8 and 12 Hz depending on the Froude number and longitudinal position which was thought to reflect the turbulence-related fluctuations, and (2) a lower frequency about 2.6 Hz linked with changes in water depth and formation of vortical structures.

Some cross-correlation analyses were performed between any two instantaneous signals of the

horizontal jump toe oscillations, vertical free surface fluctuations, instantaneous total pressure and instantaneous void fraction. Some marked maxima of correlation coefficients indicated the co-variation relationships. First, in the recirculation region, the instantaneous void fraction was mainly related to the free-surface elevation. That is, when the water level decreased, the void fraction was measured closer to the free surface and increased. Second, in the main shear layer, the air entrapment process at the impingement point was reflected by a downstream shift of jump toe together with flow bulking at the free surface and an increase in void fraction. The total pressure data suggested a strong link between the water depth variations and piezometric pressure fluctuations. Third, in the lower shear layer, the void fraction and total pressure were both related to the relative position to the toe, which determined the development of the shear layer. A downstream jump toe motion led to a decreasing void fraction and an increasing total pressure in the lower shear region. The kinetic pressure fluctuations were the dominant component to the total pressure fluctuations.

Importantly the simultaneous sampling of instantaneous free-surface, total pressure and void fraction fluctuations provided some new insights into the interactions between the turbulent and air entrainment processes. For example, the present results indicated two different sub-regions in the shear layer: the main shear layer and the lower shear layer next to the invert. The characteristic differences of each subregion were discussed in terms of the two-phase flow and turbulence properties.

Following this experimental investigation, future works may aim at:

- the miniaturisation of total pressure probe TPP to reduce and minimise scale effects and flow disturbances that may affect the output signal. This is particularly important in the upper part of the jump where negative velocities were measured;
- an amplification of TPP signal output to extent the measurements to a larger range of Froude numbers and to improve their quality with higher accuracy;
- a study of scale effects in terms of Froude and Reynolds similitude of pressure field that may occur in such violent flows as it has been previously demonstrated for the two-phase flow properties;
- the analysis of correlation between video recordings and free surface motion. In particular, the advection of large size vortices within the roller and their impact in terms of vertical and horizontal displacements of the free surface should be investigated;
- the calibration of the TPP, including the effects of temperature and ambient pressure;
- the identification of the impact of high and low frequencies phenomena on the pressure field;
- a test of pressure probe orientation in the upper part of the flow to assess its effects on the results.

7. **ACKNOWLEDGEMENTS**

The authors thank Professor S.L. GAVRILYUK (University of Aix-Marseille, France) and Dr Carlo GUALTIERI (University of Napoli Federico II, Italy) for their expert advice and reviews.

They thank Jason Van Der GEVEL and Stewart MATTHEWS (The University of Queensland) for their technical assistance in the laboratory work. They acknowledge the program developed by Dr Stefan FELDER (The University of Queensland) for the processing of phase-detection probe data. The financial support of the Australian Research Council (Grant DP120100481) is acknowledged. The second author acknowledges the final support of ESTACA (Laval, France), of Groupama (Centre Manche), and of the School of Civil Engineering at the University of Queensland.

APPENDIX A. EXPERIMENTAL DATA: TWO-PHASE FLOW AND PRESSURE MEASUREMENTS

The conductivity phase-detection probe and total pressure probe were mounted side by side and sampled simultaneously. The elevations and longitudinal positions of the probe tips were identical, and the transversal distance between the probes was 9 mm. Measurements of instantaneous void fraction and total pressure were conducted at 13 to 26 points from above the channel bed to the free surface within a cross section of jump roller. Three cross sections were scanned for Froude number Fr_1 = 3.8 and four cross-sections for Fr_1 = 5.1, 7.5 and 8.5, all flows having the same inflow depth d_1 = 0.02 m. This appendix presents the basic experimental data for all measurement points. These basic results include the time-averaged void fraction C, bubble count rate F, air-water interfacial velocity V and turbulence intensity Tu, which were measured with the phase-detection probe or deduced from its signal, and the time-averaged total pressure P, pressure fluctuations p', skewness and excess kurtosis of the pressure signal Sk and Ku and maximum and minimum instantaneous pressure p_{max} and p_{min} measured with the pressure probe. In addition, the total pressure was calculated as:

$$P = \int_{y}^{y_{90}} (1-C) \times \rho_w \times g \times dy + \frac{1}{2} \times (1-C) \times \rho_w \times V^2 \qquad (A.1)$$

where C and V are the measured two-phase flow properties, ρ_w is the density of water and y_{90} is the vertical position where C = 0.9. In Equation (A.1), right hand side, the first term is the piezometric pressure P_0 and the second term is the kinetic pressure P_k.

Note that, for some sampling locations, meaningless velocity and turbulence intensity data were obtained because of some intrinsic limitation of experimental and data processing techniques. These erroneous data and subsequent calculation results were eliminated. Further, although the experimentally measured pressure data were only valid in the turbulent shear layer, those data in the recirculation region were included for completeness.

The probability distribution functions of the relative instantaneous total pressure $(p-P)/(0.5 \times \rho_w \times V_1^2)$ are shown in Figure A-1 at four characteristic vertical positions including the elevation of maximum mean total pressure y_{Pmax}, maximum pressure fluctuation $y_{p'max}$, maximum bubble count rate y_{Fmax} and maximum void fraction y_{Cmax}. All results are shown at the same distance to the jump toe: $(x-x_1)/d_1$ = 8.35.

Notation

C time-averaged void fraction measured with phase-detection probe;

d_1 inflow depth;

F time-averaged bubble count rate measured with phase-detection probe;

Fr_1 inflow Froude number of hydraulic jump;

g gravity acceleration;

P time-averaged total pressure measured with pressure probe;

P_o piezometric pressure calculated using two-phase flow data;

P_k kinetic pressure calculated using two-phase flow data;

p instantaneous total pressure data;

p_{max} maximum instantaneous total pressure;

p_{min} minimum instantaneous total pressure;

p' standard deviation of total pressure fluctuations measured with pressure probe;

Tu turbulence intensity derived from correlation analysis of phase-detection probe signals;

V time-averaged air-water interfacial velocity derived from phase-detection probe signals;

x longitudinal distance from the upstream vertical gate;

x_1 jump toe position;

y vertical elevation above the channel bed;

y_{Cmax} elevation of the local maximum void fraction;

y_{Fmax} elevation of the maximum bubble count rate;

y_{Pmax} elevation of the maximum mean total pressure;

$y_{p'max}$ elevation of the maximum total pressure fluctuations;

y_{90} vertical elevation where C = 0.90;

Sk skewness of instantaneous total pressure;

Ku excess kurtosis of instantaneous total pressure;

ρ_w density of water.

Fr_1 = 3.8, $(x-x_1)/d_1$ = 4.15:

y (mm)	C	F	V (m/s)	Tu	P (Pa)	p' (Pa)	Sk	Ku	p_{min} (Pa)	p_{max} (Pa)	P_o (Pa)	P_k (Pa)	P_o+P_k (Pa)
5	0.0000	0.050	0.740	7.768	365.81	338.81	-0.431	0.190	-1330.61	1745.32	588.85	273.64	862.49
10	0.0001	0.089	1.343	0.655	498.99	352.28	0.109	-0.379	-1658.68	1991.37	539.85	901.17	1441.03
15	0.0028	1.956	1.169	0.566	1599.46	300.52	-0.736	1.192	-428.28	3303.79	490.86	681.81	1172.66
19	0.0064	4.000	1.250	0.629	1078.58	847.63	-1.256	2.077	-797.36	3262.78	441.93	776.23	1218.16
23	0.0152	8.328	1.098	0.758	1271.16	431.45	-0.657	-0.252	-1043.54	3385.81	402.91	594.15	997.06
27	0.0359	17.733	1.250	1.066	1101.22	490.84	-0.362	-0.778	-715.34	3754.89	364.13	753.21	1117.34
30	0.0659	25.028	1.066	1.021	591.61	465.04	0.172	-0.660	-1535.65	3878.04	325.93	530.92	856.86
33	0.0704	24.467	1.007	1.031	555.03	450.01	0.309	-0.217	-1494.64	3303.79	298.03	471.30	769.33
36	0.1043	24.728	0.929	1.499	423.73	317.12	0.944	1.061	-797.36	3016.73	270.63	386.90	657.53
39	0.1225	20.472	1.098	2.830	76.21	238.57	1.025	2.491	-1125.56	2237.43	243.80	529.42	773.22
42	0.1196	17.539	1.007	2.678	-23.24	206.23	1.051	2.929	-1207.58	2155.41	217.73	446.33	664.06
46	0.0866	14.256	1.169	4.134	-48.05	199.71	0.960	2.745	-1699.69	2483.61	191.89	624.52	816.41
50	0.1031	13.178	1.250	3.731	-27.62	158.53	0.198	2.654	-1084.55	1704.31	156.73	700.72	857.45
54	0.2499	19.211	--	--	-62.67	126.11	0.239	2.438	-1412.62	1581.28	121.25	--	--
58	0.2935	19.156	--	--	-75.31	120.86	0.074	1.944	-1043.54	1212.20	88.97	--	--
62	0.4678	19.861	--	--	-96.29	115.91	0.002	1.959	-1084.55	843.12	60.42	--	--
66	0.5431	16.211	--	--	-94.96	114.68	-0.014	2.237	-1166.57	1253.21	36.14	--	--
70	0.8532	7.422	--	--	-83.12	109.55	-0.021	2.422	-1043.54	1007.16	16.76	--	--
74	0.8957	5.844	--	--	197.88	112.27	0.134	2.879	-715.34	1253.21	4.92	--	--

Fr_1 = 3.8, $(x-x_1)/d_1$ = 8.35:

y (m)	C	F	V (m/s)	Tu	P (Pa)	p' (Pa)	Sk	Ku	p_{min} (Pa)	p_{max} (Pa)	P_o (Pa)	P_k (Pa)	P_o+P_k (Pa)
5	0.0005	0.322	0.788	0.128	914.62	257.65	0.405	0.167	-387.27	2278.44	749.74	310.35	1060.08
10	0.0019	1.033	1.098	0.652	979.42	263.11	0.213	-0.124	-264.25	2852.69	700.75	602.19	1302.94
15	0.0046	2.333	0.954	0.404	1019.99	293.58	-0.083	-0.177	-428.28	2852.69	651.81	452.91	1104.71
20	0.0092	4.539	1.066	0.736	1013.60	331.27	-0.326	-0.181	-510.30	2565.63	602.97	563.13	1166.10
25	0.0116	5.467	0.954	0.791	829.05	349.06	-0.174	-0.476	-838.37	2401.59	554.31	449.72	1004.03
30	0.0249	11.517	1.066	0.960	681.92	406.21	0.012	-0.795	-879.51	2811.68	505.82	554.22	1060.04
34	0.0307	12.489	0.929	0.873	517.63	392.53	0.268	-0.669	-920.52	2442.60	457.71	418.71	876.42
37	0.0318	12.161	0.884	0.830	25.81	665.96	-0.999	1.641	--	2606.64	419.60	378.45	798.05
40	0.0403	13.228	0.863	1.195	352.14	347.09	0.573	0.040	-920.52	2278.44	391.12	357.45	748.57
43	0.0392	12.044	0.771	0.729	461.91	304.73	0.778	0.480	-838.37	2483.61	362.78	285.78	648.56
46	0.0440	12.194	0.929	1.719	234.15	268.98	0.802	0.953	-1084.55	1950.36	334.55	412.95	747.50
50	0.0416	10.617	0.659	1.074	76.31	235.04	0.921	1.698	-961.53	1704.31	306.37	208.17	514.54
54	0.0404	9.361	0.824	1.804	-25.91	195.11	0.836	2.205	-1125.56	1540.28	268.85	325.66	594.51
58	0.0450	9.078	--	--	-84.54	179.51	0.649	1.980	-1043.54	1458.26	231.25	--	--
62	0.0459	7.861	--	--	39.41	175.34	0.140	1.374	-1166.57	1417.25	193.73	--	--
67	0.1196	11.894	--	--	72.55	121.14	0.276	2.141	-920.52	1253.21	156.31	--	--
72	0.2149	13.356	--	--	56.40	115.25	0.337	2.630	-1002.53	1294.22	111.36	--	--
77	0.5177	14.372	--	--	154.73	109.37	0.054	2.643	-920.52	1171.19	70.56	--	--
82	0.6074	10.661	1.208	4.678	137.22	106.69	0.186	2.978	-797.36	1417.25	39.51	286.63	326.14
87	0.8219	7.561	1.169	3.984	136.92	103.83	0.095	3.125	-838.37	1171.19	18.07	121.77	139.85
92	0.9421	3.017	1.007	3.660	194.98	104.99	0.110	3.233	-838.37	1417.25	4.09	29.36	33.45

Fr_1 = 3.8, $(x-x_1)/d_1$ = 12.5:

y (m)	C	F	V (m/s)	Tu	P (Pa)	p' (Pa)	Sk	Ku	p_{min} (Pa)	p_{max} (Pa)	P_o (Pa)	P_k (Pa)	P_o+P_k (Pa)
10	0.0019	0.689	0.929	0.315	1323.15	214.24	0.300	0.216	186.85	2688.65	917.20	431.15	1348.34
20	0.0054	2.222	0.843	0.510	1217.10	261.27	0.014	0.117	-182.23	2565.63	819.29	353.43	1172.72
30	0.0104	4.117	0.806	0.561	1122.95	281.50	0.220	-0.309	-469.29	2606.64	721.65	321.10	1042.74
40	0.0179	6.528	0.884	0.915	1011.69	284.30	0.477	-0.073	-141.22	2565.63	624.42	383.87	1008.29
50	0.0234	6.961	0.697	0.676	790.89	235.13	0.736	0.816	-305.25	2237.43	527.80	237.31	765.11
60	0.0237	5.894	0.647	1.302	624.51	185.30	0.717	1.447	-387.27	1868.35	431.82	204.54	636.36
70	0.0163	3.933	0.906	3.132	575.29	158.93	0.620	1.573	-551.31	1786.33	336.13	403.94	740.07
80	0.0285	4.283	0.740	2.481	466.56	137.12	0.519	2.018	-469.29	1581.28	240.09	265.84	505.93
85	0.0995	5.928	1.133	4.628	346.11	139.03	0.554	1.900	-551.31	1540.28	144.29	577.77	722.06
90	0.2726	9.861	1.066	3.648	384.01	117.39	0.377	2.441	-633.33	1540.28	98.43	413.45	511.87
95	0.4662	8.817	0.929	2.760	307.10	114.15	0.290	2.302	-674.34	1294.22	58.54	230.60	289.15
100	0.7511	7.783	0.980	2.874	371.93	107.79	0.153	2.690	-592.32	1581.28	27.64	119.44	147.08
105	0.9033	3.750	0.771	1.869	319.17	106.71	0.109	3.292	-674.34	1458.26	8.47	28.75	37.22

Fr_1 = 5.1, $(x-x_1)/d_1$ = 4.15:

y (m)	C	F	V (m/s)	Tu	P (Pa)	p' (Pa)	Sk	Ku	p_{min} (Pa)	p_{max} (Pa)	P_o (Pa)	P_k (Pa)	P_o+P_k (Pa)
4	0.0001	0.083	--	--	3238.75	365.53	0.220	0.057	1659.52	5359.77	607.50	--	--
7	0.0008	0.906	1.726	0.888	3447.38	410.51	-0.146	0.351	919.54	5749.24	568.30	1488.64	2056.94
10	0.0024	2.544	1.908	0.886	3651.86	430.88	-0.774	1.771	997.43	5671.34	538.91	1815.64	2354.55
13	0.0035	3.444	2.014	0.830	3796.60	416.40	-1.685	5.645	880.60	6021.86	509.56	2020.81	2530.38
16	0.0146	12.694	1.813	0.964	3551.17	656.63	-1.405	1.833	296.28	6956.69	480.25	1618.53	2098.78
19	0.0279	22.733	1.726	0.794	3295.46	781.82	-0.956	0.050	296.28	6800.78	451.12	1448.35	1899.46
22	0.0545	37.689	1.813	1.076	3020.37	873.66	-0.648	-0.676	296.28	7501.94	422.34	1553.13	1975.47
25	0.0889	53.006	1.648	0.969	2545.37	881.38	-0.071	-1.068	101.55	8631.50	394.15	1236.77	1630.92
28	0.1779	62.889	1.648	1.313	1783.44	729.09	0.831	0.076	-599.48	8631.50	366.86	1115.96	1482.82
31	0.2059	53.100	1.510	1.817	1317.62	540.47	1.531	2.697	-755.39	8047.18	341.38	905.86	1247.24
34	0.2184	41.272	1.576	2.851	965.41	384.65	2.050	6.365	-365.80	5320.71	317.62	970.79	1288.41
37	0.1426	41.622	1.394	2.028	1173.38	506.43	1.270	1.831	-677.50	6138.70	294.46	833.30	1127.76
40	0.1443	30.444	1.394	3.270	867.73	344.55	1.679	4.809	-677.50	5281.76	270.37	831.68	1102.05
43	0.1434	23.139	1.726	4.851	685.67	246.15	1.894	8.312	-560.54	4152.32	245.19	1276.18	1521.36
46	0.1376	18.389	--	--	567.50	199.61	1.804	9.599	-1300.64	3645.90	220.01	--	--
49	0.1692	18.128	-1.813	-5.697	525.34	152.70	1.298	8.007	-1183.80	3100.65	194.75	1364.72	1559.46
52	0.1888	17.067	--	--	457.20	129.81	0.641	4.429	-716.44	2711.19	169.85	--	--
55	0.2437	18.611	-1.250	-3.977	439.54	119.09	0.457	3.673	-560.54	1893.20	145.72	590.89	736.61
59	0.4434	18.228	-1.133	-3.828	419.08	111.60	0.211	2.338	-911.17	1932.14	122.67	357.11	479.79
63	0.4254	22.328	-1.169	-4.046	284.38	110.36	0.161	2.055	-1028.01	1698.47	96.94	392.87	489.81
68	0.3969	17.350	-1.250	-4.489	377.39	112.46	0.158	2.287	-989.07	1854.25	74.77	471.20	545.97
73	0.6670	16.567	-1.343	-4.948	328.87	107.62	0.096	1.877	-1261.69	1893.20	45.91	300.13	346.04
78	0.7773	12.567	-1.295	-4.467	324.68	108.65	0.081	1.460	-833.28	1815.30	22.98	186.66	209.64
83	0.8838	7.294	-1.343	-4.569	321.34	109.50	0.097	1.560	-989.07	1815.30	9.36	104.72	114.08
88	0.9459	3.989	-1.250	-3.837	334.51	108.87	0.066	1.618	-911.17	1698.47	1.06	42.26	43.32

Fr_1 = 5.1, $(x-x_1)/d_1$ = 8.35:

y (m)	C	F	V (m/s)	Tu	P (Pa)	p' (Pa)	Sk	Ku	p_{min} (Pa)	p_{max} (Pa)	P_o (Pa)	P_k (Pa)	P_o+P_k (Pa)
4	0.0018	1.833	1.450	0.500	1797.60	497.01	0.275	-0.039	-833.28	4658.62	810.62	1049.39	1860.01
8	0.0055	4.961	1.394	0.614	1903.51	508.46	0.126	-0.335	-248.97	4697.57	771.46	966.57	1738.03
12	0.0099	8.200	1.576	0.800	2001.74	548.73	-0.158	-0.355	-171.07	4853.35	732.40	1229.76	1962.16
16	0.0150	12.161	1.510	0.839	2047.88	614.92	-0.390	-0.295	-365.80	5398.72	693.50	1123.60	1817.10
20	0.0244	18.711	1.576	1.137	2002.68	686.25	-0.410	-0.550	-638.55	5866.07	654.79	1211.78	1866.57
24	0.0379	27.178	1.576	0.944	1861.12	768.17	-0.267	-0.901	-599.48	6177.64	616.36	1194.98	1811.34
28	0.0629	37.867	1.576	1.201	1536.99	796.58	0.090	-1.049	-638.55	6099.75	578.38	1163.92	1742.29
32	0.0823	41.778	1.343	1.235	1194.81	720.88	0.475	-0.660	-755.39	6645.00	541.15	827.07	1368.22
36	0.0956	40.511	1.343	1.576	928.63	636.49	0.765	-0.059	-950.12	5164.92	504.80	815.16	1319.96
40	0.1041	36.083	1.394	2.064	724.80	557.68	1.028	0.828	-1573.26	4541.78	469.08	870.77	1339.86
44	0.0948	30.867	1.250	1.899	594.97	458.01	1.207	1.708	-1144.85	4230.21	433.80	707.16	1140.95
48	0.0930	28.117	1.250	2.222	488.89	403.88	1.305	2.442	-1456.42	4619.67	398.50	708.57	1107.07
52	0.0964	23.300	1.208	3.202	341.27	314.33	1.466	4.207	-1534.31	3684.84	362.98	659.68	1022.66
56	0.0905	16.456	1.576	4.384	189.65	222.48	1.309	4.899	-1690.10	2750.13	327.49	1129.58	1457.07
60	0.0881	14.306	--	--	162.91	194.07	1.189	5.263	-1066.96	2516.46	291.95	--	--
65	0.0733	12.061	--	--	145.87	164.26	0.751	3.544	-1378.53	1971.09	256.26	--	--
70	0.0938	12.444	--	--	118.98	140.42	0.596	3.028	-989.07	2048.98	211.21	--	--
75	0.1970	17.833	--	--	73.89	115.56	0.279	2.100	-989.07	1542.68	166.31	--	--
80	0.3422	17.561	--	--	68.76	108.76	0.146	1.718	-1222.74	1464.79	124.43	--	--
85	0.4420	17.056	--	--	61.71	108.36	0.153	1.796	-794.33	1347.95	88.64	--	--
90	0.6448	13.783	--	--	22.52	106.63	0.123	1.629	-1144.85	1270.06	58.86	--	--
95	0.6668	12.500	--	--	22.56	106.54	0.140	1.539	-1028.01	1386.90	36.48	--	--
100	0.8176	8.178	--	--	30.00	105.79	0.104	1.645	-872.23	1114.27	19.62	--	--
105	0.8971	4.972	--	--	28.12	105.78	0.133	1.766	-872.23	1075.33	6.99	--	--

Fr_1 = 5.1, $(x-x_1)/d_1$ = 12.5:

y (m)	C	F	V (m/s)	Tu	P (Pa)	p' (Pa)	Sk	Ku	p_{min} (Pa)	p_{max} (Pa)	P_o (Pa)	P_k (Pa)	P_o+P_k (Pa)
5	0.0038	2.894	1.394	1.270	1992.69	590.42	0.315	-0.090	-528.28	5549.40	977.32	968.29	1945.60
10	0.0082	6.250	1.576	1.137	2240.72	630.30	0.140	-0.314	-478.88	5252.95	928.41	1231.90	2160.31
14	0.0114	8.383	1.295	0.657	2367.33	653.32	0.060	-0.424	-133.02	5401.17	879.70	828.50	1708.20
18	0.0166	11.950	1.295	0.806	2367.83	690.52	0.014	-0.512	-34.20	5598.81	840.89	824.15	1665.04
22	0.0213	14.761	1.295	0.806	2306.82	723.61	0.024	-0.614	-380.06	5549.40	802.23	820.20	1622.43
26	0.0303	20.050	1.450	0.938	2272.46	794.14	-0.022	-0.729	-824.73	6142.45	763.78	1019.41	1783.18
30	0.0394	24.489	1.394	1.095	2101.62	825.23	0.145	-0.764	-429.47	6389.49	725.59	933.60	1659.19
34	0.0406	22.772	1.250	1.071	2002.90	758.87	0.326	-0.580	-528.28	5747.03	687.76	749.52	1437.28
38	0.0446	23.744	1.169	1.137	1869.11	737.90	0.472	-0.434	-627.10	5747.03	650.12	653.19	1303.31
42	0.0446	21.267	1.169	1.774	1809.11	663.66	0.632	-0.071	-923.55	5351.77	612.60	653.24	1265.83
46	0.0536	24.067	1.007	1.071	1538.62	639.21	0.818	0.395	-1071.78	5549.40	575.14	479.81	1054.95
50	0.0476	20.389	1.098	1.299	1539.80	579.73	0.890	0.688	-874.14	5203.54	537.87	574.60	1112.46
54	0.0493	19.572	1.208	2.223	1427.16	534.34	1.086	1.344	-478.88	5302.36	500.65	694.07	1194.72
58	0.0530	19.161	1.098	2.069	1256.50	469.12	1.144	1.925	-676.51	4660.05	463.35	571.39	1034.74
62	0.0549	17.717	1.066	2.102	971.39	398.87	1.153	2.436	-725.92	4116.56	426.15	537.14	963.29
66	0.0502	15.278	1.036	2.751	821.76	347.33	1.255	3.667	-1121.18	3523.50	389.07	509.44	898.51
70	0.0614	16.806	0.906	1.996	809.53	306.88	1.211	3.859	-923.55	3622.32	351.93	385.43	737.36
75	0.0678	13.872	--	--	542.68	226.03	0.843	3.187	-1615.27	3177.65	314.91	--	--
80	0.0607	12.483	--	--	405.32	217.45	1.046	5.064	-1269.41	3029.42	269.08	--	--
85	0.0949	14.594	--	--	357.41	183.72	0.630	3.267	-1615.27	2485.93	223.23	--	--
90	0.1128	14.289	--	--	325.29	162.82	0.528	1.989	-1121.18	2189.48	178.04	--	--
95	0.2122	17.467	--	--	276.10	154.98	0.620	2.745	-1071.78	1892.88	134.13	--	--
100	0.3543	19.700	--	--	242.02	143.57	0.346	1.167	-923.55	1645.83	93.09	--	--
106	0.6220	16.278	--	--	224.25	138.70	0.260	0.875	-1417.63	1645.83	57.97	--	--
112	0.7649	11.489	--	--	222.95	139.15	0.212	0.863	-1170.59	1497.61	27.88	--	--
118	0.9246	4.483	--	--	219.73	138.09	0.201	0.784	-874.14	1547.02	9.85	--	--

Fr_1 = 5.1, $(x-x_1)/d_1$ = 18.75:

y (m)	C	F	V (m/s)	Tu	P (Pa)	p' (Pa)	Sk	Ku	p_{min} (Pa)	p_{max} (Pa)	P_o (Pa)	P_k (Pa)	P_o+P_k (Pa)
5	0.0035	1.933	1.066	0.451	1765.82	422.03	0.559	0.241	-187.64	4210.16	1207.12	566.37	1773.49
10	0.0073	3.867	0.906	0.538	1771.61	432.62	0.506	0.092	59.40	4012.52	1158.20	407.66	1565.87
15	0.0114	6.606	1.133	0.733	1854.10	504.47	0.341	-0.200	-533.50	4951.28	1109.47	634.33	1743.79
20	0.0143	8.061	1.066	0.888	1779.69	518.62	0.350	-0.204	-237.05	5198.32	1060.92	560.22	1621.14
25	0.0148	7.567	0.884	0.568	1644.69	477.33	0.504	-0.022	-88.83	4308.97	1012.55	385.06	1397.62
30	0.0181	9.572	0.788	0.582	1627.78	523.04	0.425	-0.162	-286.46	4605.42	964.27	304.90	1269.17
35	0.0177	8.244	0.863	0.839	1452.50	439.82	0.616	0.188	-138.24	4308.97	916.07	365.87	1281.95
40	0.0195	9.017	1.036	0.982	1357.02	466.03	0.629	0.125	-237.05	4308.97	867.95	525.92	1393.86
45	0.0242	11.189	0.843	0.840	1289.01	493.99	0.636	0.099	-681.73	4556.02	819.86	346.76	1166.62
50	0.0276	11.994	0.929	1.121	1134.57	480.09	0.773	0.430	-879.36	4111.34	771.93	420.07	1192.00
55	0.0336	14.172	0.684	0.822	975.76	469.98	0.915	0.829	-879.36	3666.51	724.19	226.03	950.23
60	0.0359	13.944	0.824	0.932	871.28	434.71	0.964	1.103	-632.32	3468.88	676.69	327.20	1003.89
65	0.0365	13.817	1.036	1.737	766.71	406.98	1.087	1.669	-1225.22	3913.55	629.40	516.76	1146.16
72	0.0395	13.372	--	--	586.40	363.73	1.252	2.533	-1027.59	3172.43	582.17	--	--
79	0.0325	10.772	0.906	2.008	523.15	317.31	1.160	2.531	-928.77	3024.20	516.18	397.29	913.47
86	0.0337	10.333	0.518	0.477	351.51	271.21	1.310	3.844	-1076.99	2925.39	450.05	129.57	579.62
93	0.0328	9.300	0.342	0.381	223.63	239.62	1.203	3.858	-1027.59	2332.49	383.72	56.56	440.28
100	0.0303	8.211	0.558	--	158.47	220.12	1.241	4.954	-928.77	2530.12	317.40	150.80	468.19
108	0.0464	8.933	0.980	3.180	69.94	205.95	0.947	2.844	-1373.44	2381.90	250.96	457.67	708.63
116	0.1081	10.867	1.066	4.579	11.28	846.27	0.926	2.857	-1126.40	2036.04	175.57	506.94	682.51
124	0.4202	15.256	1.066	4.616	-59.58	190.26	1.709	8.196	-1669.89	2628.94	103.23	329.55	432.78
132	0.7627	9.672	--	--	-68.30	153.54	0.911	3.750	-1126.40	1640.62	45.53	--	--
140	0.8928	5.461	1.007	3.719	-48.41	173.47	1.702	8.712	-1472.26	2184.26	13.50	54.35	67.86

Fr_1 = 7.5, $(x-x_1)/d_1$ = 4.15:

y (m)	C	F	V (m/s)	Tu	P (Pa)	p' (Pa)	Sk	Ku	p_{min} (Pa)	p_{max} (Pa)	P_o (Pa)	P_k (Pa)	P_o+P_k (Pa)
4	0.0003	0.506	2.788	0.651	5267.08	1000.29	0.122	-0.008	-145.91	9983.57	622.65	3886.59	4509.24
8	0.0010	1.644	2.788	0.439	6516.55	917.68	-0.577	1.065	150.54	11070.70	583.46	3883.85	4467.31
12	0.0186	23.250	2.788	1.014	6639.51	1473.35	-1.519	2.707	-541.17	14529.44	544.28	3815.62	4359.90
16	0.0345	39.489	2.788	0.946	6815.73	1759.38	-1.682	2.445	-788.37	16901.35	505.47	3753.80	4259.27
20	0.0787	73.833	2.788	1.064	5986.60	2213.09	-0.898	-0.212	-640.14	19124.87	467.31	3581.65	4048.96
24	0.1315	107.917	2.589	1.160	4448.65	2318.40	-0.059	-1.138	-1331.86	17889.51	430.33	2911.36	3341.68
28	0.2220	122.894	2.417	1.404	2804.93	2020.90	0.751	-0.253	-2072.99	19470.73	395.25	2271.99	2667.24
32	0.2725	104.878	2.132	1.805	1605.52	1454.94	1.638	2.782	-1727.13	16308.29	362.97	1653.98	2016.96
36	0.2637	82.950	2.014	2.636	1095.34	1034.43	2.221	6.387	-3555.39	13146.01	333.46	1493.04	1826.51
40	0.2599	57.600	2.014	4.114	643.16	644.45	3.058	14.819	-2171.80	10329.42	304.77	1500.92	1805.69
46	0.2007	47.672	2.014	4.638	599.23	564.73	2.979	16.050	-2221.21	9242.44	275.84	1620.93	1896.77
52	0.1866	34.150	--	--	446.12	329.10	2.915	23.012	-1578.90	6376.45	230.58	--	--
58	0.1881	31.194	--	--	399.97	292.18	2.525	18.281	-2320.03	5190.65	183.16	--	--
64	0.2716	30.989	-1.169	-3.863	334.79	189.31	1.006	8.747	-1628.31	4004.70	135.38	498.02	633.41
70	0.5166	29.522	-0.980	-3.310	318.56	167.14	0.280	2.448	-1381.27	2966.97	90.10	231.99	322.08
76	0.7165	20.978	-0.980	-3.203	337.30	164.78	0.161	1.416	-1677.72	2324.66	54.47	136.06	190.53
82	0.7474	19.311	-0.929	-2.913	311.49	163.13	0.151	1.587	-1134.23	2374.07	31.93	109.11	141.04
88	0.8352	13.994	-0.954	-2.664	336.91	160.46	0.083	0.907	-837.78	2176.44	16.16	74.99	91.15
94	0.9636	4.289	-0.824	-2.029	373.68	154.18	0.144	1.134	-1529.49	2374.07	3.89	12.36	16.25

Fr_1 = 7.5, $(x-x_1)/d_1$ = 8.35:

y (m)	C	F	V (m/s)	Tu	P (Pa)	p' (Pa)	Sk	Ku	p_{min} (Pa)	p_{max} (Pa)	P_o (Pa)	P_k (Pa)	P_o+P_k (Pa)
6	0.0068	11.289	2.589	0.781	5025.84	1358.66	-0.153	-0.216	-195.32	11021.29	803.40	3329.49	4132.89
12	0.0222	28.322	2.589	1.017	5890.77	1581.54	-0.974	0.854	-640.14	15221.31	744.80	3277.82	4022.62
17	0.0503	53.822	2.589	1.067	5561.99	1985.46	-0.806	-0.192	-887.19	16555.49	686.85	3183.56	3870.41
22	0.0809	78.711	2.417	1.170	4494.47	2151.42	-0.188	-1.063	-2369.44	17741.29	639.63	2683.82	3323.45
26	0.1118	92.861	2.417	1.332	3809.37	2147.66	0.127	-1.073	-2616.63	19223.69	593.84	2593.71	3187.56
30	0.1671	108.267	2.266	1.497	2743.41	1956.72	0.651	-0.456	-2764.86	19767.18	558.42	2137.60	2696.03
34	0.2111	102.244	2.132	1.783	1802.28	1594.21	1.260	1.274	-2270.62	18482.57	524.69	1793.55	2318.24
38	0.2067	89.083	1.908	2.047	1409.90	1314.22	1.524	2.467	-2715.45	16950.75	492.90	1443.78	1936.68
42	0.2073	73.850	1.908	2.567	442.57	1048.29	1.990	5.197	-3456.57	12305.91	461.89	1442.74	1904.64
46	0.1779	65.772	1.813	2.579	284.57	933.21	1.950	5.383	-3357.76	12058.87	430.81	1350.39	1781.20
51	0.1819	49.972	1.813	3.743	-32.92	618.59	2.433	10.565	-3555.39	9588.30	399.16	1343.77	1742.93
56	0.1599	38.611	--	--	-180.06	478.74	2.693	14.801	-2666.04	7809.45	358.97	--	--
61	0.1477	30.406	--	--	-252.52	333.84	2.224	12.984	-3011.90	4992.87	318.35	--	--
66	0.1345	26.578	--	--	-296.66	259.29	1.731	12.642	-3011.90	4548.19	276.88	--	--
72	0.1927	28.594	-1.343	-4.189	-333.36	198.63	0.979	6.579	-2221.21	2818.75	234.80	727.64	962.44
78	0.2793	35.244	-1.343	-4.858	-350.58	172.44	0.572	3.273	-1727.13	1929.40	185.62	649.55	835.16
84	0.3246	33.206	-1.394	-5.149	-346.48	167.93	0.538	3.535	-1875.35	2275.25	140.69	656.49	797.18
90	0.5233	31.756	-1.250	-4.824	-342.89	156.70	0.226	0.919	-1825.94	1286.93	99.64	372.38	472.03
96	0.6576	27.050	-1.250	-5.117	-338.39	155.97	0.280	1.682	-1727.13	1978.80	65.77	267.49	333.26
102	0.7510	20.711	-1.208	-4.256	-335.93	155.35	0.211	1.039	-1677.72	1781.17	41.69	181.80	223.49
108	0.7611	19.906	-1.450	-5.483	-328.37	155.73	0.279	1.653	-2468.41	1978.80	24.31	251.10	275.40
114	0.9253	7.817	-1.066	-3.539	-295.11	157.00	0.198	1.482	-2270.62	2324.66	9.96	42.47	52.44

Fr_1 = 7.5, $(x-x_1)/d_1$ = 12.5:

y (m)	C	F	V (m/s)	Tu	P (Pa)	p' (Pa)	Sk	Ku	p_{min} (Pa)	p_{max} (Pa)	P_o (Pa)	P_k (Pa)	P_o+P_k (Pa)
5	0.0076	11.928	2.417	0.786	3887.35	1347.24	0.057	-0.303	-2122.39	11268.34	1003.29	2897.99	3901.29
10	0.0162	21.983	2.589	0.955	5008.24	1451.65	-0.565	0.171	-788.37	13146.01	954.48	3298.05	4252.53
15	0.0368	42.350	2.266	1.159	4193.67	1701.30	-0.224	-0.654	-1480.09	12602.36	906.06	2472.00	3378.06
20	0.0621	64.783	2.417	1.112	4485.34	2025.72	-0.398	-0.845	-1974.17	16209.48	858.36	2738.92	3597.28
25	0.0839	79.339	2.417	1.170	3723.71	2029.20	0.012	-1.046	-1430.68	16258.88	811.78	2675.21	3487.00
30	0.1009	82.878	2.266	1.519	2986.92	1871.63	0.350	-0.815	-1480.09	15715.39	766.36	2307.59	3073.95
35	0.1347	90.100	2.014	1.486	2248.19	1736.30	0.744	-0.213	-2320.03	16357.70	721.88	1754.66	2476.55
40	0.1316	79.472	1.908	1.764	1765.59	1479.20	1.011	0.536	-2616.63	12009.46	678.66	1580.58	2259.23
45	0.1461	73.350	1.576	1.669	1216.91	1235.16	1.374	1.930	-2616.63	11564.79	636.18	1060.56	1696.74
50	0.1731	63.806	1.648	2.700	677.52	896.46	1.872	4.895	-2814.26	11317.74	593.98	1122.46	1716.44
56	0.1563	51.839	1.813	3.733	517.11	724.08	1.978	6.260	-2666.04	8204.71	552.80	1385.83	1938.63
62	0.1381	33.378	1.813	5.255	157.76	432.81	2.170	11.296	-2369.44	6327.04	503.69	1415.72	1919.41
68	0.1284	29.694	--	--	121.78	391.13	1.942	9.748	-2715.45	5734.14	453.55	--	--
74	0.1066	22.039	--	--	26.47	289.20	1.674	9.946	-2616.63	4202.33	402.58	--	--
80	0.1190	20.089	--	--	-31.86	240.29	1.151	7.502	-1727.13	3955.29	350.69	--	--
87	0.1559	21.733	-1.208	-4.432	-61.11	190.74	0.714	5.222	-1727.13	2966.97	298.52	616.19	914.72
94	0.1485	18.172	-1.343	-4.609	-76.35	195.44	0.734	4.317	-1677.72	2423.48	239.36	767.46	1006.81
101	0.2299	19.094	-1.169	-4.548	-91.65	173.90	0.304	1.837	-1628.31	2127.03	181.20	526.53	707.73
108	0.4180	22.328	-1.133	-4.408	-112.49	156.83	0.351	2.075	-1282.45	1830.58	125.58	373.44	499.01
115	0.5457	21.167	-1.133	-4.403	-108.75	154.62	0.169	0.836	-1233.04	1879.99	79.20	291.46	370.66
122	0.7874	13.867	-1.098	-3.881	-97.88	152.37	0.144	0.881	-1677.72	1534.13	43.65	128.27	171.92
129	0.8539	9.978	-1.133	-3.888	-85.09	152.45	0.160	0.900	-1430.68	1781.17	20.78	93.74	114.52
136	0.8989	7.189	-1.036	-3.642	-138.78	153.09	0.163	0.846	-1381.27	1484.72	8.48	54.20	62.68

Fr_1 = 7.5, $(x-x_1)/d_1$ = 18.75:

y (m)	C	F	V (m/s)	Tu	P (Pa)	p' (Pa)	Sk	Ku	p_{min} (Pa)	p_{max} (Pa)	P_o (Pa)	P_k (Pa)	P_o+P_k (Pa)
6	0.0150	17.544	2.132	1.142	3226.56	1197.87	0.309	-0.310	-1035.41	9291.85	1298.64	2239.40	3538.04
12	0.0278	30.733	2.014	1.269	3286.89	1263.78	0.245	-0.391	-837.78	10428.24	1240.28	1971.40	3211.68
17	0.0382	39.883	2.014	1.030	3311.45	1395.04	0.204	-0.550	-1282.45	10329.42	1182.74	1950.33	3133.07
22	0.0479	47.361	2.014	1.221	3168.94	1476.49	0.242	-0.603	-1183.64	10625.87	1135.36	1930.74	3066.10
27	0.0628	58.000	2.014	1.262	3035.54	1599.88	0.256	-0.705	-1183.64	10922.48	1088.47	1900.54	2989.02
32	0.0649	56.450	1.813	1.179	2605.89	1447.98	0.460	-0.435	-1825.94	10675.28	1042.18	1536.04	2578.22
37	0.0752	60.233	1.908	1.467	2327.01	1421.22	0.626	-0.254	-3209.53	10774.10	996.31	1683.08	2679.40
42	0.0860	61.367	1.726	1.486	2034.27	1311.94	0.774	0.138	-2023.58	11416.56	950.74	1361.75	2312.49
47	0.1023	63.156	1.648	1.569	1569.23	1240.50	1.050	0.857	-1924.76	9884.75	905.69	1218.58	2124.27
52	0.0985	58.856	1.648	1.803	1395.35	1122.38	1.142	1.267	-2369.44	9094.22	861.31	1223.77	2085.08
57	0.1112	56.444	1.648	2.261	993.55	972.41	1.387	2.436	-2221.21	8599.98	817.23	1206.56	2023.79
63	0.1106	51.228	1.394	2.239	767.16	836.13	1.526	3.407	-2369.44	8797.61	773.37	864.41	1637.78
69	0.1141	43.833	1.450	2.796	485.97	660.13	1.734	5.483	-3209.53	6969.35	721.09	931.27	1652.36
76	0.0882	36.289	1.510	2.957	528.01	627.45	1.655	4.843	-2666.04	6574.08	668.90	1040.06	1708.96
83	0.0879	26.700	1.726	4.486	186.15	441.57	1.516	5.455	-2468.41	5190.65	607.24	1358.97	1966.21
90	0.0770	19.400	--	--	-1.42	324.00	1.586	8.347	-2418.84	3955.29	544.68	--	--
97	0.0581	20.506	1.576	4.418	164.00	379.54	1.284	4.848	-2221.21	3708.25	481.73	1169.83	1651.57
104	0.0571	14.517	--	--	-86.54	272.47	1.370	7.968	-2023.58	3560.02	417.77	--	--
111	0.0495	13.189	-0.980	-4.736	-107.28	250.34	0.945	4.169	-2122.39	3065.79	353.12	456.16	809.28
118	0.0570	12.528	--	--	-125.61	224.39	0.715	3.203	-2023.58	2324.66	288.18	--	--
125	0.1520	17.178	--	--	-253.97	175.63	0.439	1.894	-1727.13	1731.76	223.23	--	--
132	0.2951	19.272	--	--	-257.63	164.54	0.375	1.968	-2122.39	2028.21	161.80	--	--
139	0.3859	18.272	--	--	-264.01	157.41	0.231	1.181	-1677.72	1336.34	108.54	--	--
146	0.6111	17.983	--	--	-264.97	153.38	0.306	1.357	-1578.90	1583.54	63.30	--	--
153	0.8267	11.139	--	--	-242.31	152.12	0.180	0.622	-1628.31	1138.71	28.89	--	--
160	0.8932	7.750	--	--	-245.65	154.04	0.342	2.140	-1825.94	1830.58	9.61	--	--

Fr_1 = 8.5, $(x-x_1)/d_1$ = 4.15:

y (m)	C	F	V (m/s)	Tu	P (Pa)	p' (Pa)	Sk	Ku	p_{min} (Pa)	p_{max} (Pa)	P_o (Pa)	P_k (Pa)	P_o+P_k (Pa)
5	0.0008	1.433	3.295	0.599	6464.64	1235.43	-0.157	-0.176	-469.19	13486.75	606.44	5425.54	6031.98
10	0.0030	5.461	3.295	0.915	6899.18	1294.32	-0.678	1.000	-940.64	14523.93	557.46	5413.64	5971.11
15	0.0178	24.889	3.295	1.038	7389.91	1579.98	-1.882	4.595	-1506.66	18955.81	508.56	5333.13	5841.68
19	0.0420	50.422	3.295	1.094	7149.44	2043.81	-1.653	2.496	-2072.40	20181.57	460.07	5201.71	5661.78
23	0.1003	106.667	3.295	1.257	5712.11	2637.65	-0.663	-0.592	-2166.69	23953.42	422.04	4885.54	5307.59
27	0.1980	160.144	3.021	1.128	4070.19	2746.20	0.095	-0.903	-2543.84	29517.06	385.63	3659.22	4044.85
31	0.2274	145.872	2.788	1.503	2292.55	2263.46	0.819	-0.046	-3392.44	22444.79	352.28	3003.80	3356.07
35	0.2608	125.278	2.589	1.784	1200.08	1745.71	1.520	2.371	-3486.73	21596.19	321.42	2478.09	2799.50
39	0.2571	99.483	2.266	2.307	563.90	1253.26	2.152	6.386	-2260.98	17352.89	291.78	1906.68	2198.46
44	0.2656	59.411	--	--	-38.37	666.53	3.012	17.073	-3203.87	11600.68	262.73	--	--
49	0.2345	44.961	--	--	-170.68	475.92	2.619	19.662	-2638.13	9620.61	226.54	--	--
54	0.1833	40.611	--	--	-164.23	494.42	2.378	14.903	-2638.13	8394.56	189.79	--	--
59	0.2721	33.911	-1.295	-4.090	-247.86	379.49	1.552	14.370	-3015.29	5471.31	151.02	610.05	761.07
64	0.3171	27.072	-1.133	-3.780	-270.92	329.86	0.885	9.353	-2921.00	4528.42	113.18	438.15	551.33
69	0.4458	33.094	-1.098	-3.770	-264.80	313.46	0.287	2.199	-2355.26	3962.68	78.62	334.37	412.99
75	0.6992	22.600	-1.007	-3.189	-198.02	326.23	0.476	4.095	-2638.13	3491.24	48.31	152.49	200.80
81	0.8147	17.361	-1.007	-2.995	-174.22	350.29	0.501	7.065	-3675.31	4434.13	23.17	93.96	117.13
87	0.8833	12.794	-0.954	-2.499	-131.71	352.73	0.719	7.733	-3109.58	3868.40	8.88	53.10	61.98

Fr_1 = 8.5, $(x-x_1)/d_1$ = 8.35:

y (m)	C	F	V (m/s)	Tu	P (Pa)	p' (Pa)	Sk	Ku	p_{min} (Pa)	p_{max} (Pa)	P_o (Pa)	P_k (Pa)	P_o+P_k (Pa)
5	0.0031	6.333	3.021	0.767	6543.53	1435.51	-0.209	-0.151	2.25	12732.15	817.38	4548.47	5365.84
10	0.0066	11.572	3.295	0.915	6892.94	1448.70	-0.560	0.425	-469.19	14618.22	768.45	5394.24	6162.70
15	0.0218	29.083	3.295	1.118	7591.16	1693.36	-1.559	2.920	-1034.93	16975.74	719.69	5311.68	6031.37
20	0.0575	70.761	3.295	1.358	6577.11	2317.85	-0.889	-0.057	-1412.37	18201.50	671.39	5117.97	5789.35
24	0.0950	104.644	3.021	1.226	5643.17	2563.25	-0.376	-0.947	-1600.95	19992.99	624.33	4129.44	4753.77
28	0.1468	135.017	2.788	1.268	4452.40	2554.89	0.109	-1.074	-2072.40	21596.19	588.12	3317.15	3905.27
32	0.1703	140.978	2.589	1.350	3432.35	2311.93	0.508	-0.669	-2732.42	20370.14	553.66	2781.17	3334.83
36	0.1909	134.350	2.589	1.773	2475.23	1994.82	0.919	0.223	-2732.42	18390.07	520.67	2712.40	3233.07
40	0.2202	122.833	2.266	1.854	1667.74	1600.84	1.404	1.998	-2072.40	16881.45	488.55	2001.36	2489.91
45	0.2535	97.467	2.132	2.675	914.80	1122.35	2.037	5.913	-4335.33	15183.95	457.41	1697.16	2154.57
50	0.2248	73.639	2.014	3.319	506.98	838.66	2.338	9.145	-2543.84	11883.55	420.01	1572.08	1992.09
55	0.1866	62.467	2.014	3.937	371.76	719.76	2.259	10.203	-3203.87	11506.39	382.73	1649.51	2032.24
60	0.1721	41.922	--	--	90.38	518.90	2.037	11.633	-2826.71	9337.45	343.81	--	--
66	0.1596	36.922	--	--	-174.93	417.29	1.473	8.778	-2732.42	6980.23	303.59	--	--
72	0.1777	33.094	--	--	-275.33	352.24	0.768	5.535	-3203.87	4905.57	254.55	--	--
78	0.1732	30.761	-1.169	-3.982	-326.03	321.98	0.417	2.614	-2638.13	3302.66	205.66	565.27	770.94
84	0.3238	34.633	-1.169	-4.331	-350.22	294.86	0.180	1.415	-2355.26	2454.06	157.18	462.28	619.46
90	0.4637	34.950	-1.066	-3.829	-316.20	299.70	0.259	1.891	-2355.26	2548.35	112.99	304.80	417.79
96	0.5352	32.617	-1.098	-3.739	-317.62	291.41	0.132	1.147	-2732.42	2170.90	77.35	280.43	357.78
102	0.5960	31.661	-1.036	-3.707	-310.47	306.13	0.337	2.237	-2826.71	3208.37	47.92	216.71	264.62
108	0.8259	19.178	-0.980	-3.375	-208.85	318.92	0.202	3.047	-3581.02	4151.26	22.37	83.57	105.94
114	0.9369	7.661	-0.906	-2.641	-36.18	334.09	0.197	0.641	-2072.40	2454.06	5.37	25.93	31.30

Fr_1 = 8.5, $(x-x_1)/d_1$ = 12.5:

y (m)	C	F	V (m/s)	Tu	P (Pa)	p' (Pa)	Sk	Ku	p_{min} (Pa)	p_{max} (Pa)	P_o (Pa)	P_k (Pa)	P_o+P_k (Pa)
6	0.0083	14.828	3.021	0.839	4084.70	977.19	-0.207	-0.105	-1695.57	8736.09	992.26	4524.74	5517.00
12	0.0282	40.228	3.021	1.042	4594.12	1134.58	-0.731	0.276	138.19	10299.30	933.70	4434.07	5367.77
18	0.0625	75.794	2.788	1.082	4614.56	1334.98	-0.431	-0.649	-463.01	13185.34	875.98	3644.60	4520.58
24	0.0978	104.872	2.788	1.283	3305.74	1392.10	0.030	-0.975	-1966.11	12764.41	819.84	3507.57	4327.41
28	0.1248	120.300	2.589	1.302	3215.05	1371.69	0.263	-0.926	-1364.91	11591.97	765.76	2934.01	3699.77
32	0.1522	126.361	2.589	1.475	2522.42	1300.32	0.655	-0.417	-192.47	11862.61	730.92	2842.11	3573.03
36	0.1560	118.928	2.417	1.668	2408.62	1128.13	0.847	0.101	-763.61	10720.23	697.15	2464.60	3161.75
40	0.2009	115.517	2.132	1.797	1884.51	938.47	1.346	1.707	-583.25	9607.92	663.99	1816.80	2480.79
44	0.2206	100.567	2.132	2.236	1620.76	748.42	1.709	3.751	-2356.98	10058.82	631.78	1771.90	2403.68
49	0.1809	88.517	2.014	2.461	1878.11	670.86	1.770	4.306	-1996.17	8074.68	600.84	1661.12	2261.97
54	0.1638	77.356	1.908	2.596	1894.89	612.60	1.869	5.068	318.64	8255.04	561.68	1521.88	2083.56
60	0.1611	55.928	2.014	4.091	1303.98	412.18	2.110	8.206	-463.01	6150.74	521.12	1701.25	2222.37
66	0.1503	37.811	--	--	1256.43	309.11	2.174	10.712	-102.29	5218.79	471.88	--	--
72	0.1210	28.461	-1.343	-4.008	986.82	280.44	1.385	7.552	-583.25	4046.36	422.23	792.19	1214.42
78	0.1060	24.389	-1.450	-4.787	1070.73	198.83	1.430	9.674	-132.35	3805.88	371.41	939.83	1311.24
84	0.1522	25.300	-1.394	-4.280	1077.29	145.89	1.207	10.751	48.01	3505.18	319.28	823.98	1143.26
90	0.2552	28.261	-1.208	-4.319	1162.62	165.66	0.195	1.131	-12.11	3024.22	268.07	543.72	811.79
97	0.2010	27.067	-1.066	-3.688	1365.37	133.30	0.448	3.206	529.06	3144.46	221.25	454.14	675.39
104	0.4649	30.806	-1.066	-3.821	1222.30	202.97	0.120	2.125	559.12	2573.32	168.30	304.14	472.44
111	0.4799	26.206	-1.133	-4.240	769.87	307.01	0.077	1.284	48.01	1761.61	122.54	333.69	456.23
118	0.5725	25.600	-1.098	-4.299	363.02	178.10	0.165	1.921	-252.59	1761.61	86.34	257.94	344.29
125	0.6714	23.772	-1.208	-5.041	1019.18	447.86	-0.023	0.364	-102.29	2272.63	53.84	239.88	293.72
132	0.8040	17.089	-1.066	-3.996	1065.66	272.97	0.222	1.355	378.76	2152.39	27.91	111.38	139.29
139	0.9069	8.750	-1.036	-3.355	755.64	175.32	0.201	1.167	-252.59	2483.05	9.91	49.91	59.83

Fr_1 = 8.5, $(x-x_1)/d_1$ = 18.75:

y (m)	C	F	V (m/s)	Tu	P (Pa)	p' (Pa)	Sk	Ku	p_{min} (Pa)	p_{max} (Pa)	P_o (Pa)	P_k (Pa)	P_o+P_k (Pa)
6	0.0164	26.828	2.589	1.026	4547.80	1749.79	0.121	-0.374	-2666.04	14084.76	1312.14	3297.23	4609.37
12	0.0341	47.011	2.589	0.955	4989.69	2036.02	-0.128	-0.539	-1578.90	16258.88	1253.82	3237.98	4491.80
18	0.0494	62.717	2.417	1.122	4307.51	2080.51	0.110	-0.691	-2468.41	14578.85	1196.50	2775.83	3972.34
24	0.0726	81.483	2.589	1.325	3990.55	2294.67	0.170	-0.827	-2666.04	16456.52	1140.16	3108.89	4249.05
30	0.0759	82.411	2.417	1.351	3549.11	2114.45	0.356	-0.652	-1875.35	15023.68	1084.95	2698.48	3783.42
35	0.1016	93.111	2.266	1.420	2846.97	2046.89	0.606	-0.371	-3654.21	16160.07	1030.51	2305.64	3336.15
40	0.1059	91.911	2.132	1.438	2341.70	1880.82	0.826	0.090	-2962.49	14924.86	985.86	2032.69	3018.55
45	0.1198	89.428	2.132	1.835	1795.83	1669.82	1.068	0.864	-3209.53	13195.41	941.95	2001.02	2942.97
50	0.1354	85.539	1.908	1.855	1319.06	1474.85	1.292	1.728	-4049.47	11811.83	898.48	1573.61	2472.09
55	0.1505	79.233	1.908	2.392	797.80	1216.29	1.694	3.736	-3011.90	11218.93	855.73	1546.05	2401.78
60	0.1411	70.250	1.648	2.138	611.90	1062.33	1.784	4.604	-3505.98	10625.87	813.74	1165.96	1979.69
66	0.1349	60.100	1.648	2.831	415.90	890.91	1.844	5.326	-2962.49	9341.26	771.88	1174.40	1946.28
72	0.1161	51.917	1.648	2.758	285.89	795.01	1.948	6.786	-3011.90	8303.53	721.19	1199.86	1921.05
78	0.1084	41.233	1.726	3.895	57.53	630.61	1.937	7.762	-3061.31	6771.72	669.77	1328.35	1998.13
85	0.0940	24.711	--	--	-334.92	383.56	1.670	9.091	-2666.04	4251.74	617.58	--	--
92	0.0775	22.389	--	--	-179.59	388.61	1.397	7.158	-2863.67	4449.37	555.92	--	--
99	0.0687	19.778	--	--	-238.73	340.01	1.349	7.619	-2468.41	3856.47	493.20	--	--
106	0.0714	16.939	-1.295	-4.721	-460.94	253.12	0.983	5.790	-2320.03	2769.34	429.61	778.19	1207.80
113	0.0789	15.889	-1.250	-4.651	-481.92	241.11	0.826	4.638	-2517.81	2077.62	365.82	719.65	1085.47
120	0.1194	18.444	--	--	-458.45	192.24	0.779	5.005	-2122.39	2374.07	302.37	--	--
128	0.1365	22.578	--	--	-538.68	185.05	0.517	2.575	-1825.94	1484.72	240.57	--	--
136	0.2898	26.983	--	--	-238.09	121.96	0.443	5.252	-2616.63	2077.62	172.20	--	--
144	0.5417	24.333	--	--	-274.20	135.70	0.159	3.580	-2616.63	1879.99	110.52	--	--
152	0.6746	20.750	--	--	-296.89	106.04	0.179	5.825	-3110.71	2028.21	64.72	--	--
160	0.7332	17.439	--	--	-306.94	110.81	0.408	8.250	-2418.84	1830.58	34.00	--	--
168	0.9401	5.772	-1.169	-4.295	--	--	--	--	--	--	10.78	40.98	51.76

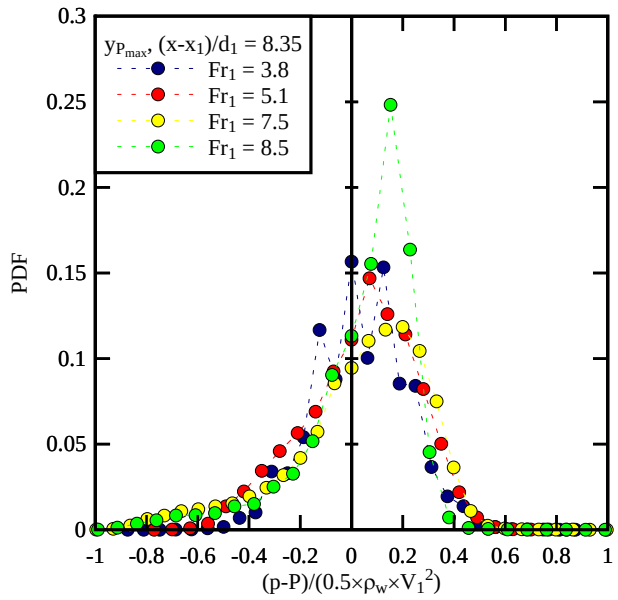

(A) $y = y_{Pmax}$, $(x-x_1)/d_1 = 8.35$

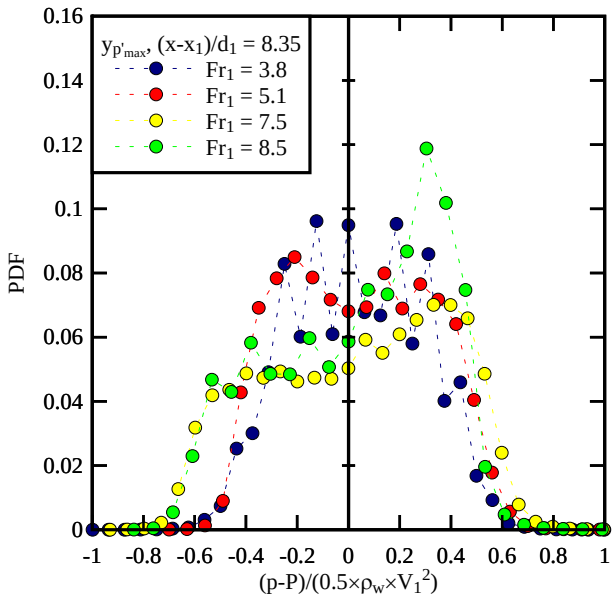

(B) $y = y_{p'max}$, $(x-x_1)/d_1 = 8.35$

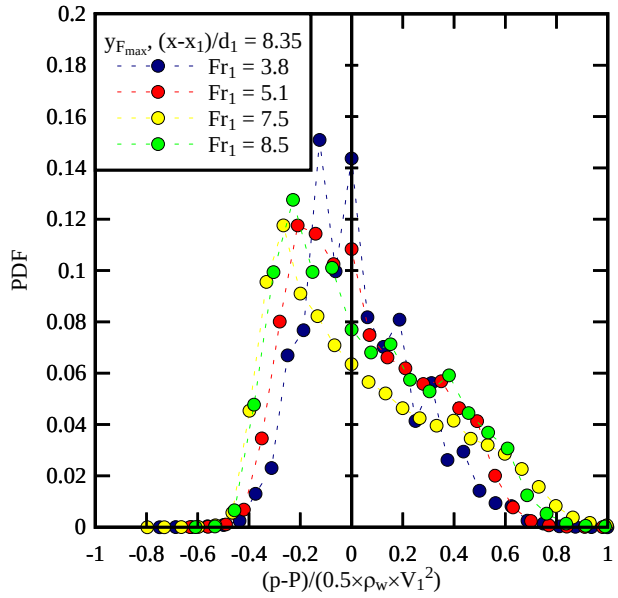

(C) $y = y_{Fmax}$, $(x-x_1)/d_1 = 8.35$

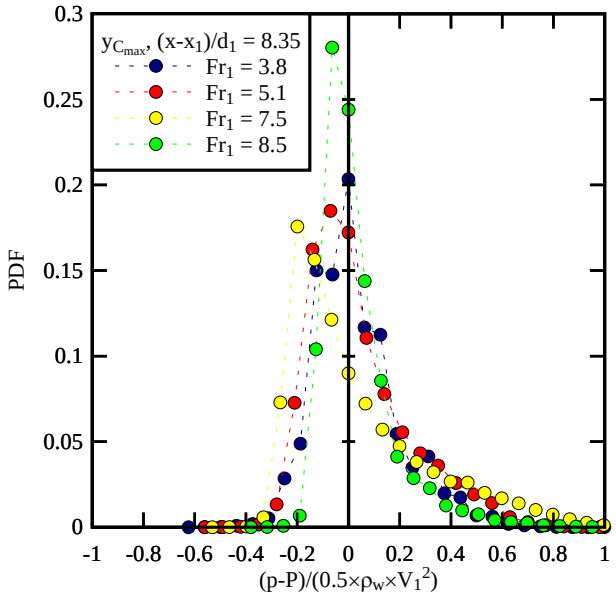

(D) $y = y_{Cmax}$, $(x-x_1)/d_1 = 8.35$

Fig A-1 – Probability distribution functions of dimensionless instantaneous total pressure at some characteristic vertical elevations in hydraulic jumps

APPENDIX B. CHARACTERISTIC PRESSURE AND TWO-PHASE FLOW PROPERTIES

The vertical distributions of total pressure and air-water flow properties exhibited some characteristic profiles in a cross section of jump roller (Fig. B-1). The profile shape may depend upon the flow conditions and the cross-sectional location. Typically, at a cross-section with the roller, the void fraction reached a local maximum C_{max} in the air-water shear layer at an elevation y_{Cmax}, and the elevation y_* marked the vertical elevation above which the void fraction increased monotically to unity (Fig. B-1). The bubble count rate data highlighted a maximum bubble count rate F_{max} at an elevation y_{Fmax} in the air-water shear layer.

This appendix summarises the characteristic total pressure and air-water flow properties for all experimental flow conditions.

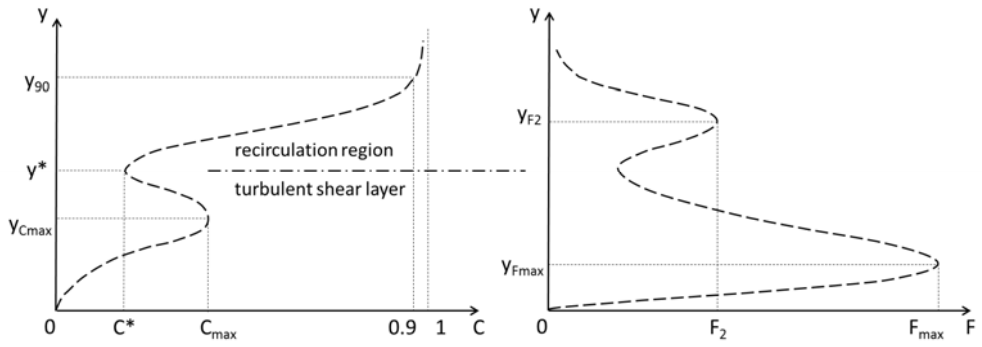

Fig B-1 - Sketch of characteristic air-water flow properties in a hydraulic jump roller.

Notation

C_{max} maximum void fraction in turbulent shear layer;

d_1 inflow depth;

F_{max} maximum bubble count rate in turbulent shear layer;

Fr_1 inflow Froude number;

P_{max} maximum mean total pressure in turbulent shear layer;

p'_{max} maximum standard deviation of total pressure in turbulent shear layer;

Q flow rate;

Re Reynolds number;

W channel width;

x_1 longitudinal position of jump toe;

y_{Cmax} elevation of the local maximum void fraction;

y_{Fmax} elevation of the maximum bubble count rate;

y_{F2} elevation of the secondary peak of bubble count rate;

y_{Pmax} elevation of the maximum mean total pressure;

$y_{p'max}$ elevation of the maximum total pressure fluctuations;

y_{90} elevation where the void fraction equals 0.9;

y_* elevation of the boundary between turbulent shear layer and recirculation region;

η mean (time-averaged) water level measured with the displacement meter.

Q (m^3/s)	W (m)	d_1 (m)	V_1 (m/s)	x_1 (m)	Fr_1	Re	x-x_1 (m)	C_{max}	y_{Cmax} (m)	F_{max} (Hz)	y_{Fmax} (m)	y_* (m)	y_{F2} (m)	η (m)	y_{90} (m)
0.0179	0.5	0.02	1.79	0.83	3.8	3.5×10^4	0.083	0.1225	0.039	25.028	0.030	0.046	0.062	0.055	0.074
							0.167	0.0440	0.046	13.228	0.040	0.054	0.077	0.087	0.089
							0.250	0.0237	0.060	6.961	0.050	0.070	0.090	0.099	0.105
0.0239	0.5	0.02	2.39	0.83	5.1	4.8×10^4	0.083	0.2184	0.034	62.889	0.028	0.046	0.063	0.061	0.083
							0.167	0.1041	0.040	41.778	0.032	0.065	0.078	0.097	0.105
							0.250	0.0549	0.062	24.489	0.030	0.066	0.100	0.113	0.117
							0.375	0.0395	0.072	14.172	0.055	0.100	0.124	0.131	0.140
0.0347	0.5	0.02	3.47	0.83	7.5	6.8×10^4	0.083	0.2725	0.032	122.894	0.028	0.052	0.064	0.063	0.090
							0.167	0.2111	0.034	108.267	0.030	0.066	0.078	0.106	0.112
							0.250	0.1731	0.050	90.100	0.035	0.074	0.108	0.119	0.136
							0.375	0.1141	0.069	63.156	0.047	0.111	0.132	0.146	0.160
0.0397	0.5	0.02	3.97	0.83	8.5	8.0×10^4	0.083	0.2656	0.044	160.144	0.027	0.054	0.069	0.064	0.090
							0.167	0.2535	0.045	140.978	0.032	0.066	0.090	0.090	0.112
							0.250	0.2206	0.044	126.361	0.032	0.078	0.104	0.117	0.139
							0.375	0.1505	0.055	93.111	0.035	0.099	0.136	0.141	0.168

Q (m^3/s)	W (m)	d_1 (m)	V_1 (m/s)	x_1 (m)	Fr_1	Re	x-x_1 (m)	P_{max} (Pa)	y_{Pmax} (m)	p'_{max} (Pa)	$y_{p'max}$ (m)
0.0179	0.5	0.02	1.79	0.83	3.8	3.5×10^4	0.083	1599.5	0.015	490.8	0.028
							0.167	1013.6	0.015	406.2	0.030
							0.250	--	--	284.3	0.037
0.0239	0.5	0.02	2.39	0.83	5.1	4.8×10^4	0.083	3796.6	0.013	881.4	0.025
							0.167	2047.9	0.016	796.6	0.028
							0.250	2214.4	0.018	825.2	0.030
							0.375	1854.1	0.015	523.0	0.030
0.0347	0.5	0.02	3.47	0.83	7.5	6.8×10^4	0.083	6815.7	0.016	2318.4	0.024
							0.167	5890.8	0.012	2151.4	0.024
							0.250	5008.2	0.010	2029.2	0.025
							0.375	3311.4	0.017	1599.9	0.027
0.0397	0.5	0.02	3.97	0.83	8.5	8.0×10^4	0.083	7389.9	0.015	2746.2	0.027
							0.167	7591.2	0.015	2563.3	0.025
							0.250	4614.6	0.018	--	0.024
							0.375	4989.7	0.012	2294.7	0.024

APPENDIX C. VERTICAL PROFILES OF MEAN TOTAL PRESSURE AND PRESSURE FLUCTUATIONS

The total pressure relative to the atmospheric pressure was measured within the jump roller with a pressure transducer mounted facing the impinging flow (Fig. C-1). The pressure probe was manufactured by MeasureX and the pressure transmitter model was MRV21. The sensitive part had a 5 mm outer diameter. The pressure measurement range goes from 0 to 1.5 bars with a corresponding output voltage between 0 and 62.19 mV (data from the manufacturer). For the present experiments, an amplifier was added to provide a larger output voltage range (up to 1 V), allowing a higher resolution. Further the amplification system high-pass-filtered the signal to eliminate noises above 2 kHz. Prior to the experiments, a daily calibration (static and/or dynamic) was conducted and regularly checked, because the output voltage appeared to be temperature sensitive. The pressure probe was mounted inside a mounting tube (Fig. C-1). The pressure probe was scanned at 5 kHz for 180 s. During the experiments, the probe sensor was mounted as close as possible as to the phase-detection probe: the transversal distance between both was adjusted to Δz_{PP} = 9 mm (Fig. C-1). The probes were carefully aligned with the flow direction as well as the acoustic displacement meters located above.

The data were recorded at a number of vertical positions within the roller, and they yielded the vertical of total pressure. Based on the measured void fraction and interfacial velocity collected using the phase-detection probe, the static and kinetic pressures were estimated as:

$$P_o = \int_{y}^{y_{90}} (1-C) \times \rho_w \times g \times dy \quad (C.1)$$

$$P_k = \frac{1}{2} \times (1-C) \times \rho_w \times V^2 \quad (C.2)$$

where P_o is the static pressure, P_k is the kinetic pressure, C is the local void fraction, V is the local interfacial velocity, y_{90} is the elevation where C = 0.9, ρ_w the density of water and g the gravity acceleration. The sum of the static and kinetic pressures was compared with the experimental results to validate the measurements.

This appendix presents the comparisons between the measured mean pressure profiles and the calculated values for the full data set, followed by a comparison between the dimensionless pressure fluctuations and turbulence intensity. The calibration data of the pressure probe are also provided; herein the calibration curves varied daily and the reason was not yet confirmed. Note that the pressure measurements in the recirculation region can be meaningless because of the reversed flow that placed the pressure transducer in the wake of the probe.

Notation

C time-averaged void fraction measured with phase-detection probe;

Fr_1 inflow Froude number;

g gravity acceleration;

P time-averaged total pressure measured with pressure probe;

P_o piezometric pressure calculated using measured two-phase flow data;

P_k kinetic pressure calculated using measured two-phase flow data;

p' standard deviation of total pressure fluctuations measured with pressure probe;

Tu turbulence intensity derived from correlation analysis of phase-detection probe signals;

V (a) time-averaged air-water interfacial velocity derived from phase-detection probe signals;
(b) voltage signal of the pressure probe;

x longitudinal position;

x_1 longitudinal position of the jump toe;

y vertical elevation above the channel bed;

y_{90} vertical elevation where C = 0.9;

ρ_w density of water.

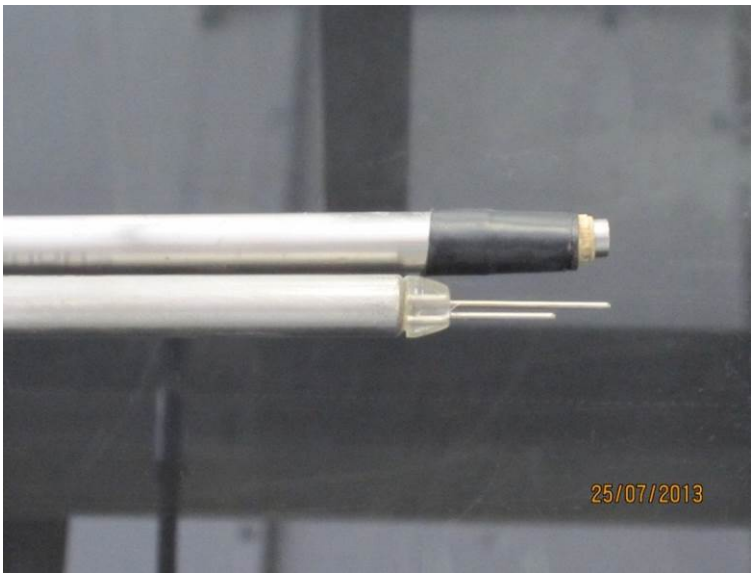

Fig C-1 - Pressure probe and dual-tip conductivity phase-detection probe mounted together - Flow direction from right to left

C.1. CALIBRATION OF PRESSURE PROBE

Date	Profile	Fr_1	$x-x_1$	Calibration
240713	1	3.8	0.083	P (Pa) = 127357×V -109142
240713	2		0.167	P (Pa) = 127357×V -109142
240713	3		0.250	P (Pa) = 127357×V -109142
150713	1	5.1	0.083	P (Pa) = 120951×(V +0.012)-107906
150713	2		0.167	P (Pa) = 120951×(V +0.012)-107906
160713	3		0.250	P (Pa) = 153442×(V -0.007)-132905
160713	4		0.375	P (Pa) = 153442×(V -0.008)-132905
170713	1	7.5	0.083	P (Pa) = 153442×V -132905
170713	2		0.167	P (Pa) = 153442×V -132905
180713	3		0.250	P (Pa) = 153442×V -132905
180713	4		0.375	P (Pa) = 153442×V -132905
230713	1	8.5	0.083	P (Pa) = 292823×V -134065
230713	2		0.167	P (Pa) = 292823×V -134065
220713	3		0.250	P (Pa) = 93354×V -69900
190713	4		0.375	P (Pa) = 153442×V -132905

C.2. MEAN TOTAL PRESSURE PROFILES, COMPARED WITH THEORETICAL VALUES BASED UPON AIR-WATER FLOW MEASUREMENTS

$\underline{Fr_1 = 3.8}$

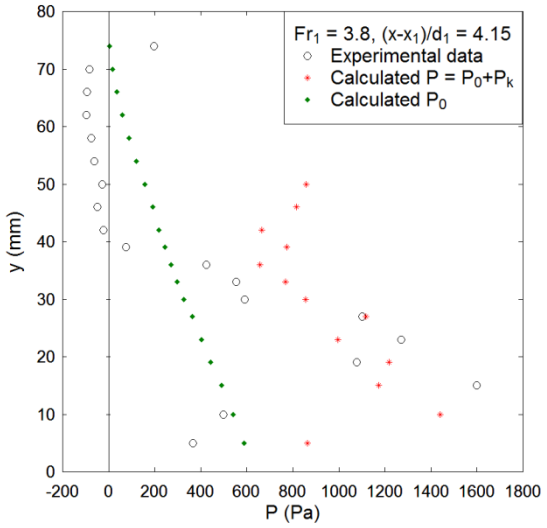

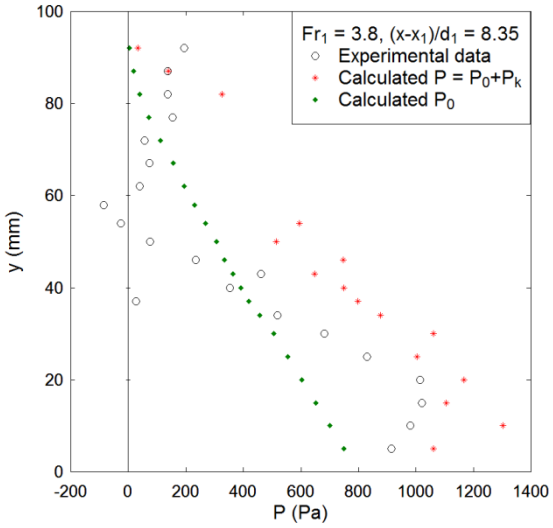

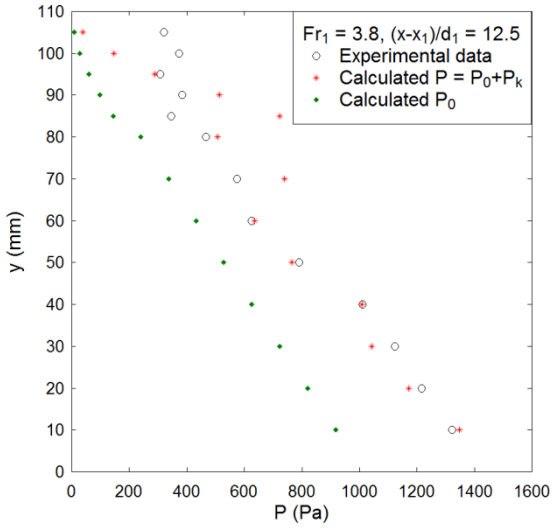

$\underline{Fr_1 = 5.1}$

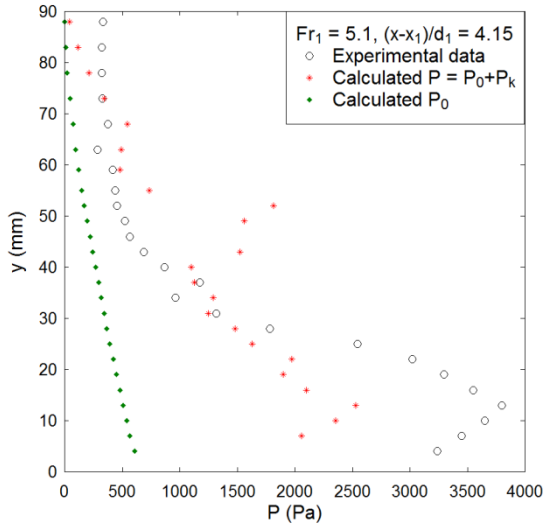

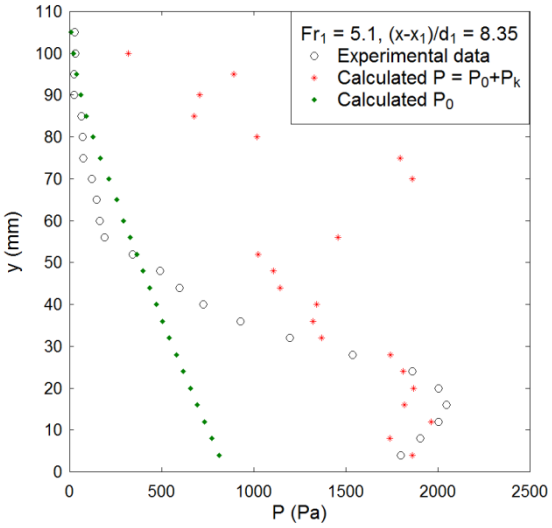

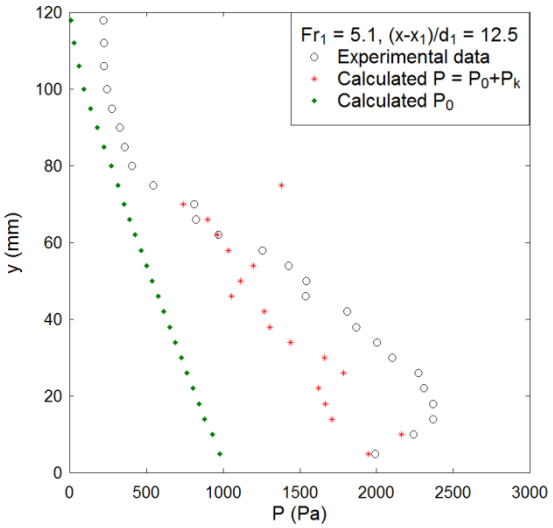

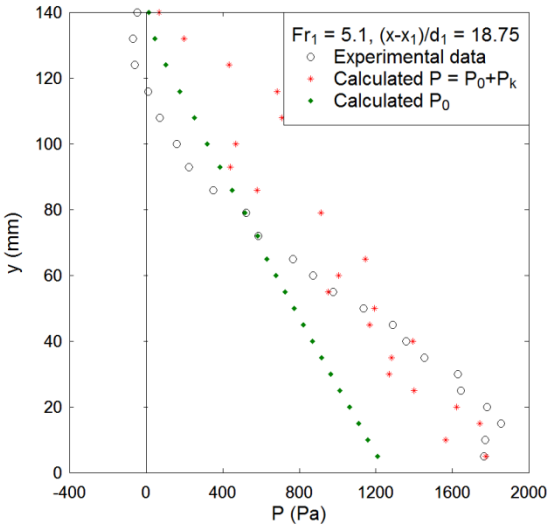

Fr_1 = 7.5

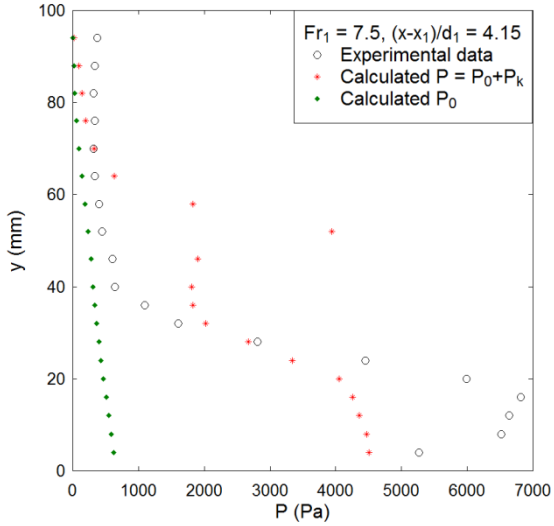
Fr1 = 7.5, (x-x1)/d1 = 4.15
Experimental data
Calculated P = P0+Pk
Calculated P0
y (mm)
P (Pa)

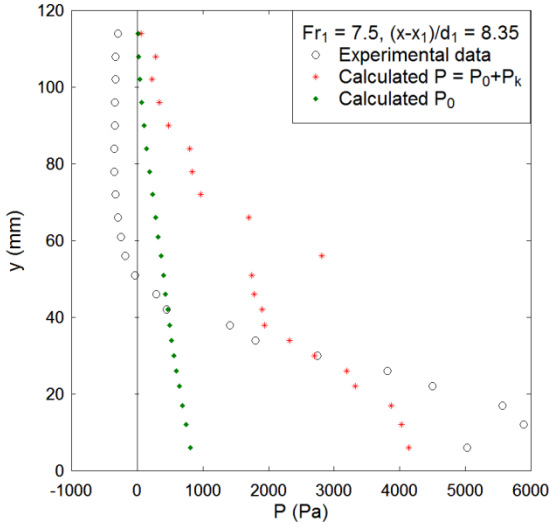
Fr1 = 7.5, (x-x1)/d1 = 8.35
Experimental data
Calculated P = P0+Pk
Calculated P0
y (mm)
P (Pa)

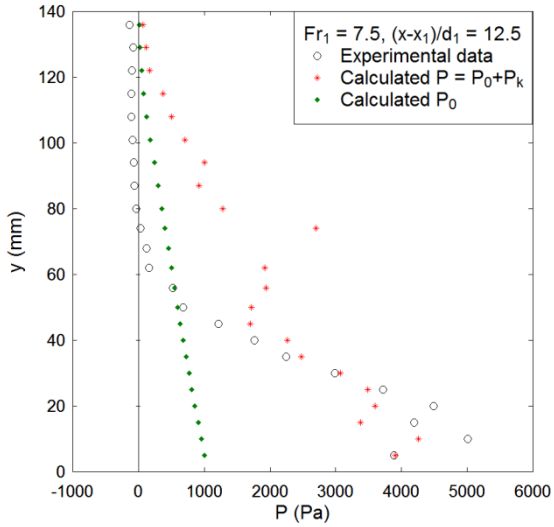
Fr1 = 7.5, (x-x1)/d1 = 12.5
Experimental data
Calculated P = P0+Pk
Calculated P0
y (mm)
P (Pa)

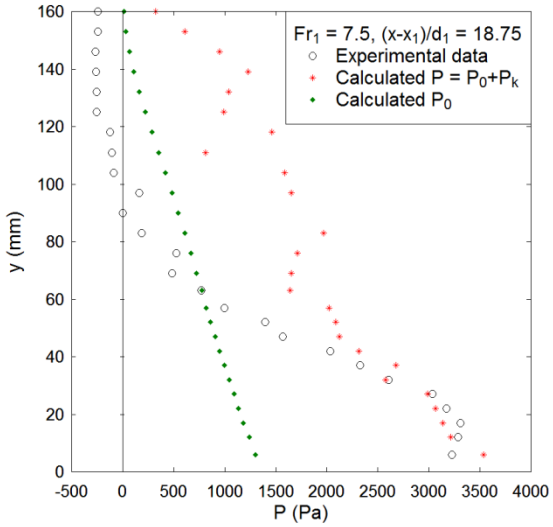
Fr1 = 7.5, (x-x1)/d1 = 18.75
Experimental data
Calculated P = P0+Pk
Calculated P0
y (mm)
P (Pa)

Fr_1 = 8.5

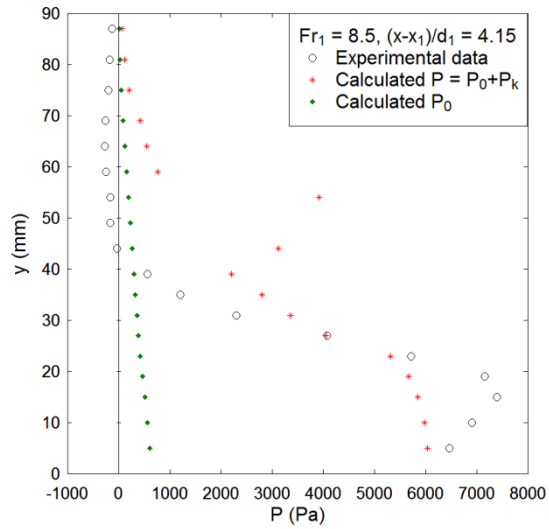
Fr1 = 8.5, (x-x1)/d1 = 4.15
Experimental data
Calculated P = P0+Pk
Calculated P0
y (mm)
P (Pa)

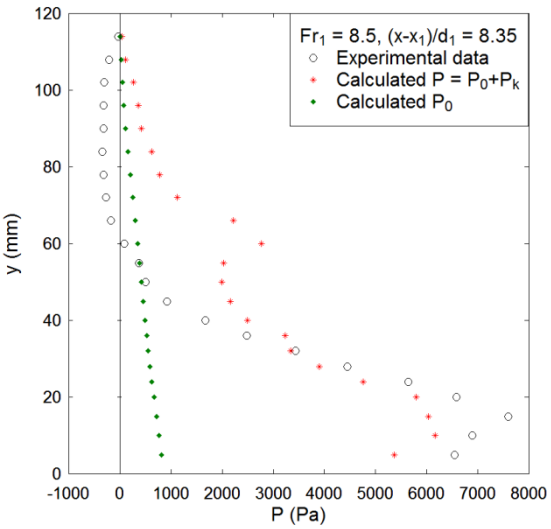
Fr1 = 8.5, (x-x1)/d1 = 8.35
Experimental data
Calculated P = P0+Pk
Calculated P0
y (mm)
P (Pa)

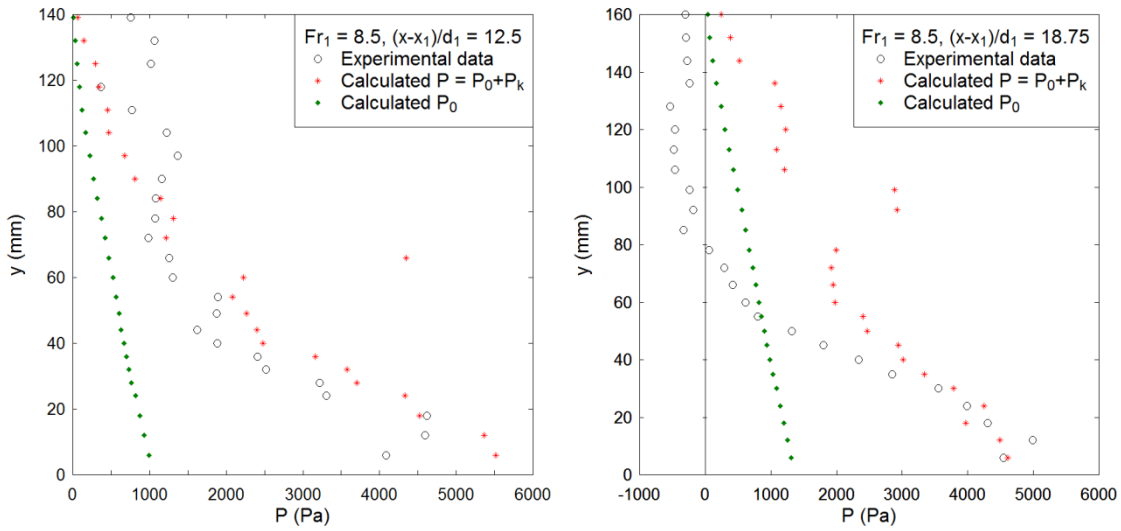

C.3. TOTAL PRESSURE FLUCTUATIONS, COMPARED WITH TURBULENCE INTENSITY

$\underline{Fr_1 = 3.8}$

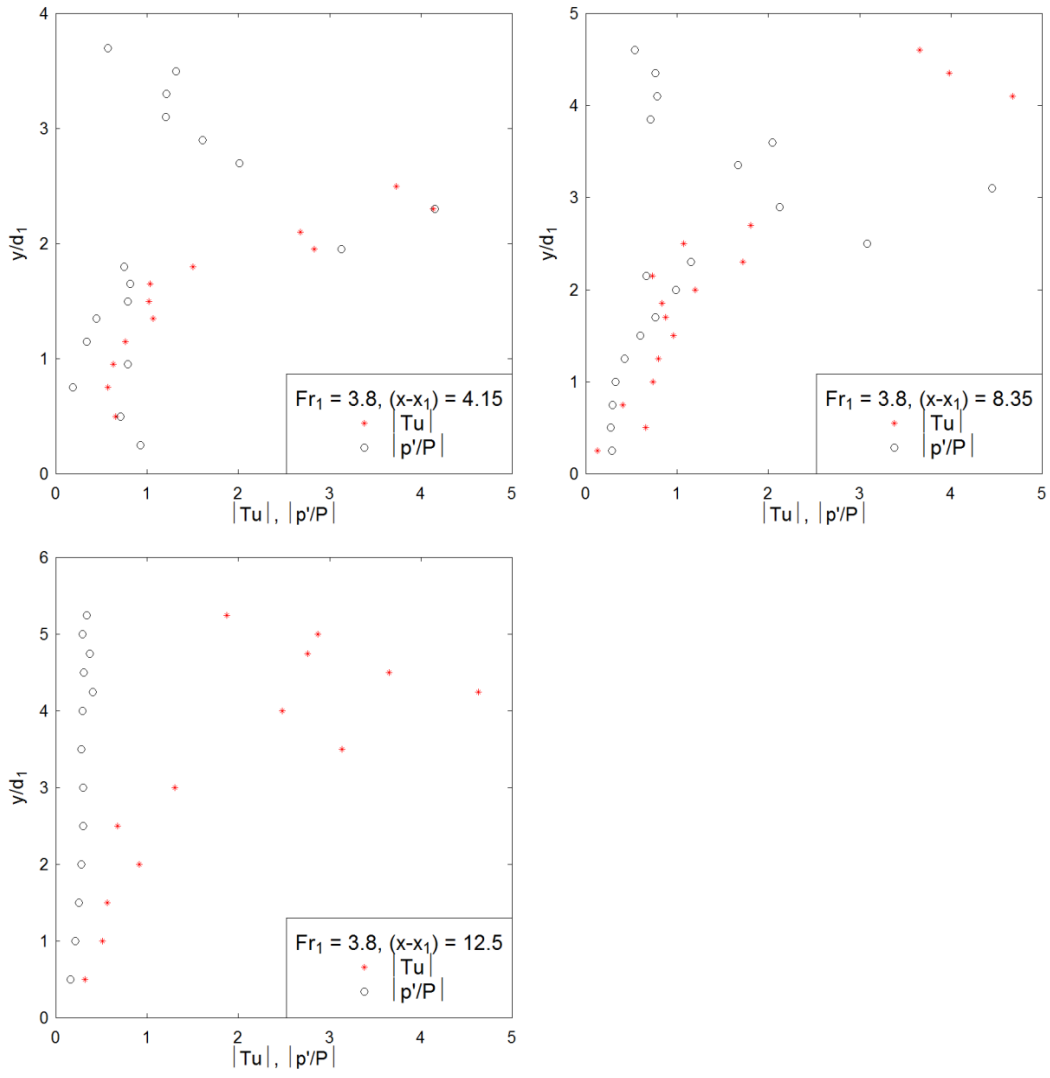

Fr_1 = 5.1

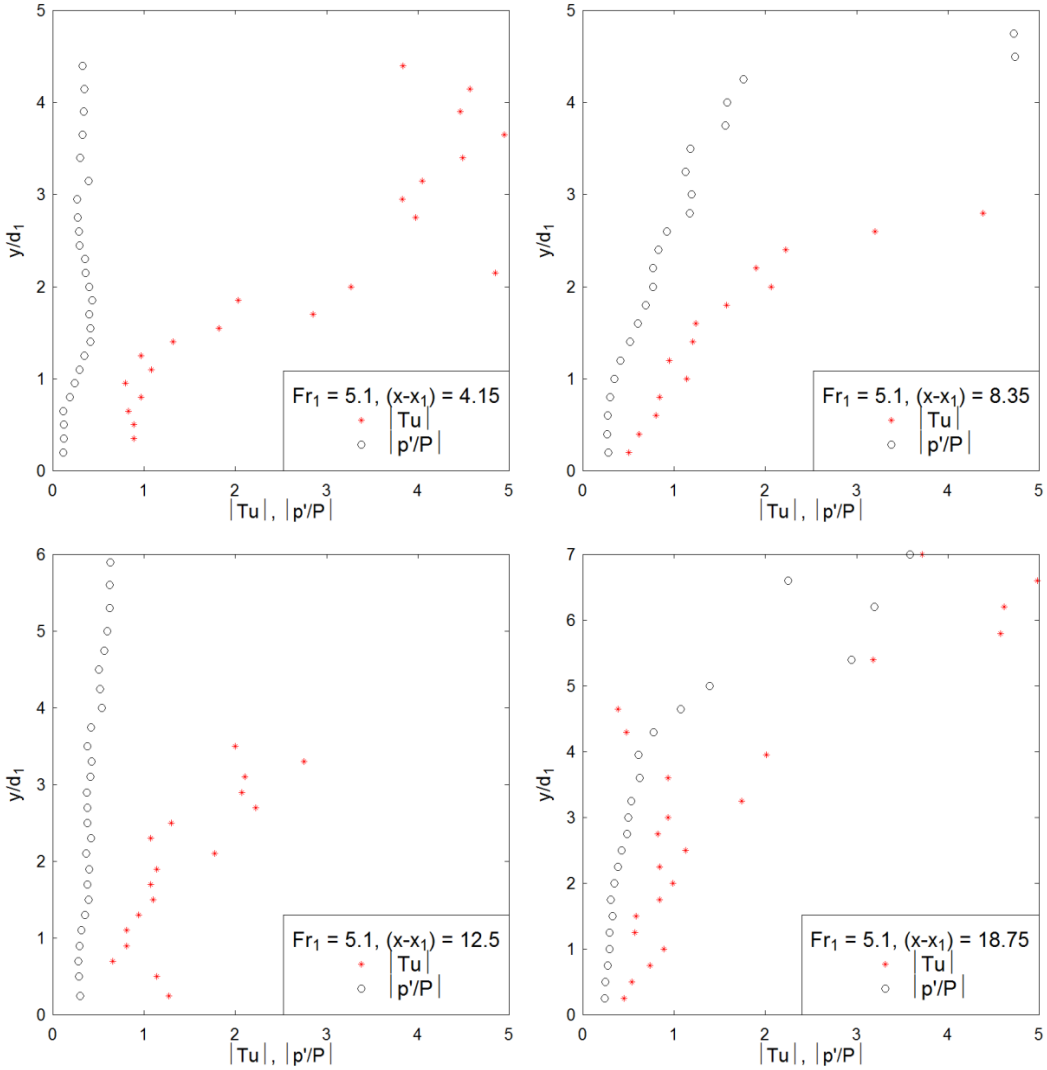
Fr1 = 5.1, (x-x1) = 4.15
Fr1 = 5.1, (x-x1) = 8.35
Fr1 = 5.1, (x-x1) = 12.5
Fr1 = 5.1, (x-x1) = 18.75
|Tu|
|p'/P|
y/d1
|Tu|, |p'/P|

Fr_1 = 7.5

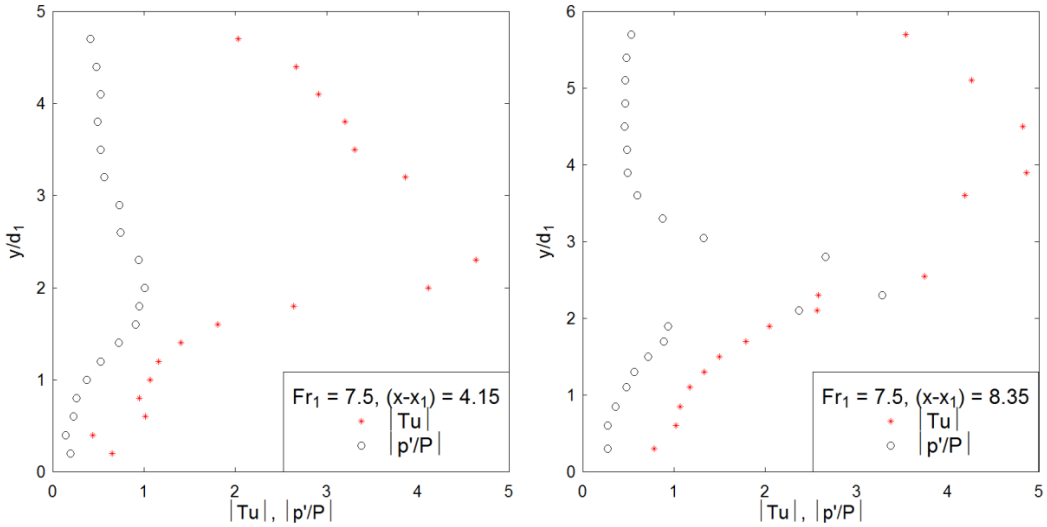
Fr1 = 7.5, (x-x1) = 4.15
Fr1 = 7.5, (x-x1) = 8.35
|Tu|
|p'/P|
y/d1
|Tu|, |p'/P|

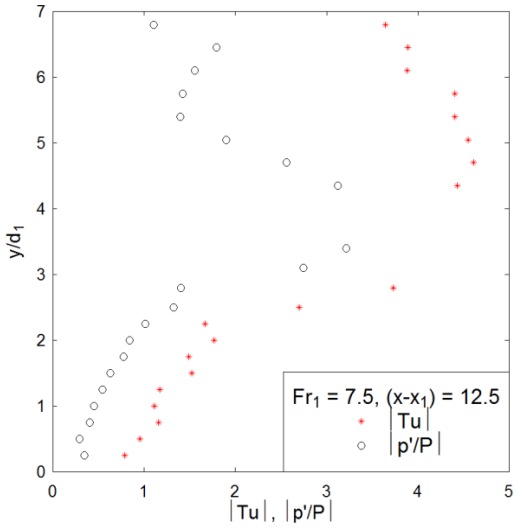

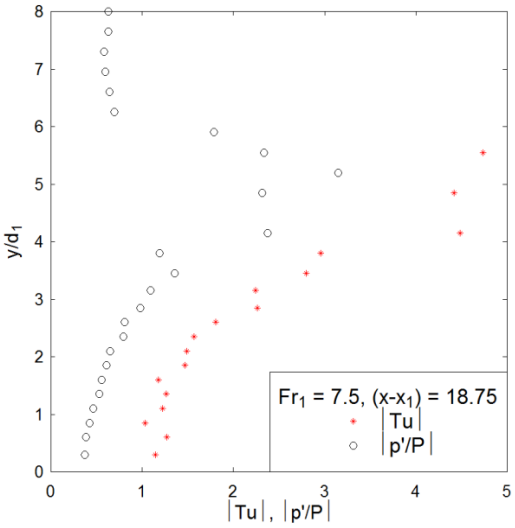

$\underline{Fr_1 = 8.5}$

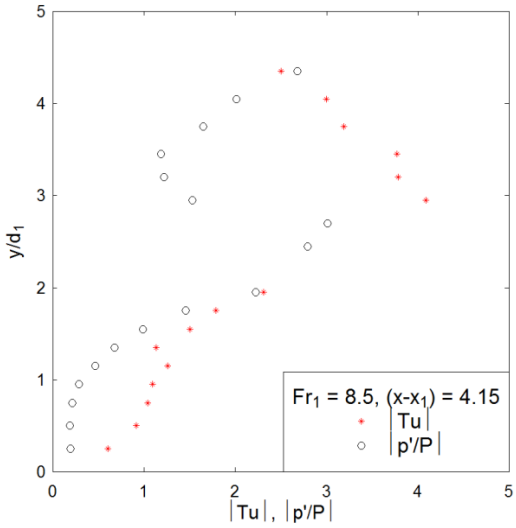

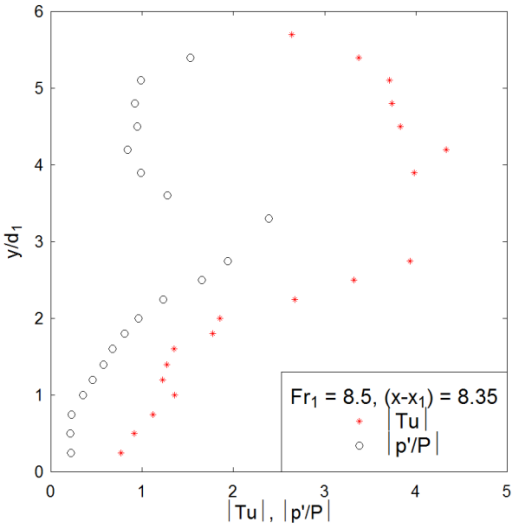

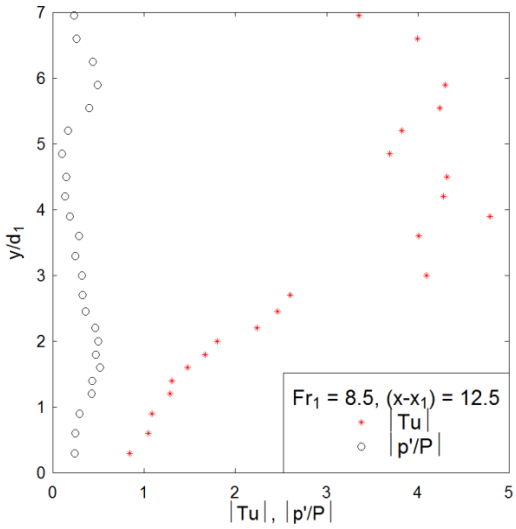

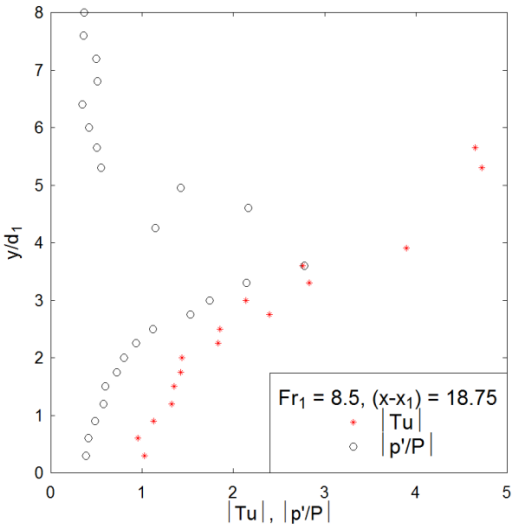

APPENDIX D. VERTICAL PROFILES OF MAXIMUM CORRELATION COEFFICIENTS BETWEEN MEASURED PARAMETERS

The instantaneous free surface location, pressure and void fraction were measured simultaneously with two acoustic displacement meters (ADMs), a total pressure probe (TPP) and a phase-detection probe (PDP). The position of the free surface was measured in both horizontal and vertical directions. The relative positions of the instruments are sketched in Figure D-1. Some cross-correlation analysis was performed between the signals. The correlation functions revealed some co-variation between the corresponding phenomena by exhibiting a maximum/minimum correlation coefficient with zero time lag. As sketched in Figure D-1, the correlation coefficients are denoted as R_{ij} with i,j = x,y,c,p , where the subscript x refers to the horizontal jump front oscillations, y to the vertical free surface fluctuations, c to the instantaneous void fraction and p to the instantaneous total pressure. The order of the subscripts is in accordance with the order of the correlation. See notations for the details of the coefficients.

The peak values of the correlation functions $(R_{ij})_{max}$ were obtained at various elevations and several cross sections along the roller. Note an exception: the correlation between the horizontal and vertical roller surface motions R_{xy} was independent of the vertical position of the probes. The results in terms of $(R_{xy})_{max}$ were separately shown in Chapter 3. For the other correlation functions, the vertical distributions of maximum/minimum correlation coefficients were recorded. The results showed some different trends in different flow regions, implying complicated flow regimes in the roller. They were discussed in Chapter 5. This appendix presents all vertical profiles of the maximum correlation coefficients for R_{xc} and R_{yc} (Section D.1), R_{xp} and R_{yp} (Section D.2) and R_{pc} (Section D.3). The time-averaged void fraction profiles are also plotted for reference, and the relative pressure fluctuations to the maximum pressure p'/P_{max} is included for $(R_{pc})_{max}$. The data related to the instantaneous pressure were restricted to the turbulent shear layer because the pressure measurements were only validated in the positive velocity flow region. Some data points were omitted when no clear correlation coefficient maximum was observed.

The experiments were conducted for four inflow Froude numbers Fr_1 = 3.8, 5.1, 7.5 and 8.5 with a constant inflow depth d_1 = 0.02 m and corresponding Reynolds numbers from 3.5×10^4 to 8.0×10^4. The longitudinal positions of the cross sections were $(x-x_1)/d_1$ = 4.15, 8.35, 12.5 and 18.75. More details on flow conditions were reported in Chapter 2.

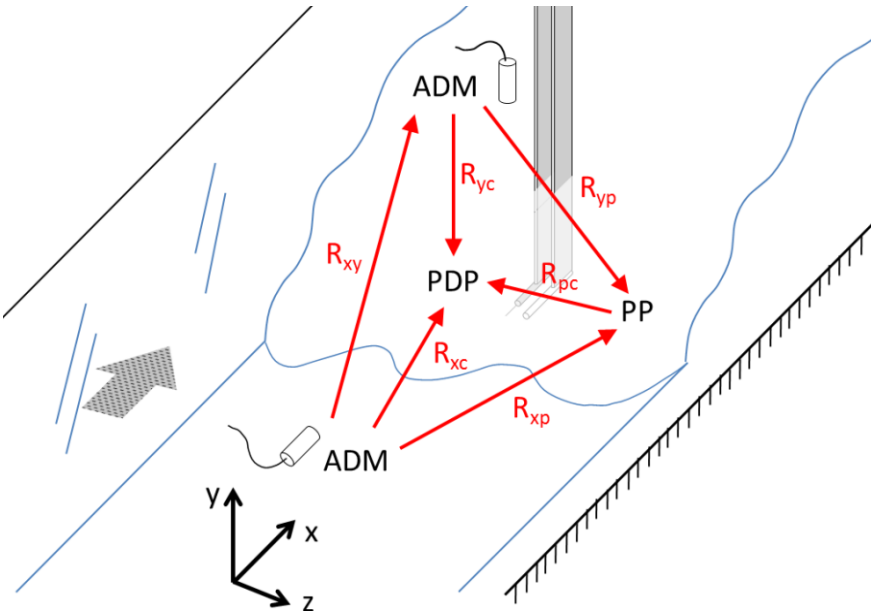

Fig D-1 - Sketch of instrumental setup and correlation coefficients - Flow direction from bottom left to top right

Notation

C	time-averaged void fraction;
c	instantaneous void fraction;
d_1	inflow depth;
Fr_1	inflow Froude number;
P	time-averaged total pressure;
P_{max}	maximum time-averaged total pressure;
p	instantaneous total pressure;
p'	standard deviation of total pressure fluctuations measured with pressure probe;
R_{max}	maximum normalised correlation coefficient;
$(R_{xy})_{max}$	maximum correlation coefficient between the horizontal jump toe oscillations & vertical free surface fluctuations;
$(R_{xc})_{max}$	maximum correlation coefficient between the horizontal jump toe oscillations & instantaneous void fraction;
$(R_{yc})_{max}$	maximum correlation coefficient between the vertical free surface fluctuations & instantaneous void fraction;
$(R_{xp})_{max}$	maximum correlation coefficient between the horizontal jump toe oscillations & instantaneous total pressure;
$(R_{yp})_{max}$	maximum correlation coefficient between the vertical free surface fluctuations & instantaneous total pressure;

$(R_{pc})_{max}$ maximum correlation coefficient between the instantaneous void fraction & instantaneous total pressure;

x longitudinal position of probe;

x_1 longitudinal position of jump toe;

y vertical position of probe;

D.1. $(R_{xc})_{max}$ & $(R_{yc})_{max}$ - CORRELATION BETWEEN ROLLER SURFACE DEFORMATIONS AND INSTANTANEOUS VOID FRACTION

Fr_1 = 3.8

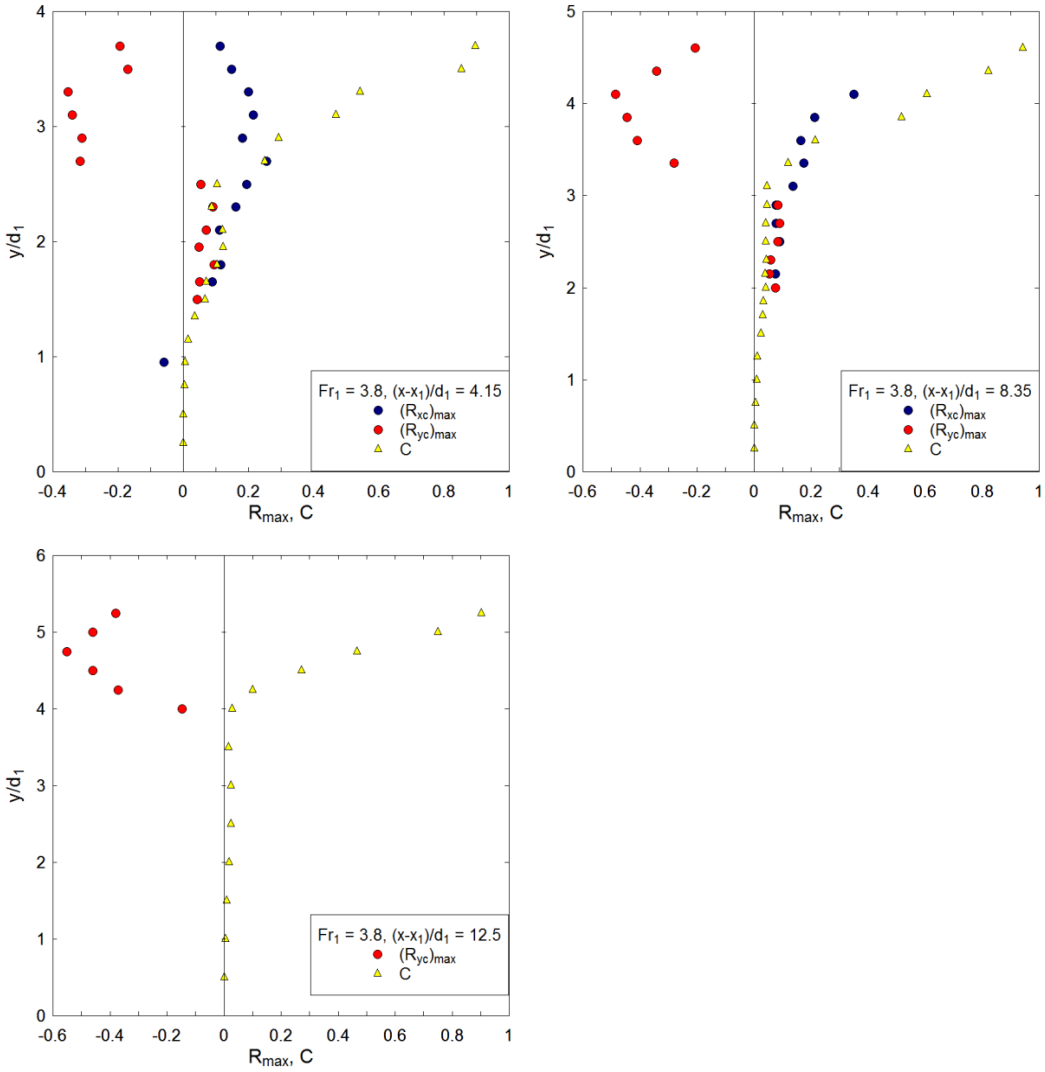

Fr_1 = 5.1

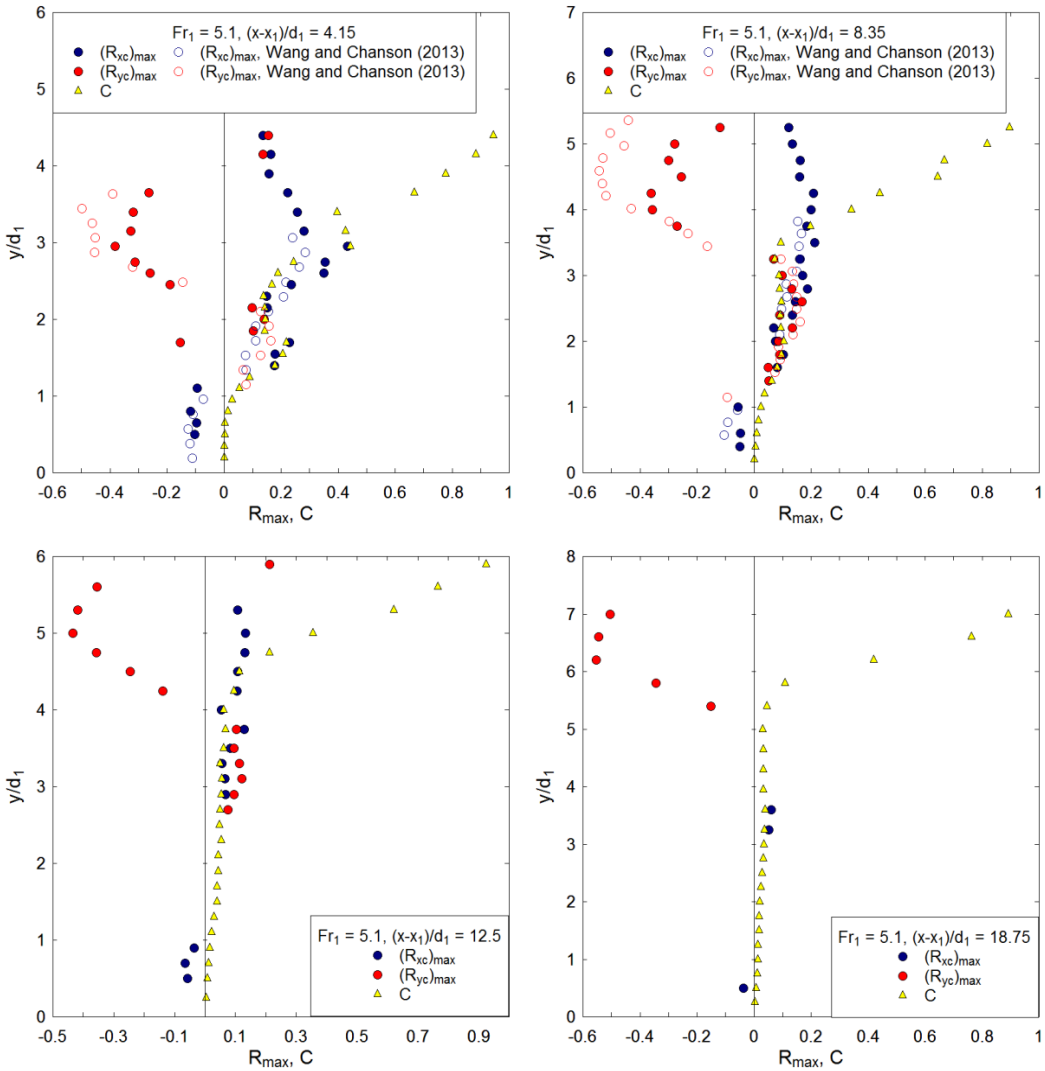
Fr1 = 5.1, (x-x1)/d1 = 4.15
(Rxc)max
(Ryc)max
C
(Rxc)max, Wang and Chanson (2013)
(Ryc)max, Wang and Chanson (2013)
Fr1 = 5.1, (x-x1)/d1 = 8.35
Fr1 = 5.1, (x-x1)/d1 = 12.5
Fr1 = 5.1, (x-x1)/d1 = 18.75
y/d1
Rmax, C

Fr_1 = 7.5

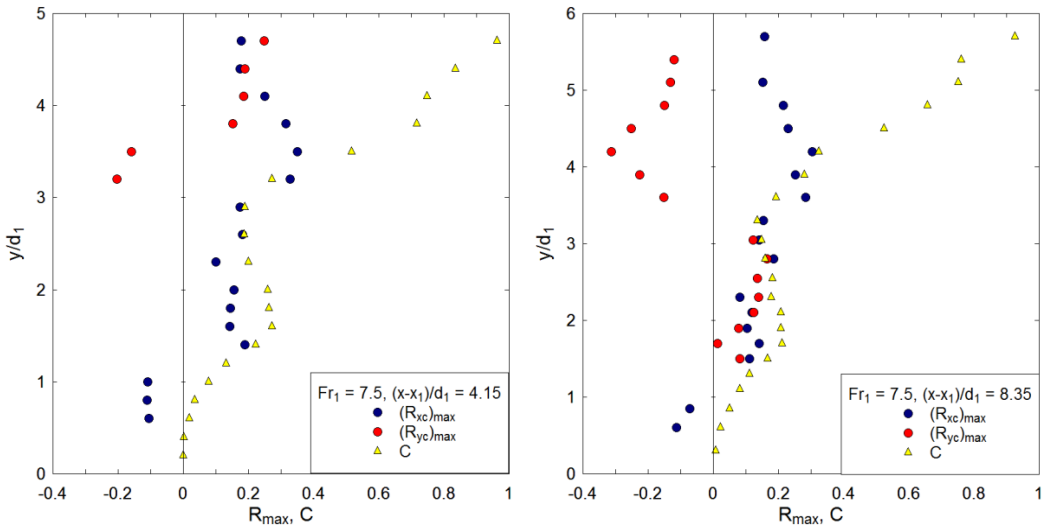
Fr1 = 7.5, (x-x1)/d1 = 4.15
(Rxc)max
(Ryc)max
C
Fr1 = 7.5, (x-x1)/d1 = 8.35
y/d1
Rmax, C

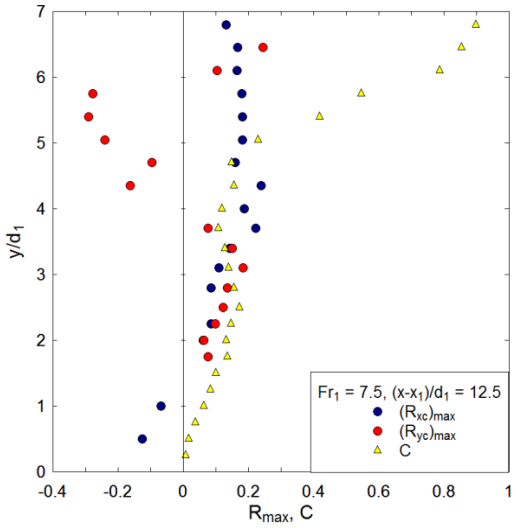

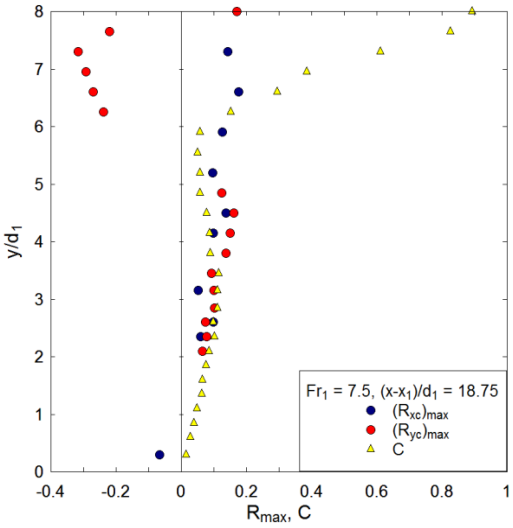

$\underline{Fr_1} = 8.5$

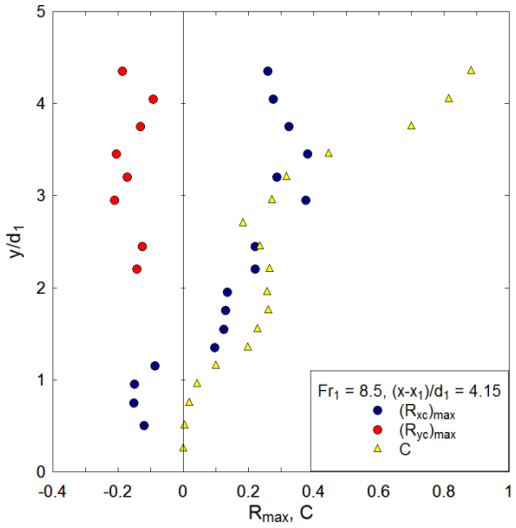

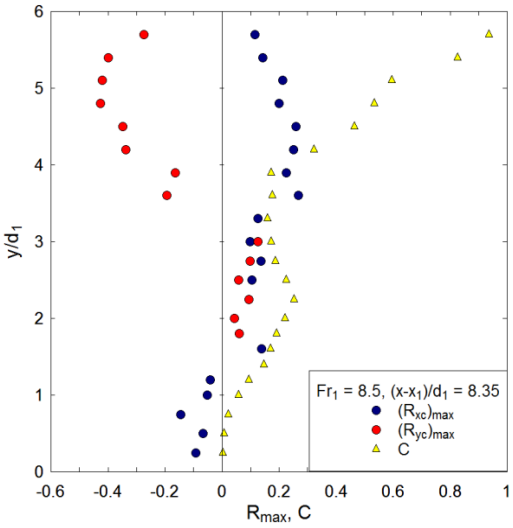

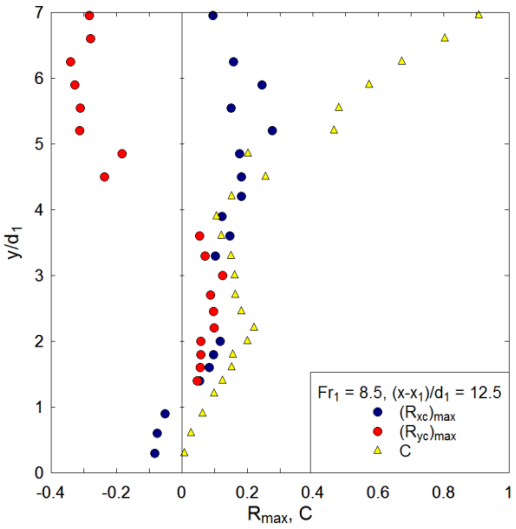

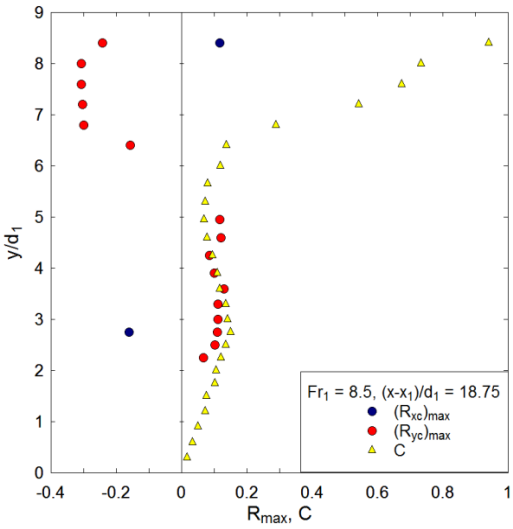

D.2. $(R_{xp})_{max}$ & $(R_{yp})_{max}$ - CORRELATION BETWEEN ROLLER SURFACE DEFORMATIONS AND INSTANTANEOUS TOTAL PRESSURE

$\underline{Fr_1 = 3.8}$

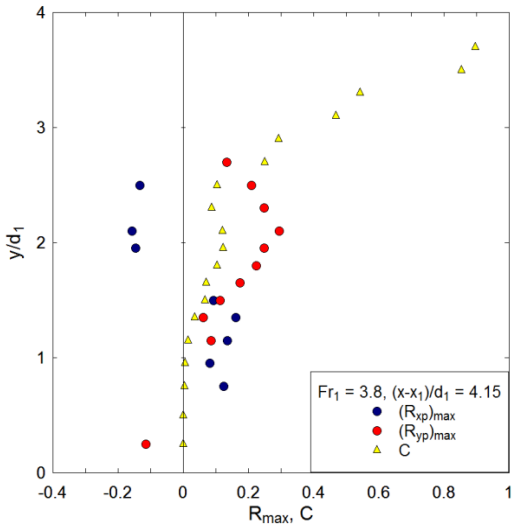

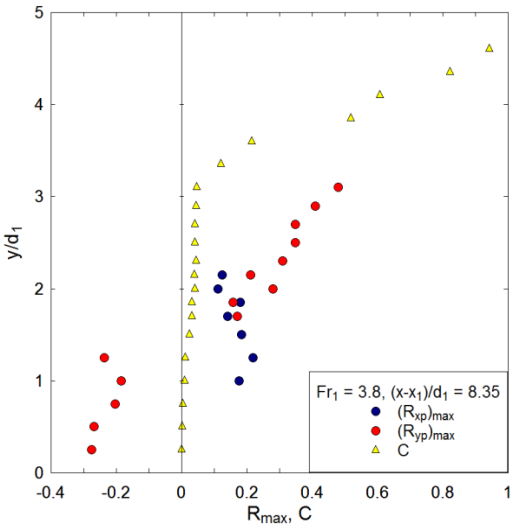

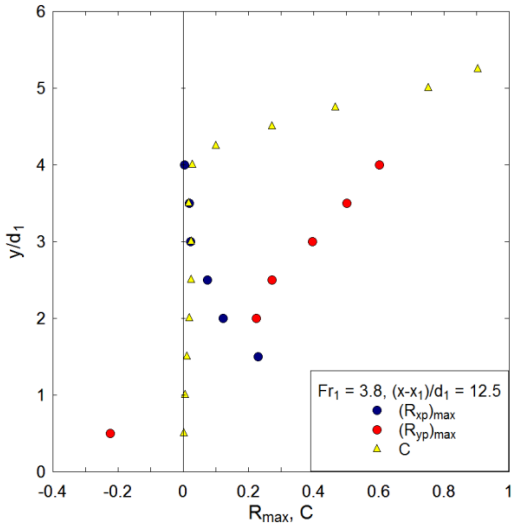

$\underline{Fr_1 = 5.1}$

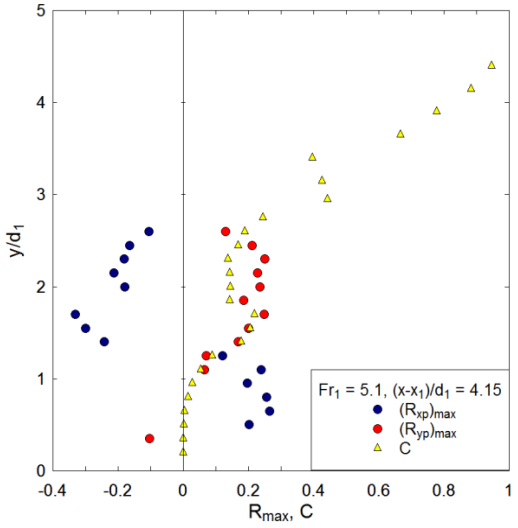

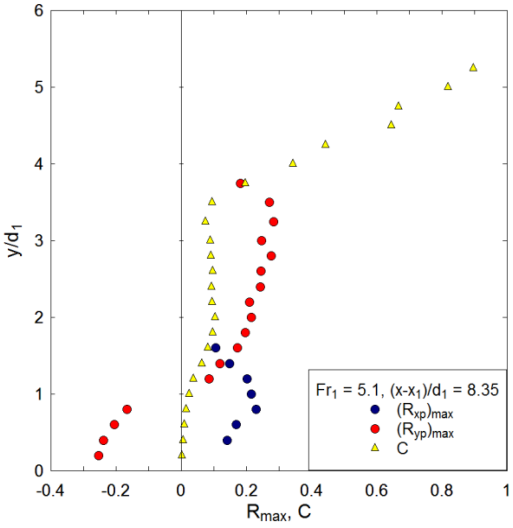

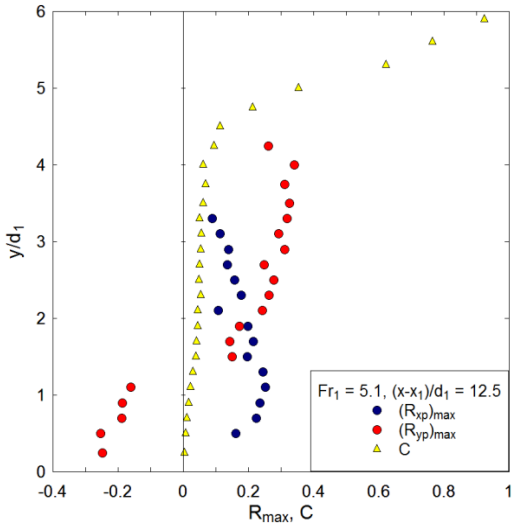

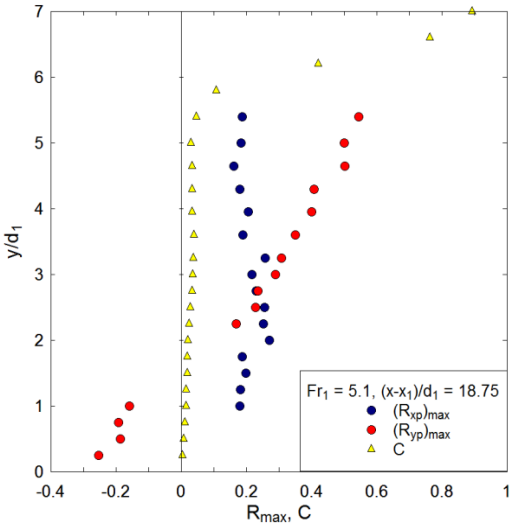

$\underline{Fr_1}$ = 7.5

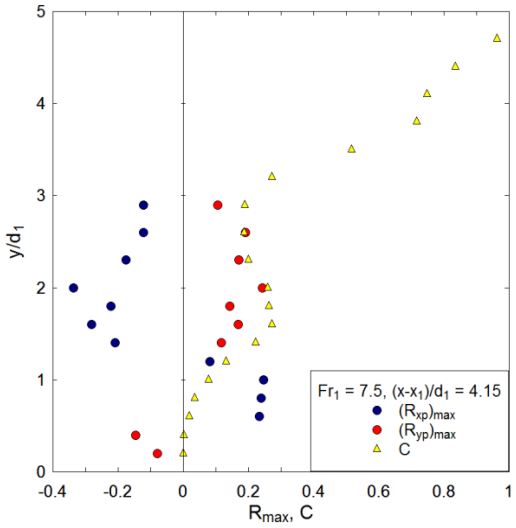

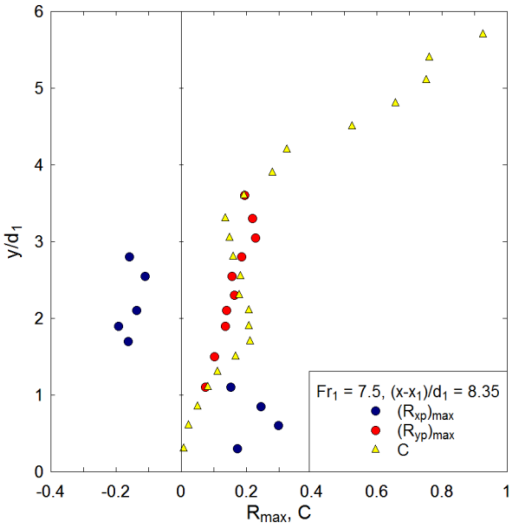

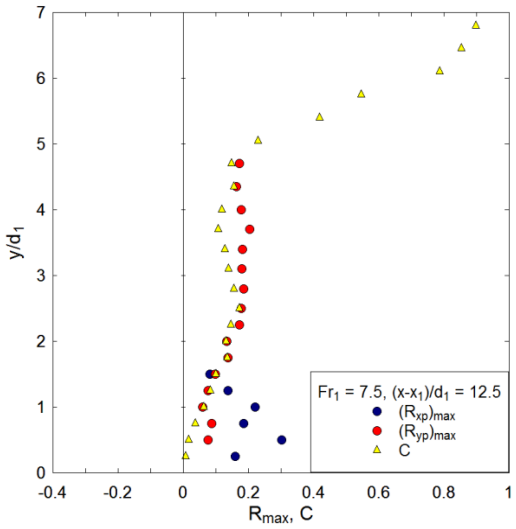

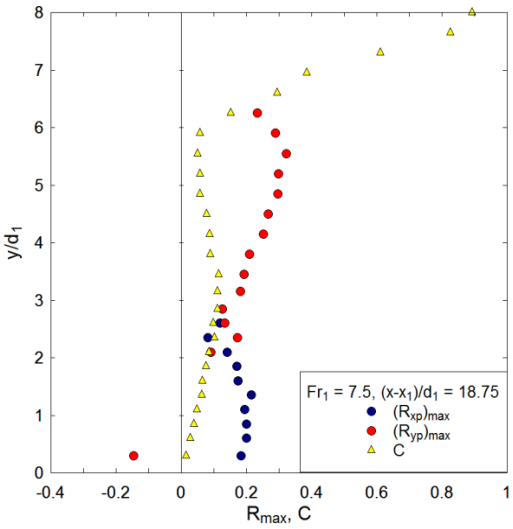

$Fr_1 = 8.5$

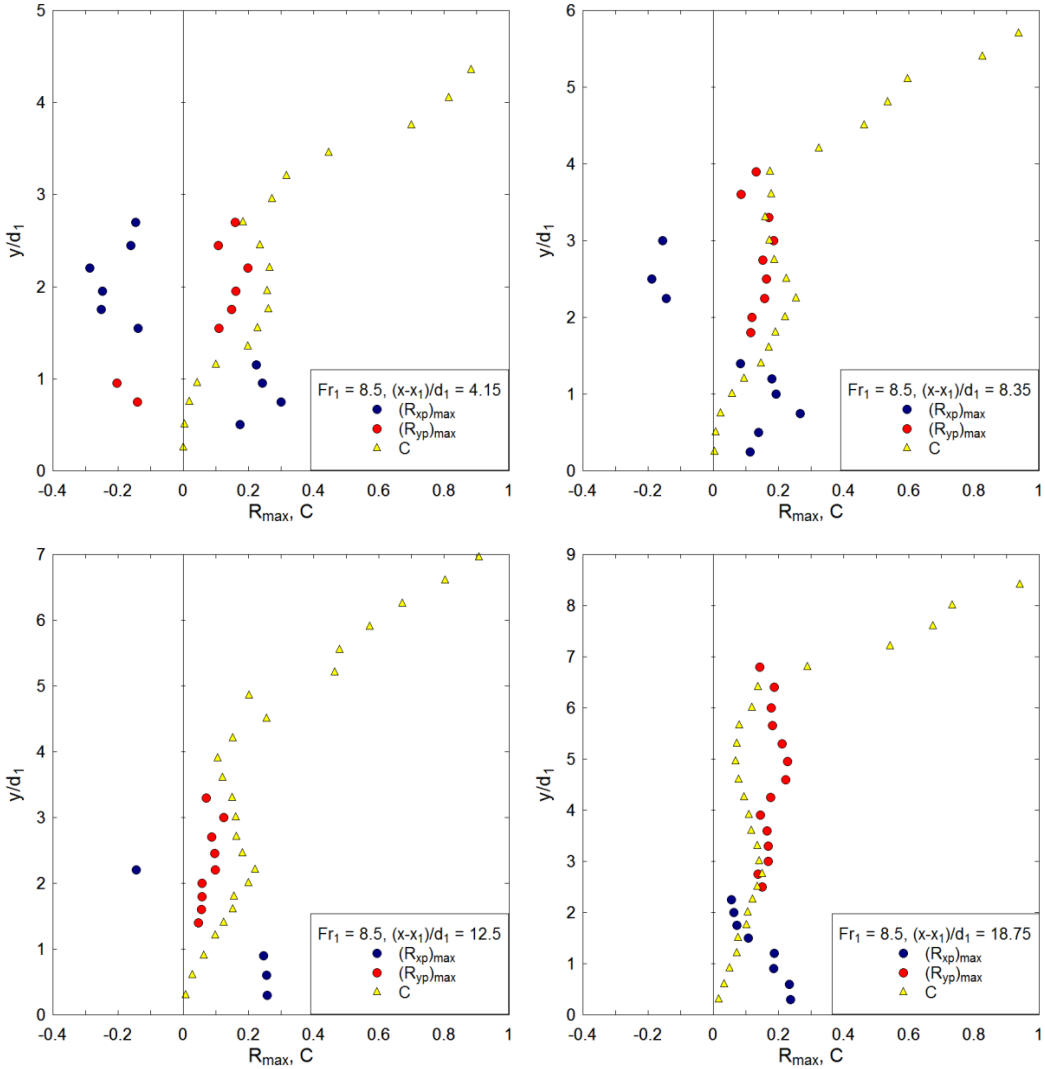
y/d1
Rmax, C
Fr1 = 8.5, (x-x1)/d1 = 4.15
(Rxp)max
(Ryp)max
C
Fr1 = 8.5, (x-x1)/d1 = 8.35
Fr1 = 8.5, (x-x1)/d1 = 12.5
Fr1 = 8.5, (x-x1)/d1 = 18.75

D.3. $(R_{pc})_{max}$ - CORRELATION BETWEEN INSTANTANEOUS TOTAL PRESSURE AND INSTANTANEOUS VOID FRACTION

Fr_1 = 3.8

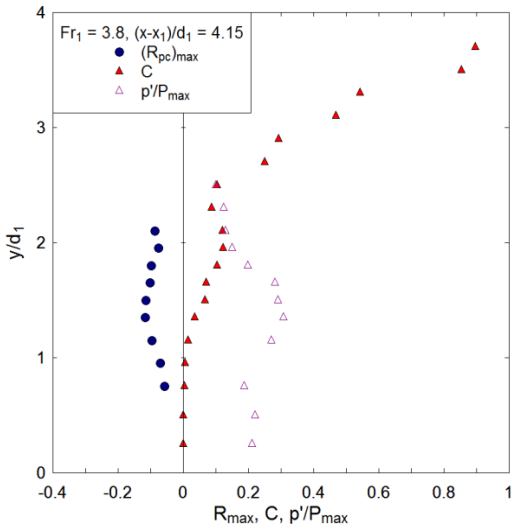

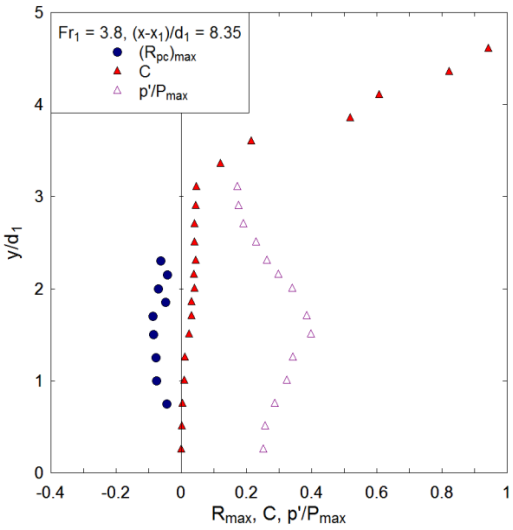

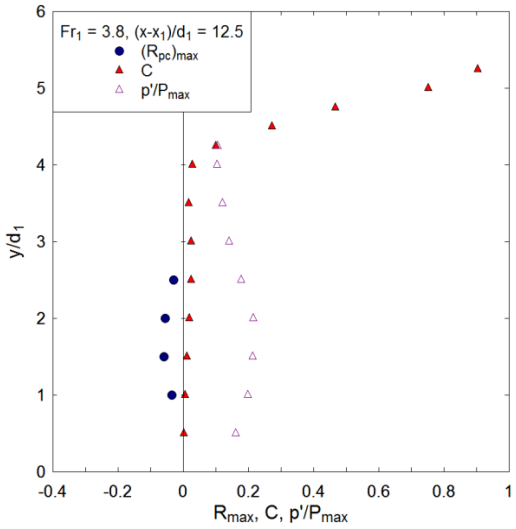

Fr_1 = 5.1

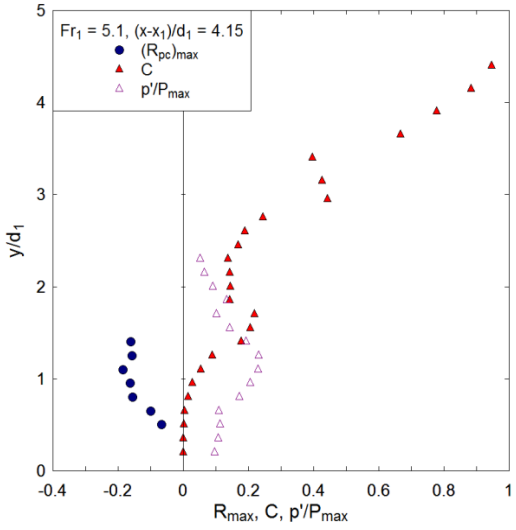

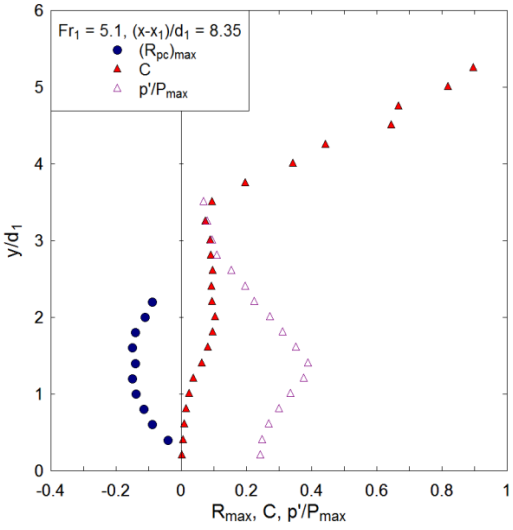

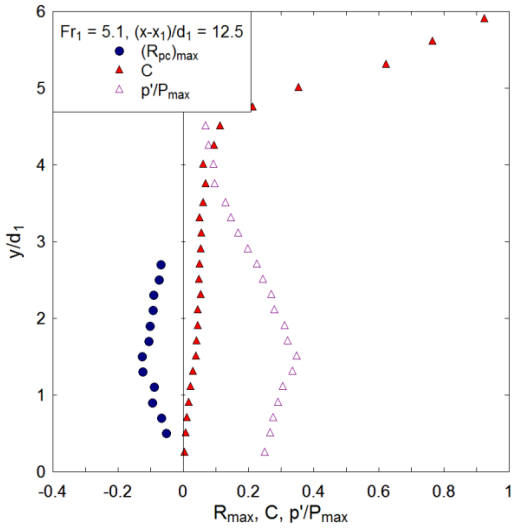

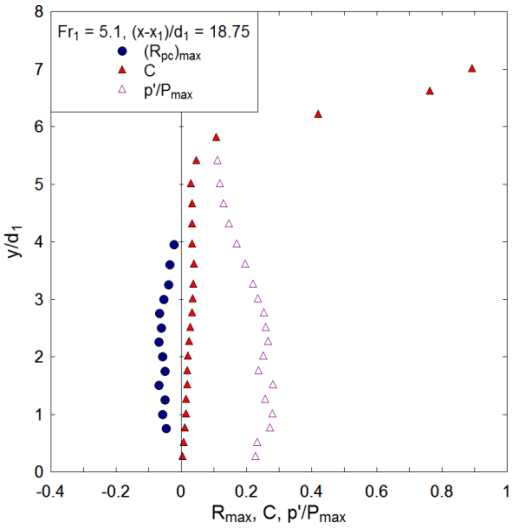

$\underline{Fr_1 = 7.5}$

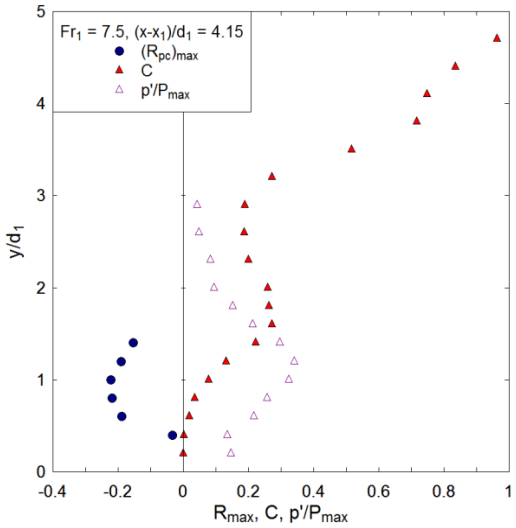

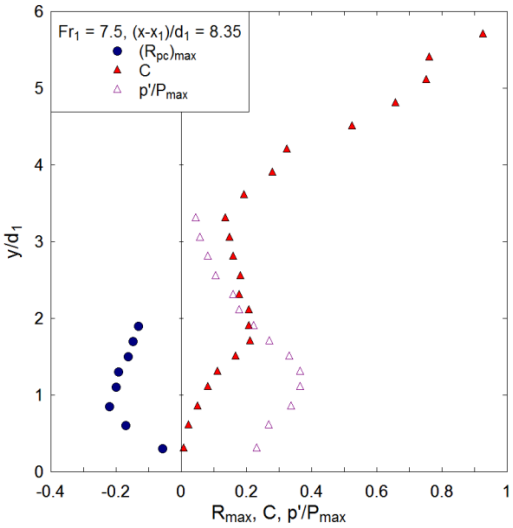

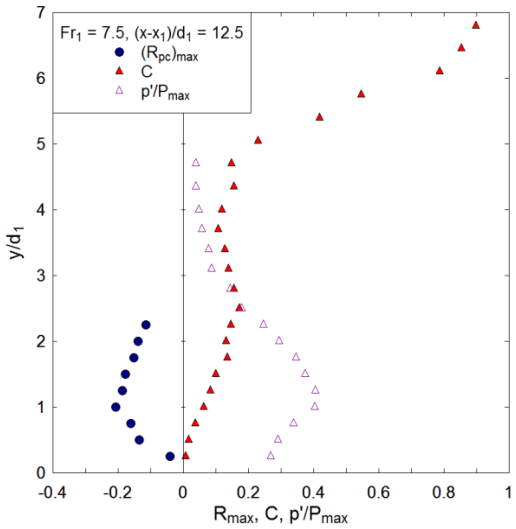

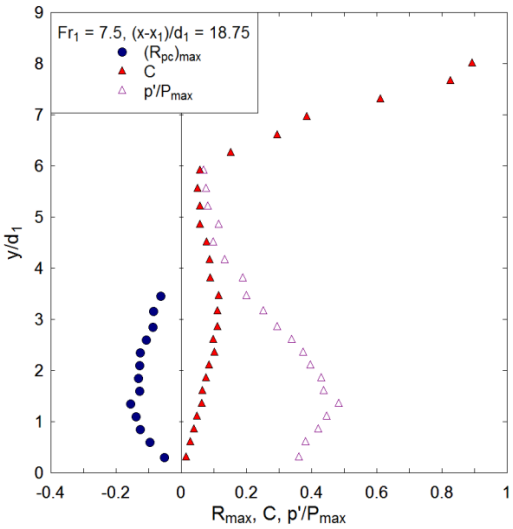

Fr_1 = 8.5

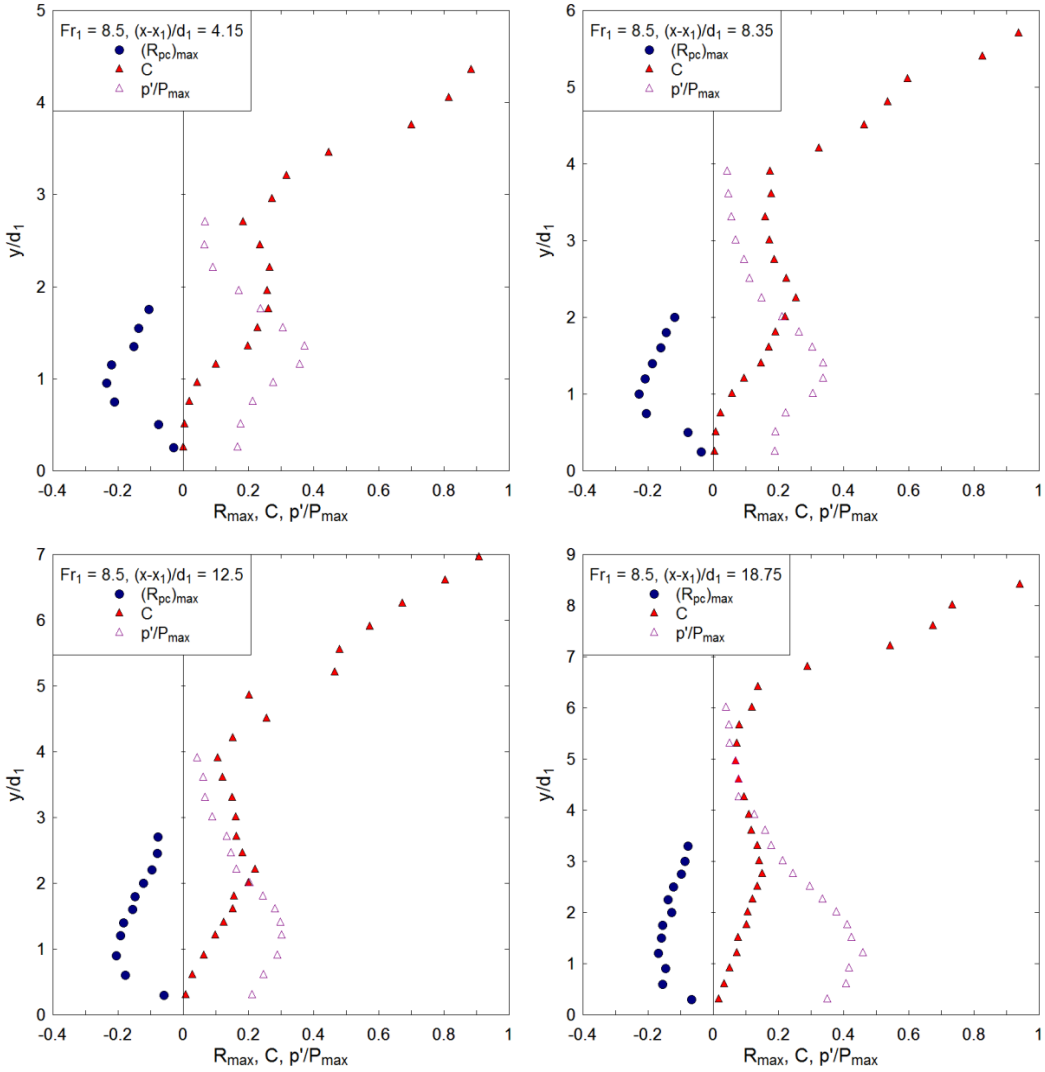
Fr1 = 8.5, (x-x1)/d1 = 4.15
(Rpc)max
C
p'/Pmax
y/d1
Rmax, C, p'/Pmax
Fr1 = 8.5, (x-x1)/d1 = 8.35
(Rpc)max
C
p'/Pmax
y/d1
Rmax, C, p'/Pmax
Fr1 = 8.5, (x-x1)/d1 = 12.5
(Rpc)max
C
p'/Pmax
y/d1
Rmax, C, p'/Pmax
Fr1 = 8.5, (x-x1)/d1 = 18.75
(Rpc)max
C
p'/Pmax
y/d1
Rmax, C, p'/Pmax

APPENDIX E. FREE SURFACE PROFILE AND FLUCTUATIONS

The water level fluctuations above the jump roller were measured with a series of acoustic displacement meters along the channel centreline. Depending upon the longitudinal positions of the phase-detection and pressure probes, the positions of acoustic displacement meters covered a wide range of longitudinal positions $(x-x_1)/d_1$ ranging from 0.9 up to 39, where x_1 is the jump toe location and d_1 is the inflow depth. The instantaneous free surface elevations were recorded at 5 kHz for 180 s, although the specifications of the displacement meters indicated a 50 ms response time. The raw signals were treated with removal of erroneous spikes before the data statistics were calculated. The removed points accounted for less than 3% of total number of data points.

In this appendix, the calibration details and positions of displacement meters are summarised. Then the mean water elevation η and standard deviation η' data are summarised at each longitudinal position for all experiments. Results for identical flow conditions indicate multiple runs for checking and data consistency. The time-averaged water depths at the corresponding longitudinal positions outlined the mean free surface profile, while the standard deviations of water level signals characterised the turbulent fluctuations in the roller free-surface.

Notation

d_1 inflow depth;
Fr_1 inflow Froude number;
Q flow rate;
Re Reynolds number;
V voltage output of acoustic displacement meters;
x longitudinal position;
x_1 longitudinal position of jump toe;
η mean water elevation above the invert;
η_{inst} instantaneous water surface positions recorded with acoustic displacement meter;
η' standard deviation of water level fluctuations.

E.1. ACOUSTIC DISPLACEMENT METERS POSITIONS AND CALIBRATION DATA

Series	Profile	Sensor No.	Calibration relationship	x_1 (m)	Sensor orientation	y (m)
240713 $Fr_1 = 3.8$	1	0	$\eta_{inst} = 0.0281 \times V + 0.0674$	-0.23	Horizontal	0.05
		1	$\eta_{inst} = 0.0220 \times V + 0.0298$	0.083*	Vertical	0.286
		2	$\eta_{inst} = 0.0248 \times V + 0.0505$	0.283	Vertical	0.3065
		3	$\eta_{inst} = 0.0251 \times V + 0.0491$	0.433	Vertical	0.307
		4	$\eta_{inst} = 0.0249 \times V + 0.0498$	0.583	Vertical	0.365
240713 $Fr_1 = 3.8$	2	0	$\eta_{inst} = 0.0281 \times V + 0.0674$	-0.23	Horizontal	0.05
		1	$\eta_{inst} = 0.0220 \times V + 0.0298$	0.017	Vertical	0.268
		2	$\eta_{inst} = 0.0248 \times V + 0.0505$	0.167*	Vertical	0.3065
		3	$\eta_{inst} = 0.0251 \times V + 0.0491$	0.367	Vertical	0.307
		4	$\eta_{inst} = 0.0249 \times V + 0.0498$	0.632	Vertical	0.365
240713 $Fr_1 = 3.8$	3	0	$\eta_{inst} = 0.0281 \times V + 0.0674$	-0.23	Horizontal	0.05
		1	$\eta_{inst} = 0.0220 \times V + 0.0298$	0.090	Vertical	0.268
		2	$\eta_{inst} = 0.0248 \times V + 0.0505$	0.250*	Vertical	0.3065
		3	$\eta_{inst} = 0.0251 \times V + 0.0491$	0.450	Vertical	0.307
		4	$\eta_{inst} = 0.0249 \times V + 0.0498$	0.720	Vertical	0.365
150713 $Fr_1 = 5.1$	1	0	$\eta_{inst} = 0.0281 \times V + 0.0674$	-0.23	Horizontal	0.05
		1	$\eta_{inst} = 0.0220 \times V + 0.0298$	0.083*	Vertical	0.269
		2	$\eta_{inst} = 0.0248 \times V + 0.0505$	0.283	Vertical	0.3065
		3	$\eta_{inst} = 0.0251 \times V + 0.0491$	0.433	Vertical	0.307
		4	$\eta_{inst} = 0.0249 \times V + 0.0498$	0.613	Vertical	0.384
150713 $Fr_1 = 5.1$	2	0	$\eta_{inst} = 0.0281 \times V + 0.0674$	-0.23	Horizontal	0.05
		1	$\eta_{inst} = 0.0220 \times V + 0.0298$	0.017	Vertical	0.269
		2	$\eta_{inst} = 0.0248 \times V + 0.0505$	0.167*	Vertical	0.3065
		3	$\eta_{inst} = 0.0251 \times V + 0.0491$	0.437	Vertical	0.307
		4	$\eta_{inst} = 0.0249 \times V + 0.0498$	0.637	Vertical	0.384
160713 $Fr_1 = 5.1$	3	0	$\eta_{inst} = 0.0281 \times V + 0.0674$	-0.23	Horizontal	0.05
		1	$\eta_{inst} = 0.0220 \times V + 0.0298$	0.090	Vertical	0.269
		2	$\eta_{inst} = 0.0248 \times V + 0.0505$	0.250*	Vertical	0.3065
		3	$\eta_{inst} = 0.0251 \times V + 0.0491$	0.450	Vertical	0.307
		4	$\eta_{inst} = 0.0249 \times V + 0.0498$	0.730	Vertical	0.384
160713 $Fr_1 = 5.1$	4	0	$\eta_{inst} = 0.0281 \times V + 0.0674$	-0.23	Horizontal	0.05
		1	$\eta_{inst} = 0.0220 \times V + 0.0298$	0.090	Vertical	0.269
		2	$\eta_{inst} = 0.0248 \times V + 0.0505$	0.235	Vertical	0.3065
		3	$\eta_{inst} = 0.0251 \times V + 0.0491$	0.375*	Vertical	0.307
		4	$\eta_{inst} = 0.0249 \times V + 0.0498$	0.575	Vertical	0.365
170713 $Fr_1 = 7.5$	1	0	$\eta_{inst} = 0.0281 \times V + 0.0674$	-0.23	Horizontal	0.05
		1	$\eta_{inst} = 0.0220 \times V + 0.0298$	0.083*	Vertical	0.269
		2	$\eta_{inst} = 0.0248 \times V + 0.0505$	0.283	Vertical	0.3065
		3	$\eta_{inst} = 0.0251 \times V + 0.0491$	0.483	Vertical	0.307
		4	$\eta_{inst} = 0.0249 \times V + 0.0498$	0.733	Vertical	0.365

170713 Fr_1 = 7.5	2	0	η_{inst} = 0.0281×V+0.0674	-0.23	Horizontal	0.05
		1	η_{inst} = 0.0220×V+0.0298	0.017	Vertical	0.269
		2	η_{inst} = 0.0248×V+0.0505	0.167*	Vertical	0.3065
		3	η_{inst} = 0.0251×V+0.0491	0.417	Vertical	0.307
		4	η_{inst} = 0.0249×V+0.0498	0.667	Vertical	0.365
180713 Fr_1 = 7.5	3	0	η_{inst} = 0.0281×V+0.0674	-0.23	Horizontal	0.05
		1	η_{inst} = 0.0220×V+0.0298	0.090	Vertical	0.286
		2	η_{inst} = 0.0248×V+0.0505	0.250*	Vertical	0.3065
		3	η_{inst} = 0.0251×V+0.0491	0.500	Vertical	0.307
		4	η_{inst} = 0.0249×V+0.0498	0.750	Vertical	0.365
180713 Fr_1 = 7.5	4	0	η_{inst} = 0.0281×V+0.0674	-0.23	Horizontal	0.05
		1	η_{inst} = 0.0220×V+0.0298	0.090	Vertical	0.286
		2	η_{inst} = 0.0248×V+0.0505	0.230	Vertical	0.3065
		3	η_{inst} = 0.0251×V+0.0491	0.375*	Vertical	0.307
		4	η_{inst} = 0.0249×V+0.0498	0.625	Vertical	0.365
230713 Fr_1 = 8.5	1	0	η_{inst} = 0.0281×V+0.0674	-0.23	Horizontal	0.05
		1	η_{inst} = 0.0220×V+0.0298	0.083*	Vertical	0.286
		2	η_{inst} = 0.0248×V+0.0505	0.283	Vertical	0.3065
		3	η_{inst} = 0.0251×V+0.0491	0.483	Vertical	0.307
		4	η_{inst} = 0.0249×V+0.0498	0.783	Vertical	0.365
230713 Fr_1 = 8.5	2	0	η_{inst} = 0.0281×V+0.0674	-0.23	Horizontal	0.05
		1	η_{inst} = 0.0220×V+0.0298	0.017	Vertical	0.286
		2	η_{inst} = 0.0248×V+0.0505	0.167*	Vertical	0.3065
		3	η_{inst} = 0.0251×V+0.0491	0.367	Vertical	0.307
		4	η_{inst} = 0.0249×V+0.0498	0.667	Vertical	0.365
220713 Fr_1 = 8.5	3	0	η_{inst} = 0.0281×V+0.0674	-0.23	Horizontal	0.05
		1	η_{inst} = 0.0220×V+0.0298	0.090	Vertical	0.286
		2	η_{inst} = 0.0248×V+0.0505	0.250*	Vertical	0.3065
		3	η_{inst} = 0.0251×V+0.0491	0.450	Vertical	0.307
		4	η_{inst} = 0.0249×V+0.0498	0.710	Vertical	0.365
190713 Fr_1 = 8.5	4	0	η_{inst} = 0.0281×V+0.0674	-0.23	Horizontal	0.05
		1	η_{inst} = 0.0220×V+0.0298	0.090	Vertical	0.286
		2	η_{inst} = 0.0248×V+0.0505	0.230	Vertical	0.3065
		3	η_{inst} = 0.0251×V+0.0491	0.375*	Vertical	0.307
		4	η_{inst} = 0.0249×V+0.0498	0.625	Vertical	0.365

Note: *: position of the phase-detection probe and pressure probe.

E.2. FREE SURFACE PROFILES AND FLUCTUATIONS: MEAN WATER LEVEL AND STANDARD DEVIATIONS

Q = 0.0179 m^3/s, d_1 = 0.02 m, x_1 = 0.83 m, Fr_1 = 3.8, Re = 3.5×10^4

$x-x_1$	(m)	0.017	0.083	0.09	0.167	0.25	0.283	0.367	0.433
η	(m)	0.0471	0.0554	0.0676	0.0873	0.0992	0.0997	0.1057	0.1059
η'	(m)	0.00705	0.00639	0.00858	0.00618	0.00548	0.00426	0.00309	0.00312
$x-x_1$	(m)	0.45	0.583	0.632	0.72				
η	(m)	0.1050	0.1044	0.1030	0.1025				
η'	(m)	0.00268	0.00234	0.00216	0.00211				

Q = 0.0239 m^3/s, d_1 = 0.02 m, x_1 = 0.83 m, Fr_1 = 5.1, Re = 4.8×10^4

$x-x_1$	(m)	0.017	0.083	0.09	0.167	0.235	0.25	0.283	0.375
η	(m)	0.0543	0.0498	0.0630	0.1024	0.1045	0.1129	0.1146	0.1315
η'	(m)	0.01119	0.01027	0.01100	0.00998	0.01096	0.01046	0.00836	0.00824
$x-x_1$	(m)	0.433	0.437	0.45	0.575	0.613	0.637	0.73	
η	(m)	0.1324	0.1390	0.1395	0.1369	0.1365	0.1385	0.1396	
η'	(m)	0.00718	0.00631	0.00652	0.00564	0.00533	0.00441	0.00420	

Q = 0.0347 m^3/s, d_1 = 0.02 m, x_1 = 0.83 m, Fr_1 = 7.5, Re = 6.8×10^4

$x-x_1$	(m)	0.017	0.083	0.09	0.167	0.23	0.25	0.283	0.375
η	(m)	0.0442	0.0478	0.0749	0.1065	0.1186	0.1190	0.1261	0.1465
η'	(m)	0.01176	0.01165	0.01351	0.01365	0.01499	0.01522	0.01286	0.01578
$x-x_1$	(m)	0.417	0.483	0.5	0.625	0.667	0.733	0.75	
η	(m)	0.1553	0.1572	0.1725	0.1930	0.1950	0.1956	0.1991	
η'	(m)	0.01449	0.01392	0.01350	0.01074	0.00997	0.00969	0.00935	

Q = 0.0397 m^3/s, d_1 = 0.02 m, x_1 = 0.83 m, Fr_1 = 8.5, Re = 8.0×10^4

$x-x_1$	(m)	0.017	0.083	0.09	0.167	0.23	0.25	0.283	0.367
η	(m)	0.0514	0.0639	0.0670	0.0898	0.1104	0.1112	0.1299	0.1416
η'	(m)	0.00909	0.01286	0.01351	0.01443	0.01428	0.01564	0.01434	0.01526
$x-x_1$	(m)	0.375	0.45	0.483	0.625	0.667	0.71	0.783	
η	(m)	0.1392	0.1581	0.1640	0.1937	0.2006	0.2056	0.2153	
η'	(m)	0.01464	0.01444	0.01489	0.01498	0.01544	0.01419	0.01336	

APPENDIX F. PHOTOGRAPHIC OBSERVATIONS OF EXPERIMENTS

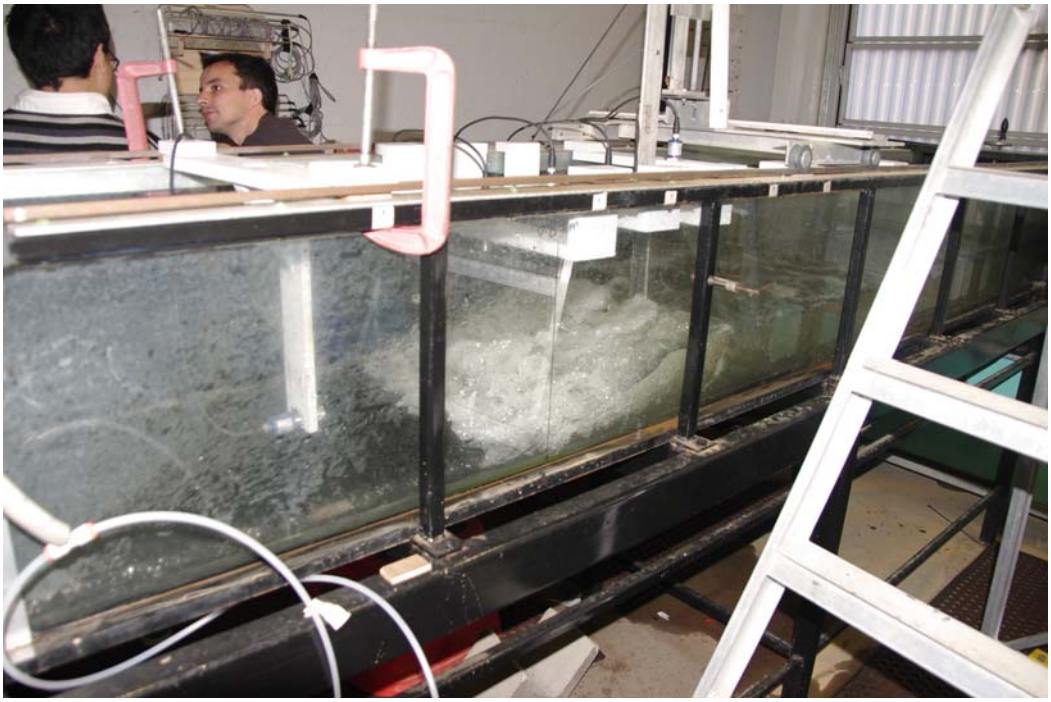

(A) General view

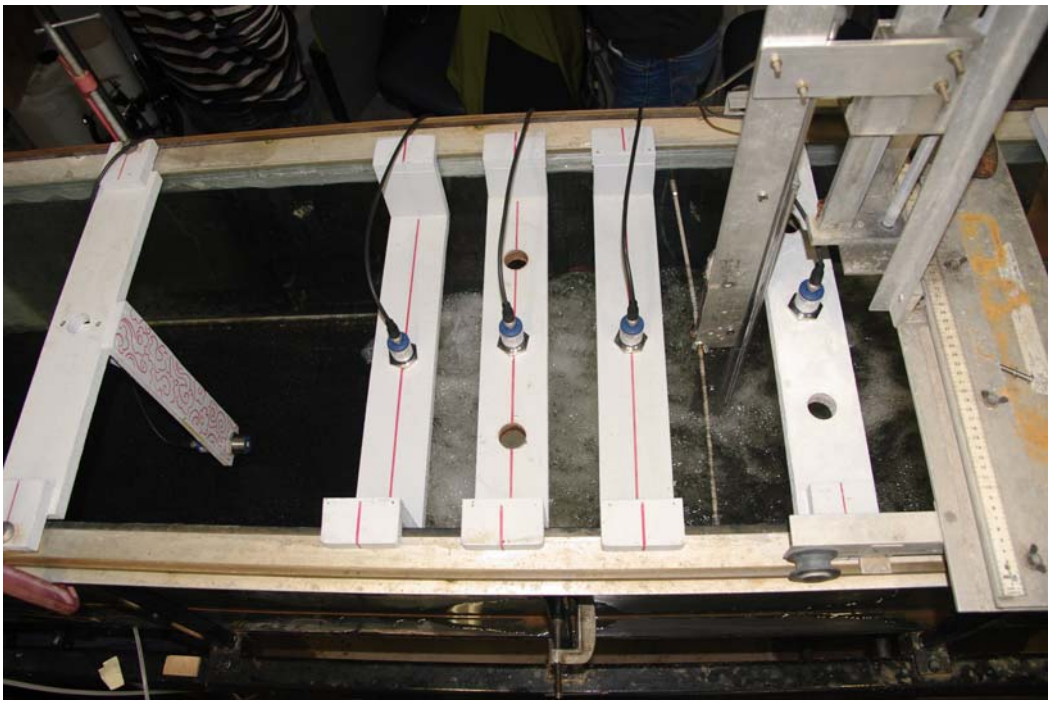

(B) Top view with acoustic displacement meters, and phase-detection probe and pressure probe mounted side by side

Fig. F-1 - Hydraulic jump experiment - Flow conditions: Q = 0.0241 m^3/s, d_1 = 0.020 m, x_1 = 0.83 m, Fr_1 = 5.1, Re = 4.8×10^4, flow direction from left to right

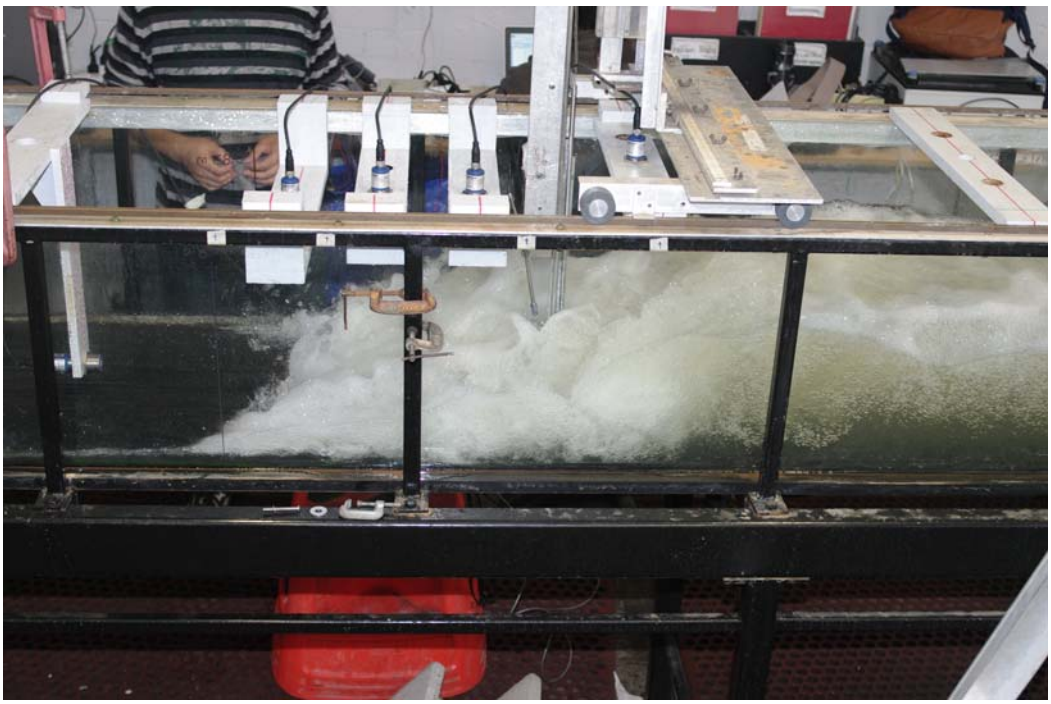

(A) Side view, flow direction from left to right

(B) Three-quarter view highlighting large air-water projection, flow direction from left to right

(C) Looking downstream, viewed from upstream of jump toe - Inset: details of air-water projection

Fig. F-2 - Hydraulic jump experiment - Flow conditions: Q = 0.0399 m^3/s, d_1 = 0.020 m, x_1 = 0.83 m, Fr_1 = 8.5, Re = 7.9×10^4 - Shutter speed: 1/80 s

(A) Side view, flow direction from left to right

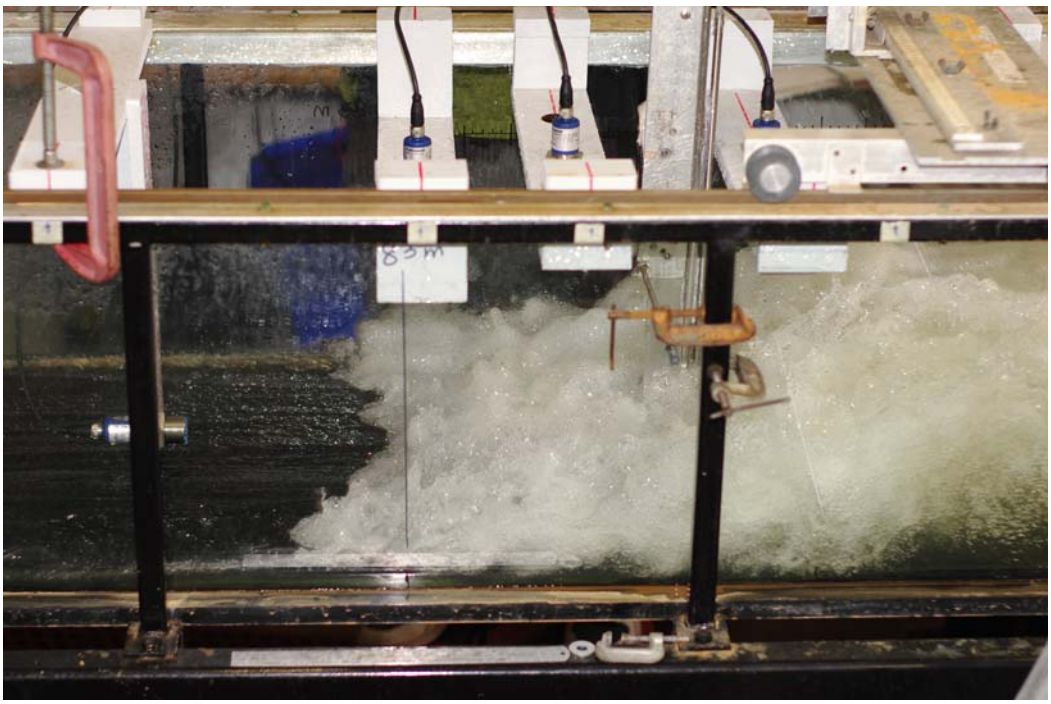

(B) Details of acoustic displacement meters and probes (shutter speed: 1/100 s)

(C) Looking downstream, viewed from upstream of jump toe -Shutter speed: 1/125 s (Left) and 1/100 s (Right)

Fig. F-3 - Hydraulic jump experiment - Flow conditions: Q = 0.0399 m^3/s, d_1 = 0.020 m, x_1 = 0.83 m, Fr_1 = 8.5, Re = 7.9×10^4

REFERENCES

ABDUL KHADER, M.H. and ELANGO, K. (1974). "Turbulent Pressure Field beneath a Hydraulic Jump." *Journal of Hydraulic Research*, Vol. 12, No. 4, pp 469-489.

AVERY, S.T., and NOVAK, P. (1978). "Oxygen Transfer at Hydraulic Structures." *Jl of Hyd. Div.*, ASCE, Vol. 104, No. HY11, pp. 1521-1540.

BELANGER, J.B. (1841). "Notes sur l'hydraulique". (Notes on hydraulic Engineering). *Ecole Royale des Ponts et Chaussées*, Paris, France, session 1841-1842, 223 pages (in French).

BEN MEFTAH, M., DE SERIO, F., MOSSA, M., and POLLIO, A. (2007). "Analysis of the Velocity Field in a Large Rectangular Channel with Lateral Shockwave." *Env. Fluid Mech.*, Vol., 7, No. 6, pp. 519-536 (DOI: 10.1007/s10652-007-9034-7).

BIDONE, G. (1819). "Le remou et sur la propagation des ondes." *Report to Académie Royale des Sciences de Turin*, séance 12 déc, vol. XXV, pp. 21-112 & 4 plates (in French).

BRATTBERG, T., CHANSON, H., and TOOMBES, L. (1998). "Experimental Investigations of Free-Surface Aeration in the Developing Flow of Two-Dimensional Water Jets." *Journal of Fluids Engineering*, Transactions ASME, Vol. 120, No. 4, pp. 738-744.

BROWN, G.L., and ROSHKO, A. (1971). "The Effect of Density Difference on the Turbulent Mixing Layer." *Proc. AGARD Specialist Meeting on Turbulent Shear Flows*, Advisory Group for Aeronautical Research and Development, London, UK, AGARD-OP-93, 23-1.

BROWN, G.L., and ROSHKO, A. (1974). "On density effects and large structure in turbulent mixing layers." *Journal of Fluid Mechanics*, Vol. 64, Part 4, pp. 775-816.

CHACHEREAU, Y. and CHANSON, H. (2011a). "Bubbly Flow Measurements in Hydraulic Jumps with Small Inflow Froude Numbers." *International Journal of Multiphase Flow*, Vol. 37, No. 6, pp 555-564.

CHACHEREAU, Y. and CHANSON, H. (2011b). "Free Surface Fluctuations and Turbulence in Hydraulic Jumps." *Experimental, Thermal and Fluid Science*, Vol. 35, No. 6, pp 896-909.

CHANSON, H. (1989). "Study of Air Entrainment and Aeration Devices." *Journal of Hydraulic Research*, IAHR, Vol. 27, No. 3, pp. 301-319.

CHANSON, H. (1995). "Air Entrainment in Two-Dimensional Turbulent Shear Flows with Partially Developed Inflow Conditions." *International Journal of Multiphase Flow*, Vol. 21, No. 6, pp 1107-1121.

CHANSON, H. (1997). "Air Bubble Entrainment in Free-Surface Turbulent Shear Flows." *Academic Press*, London, UK, 401 pages.

CHANSON, H. (2002). "Air-Water Flow Measurements with Intrusive Phase-Detection Probes. Can we Improve their Interpretation?" *Journal of Hydraulic Engineering*, Trans. ASCE, Vol. 128, No. 3, pp 252-255.

CHANSON, H. (2006). "Air Bubble Entrainment in Hydraulic Jumps. Similitude and Scale Effects." *Report No. CH57/05*, Dept. of Civil Engineering, The University of Queensland, Brisbane, Australia, 119 pages (ISBN 1864998423).

CHANSON, H. (2007). "Bubbly Flow Structure in Hydraulic Jump." *European Journal of Mechanics B/Fluids*, Vol. 26, No. 3, pp 367-384.

CHANSON, H. (2007b). "Dynamic Similarity and Scale Effects Affecting Air Bubble Entrainment in Hydraulic Jumps." *Proc. 6th International Conference on Multiphase Flow ICMF 2007*, Leipzig, Germany, July 9-13, M. SOMMERFIELD Editor, Session 7, Paper S7_Mon_B_S7_Mon_B_3, 11 pages (CD-ROM).

CHANSON, H. (2009). "Current Knowledge in Hydraulic Jumps and Related Phenomena. A Survey of Experimental Results." *European Journal of Mechanics B/Fluids*, Vol. 28, No. 2, pp 191-210.

CHANSON, H. (2009b). "Development of the Bélanger Equation and Backwater Equation by Jean-Baptiste Bélanger (1828)." *Journal of Hydraulic Engineering*, ASCE, Vol. 135, No. 3, pp. 159-163 (DOI: 10.1061/(ASCE)0733-9429(2009)135:3(159)).

CHANSON, H. (2010). "Convective Transport of Air Bubbles in Strong Hydraulic Jumps." *International Journal of Multiphase Flow*, Vol. 36, No. 10, pp 798-814.

CHANSON, H. (2011a). "Turbulent Shear-Stresses in Hydraulic Jumps and Decelerating Surges. An Experimental Study." *Earth Surface Processes and Landforms*, Vol. 36, No. 2, pp 180-189.

CHANSON, H. (2011b). "Bubbly Two-Phase Flow in Hydraulic Jumps at Large Froude Numbers" *Journal of Hydraulic Engineering*, ASCE, Vol. 137, No. 4, pp 451-460.

CHANSON, H. (2012). "Momentum Considerations in Hydraulic Jumps and Bores." *Journal of Irrigation and Drainage Engineering*, ASCE, Vol. 138, No. 4, pp. 382-385 (DOI 10.1061/(ASCE)IR.1943-4774.0000409).

CHANSON, H. (2013). "Tidal Bore Research: Field Works, Physical Modeling, CFD & More." *Proc. 35th IAHR World Congress*, Chengdu, China, 8-13 Sept., WANG Z., LEE, J.H.W., GAO, J., and CAO S. Editors, Invited lecture, Paper A12210, 11 pages.

CHANSON, H. (2013). "Hydraulics of Aerated Flows: Qui Pro Quo?" *Journal of Hydraulic Research*, IAHR, Invited Vision paper, Vol. 51, No. 3, pp. 223-243 (DOI: 10.1080/00221686.2013.795917).

CHANSON, H., AOKI, S., and HOQUE, A. (2006). "Bubble Entrainment and Dispersion in Plunging Jet Flows: Freshwater versus Seawater." *Journal of Coastal Research*, Vol. 22, No. 3, May, pp. 664-677 (DOI:10.2112/03-0112.1).

CHANSON, H., and BRATTBERG, T. (2000). "Experimental Study of the Air-Water Shear Flow in a Hydraulic Jump." *International Journal of Multiphase Flow*, Vol. 26, No. 4, pp 583-607.

CHANSON, H., and CAROSI, G. (2007). "Advanced Post-Processing and Correlation Analyses in High-Velocity Air-Water Flows." *Environmental Fluid Mechanics*, Vol. 7, No. 6, pp. 495-508 (DOI 10.1007/s10652-007-9038-3).

CHANSON, H., and CHACHEREAU, Y. (2013). "Scale Effects Affecting Two-Phase Flow Properties in Hydraulic Jumps with Small Inflow Froude Number." *Experimental, Thermal and Fluid Science*, Vol. 45, pp 234-242.

CHANSON, H., and GUALTIERI, C. (2008). "Similitude and Scale Effects of Air Entrainment in Hydraulic Jumps." *Journal of Hydraulic Research*, IAHR, Vol. 46, No. 1, pp 35-44.

CHANSON, H., and MONTES, J.S. (1995). "Characteristics of Undular Hydraulic Jumps. Experimental Apparatus and Flow Patterns." *Journal of Hydraulic Engineering*, ASCE, Vol. 121, No. 2, pp 129-144.

CHANSON, H., and TOOMBES, L. (2002). "Air-Water Flows down Stepped Chutes: Turbulence and Flow Structure Observations." *International Journal of Multiphase Flow*, Vol. 27, No. 11, pp. 1737-1761.

CUMMINGS, P.D., and CHANSON, H. (1997). "Air Entrainment in the Developing Flow Region of Plunging Jets. Part 1 Theoretical Development." *Journal of Fluids Engineering*, Transactions ASME, Vol. 119, No. 3, pp. 597-602.

EAD, S.A., and RAJARATNAM, N. (2002). "Hydraulic Jumps on Corrugated Beds." *Journal of Hydraulic Engineering*, ASCE, Vol. 128, No. 7, pp. 656-663 (DOI: 10.1061/(ASCE)0733-9429(2002)128:7(656)).

FELDER, S., and CHANSON, H. (2012). "Air-Water Flow Measurements in Instationary Free-Surface Flows: a Triple Decomposition Technique." *Hydraulic Model Report No. CH85/12*, School of Civil Engineering, The University of Queensland, Brisbane, Australia, 161 pages (ISBN 9781742720494).

ERVINE, D.A. (1998). "Air entrainment in hydraulic structures: A review." *Proc. Instn Civ. Engrs, Water, Maritime & Energy*, Vol. 130, pp. 142–153.

FELDER, S., and CHANSON, H. (2014). "Triple Decomposition Technique in Air–Water Flows: Application to Instationary Flows on a Stepped Spillway." *International Journal of Multiphase Flow*, Vol. 58, pp. 139-153 & 3 videos (DOI: 10.1016/j.ijmultiphaseflow.2013.09.006).

FIOROTTO, V. and RINALDO, A. (1992). "Fluctuating Uplift and Lining Design in Spillway Stilling Basins." *Journal of Hydraulic Engineering*, Vol. 118, No. 4, pp 578–596.

FOSS, J., PANTON, R., and YARIN, A. (2007). "Nondimensional representation of the boundary-value problem." In "Springer handbook of experimental fluid mechanics", *Springer*, Heidelberg, Germany, TROPEA, A. YARIN, and J. FOSS editors, Part A, Chapter 2, C, pp. 33–83.

GUALTIERI, C. and CHANSON, H. (2007). "Experimental Analysis of Froude Number Effect on Air Entrainment in the Hydraulic Jump." *Environmental Fluid Mechanics*, Vol. 5, pp 217-238.

GUALTIERI, C., and CHANSON, H. (2010). "Effect of Froude Number on Bubble Clustering in a Hydraulic Jump." *Journal of Hydraulic Research*, IAHR, Vol. 48, No. 4, pp. 504-508 (DOI: 10.1080/00221686.2010.491688).

HAGER, W.H. (1992). "Energy dissipators and hydraulic jumps." Water Science and Technology Library, Springer, 288 pages.

HAGER, W.H., BREMEN, R., and KAWAGOSHI, N. (1990). "Classical Hydraulic Jump : Length of Roller." *Jl of Hyd. Res.*, IAHR, Vol. 28, No. 5, pp. 591-608.

HENDERSON, F.M. (1966). "Open Channel Flow." *MacMillan Company*, New York, USA.

HOYT, J.W., and SELLIN, R.H.J. (1989). "Hydraulic Jump as 'Mixing Layer'." *Jl of Hyd. Engrg.*, ASCE, Vol. 115, No. 12, pp. 1607-1614.

KUCUKALI, S. and CHANSON, H. (2007). "Turbulence in Hydraulic Jumps: Experimental Measurements." *Research Report No. CH62/07*, Dept. of Civil Engineering, The University of Queensland, Brisbane, Australia, July, 40 pages (ISBN 9781864998825).

KUCUKALI, S., and CHANSON, H. (2008). "Turbulence Measurements in Hydraulic Jumps with Partially-Developed Inflow Conditions." *Experimental Thermal and Fluid Science*, Vol. 33, No. 1, pp. 41-53 (DOI: 10.1016/j.expthermflusci.2008.06.012).

LEANDRO, J., CARVALHO, R., CHACHEREAU, Y., and CHANSON, H. (2012). "Estimating Void Fraction in a Hydraulic Jump by Measurements of Pixel Intensity." *Experiments in Fluids*, Vol. 52, No. 5, Page 1307-1318 (DOI: 10.1007/s00348-011-1257-1).

LENNON, J.M., and HILL, D.F. (2006). "Particle Image Velocimetry Measurements of Undular and Hydraulic Jumps." *Jl of Hyd. Engrg.*, Vol. 132, No. 12, pp. 1283-1294.

LEUTHEUSSER, H.J., and SCHILLER, E.J. (1975). "Hydraulic Jump in a Rough Channel." *Water Power & Dam Construction*, Vol. 27, No. 5, pp. 186-191.

LIGGETT, J.A. (1994). "Fluid Mechanics." *McGraw-Hill*, New York, USA.

LIGHTHILL, J. (1978). "Waves in Fluids." *Cambridge University Press*, Cambridge, UK, 504 pages.

LIN, C., HSIEH, S.C., LIN, I.J., CHANG, K.A., and RAIKAR, R.V. (2012). "Flow property and self-similarity in steady hydraulic jumps." *Experiments in Fluids*, Vol. 53, pp. 1591–1616 (DOI 10.1007/s00348-012-1377-2).

LIU, M., RAJARATNAM, N. and ZHU, D.Z. (2004). "Turbulent Structure of Hydraulic Jumps of Low Froude Numbers." *Journal of Hydraulic Engineering*, Trans. ASCE, Vol. 130, No. 6, pp 511-520.

LONG, D., RAJARATNAM, N., STEFFLER, P.M. and SMY, P.R. (1991). "Structure of Flow in Hydraulic Jumps." *Journal of Hydraulic Research*, IAHR, Vol. 29, No. 2, pp 207-218.

LOPARDO, R.A., and HENNING, R.E. (1985). "Experimental Advances on Pressure Fluctuations beneath Hydraulic Jumps." *Proc. 21st IAHR Biennial Congress*, Melbourne, Australia, pp. 633-637.

LOPARDO, R.A. and ROMAGNOLI, M. (2009). "Pressure and Velocity Fluctuations in Stilling Basins." *Advances in Water Resources and Hydraulic Engineering*, Proc. 16th IAHR-APD Congress and 3rd IAHR International Symposium on Hydraulic Structures ISHS, Vol. VI, pp 2093-2098.

LOPARDO, R.A. (2013). "Extreme Velocity Fluctuations below Free Hydraulic Jumps." *Journal of Engineering*, Hindawi Publishing Corporation, Article ID 678065, 5 pages.

MADSEN, P.A. (1981). "A Model for a Turbulent Bore." *Ph.D. thesis*, Tech. Univ. of Denmark, Inst. of Hydrodyamics and Hyd. Eng., Copenhager, Denmark, 149 pages. (also *Series Paper No. 28*, Tech. Univ. of Denmark, Inst. of Hydrodyamics and Hyd. Eng., Copenhager, Denmark, 149 pages.)

MOSSA, M. and TOLVE, U. (1998). "Flow Visualization in Bubbly Two Phase Hydraulic Jumps." *Journal of Fluids Engineering*, ASME, Vol. 120, pp 160-165.

MOUAZE, D., MURZYN, F. and CHAPLIN, J.R. (2005). "Free Surface Length Scale Estimation in Hydraulic Jumps." *Journal of Fluids Engineering*, ASME, Vol. 127, pp 1191-1193.

MURZYN, F. and CHANSON, H. (2007). "Free-surface, Bubbly Flow and Turbulence Measurements in Hydraulic Jumps." *Research Report N° CH 63/07*, Department of Civil Engineering, The University of Queensland, Brisbane, Australia, 118 pages (ISBN 9781864998917).

MURZYN, F. and CHANSON, H. (2008). "Experimental Assessment of Scale Effects Affecting Two-Phase Flows Properties in Hydraulic Jumps." *Experiments in Fluids*, Vol. 45, No. 3, pp 513-521.

MURZYN, F. and CHANSON, H. (2009). "Free-Surface Fluctuations in Hydraulic Jumps: Experimental Observations." *Experimental, Thermal and Fluid Science*, Vol. 33, No. 7, pp 1055-1064.

MURZYN, F., MOUAZE, D. and CHAPLIN, J.R. (2005). "Optical Fibre Probe Measurements of Bubbly Flow in Hydraulic Jumps." *International Journal of Multiphase Flow*, Vol. 31, No. 1, pp 141-154.

MURZYN, F., MOUAZE, D. and CHAPLIN, J.R. (2007). "Air-water Interface Dynamic and Free Surface Features in Hydraulic Jumps", *Journal of Hydraulic Research*, IAHR, Vol. 45, No. 5, pp 679-685.

NOVAK, P., and CABELKA, J. (1981). "Models in Hydraulic Engineering. Physical Principles and Design Applications." *Pitman Publ.*, London, UK.

PAGLIARA, S., LOTTI, I., and PALERMO, M. (2008). "Hydraulic Jump on Rough Bed of Stream Rehabilitation Structures." *Jl of Hydro-Environment Research*, Vol. 2, No. 1, pp. 29-38.

RAJARATNAM, N. (1962). "An Experimental Study of Air Entrainment Characteristics of the Hydraulic Jump." *Journal of the Institution Engineers. India*, Vol. 42, No. 7, pp 247-273.

RAJARATNAM, N. (1965). "The Hydraulic Jump as a Wall Jet." *Journal of Hydraulic Division*, ASCE, Vol. 91, No. HY5, pp. 107-132. Discussion : Vol. 92, No. HY3, pp. 110-123 & Vol. 93, No. HY1, pp 74-76.

RESCH, F. J. and LEUTHEUSSER, H. J. (1972). "Reynolds Stress Measurements in Hydraulic Jumps." *Journal of Hydraulic Research*, Vol. 10, pp 409-429.

RESCH, F.J. and LEUTHEUSSER, H.J. (1972b). "Le Ressaut Hydraulique: mesure de Turbulence dans la Région Diphasique." ('The Hydraulic Jump: Turbulence Measurements in the Two-Phase Flow Region.'), *La Houille Blanche*, No. 4, pp 279-293 (in French).

RESCH, F.J., LEUTHEUSSER, H.J. and ALEMU, S. (1974). "Bubbly Two-phase Flow in Hydraulic Jump." *Journal of Hydraulic Engineering*, ASCE, Vol. 100, pp 137-149.

RICHARD, G. (2013). "Élaboration d'un modèle d'écoulements turbulents en faible profondeur: Application au ressaut hydraulique et aux trains de rouleaux." ('Elaboration of a model of turbulent shallow water flows: Application to the hydraulic jump and roll waves.') *Ph.D. thesis*, University of Aix-Marseille, Institut Universitaire des Systèmes Thermiques Industriels IUSTI, France, 212 pages (in French).

RICHARD, G.L., and GAVRILYUK, S.L. (2013). "The Classical Hydraulic Jump in a Model of Shear Shallow-Water Flows." *Journal of Fluid Mechanics*, Vol. 725, pp. 492-521.

ROACHE, P.J. (2009). "Perspective:Validation – what does it mean?" *Jl of Fluids Engineering*, ASME, Vol. 131, Paper 034503 (DOI: 10.1115/1.3077134).

ROUSE, H., SIAO, T.T. and NAGARATNAM, S. **(**1959). "Turbulence Characteristics of the Hydraulic Jump." Trans. ASCE, Vol. 124, pp 926-966.

TOOMBES, L. (2002). "Experimental Study of Air-Water Flow Properties on Low-Gradient Stepped Cascades." *Ph.D. thesis*, Dept of Civil Engineering, The University of Queensland, Brisbane, Australia.

VALIANI, A. (1997). "Linear and Angular Momentum Conservation in Hydraulic Jump." *Journal of Hydraulic Research*, IAHR, Vol. 35, No. 3, pp. 323-354.

VASILIEV, O.F., and BUKREYEV, V.I. (1967). "Statistical Characteristics of Pressure Fluctuations in the Region of Hydraulic Jumps. " *Proc. 12th IAHR Biennial Congres*s, Fort Collins, USA, Vol. 2, Paper B.1, 8 pages.

YAN, Z. and ZHOU, C. (2006). "Pressure Fluctuations beneath Spatial Hydraulic Jumps." *Journal of Hydrodynamics*, Vol. 18, No. 6, pp 723-726.

WANG, H. and CHANSON, H. (2013). "Free-Surface Deformation and Two-Phase Flow Measurements in Hydraulic Jumps." *Hydraulic Model Report N° CH91/13*, School of civil Engineering, The University of Queensland, Brisbane, Australia, 108 pages (ISBN 9781742720746).

WANG, H., and CHANSON, H. (2014). "Air Entrainment and Turbulent Fluctuations in Hydraulic Jumps." *Urban Water Journal* (DOI: 10.1080/1573062X.2013.847464). (Online First)

WOOD, I.R. (1991). "Air entrainment in free-surface flows." *IAHR Hydraulic Structures Design Manual No. 4*, Hydraulic Design Considerations, Balkema Publications, Rotterdam, The Netherlands.

WU, S., and RAJARATNAM, N. (1996). "Transition from Hydraulic Jump to Open Channel Flow." *Jl of Hyd. Engrg.*, ASCE, Vol. 122, No. 9, pp. 526-528.

ZHANG, G., WANG, H. and CHANSON, H. (2013). "Turbulence and Aeration in Hydraulic Jumps: Free-Surface Fluctuation and Integral Turbulent Scale Measurements." *Environmental Fluid Mechanics*, Vol. 13, No. 2, pp 189-204.

Bibliography

BELANGER, J.B. (1828). "Essai sur la Solution Numérique de quelques Problèmes Relatifs au Mouvement Permanent des Eaux Courantes." ("Essay on the Numerical Solution of Some Problems relative to Steady Flow of Water."), *Carilian-Goeury*, Paris, France (in French).

CHACHEREAU, Y. and CHANSON, H. (2010). "Free-Surface Turbulent Fluctuations and Air-Water Flow Measurements in Hydraulic Jumps with Small Inflow Froude Numbers." *Hydraulic*

Model Report N° CH 78/10, School of Civil Engineering, The University of Queensland, Brisbane, Australia, 133 pages (ISBN 9781742720036).

CHANSON, H. (1995). "Air Bubble Entrainment in Free-surface Turbulent Flows. Experimental Investigations." *Report CH46/95*, Dept. of Civil Engineering, University of Queensland, Australia, June, 368 pages (ISBN 0867766115).

CHANSON, H. (1997). "Air Bubble Entrainment in Open Channels. Flow Structure and Bubble Size Distributions." *International Journal of Multiphase Flow*, Vol. 23, No. 1, pp 193-203 (ISSN 03019322).

CHANSON, H. (2004). "The Hydraulics of Open Channel Flow: An Introduction." *Butterworth-Heinemann*, 2nd edition, Oxford, UK, 630 pages (ISBN 978 0 7506 5978 9).

CHANSON, H., and TOOMBES, L. (2002). "Energy Dissipation and Air Entrainment in Stepped Storm Waterway: Experimental Study." *Journal of Irrigation and Drainage Engineering*, ASCE, Vol. 128, No. 5, pp 305-315.

CHANSON, H., and TOOMBES, L. (2003). "Strong Interactions between Free-Surface Aeration and Turbulence in an Open Channel Flow." *Experimental, Thermal and Fluid Science*, Vol. 27, pp 525-535.

FELDER, S. (2013). "Air-Water Flow Properties on Stepped Spillways for Embankment Dams: Aeration, Energy Dissipation and Turbulence on Uniform, Non-Uniform and Pooled Stepped Chutes." *Ph.D. thesis*, School of Civil Engineering, The University of Queensland, Brisbane, Australia.

FELDER, S. and CHANSON, H. (2013). "Two-phase Flow Measurements in Un-Stationary Free-Surface Flows: a New Signal Decomposition Technique." *Proceedings of the 8th International Conference on Multiphase Flow*, ICMF 2013, Jeju, Korea, May 26-31, 2013, 10 pages (USB key).

GONZALEZ, C.A. (2005). "An Experimental Study of Free-Surface Aeration on Embankment Stepped Chutes." *Ph.D. thesis*, Department of Civil Engineering, The University of Queensland, Brisbane, Australia.

LUBIN, P. GLOCKNER, S., and CHANSON, H. (2009). "Numerical Simulation of Air Entrainment and Turbulence in a Hydraulic Jump." *Proc. Colloque SHF Modèles Physiques Hydrauliques: Outils Indispensables du XXIe Siècle?*, Société Hydrotechnique de France, Lyon, France, 24-25 Nov., pp. 109-114.

RAJARATNAM, N. (1967). "Hydraulic Jumps." *Advances in Hydroscience*, Ed. V.T. CHOW, Academic Press, New York, USA, Vol. 4, pp. 197-280.

RAJARATNAM, N. (1968). "Hydraulic Jumps on Rough Beds." *Trans. Engrg. Institute of Canada*, Vol. 11, No. A-2, May, pp. I-VIII.

RAJARATNAM, N. (1976). "Turbulent Jets." *Elsevier Scientific*, Development in Water Science, 5, New York, USA.

STREETER, V.L. and WYLIE, E.B. (1979). "Fluid Mechanics." New-York, MacGraw-Hill Book Company (ISBN 0070622329).

THANDAVESWARA, B.S. (1974)." Self Aerated Flow Characteristics in Developing Zones and in Hydraulic Jumps." *Ph.D. thesis*, Dept. of Civil Engrg., Indian Institute of Science, Bangalore, India, 399 pages.

WANG, H., and CHANSON, H. (2013). "Two-Phase Flow Properties and Free-Surface Deformations in Hydraulic Jumps." *Proc. 8th International Conference on Multiphase Flow ICMF 2013*, Jeju, Korea, 26-31 May, Paper ICMF2013-1079, 9 pages (USB key).

Internet bibliography

Air entrainment and flow aeration in open channel flow	{http://www.uq.edu.au/~e2hchans/self_aer.html}

Open Access Repositories

OAIster	{http://www.oaister.org/}
UQeSpace	{http://espace.library.uq.edu.au/}

Bibliographic reference of the Report CH95/14

The Hydraulic Model research report series CH is a refereed publication published by the School of Civil Engineering at the University of Queensland, Brisbane, Australia.

The bibliographic reference of the present report is:

WANG, H, MURZYN, F., and D., CHANSON, H. (2014). "Pressure, Turbulence and Two-Phase Flow Measurements in Hydraulic Jumps." *Hydraulic Model Report No. CH95/14*, School of Civil Engineering, The University of Queensland, Brisbane, Australia, 154 pages (ISBN 9781742721064).

The Report CH95/14 is available, in the present form, as a PDF file on the Internet at UQeSpace:

http://espace.library.uq.edu.au/

It is listed at:

http://espace.library.uq.edu.au/list/author_id/193/

HYDRAULIC MODEL RESEARCH REPORT CH

The Hydraulic Model Report CH series is published by the School of Civil Engineering at the University of Queensland. Orders of any reprint(s) of the Hydraulic Model Reports should be addressed to the School Secretary.

School Secretary, School of Civil Engineering, The University of Queensland
Brisbane 4072, Australia - Tel.: (61 7) 3365 3619 - Fax : (61 7) 3365 4599
Url: http://www.eng.uq.edu.au/civil/ Email: enquiries@civil.uq.edu.au

Report CH	**Unit price**	Quantity	**Total price**
WANG, H, MURZYN, F., and D., CHANSON, H. (2014). "Pressure, Turbulence and Two-Phase Flow Measurements in Hydraulic Jumps." Hydraulic Model Report No. CH95/14, School of Civil Engineering, The University of Queensland, Brisbane, Australia, 154 pages (ISBN 97817427206169781742721064).	AUD$60.00		
REUNGOAT, D., CHANSON, H., and KEEVIL, C. (2014). "Turbulence, Sedimentary Processes and Tidal Bore Collision in the Arcins Channel, Garonne River (October 2013)." *Hydraulic Model Report No. CH94/14* School of Civil Engineering, The University of Queensland, Brisbane, Australia (ISBN 9781742721033).	AUD$60.00		
LENG, X., and CHANSON, H. (2014). "Propagation of Negative Surges in Rivers and Estuaries: Unsteady Turbulent Mixing including the Effects of Bed Roughness." *Hydraulic Model Report No. CH93/13*, School of Civil Engineering, The University of Queensland, Brisbane, Australia, 108 pages (ISBN 9781742720944).	AUD$60.00		
WUTHRICH, D., and CHANSON, H. (2014). "Aeration and Energy Dissipation over Stepped Gabion Spillways: a Physical Study." *Hydraulic Model Report No. CH92/13*, School of Civil Engineering, The University of Queensland, Brisbane, Australia, 171 pages and 5 video movies (ISBN 9781742720944).	AUD$60.00		
WANG, H., and CHANSON, H. (2013). "Free-Surface Deformation and Two-Phase Flow Measurements in Hydraulic Jumps". *Hydraulic Model Report No. CH91/13*, School of Civil Engineering, The University of Queensland, Brisbane, Australia, 108 pages (ISBN 9781742720746).	AUD$60.00		
SIMON, B., and CHANSON, H. (2013). "Turbulence Measurements in Tidal Bore-like Positive Surges over a Rough Bed". *Hydraulic Model Report No. CH90/12*, School of Civil Engineering, The University of Queensland, Brisbane, Australia, 176 pages (ISBN 9781742720685).	AUD$60.00		
REUNGOAT, D., CHANSON, H., and CAPLAIN, B. (2012). "Field Measurements in the Tidal Bore of the Garonne River at Arcins (June 2012)." Hydraulic Model Report No. CH89/12, School of Civil Engineering, The University of Queensland, Brisbane, Australia, 121 pages (ISBN 9781742720616).	AUD$60.00		
CHANSON, H., and WANG, H. (2012). "Unsteady Discharge Calibration of a Large V-Notch Weir." *Hydraulic Model Report No. CH88/12*, School of Civil Engineering, The University of Queensland, Brisbane, Australia, 50 pages & 4 movies (ISBN 9781742720579).	AUD$60.00		

FELDER, S., FROMM, C., and CHANSON, H. (2012). "Air Entrainment and Energy Dissipation on a 8.9° Slope Stepped Spillway with Flat and Pooled Steps." *Hydraulic Model Report No. CH86/12*, School of Civil Engineering, The University of Queensland, Brisbane, Australia, 82 pages (ISBN 9781742720531).	AUD$60.00		
FELDER, S., and CHANSON, H. (2012). "Air-Water Flow Measurements in Instationary Free-Surface Flows: a Triple Decomposition Technique." *Hydraulic Model Report No. CH85/12*, School of Civil Engineering, The University of Queensland, Brisbane, Australia, 161 pages (ISBN 9781742720494).	AUD$60.00		
REICHSTETTER, M., and CHANSON, H. (2011). "Physical and Numerical Modelling of Negative Surges in Open Channels." *Hydraulic Model Report No. CH84/11*, School of Civil Engineering, The University of Queensland, Brisbane, Australia, 82 pages (ISBN 9781742720388).	AUD$60.00		
BROWN, R., CHANSON, H., McINTOSH, D., and MADHANI, J. (2011). "Turbulent Velocity and Suspended Sediment Concentration Measurements in an Urban Environment of the Brisbane River Flood Plain at Gardens Point on 12-13 January 2011." *Hydraulic Model Report No. CH83/11*, School of Civil Engineering, The University of Queensland, Brisbane, Australia, 120 pages (ISBN 9781742720272).	AUD$60.00		
CHANSON, H. "The 2010-2011 Floods in Queensland (Australia): Photographic Observations, Comments and Personal Experience." *Hydraulic Model Report No. CH82/11*, School of Civil Engineering, The University of Queensland, Brisbane, Australia, 127 pages (ISBN 9781742720234).	AUD$60.00		
MOUAZE, D., CHANSON, H., and SIMON, B. (2010). "Field Measurements in the Tidal Bore of the Sélune River in the Bay of Mont Saint Michel (September 2010)." *Hydraulic Model Report No. CH81/10*, School of Civil Engineering, The University of Queensland, Brisbane, Australia, 72 pages (ISBN 9781742720210).	AUD$60.00		
JANSSEN, R., and CHANSON, H. (2010). "Hydraulic Structures: Useful Water Harvesting Systems or Relics." *Proceedings of the Third International Junior Researcher and Engineer Workshop on Hydraulic Structures (IJREWHS'10)*, 2-3 May 2010, Edinburgh, Scotland, R. JANSSEN and H. CHANSON (Eds), Hydraulic Model Report CH80/10, School of Civil Engineering, The University of Queensland, Brisbane, Australia, 211 pages (ISBN 9781742720159).	AUD$60.00		
CHANSON, H., LUBIN, P., SIMON, B., and REUNGOAT, D. (2010). "Turbulence and Sediment Processes in the Tidal Bore of the Garonne River: First Observations." *Hydraulic Model Report No. CH79/10*, School of Civil Engineering, The University of Queensland, Brisbane, Australia, 97 pages (ISBN 9781742720104).	AUD$60.00		
CHACHEREAU, Y., and CHANSON, H., (2010). "Free-Surface Turbulent Fluctuations and Air-Water Flow Measurements in Hydraulics Jumps with Small Inflow Froude Numbers." *Hydraulic Model Report No. CH78/10*, School of Civil Engineering, The University of Queensland, Brisbane, Australia, 133 pages (ISBN 9781742720036).	AUD$60.00		
CHANSON, H., BROWN, R., and TREVETHAN, M. (2010). " Turbulence Measurements in a Small Subtropical Estuary under King Tide Conditions." *Hydraulic Model Report No. CH77/10*, School of Civil Engineering, The University of Queensland, Brisbane, Australia, 82 pages (ISBN 9781864999969).	AUD$60.00		
DOCHERTY, N.J., and CHANSON, H. (2010). "Characterisation of Unsteady Turbulence in Breaking Tidal Bores including the Effects of Bed Roughness." *Hydraulic Model Report No. CH76/10*, School of Civil Engineering, The University of Queensland, Brisbane, Australia, 112 pages (ISBN 9781864999884).	AUD$60.00		

CHANSON, H. (2009). "Advective Diffusion of Air Bubbles in Hydraulic Jumps with Large Froude Numbers: an Experimental Study." *Hydraulic Model Report No. CH75/09*, School of Civil Engineering, The University of Queensland, Brisbane, Australia, 89 pages & 3 videos (ISBN 9781864999730).	AUD$60.00		
CHANSON, H. (2009). "An Experimental Study of Tidal Bore Propagation: the Impact of Bridge Piers and Channel Constriction." *Hydraulic Model Report No. CH74/09*, School of Civil Engineering, The University of Queensland, Brisbane, Australia, 110 pages and 5 movies (ISBN 9781864999600).	AUD$60.00		
CHANSON, H. (2008). "Jean-Baptiste Charles Joseph BÉLANGER (1790-1874), the Backwater Equation and the Bélanger Equation." *Hydraulic Model Report No. CH69/08*, Div. of Civil Engineering, The University of Queensland, Brisbane, Australia, 40 pages (ISBN 9781864999211).	AUD$60.00		
GOURLAY, M.R., and HACKER, J. (2008). "Reef-Top Currents in Vicinity of Heron Island Boat Harbour, Great Barrier Reef, Australia: 2. Specific Influences of Tides Meteorological Events and Waves." *Hydraulic Model Report No. CH73/08*, Div. of Civil Engineering, The University of Queensland, Brisbane, Australia, 331 pages (ISBN 9781864999365).	AUD$60.00		
GOURLAY, M.R., and HACKER, J. (2008). "Reef Top Currents in Vicinity of Heron Island Boat Harbour Great Barrier Reef, Australia: 1. Overall influence of Tides, Winds, and Waves." *Hydraulic Model Report CH72/08*, Div. of Civil Engineering, The University of Queensland, Brisbane, Australia, 201 pages (ISBN 9781864999358).	AUD$60.00		
LARRARTE, F., and CHANSON, H. (2008). "Experiences and Challenges in Sewers: Measurements and Hydrodynamics." *Proceedings of the International Meeting on Measurements and Hydraulics of Sewers*, Summer School GEMCEA/LCPC, 19-21 Aug. 2008, Bouguenais, Hydraulic Model Report No. CH70/08, Div. of Civil Engineering, The University of Queensland, Brisbane, Australia (ISBN 9781864999280).	AUD$60.00		
CHANSON, H. (2008). "Photographic Observations of Tidal Bores (Mascarets) in France." *Hydraulic Model Report No. CH71/08*, Div. of Civil Engineering, The University of Queensland, Brisbane, Australia, 104 pages, 1 movie and 2 audio files (ISBN 9781864999303).	AUD$60.00		
CHANSON, H. (2008). "Turbulence in Positive Surges and Tidal Bores. Effects of Bed Roughness and Adverse Bed Slopes." *Hydraulic Model Report No. CH68/08*, Div. of Civil Engineering, The University of Queensland, Brisbane, Australia, 121 pages & 5 movie files (ISBN 9781864999198)	AUD$70.00		
FURUYAMA, S., and CHANSON, H. (2008). "A Numerical Study of Open Channel Flow Hydrodynamics and Turbulence of the Tidal Bore and Dam-Break Flows." *Report No. CH66/08*, Div. of Civil Engineering, The University of Queensland, Brisbane, Australia, May, 88 pages (ISBN 9781864999068).	AUD$60.00		
GUARD, P., MACPHERSON, K., and MOHOUPT, J. (2008). "A Field Investigation into the Groundwater Dynamics of Raine Island." *Report No. CH67/08*, Div. of Civil Engineering, The University of Queensland, Brisbane, Australia, February, 21 pages (ISBN 9781864999075).	AUD$40.00		
FELDER, S., and CHANSON, H. (2008). "Turbulence and Turbulent Length and Time Scales in Skimming Flows on a Stepped Spillway. Dynamic Similarity, Physical Modelling and Scale Effects." *Report No. CH64/07*, Div. of Civil Engineering, The University of Queensland, Brisbane, Australia, March, 217 pages (ISBN 9781864998870).	AUD$60.00		
TREVETHAN, M., CHANSON, H., and BROWN, R.J. (2007). "Turbulence and Turbulent Flux Events in a Small Subtropical Estuary." Report No. CH65/07, Div. of Civil Engineering, The University of Queensland, Brisbane, Australia, November, 67 pages (ISBN 9781864998993)	AUD$60.00		

MURZYN, F., and CHANSON, H. (2007). "Free Surface, Bubbly flow and Turbulence Measurements in Hydraulic Jumps." *Report CH63/07*, Div. of Civil Engineering, The University of Queensland, Brisbane, Australia, August, 116 pages (ISBN 9781864998917).	AUD$60.00		
KUCUKALI, S., and CHANSON, H. (2007). "Turbulence in Hydraulic Jumps: Experimental Measurements." *Report No. CH62/07*, Div. of Civil Engineering, The University of Queensland, Brisbane, Australia, July, 96 pages (ISBN 9781864998825).	AUD$60.00		
CHANSON, H., TAKEUCHI, M, and TREVETHAN, M. (2006). "Using Turbidity and Acoustic Backscatter Intensity as Surrogate Measures of Suspended Sediment Concentration. Application to a Sub-Tropical Estuary (Eprapah Creek)." *Report No. CH60/06*, Div. of Civil Engineering, The University of Queensland, Brisbane, Australia, July, 142 pages (ISBN 1864998628).	AUD$60.00		
CAROSI, G., and CHANSON, H. (2006). "Air-Water Time and Length Scales in Skimming Flows on a Stepped Spillway. Application to the Spray Characterisation." *Report No. CH59/06*, Div. of Civil Engineering, The University of Queensland, Brisbane, Australia, July (ISBN 1864998601).	AUD$60.00		
TREVETHAN, M., CHANSON, H., and BROWN, R. (2006). "Two Series of Detailed Turbulence Measurements in a Small Sub-Tropical Estuarine System." *Report No. CH58/06*, Div. of Civil Engineering, The University of Queensland, Brisbane, Australia, Mar. (ISBN 1864998520).	AUD$60.00		
KOCH, C., and CHANSON, H. (2005). "An Experimental Study of Tidal Bores and Positive Surges: Hydrodynamics and Turbulence of the Bore Front." *Report No. CH56/05*, Dept. of Civil Engineering, The University of Queensland, Brisbane, Australia, July (ISBN 1864998245).	AUD$60.00		
CHANSON, H. (2005). "Applications of the Saint-Venant Equations and Method of Characteristics to the Dam Break Wave Problem." *Report No. CH55/05*, Dept. of Civil Engineering, The University of Queensland, Brisbane, Australia, May (ISBN 1864997966).	AUD$60.00		
CHANSON, H., COUSSOT, P., JARNY, S., and TOQUER, L. (2004). "A Study of Dam Break Wave of Thixotropic Fluid: Bentonite Surges down an Inclined plane." *Report No. CH54/04*, Dept. of Civil Engineering, The University of Queensland, Brisbane, Australia, June, 90 pages (ISBN 1864997710).	AUD$60.00		
CHANSON, H. (2003). "A Hydraulic, Environmental and Ecological Assessment of a Sub-tropical Stream in Eastern Australia: Eprapah Creek, Victoria Point QLD on 4 April 2003." *Report No. CH52/03*, Dept. of Civil Engineering, The University of Queensland, Brisbane, Australia, June, 189 pages (ISBN 1864997044).	AUD$90.00		
CHANSON, H. (2003). "Sudden Flood Release down a Stepped Cascade. Unsteady Air-Water Flow Measurements. Applications to Wave Run-up, Flash Flood and Dam Break Wave." *Report CH51/03*, Dept of Civil Eng., Univ. of Queensland, Brisbane, Australia, 142 pages (ISBN 1864996552).	AUD$60.00		
CHANSON, H,. (2002). "An Experimental Study of Roman Dropshaft Operation : Hydraulics, Two-Phase Flow, Acoustics." *Report CH50/02*, Dept of Civil Eng., Univ. of Queensland, Brisbane, Australia, 99 pages (ISBN 1864996544).	AUD$60.00		
CHANSON, H., and BRATTBERG, T. (1997). "Experimental Investigations of Air Bubble Entrainment in Developing Shear Layers." *Report CH48/97*, Dept. of Civil Engineering, University of Queensland, Australia, Oct., 309 pages (ISBN 0 86776 748 0).	AUD$90.00		
CHANSON, H. (1996). "Some Hydraulic Aspects during Overflow above Inflatable Flexible Membrane Dam." *Report CH47/96*, Dept. of Civil Engineering, University of Queensland, Australia, May, 60 pages (ISBN 0 86776 644 1).	AUD$60.00		

CHANSON, H. (1995). "Flow Characteristics of Undular Hydraulic Jumps. Comparison with Near-Critical Flows." *Report CH45/95*, Dept. of Civil Engineering, University of Queensland, Australia, June, 202 pages (ISBN 0 86776 612 3).	AUD$60.00		
CHANSON, H. (1995). "Air Bubble Entrainment in Free-surface Turbulent Flows. Experimental Investigations." *Report CH46/95*, Dept. of Civil Engineering, University of Queensland, Australia, June, 368 pages (ISBN 0 86776 611 5).	AUD$80.00		
CHANSON, H. (1994). "Hydraulic Design of Stepped Channels and Spillways." *Report CH43/94*, Dept. of Civil Engineering, University of Queensland, Australia, Feb., 169 pages (ISBN 0 86776 560 7).	AUD$60.00		
POSTAGE & HANDLING (per report)	AUD$10.00		
GRAND TOTAL			

OTHER HYDRAULIC RESEARCH REPORTS

Reports/Theses	Unit price	Quantity	Total price
FELDER, S. (2013). "Air-Water Flow Properties on Stepped Spillways for Embankment Dams: Aeration, Energy Dissipation and Turbulence on Uniform, Non-Uniform and Pooled Stepped Chutes." *Ph.D. thesis*, School of Civil Engineering, The University of Queensland, Brisbane, Australia.	AUD$100.00		
REICHSTETTER, M. (2011). "Hydraulic Modelling of Unsteady Open Channel Flow: Physical and Analytical Validation of Numerical Models of Positive and Negative Surges." *MPhil thesis*, School of Civil Engineering, The University of Queensland, Brisbane, Australia, 112 pages.	AUD$80.00		
TREVETHAN, M. (2008). "A Fundamental Study of Turbulence and Turbulent Mixing in a Small Subtropical Estuary." Ph.D. thesis, Div. of Civil Engineering, The University of Queensland, 342 pages.	AUD$100.00		
GONZALEZ, C.A. (2005). "An Experimental Study of Free-Surface Aeration on Embankment Stepped Chutes." *Ph.D. thesis*, Dept of Civil Engineering, The University of Queensland, Brisbane, Australia, 240 pages.	AUD$80.00		
TOOMBES, L. (2002). "Experimental Study of Air-Water Flow Properties on Low-Gradient Stepped Cascades." *Ph.D. thesis*, Dept of Civil Engineering, The University of Queensland, Brisbane, Australia.	AUD$100.00		
CHANSON, H. (1988). "A Study of Air Entrainment and Aeration Devices on a Spillway Model." *Ph.D. thesis*, University of Canterbury, New Zealand.	AUD$60.00		
POSTAGE & HANDLING (per report)	AUD$10.00		
GRAND TOTAL			

CIVIL ENGINEERING RESEARCH REPORT CE

The Civil Engineering Research Report CE series is published by the School of Civil Engineering at the University of Queensland. Orders of any of the Civil Engineering Research Report CE should be addressed to the School Secretary.

School Secretary, School of Civil Engineering, The University of Queensland
Brisbane 4072, Australia
Tel.: (61 7) 3365 3619 Fax : (61 7) 3365 4599
Url: http://www.eng.uq.edu.au/civil/ Email: hodciveng@uq.edu.au

Recent Research Report CE	Unit price	Quantity	Total price
CALLAGHAN, D.P., NIELSEN, P., and CARTWRIGHT, N. (2006). "Data and Analysis Report: Manihiki and Rakahanga, Northern Cook Islands - For February and October/November 2004 Research Trips." *Research Report CE161*, Division of Civil Engineering, The University of Queensland (ISBN No. 1864998318).	AUD$10.00		
GONZALEZ, C.A., TAKAHASHI, M., and CHANSON, H. (2005). "Effects of Step Roughness in Skimming Flows: an Experimental Study." *Research Report No. CE160*, Dept. of Civil Engineering, The University of Queensland, Brisbane, Australia, July (ISBN 1864998105).	AUD$10.00		
CHANSON, H., and TOOMBES, L. (2001). "Experimental Investigations of Air Entrainment in Transition and Skimming Flows down a Stepped Chute. Application to Embankment Overflow Stepped Spillways." *Research Report No. CE158*, Dept. of Civil Engineering, The University of Queensland, Brisbane, Australia, July, 74 pages (ISBN 1 864995297).	AUD$10.00		
HANDLING (per order)	AUD$10.00		
GRAND TOTAL			

Note: Prices include postages and processing.

PAYMENT INFORMATION

1- VISA Card

Name on the card :	
Visa card number :	

Expiry date :	
Amount :	AUD$ .....

2- Cheque/remittance payable to: THE UNIVERSITY OF QUEENSLAND and crossed "Not Negotiable".

N.B. For overseas buyers, cheque payable in Australian Dollars drawn on an office in Australia of a bank operating in Australia, payable to: THE UNIVERSITY OF QUEENSLAND and crossed "Not Negotiable".

Orders of any Research Report should be addressed to the School Secretary.

School Secretary, School of Civil Engineering, The University of Queensland
Brisbane 4072, Australia - Tel.: (61 7) 3365 3619 - Fax : (61 7) 3365 4599
Url: http://www.eng.uq.edu.au/civil/ Email: hodciveng@uq.edu.au